UNIVERSITÀ
DEGLI STUDI
DI PADOVA

Sede amministrativa: Università degli studi di Padova

Dipartimento di Ingegneria Industriale

SCUOLA DI DOTTORATO DI RICERCA IN INGEGNERIA INDUSTRIALE
INDIRIZZO: INGEGNERIA CHIMICA, DEI MATERIALI E DELLA PRODUZIONE
CICLO XXVII

CO_2 CAPTURE WITH SOLID SORBENTS: MATERIALS CHARACTERIZATION AND REACTION KINETICS

Direttore della scuola: Ch.mo Prof. Paolo Colombo
Coordinatore d'indirizzo: Ch.mo Prof. Enrico Savio
Supervisore: Egr. Ing. Matteo Strumendo

Dottorando: Alberto Biasin

To my family, friends, loves and life

Foreword

The realization of the present work of thesis involved the intellectual and financial support of many people and institutions to whom the author is very grateful.
Most of the research activity that has led to this dissertation has been carried out at the Departments of Industrial Engineering and of Geoscience, at the University of Padova (Italy), under the supervision of Prof. Matteo Strumendo, and in collaboration with Prof. Gabriella Salviulo and Dr. Federico Zorzi. Part of the work was carried out at the Department of Physics at the Illinois Institute of Technology (IIT), Chicago, IL (U.S.A), during a 6-months stay under the supervision of Prof. Carlo U. Segre. During this period, significant and novel results were obtained thanks to the experimental work performed at the Advanced Photon Source (APS) facilities, at the Argonne National Laboratory, Argonne, IL (U.S.A). Specifically, work done at Argonne and use of the Advanced Photon Source, an Office of Science User Facility operated for the U.S. Department of Energy (DOE) Office of Science by Argonne National Laboratory, were supported by the U.S. DOE under contract no. DE-AC02-06CH11357.
Financial support to this study has been provided by the University of Padova and, in part, by the National Science Foundation under grant no. DMR-086935.
Additional support from Prof. Michele Modesti and Prof. Alessandro Martucci (Department of Industrial Engineering, University of Padova) concerning the provision of experimental instrumentation has to be mentioned as well.

This thesis is based primarily on the results discussed in the below listed publications. All the material reported is original unless explicit references to studies carried out by other people are indicated.

CONTRIBUTIONS IN INTERNATIONAL JOURNALS (published or in press)

A. Biasin, C.U. Segre, G. Salviulo, F. Zorzi, M. Strumendo (2015). Investigation of CaO-CO_2 reaction kinetics by in-situ XRD using synchrotron radiation. Chem. Eng. Sci., *in press*. DOI: 10.1016/j.ces.2014.12.058.

CONTRIBUTIONS IN INTERNATIONAL JOURNALS (submitted or in preparation)

A. Biasin, C.U. Segre, M. Strumendo (2015). $CaCO_3$ crystallite evolution during CaO carbonation: critical product layer measurement by in-situ SR-XRD. *In preparation*.

F. Zorzi, A. Biasin, M. Strumendo, G. Salviulo (2015). Investigation of CaO crystallite growth kinetics by in-situ XRPD. *In preparation*.

Abstract

The enormous anthropogenic emission of carbon dioxide is most likely one of the main reasons for the global warming and the climate change problems ([1], [2], [3]). Considering the continuing and progressively growing utilization of fossil fuels, mainly in the power generation sector where fossil fuel-based combustion and gasification power plants are predominant, the development and implementation of processes that avoid the associated CO_2 emissions must be urgently identified. Carbon dioxide capture and storage, commonly termed CCS, represents a range of technologies oriented to affordably and efficiently sequester carbon dioxide from these sources and would be a possible mid-term solution to mitigate the emissions of CO_2 into the atmosphere ([4]). However, the costs (especially in terms of penalties in the power plants efficiency) associated with the current industrially available CO_2 capture techniques, such as amine-based scrubbing, are prohibitively high, thus making the development of new CO_2 sorbents an highly important research challenge.

Among several strategies currently under investigation, calcium oxide (CaO), readily obtained through a calcination stage of naturally occurring calcium carbonate ($CaCO_3$), has been proposed as an alternative CO_2 solid sorbent that could significantly reduce the costs of carbon dioxide capture systems. The technique, widely discussed in the literature and recently reviewed by several authors ([5], [6], [7] and [8]), is based on the reversible reaction $CaO_{(s)} + CO_{2\,(g)} \leftrightarrow CaCO_{3\,(s)}$ and is applied through cyclic stages of carbonation and of calcination, offering a number of advantages. However, a few issues, including especially the decline of sorbent capacity when they are cycled through multiple CO_2 capture-and release stages, still call into question its widespread deployment on industrial applications. The improvement of this technology and the development of new calcium-based solid sorbents are currently a matter of study and, despite the apparent simplicity of the chemistry involved, several aspects of the carbonation reaction and its kinetics are still not clearly understood.

The determination of the surface reaction kinetic parameters is one of the open disputes. Several contributions investigating the carbonation reaction and its kinetics have reported thus far activation energies varying in a range of about 20 ÷ 30 kJ/mol ([9], [10]) and 70 ÷ 80 kJ/mol ([11], [12], [13], [14]); a few authors otherwise asserted that the carbonation

reaction has a zero-activation energy ([15], [16]). These values were estimated from CaO conversion versus time profiles obtained from CO_2 absorption analysis carried out in a wide range of operating conditions in terms of carbonation temperatures and CO_2 partial pressures and hence, the observed uncertainty in the mentioned activation energies is reasonably related to the quality of the experimental data. The accuracy of the experimental data is a questionable matter especially when the data are obtained through the thermo-gravimetric approach because, as well known, TGA experiments are typically affected by mass transfer limitations. The external diffusion is particularly important because it weighs on the gas (CO_2) diffusion towards the solid sorbent (CaO) surface that is essential to support the carbon dioxide mole consumption due to the chemical reaction. Even though several strategies can be applied to reduce the external mass diffusion during the CaO carbonation studied in a TGA system (typically increasing the gas flow rates), evidences of a complete removal of such resistance cannot be easily provided. In fact, the typical circumstance that at high gas flow rates the conversion versus time curves can show no changes when increasing the gas flow rate does not imply that the external mass diffusion resistance is eliminated, but only that such resistance cannot be further reduced in the TGA geometry and operating conditions used. Indeed, the local velocities reached around/inside a TGA crucible (especially above the sorbent particles contained in a common sample holder) could be low even when the average velocity in the furnace is increased by increasing the gas flow rate, so that the local velocities around/inside a TGA crucible cannot be increased enough to compensate the very high consumption rate of CO_2 due to the fast carbonation surface reaction. Therefore, alternative method has to be studied in order to measure CaO conversion versus time profile actually not limited by the external mass diffusion, and to check the validity of the thermo-gravimetric data currently available.

A second aspect concerns the structural properties characterizing the solid sorbent particles and how such properties can affect the CO_2 absorption performances of CaO. Since, CaO-CO_2 is a typical gas-solid reaction, it is most likely that specific surface and pore volume distribution can affect the reaction kinetics of CaO sorbent particles, as well as their absorption capacity. Several studies have been carried out to comprehend the carbonation reaction and kinetics in terms of these structural properties (porosity, specific surface, structural parameter, or the whole pore size distribution) through the development and

application of random pore/grain models ([15], [17], [10], [13], [18], [19]). Most of these contributions related the transition from the fast regime to the slow product-layer diffusion controlled regime, characterizing the CaO carbonation, to the filling of small pores and/or to the development of a critical carbonate layer, and focused the attention on the impact of the pore size distribution on the critical $CaCO_3$ product layer thickness, for which an unambiguous value or a direct measure has not been anyway proposed. Additionally, even though CaO and $CaCO_3$ are crystalline species and their crystalline structures could reasonably affect both the carbonation reaction kinetics and mechanism, very few contributions have been focused thus far to study their impact on the carbonation reaction, insomuch as the influence of $CaO/CaCO_3$ crystalline domain sizes on the carbonation reaction with CaO-based solid sorbents has never been investigated.

The research project summarized in this work of thesis has been focused on the investigation of the CaO carbonation reaction with the goal of clarifying these unresolved aspects.

Sorbent samples were first characterized by thermo-gravimetric analysis (TGA). CaO particles, directly produced in the TGA apparatus through stages of thermal decomposition in N_2 atmosphere (temperature range from 650°C and 900°C), were tested to investigate their reactivity in the CO_2 capture process, aiming at identifying the absorption specific rates, and confirming as common TGA analysis are reasonably affected by physical limitations, mainly mass transfer resistances. The TGA unit was fed with gas consisting of pure carbon dioxide or of a N_2/CO_2 mixture so that different CO_2 partial pressures were used within a range of 0.05 and 1 bar while carbonation temperatures were varied from 450°C up to 650°C.

Some CaO sorbent samples were also preliminary prepared through a stage of calcination realized in a separate muffle furnace. Different operating conditions in terms of calcination temperatures (especially 900°C) and residence times at high temperature (from few minutes up to some hours) were used in order to produce CaO sorbent samples with different structural properties, mainly in terms of porosity and specific surface area. In fact, these factors, which are closely related to the sorbent modifications due to high temperature treatments, reasonably affect the carbonation reaction. Specific surface area

measurements by N_2 adsorption were performed to complete the characterization of the samples by means of BET analysis. The samples were afterwards tested during CO_2 absorption processes carried out in the TGA unit under a gas flow of pure carbon dioxide (total pressure of 1 bar). Based on CaO conversions and the corresponding reaction rates measured, a simple reaction mechanism was applied to determine the kinetic parameters. An activation energy of about 45 kJ/mol was estimated, but it was reasonably associated to apparent kinetic rates. Moreover, the relationship between variation of the specific surface and porosity due to sintering and their effect on the carbonation reaction were not clearly quantify because of the uncertainty of the experimental data obtained, caused by the mass-transfer limitations that affected the TGA experiments.

The X-ray powder diffraction technique was therefore applied since it can provide an alternative method to the thermo-gravimetric analysis for studying the CaO-CO_2 reaction. X-ray diffraction experiments were carried out (in collaboration with the Department of Geosciences at the University of Padova) to determine the structural changes of the sorbent samples (namely phase evolution and crystallite size modifications) as a function of temperature and CO_2 partial pressure. Several tests were performed using a high temperature reaction chamber, with a controlled gas inlet composition, both during the thermal decomposition (calcination/regeneration) and during the absorption processes. Calcination experiments, carried out in a N_2 atmosphere (total pressure = 1 bar) and a temperature range varying between 650 and 950°C, allowed to observe that, after the complete decomposition of calcium carbonate precursor, the average crystallite size of CaO domains formed (approximately of 40 nm) considerably changes, when kept for long residence times at high temperatures. We also verified that even a low concentration of CO_2 in the calcination atmosphere promotes CaO crystal size growth during the $CaCO_3$ thermal decomposition and significantly increases the size of the nascent CaO crystalline domains. After the preparation stage of thermal decomposition, carbonation experiments using fresh calcines directly produced within the reaction chamber were performed. It was observed that differences in the crystallite size of the CaO samples apparently influence the solid sorbent reactivity in the following CO_2 capture process. At the same carbonation isotherm (temperatures applied were in the range of 400-650°C), with a CO_2 partial pressure of 1 bar, samples with a larger CaO crystal size (at the beginning of carbonation) showed a lower overall carbon dioxide absorption capacity, suggesting that the carbonation

reaction (kinetics) could be affected by initial CaO sorbent particle crystallite size. Unfortunately, the low time resolution provided by the available standard laboratory instrumentation was not sufficient to obtain detailed information about the transformations occurring in the sample particles, especially during the initial very fast stage of the carbonation reaction, whereas the surface chemical reaction should reasonably occur with negligible effects of the product layer diffusion.

Therefore, in-situ synchrotron radiation X-ray powder diffraction (SR-XRPD), performed at the Advanced Photon Source (APS) facilities of the Argonne National Laboratory, was finally applied to investigate the CaO carbonation reaction more in detail. A set of CO_2 absorption experiments were conducted in a high temperature reaction capillary with a controlled atmosphere (CO_2 partial pressure of 1 bar), in the temperature range between 450°C and 750°C using CaO based sorbents obtained by calcination of commercial calcium carbonate. The evolution of the crystalline phases during CO_2 uptake by the CaO solid sorbents was monitored for a carbonation time of 20 min as a function of the carbonation temperature and of the calcination conditions. The Rietveld refinement method was applied to estimate the calcium oxide conversion during the reaction progress and the average size of the initial (at the beginning of carbonation) calcium oxide crystallites. The measured average initial carbonation rate (in terms of conversion time derivative) of 0.280 s^{-1} (± 13.2% standard deviation) is significantly higher than the values obtained by thermo-gravimetric analysis and reported thus far in the scientific literature. Additionally, a dependence of the conversion versus time curves on the initial calcium oxide crystallite size was observed and a linear relationship between the initial CaO crystallite size and the calcium oxide final conversion was identified. The evolution of the $CaCO_3$ crystalline phase during the CaO carbonation was also investigated by means of the same technique. Maximum sizes of the calcium carbonate crystalline domains were observed in the $CaCO_3$ crystallite size versus time curves, (specifically during the first rapid stage of the carbonation) and were identified as the average values of the critical $CaCO_3$ product layer thickness. A relationship between this parameter and the corresponding calcium oxide conversion (at which the transition to the second slow reaction stage occurs), as well as a dependence of the carbonate product layer thickness with the initial CaO particle porosity, were found. Finally, $CaCO_3$ critical product layer thicknesses were used to estimate the initial specific surface areas of the CaO sorbent particles afterwards utilized to calculate

the kinetic parameters of the intrinsic surface carbonation reaction. A reaction rate constant of 1.89×10^{-3} mol/m^2 s, with zero-activation energy, has been obtained.

Riassunto

Negli ultimi anni, l'interesse riguardo al problema del riscaldamento globale è cresciuto notevolmente. La comunità scientifica è concorde sul fatto che i cambiamenti climatici osservati nel mondo sono correlati alle emissioni di gas serra, in modo particolare quelle di biossido di carbonio, che sono incrementate rapidamente in seguito allo sviluppo tecnologico ed industriale ([1], [2], [3]). Il settore principalmente coinvolto nelle emissioni di CO_2 è l'industria per la generazione di energia, dove gli impianti di combustione e gassificazione che sfruttano combustibili fossili sono predominanti e contano ancora oggi per più di un terzo di tutte le emissioni antropogeniche di CO_2. Se si considera la continua e progressiva crescita nell'utilizzo di questi combustibili in tale settore, lo sviluppo e l'implementazione di processi caratterizzati da ridotte (se non assenti) emissioni di CO_2 sono questioni che devono essere urgentemente affrontate.

La cattura e lo stoccaggio dell'anidride carbonica, comunemente denominato CCS (dall'inglese *Carbon dioxide Capture and Storage*), rappresenta l'insieme delle tecnologie orientate appunto a separare l'anidride carbonica dalle correnti gassose industriali (oltre che al trasporto e allo stoccaggio della stessa in formazioni geologiche o nel fondo degli oceani in modo tale da isolarla dall'atmosfera a lungo termine) in modo efficiente ed economicamente conveniente, e rappresenta una possibile soluzione a breve termine per mitigare le emissioni di CO_2 nell'atmosfera ([1], [4]). Tuttavia, i costi associati alle tecniche di cattura della CO_2 ad oggi disponibili (come ad esempio i processi basati su lavaggi con solventi amminici) sono proibitivamente alti (soprattutto in termini di penalizzazioni nell'efficienza energetica degli impianti di produzione di energia), e rendono quindi lo sviluppo di nuovi sorbenti per la cattura del biossido di carbonio una sfida molto importante nel panorama della ricerca scientifica.

Tra le diverse strategie attualmente investigate, l'ossido di calcio (CaO), facilmente ottenuto attraverso trattamenti termici di calcinazione del carbonato di calcio ampiamente disponibile e diffuso in natura, si presta come un sorbente solido particolarmente interessante/promettente che potrebbe ridurre in modo significativo i costi associati ai processi di cattura dell'anidride carbonica. La tecnica della cattura della CO_2 attraverso sorbenti solidi a base di ossido di calcio è ampiamente discussa in letteratura e recentemente è stata riassunta da alcuni autori ([5], [6], [7], [8]). Essa fa riferimento alla

reazione reversibile $CaO_{(s)} + CO_{2\ (g)} \leftrightarrow CaCO_{3\ (s)}$ e dovrebbe essere applicata attraverso cicli di calcinazione e carbonatazione, offrendo diversi vantaggi. Tuttavia, alcune problematiche, tra cui il progressivo declino nella capacità di cattura che tali sorbenti evidenziano all'aumentare del numero di cicli di assorbimento/desorbimento, ne mettono ancora in discussione l'utilizzo diffuso in applicazioni di scala industriale.

La ricerca di miglioramenti e lo sviluppo di nuovi sorbenti solidi sono quindi una materia di studio attuale e, nonostante l'apparente semplicità della reazione chimica coinvolta, diversi aspetti riguardanti la carbonatazione del CaO non sono stati definitivamente chiariti.

La determinazione dei parametri cinetici intrinseci della reazione di carbonatazione è una delle questioni aperte. La qualità della stima della costante cinetica della reazione superficiale (necessaria per progettare i reattori per la carbonatazione) dipende dall'accuratezza dei dati sperimentali (nello specifico delle curve di conversione vs. tempo) i quali, in tutti i contributi disponibili in letteratura, sono ottenuti (al meglio delle conoscenze dell'autore) tramite un approccio termo-gravimetrico ([15], [11], [12], [9], [10], o [21]). Tuttavia, è noto che misure TGA possono essere affette da limitazioni legate a resistenze al *mass transfer*, specialmente per quanto riguarda la diffusione esterna, per cui è ragionevolmente discutibile se i risultati finora riportati in letteratura siano realmente espressione della cinetica intrinseca oppure, diversamente, riproducano soltanto una cinetica di assorbimento della CO_2 apparente.

Un altro aspetto rilevante è la dipendenza della reazione di carbonatazione dalle proprietà strutturali del sorbente. Finora, diverse ricerche hanno focalizzato l'attenzione sull'impatto della porosità e della superficie specifica, o ancora sull'impatto della distribuzione della dimensione dei pori rispetto la reazione di carbonatazione e alla sua cinetica ([15], [17], [10], [13], [18], o [19]). Anche se la superficie specifica e la distribuzione della dimensione dei pori sono parametri probabilmente rilevanti nella determinazione della cinetica di una tipica reazione gas-solido come la carbonatazione del CaO, l'impatto delle dimensioni dei domini cristallini che formano le fasi di ossido di calcio e di carbonato sulle prestazioni dei sorbenti sono informazioni non ancora disponibili in letteratura quando ci si riferisce alla reazione di carbonatazione.

Il progetto di ricerca riassunto in questo lavoro di tesi è stato quindi focalizzato sullo studio della reazione di carbonatazione del CaO e sulla caratterizzazione dei sorbenti a base di

ossido di calcio, con l'obiettivo di chiarire questi aspetti emersi dalla letteratura, ancora poco risolti.

Dopo avere affrontato il problema del surriscaldamento globale e aver riassunto le inequivocabili evidenze scientifiche riguardanti i cambiamenti climatici già discusse in dettaglio nei report dell'*Intergovernmental Panel of Climate Change* (IPCC) ([1], [2], [3]), nel Capitolo 1 sono delineate le cause di tali cambiamenti ed la CCS viene presentata come una delle possibili strategie di mitigazione delle emissioni di CO_2, focalizzando l'attenzione sullo stato dell'arte in merito alle tecnologie CCS attualmente investigate.
Successivamente, viene presentata la tecnologia della cattura dell'anidride carbonica realizzata attraverso l'utilizzo di sorbenti solidi a base di ossido di calcio. Nel Capitolo 2 vengono quindi discussi gli aspetti fondamentali riguardanti la reazione di carbonatazione del CaO, descrivendo la sua termodinamica e il tipico comportamento caratterizzato da due differenti fasi di reazione ovvero, una parte iniziale veloce, controllata nei primi istanti dalla reazione chimica alla superficie, seguita da una seconda fase più lenta, controllata dalla diffusione della CO_2 attraverso lo strato di carbonato di calcio prodotto. Altresì, nel capitolo sono riportate considerazioni sugli aspetti irrisolti riguardanti la reazione di carbonatazione riscontrati in letteratura, come la caratterizzazione/misura del *critical product layer thickness*, il quale determina la transizione tra i due regimi di reazione menzionati, ed il problema della stima dei parametri cinetici intrinseci della carbonatazione. Infine, sono proposti i principali risultati dell'investigazione preliminare condotta attraverso l'applicazione dell'approccio termo-gravimetrico.
Campioni di sorbente (i.e. particelle di ossido di calcio) direttamente prodotti in TGA tramite decomposizioni termiche di $CaCO_3$ commerciale, in atmosfera di N_2 (range di temperatura tra i 650°C e i 900°C), sono state testate per analizzare la loro reattività nella fase di cattura del biossido di carbonio, con l'obiettivo di identificare le velocità di assorbimento specifiche e confermare come i tradizionali esperimenti in TGA siano affetti da limitazioni fisiche, specialmente resistenze legate a fenomeni di *mass transfer*. Questi esperimenti sono stati condotti alimentando un classico strumento TGA sia con CO_2 pura, sia con miscele N_2/CO_2 in modo da variare la pressione parziale di anidride carbonica in un intervallo compreso tra 0.05 bar e 1 bar, e imponendo isoterme a diverse temperature di carbonatazione, fissate tra i 450°C e i 650°C.

Alcuni campioni di sorbente sono stati anche preparati attraverso fasi di calcinazione realizzate separatamente in un forno a muffola. Diverse condizioni operative sono state utilizzate in termini di temperature di calcinazione (principalmente 900°C) e tempi di residenza a tali temperature (da pochi secondi a qualche ora), in modo da produrre particelle di ossido di calcio caratterizzate da differenti proprietà strutturali, specialmente in termini di porosità e superficie specifica. Infatti, tali fattori, che sono strettamente legati alle modificazioni strutturali alle quali questi sorbenti sono soggetti per effetto dei trattamenti termici ad alta temperatura, ragionevolmente influenzano la reazione di carbonatazione. Per completare la caratterizzazione dei sorbenti così prodotti si sono eseguite dapprima misure di superficie specifica attraverso adsorbimento di N_2 e analisi BET, e in seguito se n'è testata la capacità di assorbimento di CO_2 in TGA con flussi di anidride carbonica (pressione totale di 1 bar). Sulla base dei profili di conversione e delle corrispondenti velocità di reazione, un semplice modello cinetico ([9]) è stato utilizzato per determinare i parametri della cinetica intrinseca. Anche se ragionevolmente associabile ad una cinetica di reazione apparente, un'energia di attivazione di circa 45 kJ/mol è stata stimata.

A seguito dell'incertezza sui dati sperimentali ottenuti e connessi a limitazioni legate a fenomeni di *mass transfer*, la tecnica di diffrazione ai raggi X su polveri è stata quindi applicata come metodo alternativo all'analisi termo-gravimetrica nello studio della reazione tra CaO e CO_2.

In particolare, nel Capitolo 3 è riportata una piccola descrizione dei principali fondamenti teorici alla base di questa tecnica; successivamente sono discussi i principali risultati raccolti durante una fase di studio realizzata in collaborazione con il dipartimento di Geoscienze dell'Università di Padova. Esperimenti di diffrazione in–situ sono stati condotti per determinare le variazioni strutturali che interessano i sorbenti solidi (in modo particolare, l'evoluzione nel tempo delle fasi cristalline (i.e. composizione) e le variazioni nelle dimensioni dei domini cristallini che caratterizzano le fasi stesse) in funzione della temperatura e della pressione parziale di anidride carbonica. Diversi esperimenti sono stati eseguiti usando una camera di reazione, applicata ad un diffrattometro da laboratorio, che ha permesso di controllare la composizione gassosa del sistema sia durante la fase di decomposizione/rigenerazione, sia durante il processo di assorbimento, nonché la temperatura del materiale testato. Esperimenti di calcinazione sono stati condotti anche qui

in atmosfera di N_2 (pressione totale di 1 bar) e in un intervallo di temperature tra i 650°C e i 950°C, ed hanno permesso di osservare che dopo la decomposizione completa del carbonato di calcio usato come precursore le dimensioni medie dei domini cristallini di CaO di neo formazione (approssimativamente nell'ordine dei 40 nm) cambiano considerevolmente quando il materiale è mantenuto ad alte temperature per lunghi tempi di permanenza. Inoltre, si è verificato che anche piccole concentrazioni di CO_2 nell'atmosfera nella quale è condotta la fase di decomposizione favoriscono l'accrescimento dei cristalliti di ossido di calcio, tanto che le dimensioni dei nascenti domini cristallini di CaO risultano notevolmente aumentate rispetto al caso di calcinazioni condotte in atmosfera inerte. Prove di carbonatazione hanno invece evidenziato che differenze nella dimensione iniziale (ovvero, all'inizio della carbonatazione) dei domini cristallini di ossido di calcio apparentemente sembrano influenzare la reattività del campione di sorbente solido durante il processo di assorbimento della CO_2: a parità d'isoterma di carbonatazione (temperature tra i 450°C e i 650°C), con pressioni parziali di CO_2 di 1 bar, campioni costituiti da cristalliti più grandi hanno infatti mostrato una capacità di assorbimento della CO_2 più bassa raggiungendo, al termine di esperimenti di carbonatazione nell'ordine dei 120 min, conversioni inferiori. Altresì, questa evidenza rimane confermata anche all'aumentare del numero di cicli di calcinazione/carbonatazione.

Purtroppo, la bassa risoluzione temporale caratterizzante la strumentazione di laboratorio disponibile non è stata sufficiente per ottenere informazioni dettagliate sulle trasformazioni che avvengono nella struttura cristallina delle particelle di sorbente, soprattutto durante la fase iniziale (molto veloce) della carbonatazione laddove la reazione alla superficie (i.e. cinetica intrinseca) ragionevolmente ha luogo con trascurabili effetti di diffusione attraverso il *product layer* di carbonato.

Per approfondire la caratterizzazione della carbonatazione del CaO attraverso la diffrazione dei raggi X si è pertanto scelto di incrementare le potenzialità della tecnica con l'utilizzo della radiazione da sincrotrone. Nel Capitolo 4 sono presentati i risultati sulla caratterizzazione della reazione tra CaO e CO_2 ottenuti da esperimenti di diffrazione ai raggi X in-situ condotti in collaborazione con le strutture dell'Advanced Photon Source (APS) presso l'Argonne National Laboratory (Argonnne, IL, U.S.A). Un set di esperimenti di cattura della CO_2 è stato completato utilizzando un sistema con capillare riscaldato appositamente sviluppato ([20]) per condurre prove di diffrazione da polveri controllando

l'atmosfera di reazione (pressioni parziali di CO_2 di 1 bar) e la temperatura (tra i 450°C e i 750°C), per seguire l'evoluzione delle fasi cristalline di CaO e $CaCO_3$ durante il processo di carbonatazione di particelle di ossido di calcio prodotte per decomposizione termica di carbonato di calcio commerciale. Il metodo di raffinamento Rietveld è stato poi applicato sia per quantificare la conversione dell'ossido di calcio durante il procedere della reazione, sia per stimare la dimensione media dei domini cristallini di CaO all'inizio della carbonatazione. Dai profili di conversione è stata valutata una velocità media iniziale della carbonatazione (espressa in termini di derivata della conversione rispetto al tempo) pari a 0.280 s^{-1} (deviazione standard di ± 13.2%) che è risultata significativamente più alta rispetto ai valori ottenuti da analisi termo-gravimetriche e riportati finora in letteratura ([9], [15] o [12]). E' stata inoltre osservata una dipendenza dei profili di conversione rispetto al tempo dalla dimensione iniziale dei cristalliti di ossido di calcio, come pure è stata identificata una relazione lineare tra questa grandezza e la conversione finale. Analogamente, anche l'evoluzione del carbonato di calcio durante la fase di assorbimento della CO_2 è stata monitorata: dimensioni massime dei domini cristallini di $CaCO_3$ sono state osservate nei profili del *crystallite size* del carbonato in funzione del tempo (in particolare durante la prima rapida fase della reazione), e sono state identificate come i valori medi del *critical product layer thickness*. Una relazione tra questo parametro e le corrispondenti conversioni dell'ossido di calcio, alle quali si può ragionevolmente associare la transizione alla seconda fase caratteristica della carbonatazione (i.e. regime controllato dalla diffusione della CO_2 attraverso lo strato di prodotto), è stata individuata, come anche tra il *critical product layer thickness* e la porosità iniziale delle particelle di sorbente. Infine, i valori individuati sono stati usati per stimare la superficie specifica iniziale delle particelle di CaO utilizzate negli esperimenti di carbonatazione; tali superfici sono quindi state usate nella stima dei parametri cinetici intrinseci della reazione di carbonatazione, ottenendo una costante di reazione pari a circa 1.89×10^{-3} mol/m^2 s, con energia di attivazione nulla.

Contents

List of Figures

List of Tables

Introduction

In recent years, interest in the global warming problem has been growing noticeably. The scientific community agrees that climate changes worldwide observed are related to greenhouse gas (GHGs) emissions from flue gases and other sources, most prominently to carbon dioxide emissions, which have increased rapidly due to technological and industrial development ([1], [2], [3]). The main industrial sector involved in CO_2 emissions is the power generation industry, in particular power plants based on fossil fuel combustion and coal gasification, that still account for about one third of all anthropogenic CO_2 emissions. To attenuate the rate and magnitude of climate change, mitigation policies and/or the development of new practices oriented to affordably and efficiently remove the CO_2 from industrial gas streams must be adopted ([2]). The carbon dioxide capture and storage (CCS) is one of these strategies and has the potential of reducing the GHSs emissions, especially CO_2. Among carbon dioxide capture approaches applicable to existing large point sources of CO_2, a promising cost effective technology under investigation is based on the carbonation reaction of calcium oxide. Even though attention has been paid in literature to this reaction and to its kinetics ([15], [11], [12], [14], [9], [10], [13], [21], [18], [22], [23], or [19]), several aspects of the carbonation reaction are still not clearly understood.

The determination of the surface reaction kinetic parameters can be considered one of these aspects. The quality of the estimated surface reaction rate constants (required to design carbonator reactors) is determined by the accuracy of the experimental data, specifically of the conversion versus time curves, that in all the contributions available in literature investigating the intrinsic kinetics of the carbonation reaction are obtained (to the best of author's knowledge) by the thermo-gravimetric approach ([15], [11], [12], [9], [10], or [22]). However, it is known that TGA measurements can be affected by gas phase mass transfer limitations, especially external mass diffusion, so that is reasonably questionable whether the results thus far reported in literature are a real expression of the intrinsic kinetics or, otherwise, they reproduce an apparent kinetic rate of the CO_2 absorption process.

Another relevant aspect is the dependence of the carbonation reaction on the sorbent structural properties. So far, many contributions have focused attention on the impact of porosity and specific surface area, or on the impact of the pore size distribution on the

carbonation reaction and its kinetics ([15], [17], [10], [13], [18] or [19]). Even though the specific surface area and the pore volume distribution are most likely relevant parameter in determining the kinetics of a non-catalytic gas-solid reaction such as the CaO carbonation, the impact of the calcium oxide and calcium carbonate crystallite sizes on the sorbent performances are pieces of information not available in the literature when referring to the carbonation reaction with CaO-based solid sorbents.

Therefore, the research project resulting in this dissertation aimed to clarify these unresolved issues. After a preliminary study of the carbonation reaction by means of the TGA analysis, mainly oriented to familiarize with the observations reported in the literature, a new approach in the investigation of CaO-CO_2 reaction kinetics is proposed and the estimate of novel kinetic parameters has been obtained. Specifically, we applied the in-situ X-ray powder diffraction technique (XRPD) to investigate the effect of the initial (at the beginning of carbonation) CaO crystallite size on the carbonation kinetics and to obtain a relationship between CaO conversion and initial CaO crystallite size. Additionally, since it is likely that the carbonate crystallite growth kinetics can play a significant role in understanding the kinetics of carbonation (a reaction with a crystalline product layer whose growth is a function of the crystallite growth), the influence of the average size of $CaCO_3$ crystalline domains on the carbonation reaction and kinetics has also been investigated.

The Chapter 1 deals with the global warming problem, summarizing the scientific and unequivocal evidences of the climate change discussed in details by IPCC ([1], [2], [3]). Then, the causes of change are reported and the CCS is presented as one of the prospective mitigation strategies, focusing the attention on the state-of-the-art concerning the current CCS technologies under investigation.

Afterwards, the carbon dioxide capture performed using CaO-based solid sorbents is discussed. Thus, Chapter 2 presents the fundamental aspects of the carbonation reaction, describing its thermodynamics and the typical behavior of the reaction that is characterized by two different stages: an initial fast stage controlled in the early instants by the surface reaction, followed by a second slower product layer diffusion controlled stage. Moreover, the chapter reports considerations about the unresolved issues about the carbonation reaction such as, the characterization/measurement of the critical product layer thickness,

which determines the transitions between the two mentioned stages, and the problem of the estimate of the surface reaction (i.e. intrinsic kinetics) kinetic parameters. Finally, the results of a preliminary investigation carried out through the thermo-gravimetric approach are discussed.

Chapter 3 deals instead with the characterization/investigation of the carbonation reaction by means of the X-ray Powder diffraction (XRPD) technique. A short description of the main theoretical basics regarding this analysis is reported. Afterwards, the results obtained during a preliminary study are presented and discussed. Particularly, in this chapter the main issues of a standard lab-scale diffractometer, which led to the choice of improving the investigation of the carbonation reaction are underlined.

Finally, in the Chapter 4 the improvements in the investigation of CaO-CO_2 reaction by means of X-ray powder diffraction technique are considered, especially describing in detail the analysis carried out through the use of synchrotron radiation. Specifically, the in-situ X-ray powder diffraction experiments performed in collaboration with the Advanced Photon Source (APS) facilities, at the Argonne National Laboratory, Argonne, IL, (U.S.A.), are described. It is pointed out how the time-resolved X-ray powder diffraction using synchrotron radiation (SR-XRPD) can be applied to investigate the kinetics of the chemical transformations and the microstructural evolution of the CaO samples during the CO_2 absorption process, in order to identify relationships between the calcium oxide conversion and the calcium oxide/calcium carbonate average crystallite size.

Chapter 1

The global climate change and the CCS technology

In the last 150 years, atmospheric carbon dioxide levels have increased alarmingly, correlating with the increase of the anthropogenic industrial activities. Elevated CO_2 levels have caused global warming, or more generally global climate change, with more and more devastating effects on the environment. The natural mechanisms that should reduce the increase of atmospheric CO_2 levels (namely, ocean uptake, photosynthesis, weathering) are currently not able to keep up with human "progress", which results in an excess of the CO_2 concentration in the atmosphere. To reduce the CO_2 emissions and to limit its effect on climate, mitigation actions must to be adopted.

The chapter aims to give an overview about the causes and impacts of the global climate change problem, extensively discussed by the Working Groups of the Intergovernmental Panel of Climate Change (IPCC) ([1], [2], [3]), and already summarized by the author's research group co-workers in previous works ([24], [25]). It represents the primary motivation of the subject discussed in this thesis, namely the investigation of carbon dioxide capture/sequestration performed with CaO-based solid sorbent, which is one of the prospective actions in the Carbone Capture and Storage (CCS) context, focused on reducing carbon dioxide emissions from industrial gas streams.

1.1 Definition of climate change

Climate change is defined as a change in the state of the climate identifiable by changes in the mean and/or the variability of its properties and that persists for an extended period, typically decades or longer ([2]). It refers to any change in climate over the time, due to both natural variability and as result of human activities ([2]), but its consideration is not unique, since for the United Nations Framework Convention on Climate Change (UNFCCC) the climate change refers specifically to a change of climate attributable

directly or indirectly to human activities, that alter the composition of the global atmosphere and that additionally affect the natural climate variability observable over comparable time periods ([2]). The international organism that collects and analyzes climate change data is the Intergovernmental Panel on Climate Change (IPCC). Instituted in 1988 by the World Meteorological Organization (WMO) and by the United Nations Environmental Program (UNEP), it provides a comprehensive assessment of the physical science basis of climate change, and produces scientific, technical and socioeconomic guidelines oriented to understand how human activities have influenced global warming/climate change and how these could be controlled/mitigated.

1.1.1 Observed changes in the climate system

The evidences of climate change derive on the observations of the atmosphere, land, oceans and cryosphere. Observations of the climate system are based on direct measurements and remote sensing from satellites and other platforms. Global-scale observation, which began in the mid-19th century for temperature and other variables thanks to the development of the new instrumental era, have provided more comprehensive and diverse sets of information available starting from 1950s, as well as paleo-climate reconstructions that extend some records back hundreds to millions of year. Together, all the information collected provide a comprehensive view of the variability and long-term changes in the atmosphere, oceans, cryosphere and land surface, allowing us to project in the future the evolution of the planet's climate change.

The warming of the climate system is unequivocal as is evident from the increase in global average air and ocean temperatures, widespread melting of snow and ice and rising global average sea level ([1], [2], [3]). Global mean surface air temperatures over land and oceans have increased over the last 100 years. The temperature increase is widespread over the globe, with stronger effect at most high northern latitude and with land regions that warm faster than the oceans. The globally averaged combined land and ocean surface temperature data, calculated by a linear trend, show a warming of 0.85°C over the period 1880 to 2012 ([3]). As highlight in Figure 1.1a, the total increase between the average of the 1850-1900 period and the 2003-2012 period has been estimated equal to 0.78°C whereas, from 1906 to 2005, the increase of the superficial mean global temperature was

limited at 0.74°C ([2]). For the longest period for which calculation of regional trends is sufficiently complete (1901 to 2012), almost the entire global has experienced surface warming (Figure 1.1b).

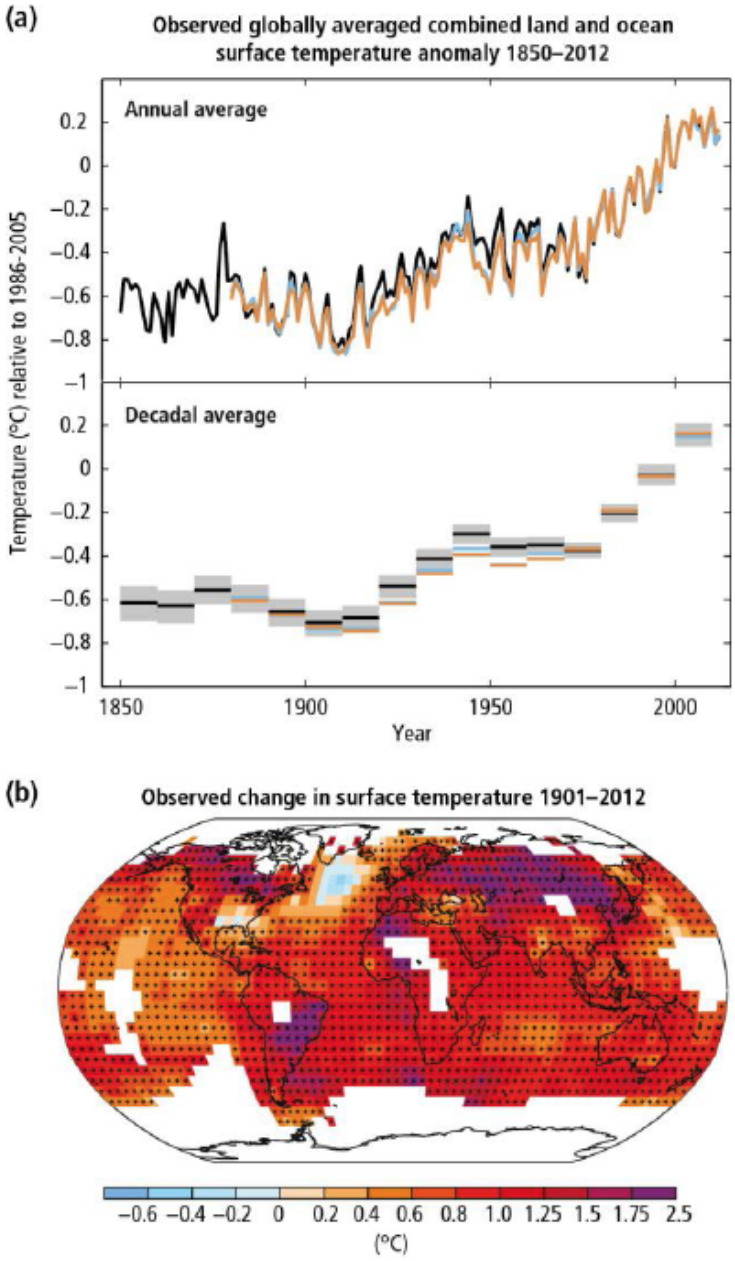

Figure 1.1: *(a) Observed global mean combined land and ocean surface temperature anomalies, from 1850 to 2012 from three data sets. Top panel: annual mean values. Bottom panel: decadal mean values including the estimate of uncertainty. Anomalies are relative to the mean of 1961−1990. (b) Map of the observed surface temperature change from 1901 to 2012. Source: Working group I contribution to the fifth assessment report of IPCC 2013 (*[26]*).*

Accordingly, temperature measurements in the oceans show a continuing increase in the heat content: on a global scale, the ocean warming is largest near the surface, with a warming rate of about 0.11°C per decade in the upper 75 m over the period 1971 to 2010 ([3]) (Figure 1.2).

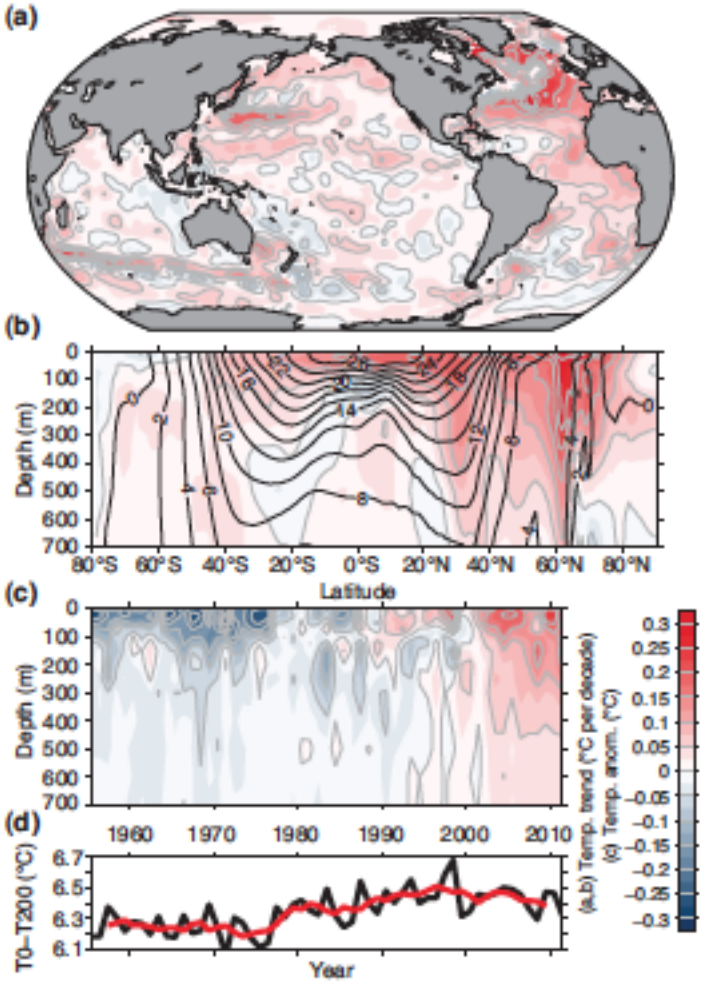

Figure 1.2: (a) *Depth-averaged 0 to 700 m temperature trend for 1971–2010. (b) Zonally averaged temperature trends for 1971–2010 with zonally averaged mean temperature over-plotted (black contours in degrees Celsius). (c) Globally averaged temperature anomaly relative to the 1971–2010 mean. (d) Globally averaged temperature difference between the ocean surface and 200 m depth (black: annual values, red: 5-year running mean). Source: Working group I contribution to the fifth assessment report of IPCC 2013 (*[26]*).*

Even though the relatively sparse sampling before 1970s prevents to determine with sufficient certainty changes prior this period, it is likely that the upper part of the oceans

(0-700 m) warmed from 1870s, as well as, based on 5-year average, it has been recently estimated that deeper in the oceans, waters from 700 to 2000 m have warmed by 0.015°C per decade on average between 1957 to 2009, and from 3000 m to the bottom from 1992 to 2005, with the largest warming observable in the Southern Hemisphere (Figure 1.3).

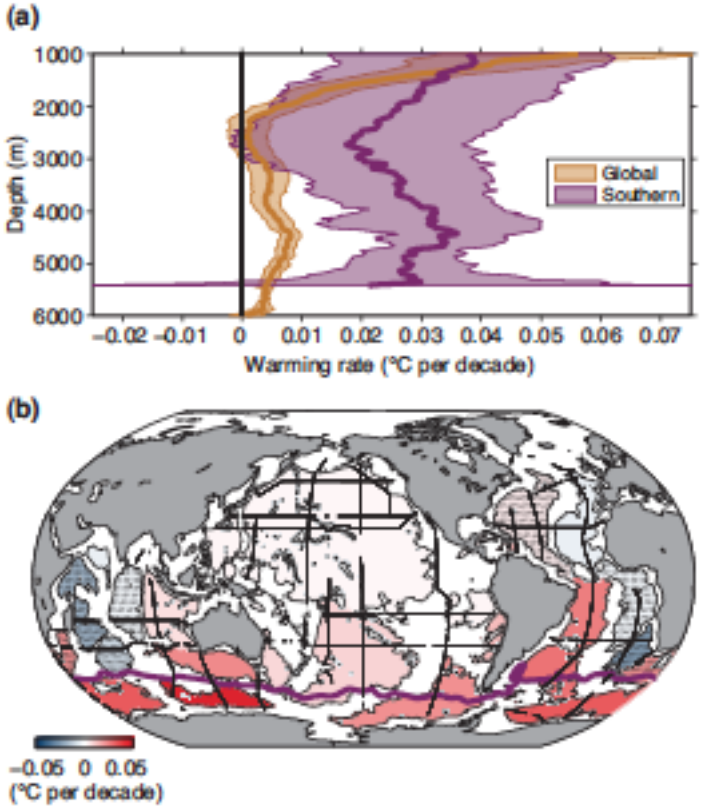

Figure 1.3: *(a) Areal mean warming rates (°C per decade) versus depth both global (orange) and south of the Sub-Antarctic Front (purple), centred on 1992–2005. (b) Mean warming rates (°C per decade) below 4000 m (color bar) estimated for deep ocean basins (thin black outlines), centred on 1992–2005. The position of the Sub-Antarctic front (purple line) is shown. Source: Working group I contribution to the fifth assessment report of IPCC 2013 (*[26]*).*

The rise of air and water mean global temperatures have affected other climate aspects, as the sea level and the snow and ice extent. Sea level data indicate a transition in the late 19th to the early 20th century from relative low mean rates of rise over the previous two millennia to higher rates of rise. Over the period 1901-2010, global average sea level rose by 0.19 m (Figure 1.4a), with a mean rate of increase estimated of about 1.7 mm/yr between 1901 and 2010, 2.0 mm/yr between 1971 and 2010, and 3.2 mm/yr between 1993

and 2010 ([2], [3]). Tide-gauge and satellite altimeter data are consistent regarding the higher rate of the latter period (Figure 1.4b) ([26]).

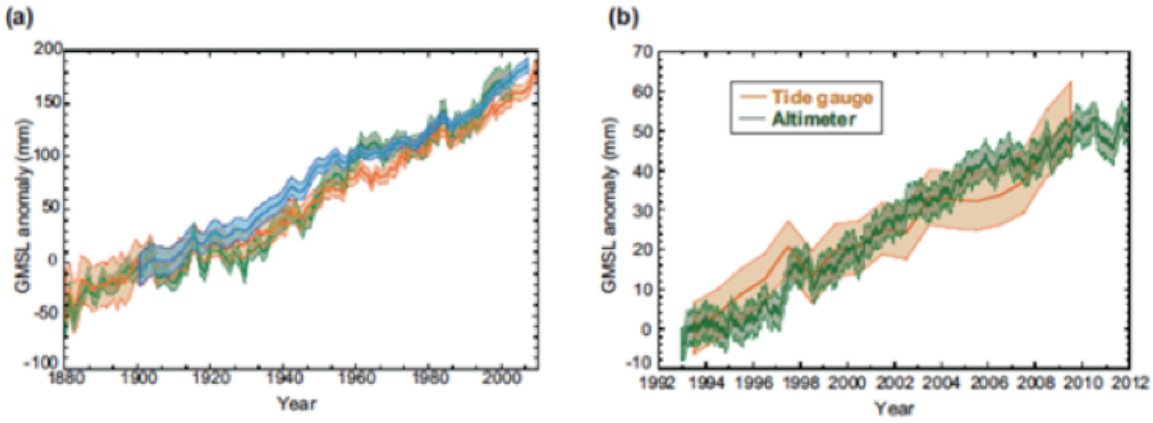

Figure 1.4: *(a) Yearly global average mean sea level (GMLS, in mm) from different measuring approaches. (b) GMSL (1993–2010) from tide gauges and altimetry with seasonal variations removed and smoothed with a 60-day running mean. Source: Working group I contribution to the fifth assessment report of IPCC 2013 (*[26]*).*

Although, glacier mass loss and ocean thermal expansion from warming together can explain about 75% of the observed global mean sea level rise since the early 1970s, over the period 1993 to 2010 global mean sea level rise is consistent with the sum of the other observed contributions from ocean thermal expansion due to warming (1.1 mm/yr), from changes in glaciers (0.76 mm/yr), Greenland ice sheet (0.33 mm/yr), Antarctic ice sheet (0.27 mm/yr), and land water storage (0.38 mm/yr). The sum of these contributions is roughly 2.8 mm/yr ([26]).

Observations concerning glaciers underline that they lost mass and contributed to sea level rise throughout the 20th century. Nevertheless, glaciers are continuing to shrink almost worldwide. The average rate of ice loss from glaciers around the world, excluding glaciers on the periphery of the ice sheets, was very likely estimated around 226 Gt/yr and 275 Gt/yr, respectively over the periods 1971 to 2009, and 1993 to 2009 ([3], [26]). The average rate of ice loss from the Greenland ice sheet has substantially increased, resulting in a larger mass loss over 2002 to 2011 (215 Gt/yr) than over 1992 to 2011 (34 Gt/yr). The mean rate of ice loss from the Antarctic ice sheet has increased from about 30 Gt/yr over the period 1992-2001 to approximately 147 Gt/yr over the period 2002 to 2011 ([3], [26])

(Figure 1.5). The annual mean Arctic sea ice extent decreased over the period 1979 to 2012 with a rate that was approximately in the range from 3.5 to 4.1 % per decade (range of 0.45 to 0.51 million km^2 per decade), and very likely in the range 9.4 to 13.6% per decade (range of 0.73 to 1.07 million km^2 per decade) for the summer sea ice minimum (perennial sea ice).

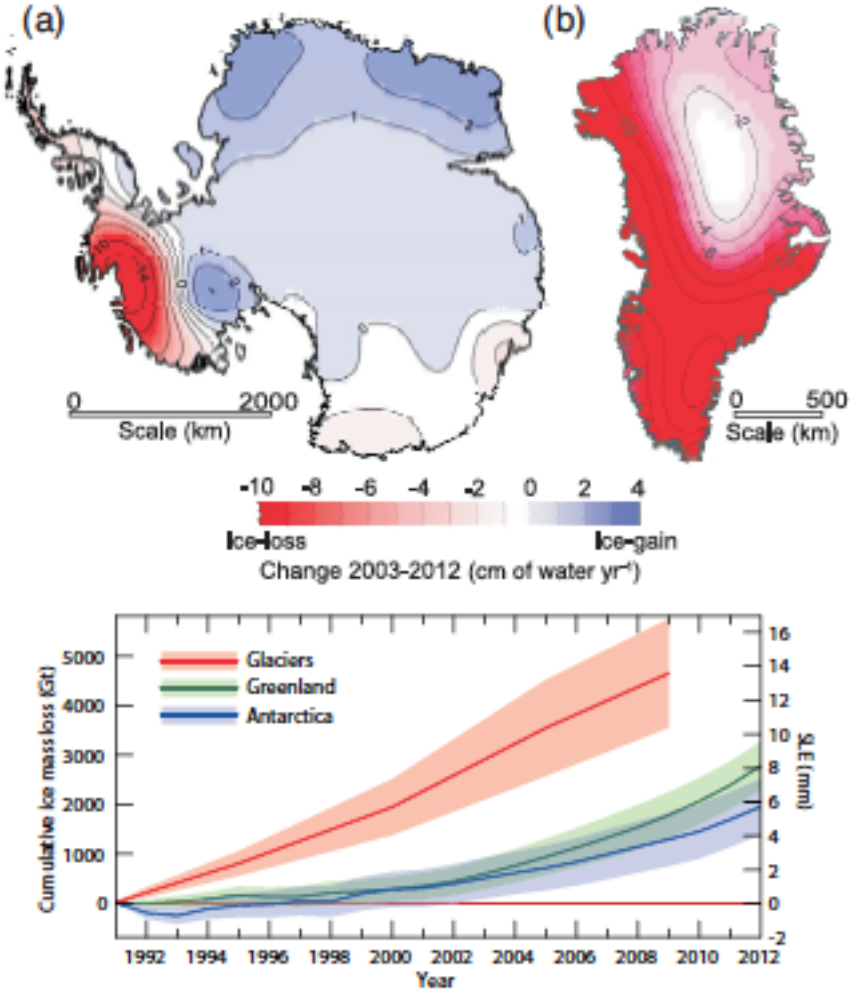

Figure 1.5: *(Top) Distribution of ice loss determined from Gravity Recovery and Climate Experiment (GRACE) time-variable gravity for (a) Antarctica and (b) Greenland, shown in centimeters of water per year for the period 2003-2012. (Bottom) The assessment of the total loss of ice from glaciers and ice sheets in terms of mass (Gt) and sea level equivalent (SLE, in mm) from 1992. The contribution from glaciers excludes those on the periphery of the ice sheets. Source: Working group I contribution to the fifth assessment report of IPCC 2013 (*[26]*).*

Additionally, there is very high confidence that the extent of Northern Hemisphere snow cover has decreased since the mid-20th century by 1.6% per decade during spring, and 11.7% per decade during summer, over the 1967 to 2012 period. Permafrost temperatures have also increased in most regions of the Northern Hemisphere since the early 1980s, with reductions in thickness and areal extent in some regions. The increase in permafrost temperatures has occurred in response to increased surface temperature and changing snow cover ([2], [3], [26]).

Because of these unprecedented, anomalous and unpredicted environmental transformations, other changes in many extreme weather and climate events have been also observed since about 1950s. Although confidence in precipitation change averaged over global land areas is low prior this period, it was estimated that precipitations averaged over the mid-latitude land areas of the Northern Hemisphere have increased since the early of 20th century, as shown in Figure 1.6 ([2], [3], [26]).

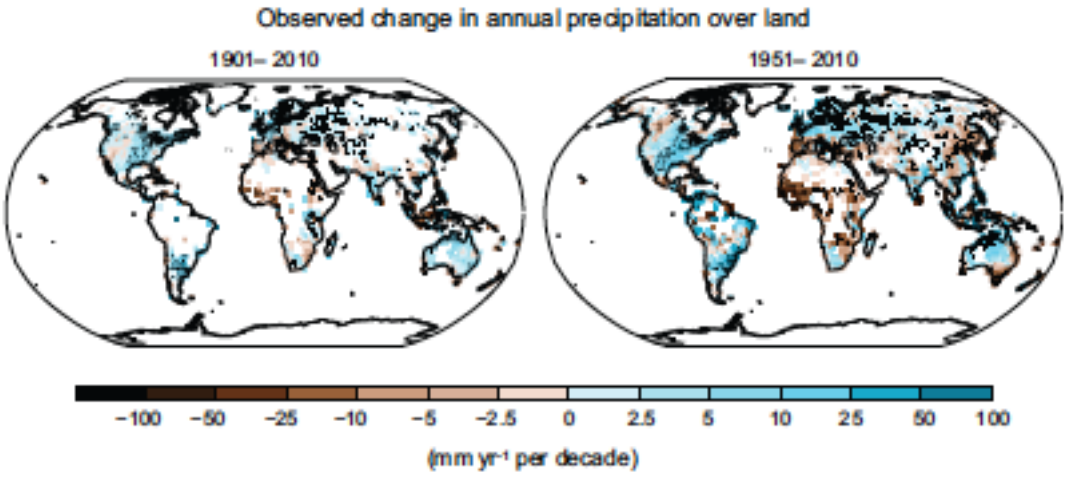

Figure 1.6: *Maps of observed precipitation change from 1901 to 2010 and from 1951 to 2010. Source: Working group I contribution to the fifth assessment report of IPCC 2013 (*[26]*).*

Frequency of heavy precipitations has increased over most areas as well as the incidence of extreme high sea levels at a broad range of sites worldwide ([2]). Specifically, from 1900 to 2005, the frequency and/or intensity of heavy precipitation events increased significantly in eastern parts of the North and South America, northern Europe and northern and central Asia, whereas precipitation declined in the Sahel, in the Mediterranean, in southern Africa and in parts of southern Asia ([2]). Globally, the area affected by drought has increased

since the 1970s ([2]) even though there are more land regions where the number of heavy precipitation events has increased than where it has decreased. Additionally, some other weather events have changed in frequency and/or intensity over the last 50 years such as cold days, cold nights and frosts that have become less frequent over most land areas, while the number of warm days and nights has increased on the global scale, as well as heat waves, fluvial floods and tropical cyclone activity ([3]).

1.1.2 Climate change impacts

In front of all the climate changes monitored in the recent decades, irrespective of their causes, it is widely recognized that they have determined impacts on natural and human systems on all continents and across the oceans, indicating how these "dimensions" are sensitive to climate transformations ([2], [3]). Evidence of observed climate-change impacts is strongest and most comprehensive for the nature, insomuch as more than 89% of the significant variations in the physical and biological systems are consistent with a response expected to the occurring global warming ([2]). Many terrestrial, freshwater, and marine species have shifted their geographic ranges, seasonal activities, migration patterns, abundances, and species interactions in order to adapt themselves to the ongoing climate change. Some warm-water corals and their reefs have responded to warming with species replacement, bleaching, and decreased coral cover causing habitat loss. Ocean acidification, salinity increase and reduced O_2 solubility in warmer waters, have contributed to the constraining of fish habitat resulting in algal, plankton and fish migrations towards high latitude areas ([2], [3]). Natural fish migration in rivers and lakes has started to happen earlier, and species extinction now occurs with rates higher than those ones estimated for the past millions of year. Global warming is also affecting terrestrial biological systems, mainly due to the earlier timing of spring events including leaf unfolding, bird migration, egg laying, poleward and upward shifts in habitat of plants and animals ([2]). Ecosystems connected to snow, ice and frozen ground as high-latitude and high-elevation regions have been affected by enlargement and increased numbers of glacial lakes, increasing ground instability due to permafrost warming, rock avalanches in mountain regions, as well as changes in some Arctic and Antarctic ecosystems such those in sea-ice biomes and predators at high levels of the food web. Glaciers shrinkage has

begun to significantly impact runoff and water resources downstream. Melting of snows and ices, in addition to changing in precipitation events in many regions, are altering hydrological systems, modifying water resources in terms of quantity and quality ([2], [3]). Moreover, increased tree mortality, observed in many places worldwide, has been attributed to climate change in several regions, as well as the increase in frequency and/or intensity of ecosystem disturbances such as droughts, windstorms, fires, and pest outbreaks ([3]).

Concerning impacts of climate change on human systems, it has been observed that the contributions are less distinguishable from other influences. Impacts on human systems are often geographically heterogeneous because they depend not only on changes in climate variables but also on social and economic factors and hence, the changes are more easily observed at local levels while attribution remains difficult. Assessment of many studies covering a wide range of regions and agricultural crops have shown for example that climate change has negatively affected wheat and maize yields for many regions and in the global aggregate ([3]). Partially negative effects on rice and soybean yields have also been recorded. Observed impacts are related mainly to production aspects of food security rather than to access or other components of food security. For example, periods of rapid food and cereal price increase have become more common following climate extremes in key producing regions, indicating a sensitivity of current markets to climate variations among other factors ([3]). Considering human health, at present the worldwide burden of human ill-health from climate change is relatively small compared with effects of other stressors and is not well quantified. However, there has been increased heat-related mortality and decreased cold-related mortality in some regions as a result of warming, as well as local changes in temperature and rainfall have altered the distribution of some water-borne illnesses and disease vectors ([3]).

1.2 Causes of climate change

The main causes of the continuous transformations observed in the climate system, as well as in any natural and human system impacted by climate, can be ascribed to human activities. Human activities affect the Earth's surface and atmospheric composition in different ways, especially through the related constant increase of the anthropogenic

greenhouse gas (GHG) emissions. These substances, that primarily include carbon dioxide (CO_2), methane (CH_4), nitrous oxide (N_2O) and the halocarbons (a group of gases containing fluorine, chlorine and bromine (namely, CFCs)), basically alter the energy balance of the Earth and are responsible for keeping the planet's surface warm. It has been estimated ([1]) that without greenhouse gases the average temperature of the Earth surface would be significantly lower while, an increase of GHGs concentration in the atmosphere determines an increase in the global mean temperature because of the so called "greenhouse effect". The principal mechanism behind this phenomenon is that the radiant energy from the sun can penetrate Earth's atmosphere more easily than the long wavelength infrared radiation that is emitted back from the Earth's surface. In other words, Earth's atmosphere (in which GHGs accumulate in high concentrations) works in a way similar to a window glass of a greenhouse, which allows for visible light and short wave thermal radiation to enter, but prevent longer wave thermal radiation from exiting, causing the greenhouse to warm. This is a very simplistic description of the problem but it is sufficient to understand the behavior of the GHGs as drivers of the climate change.

Radiative forcing (RF) is a measure used to quantify the influence that these drivers have in perturbing the balance of incoming and outgoing energy in the Earth-atmosphere system, and it is expressed in W/m^2. Each greenhouse gas has different radiative properties and lifetimes in the atmosphere so that the climate change response is different for each GHG, and is a function of its atmospheric concentration. In general, positive RF values lead to warming while, on the contrary, if RF is negative it refers to a cooling trend. In order to compare the different influences, these are expressed through a common metric based on the radiative forcing of carbon dioxide, namely the CO_2 equivalent emission, which is defined as the amount of CO_2 emission that would cause the same time-integrated radiative forcing, over a given time horizon, as an emitted amount of a long-lived GHG or a mixture of GHGs. The total anthropogenic GHG radiative forcing for 2011 relative to 1750 has been estimated equal to 2.3 W/m^2 (uncertainty range 1.1 to 3.3 W/m^2) (Figure 1.7), and it is increased since the beginning of the industrial era ([3]). This value unequivocally justifies the warming globally observed, even considering the cooling effect produced by other anthropogenic contributions such as aerosols (namely a mix of sulfates, organic carbon, black carbon, nitrates and dusts, with a total radiative forcing of –0.5 W/m^2) and the indirect cloud albedo (radiative forcing of –0.7 W/m^2) that counteracts the

GHGs warming impact, with a resulting net effect of anthropogenic activities of +1.6 W/m^2. This result basically corresponds to a CO_2-equivalent concentration of GHGs of approximately 430 ppm (uncertainty range 340 ÷ 520 ppm) ([3]), which is still progressively increasing.

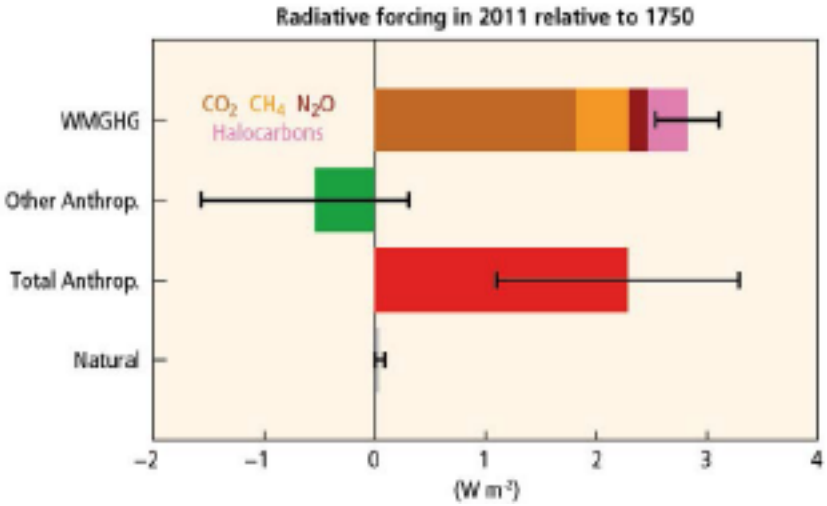

Figure 1.7: *Radiative forcing (RF) of climate change during the industrial era (1750–2011). Bars show RF from well-mixed greenhouse gases (WMGHG), other anthropogenic forcings, total anthropogenic forcings and natural forcings. The error bars indicate the 5%-95% uncertainty. Other anthropogenic forcings include aerosol, land-use surface reflectance and ozone changes. Natural forcings include solar and volcanic effects. Source: IPCC synthesis report 2014 (*[3]*).*

Anthropogenic greenhouse gas emissions have globally grown since the pre-industrial era, with an increase of about 80% between 1970 and 2010, and larger absolute increase in the period 2000-2010. GHG emissions grew on average by 1.0 $GtCO_2$-eq (2.2%) per year, from 2000 to 2010, compared to 0.4 $GtCO_2$-eq (1.3%) per year, from 1970 to 2000 (Figure 1.8). Total anthropogenic GHG emissions from 2000 to 2010 were the highest in human history and reached approximately 49 $GtCO_2$-eq/yr in 2010. Carbon dioxide is the most important among the anthropogenic GHGs because it is emitted in the highest amounts. Its annual emissions have increased between 1970 and 2010 by about 95%, from approximately 19 to 37 Gt, and represented roughly the 76% of the total anthropogenic GHG emissions in 2010, as reported in Figure 1.8 ([3]).

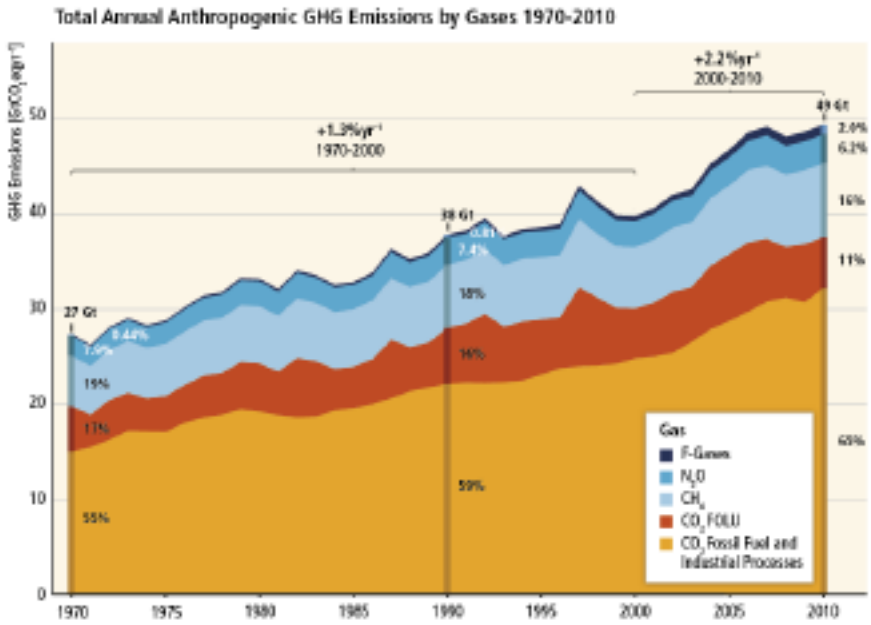

Figure 1.8: *Total annual anthropogenic GHG emissions ($GtCO_2$-eq/yr) for the period 1970 to 2010, by gases: CO_2 from fossil fuel combustion and industrial processes; CO_2 from Forestry and Other Land Use (FOLU); methane (CH_4); nitrous oxide (N_2O); fluorinated gases covered under the Kyoto Protocol (F-gases). Source: IPCC synthesis report 2014 (*[3]*).*

Prior the 1750, the atmospheric concentration of CO_2 fluctuated roughly between 180 ppm and 290 ppm for at least about two thousand years ([1]). Then, CO_2 concentration started to exponentially increase: cumulative anthropogenic CO_2 emissions of about 2040 Gt were added to the atmosphere between 1750 and 2011. Since 1970 cumulative CO_2 emissions from fossil fuel (coal, gas, oil and gas flaring) combustion and cement production have tripled, releasing roughly 375 Pg (1 Pg = 1×10^{15} g) of carbon dioxide. Land use change activities, mainly deforestation, have contributed adding approximately an additional 180 Pg, and increasing the CO_2 cumulative emissions by about 40% ([3]). This carbon released by human activities is called anthropogenic carbon, and even though large amounts emitted are absorbed by terrestrial ecosystems (namely, the so called "carbon sinks" that include ocean uptake, photosynthesis and other natural carbon cycle reservoirs), almost half of these anthropogenic CO_2 emissions (880 ± 35 $GtCO_2$) have remained in the atmosphere since the 1750 (Figure 1.9) ([3]). The power and industry sectors combined dominate the current global GHG emissions (Figure 1.10)), especially for carbon dioxide, since they account for about 60% of the total CO_2 emitted from human activities.

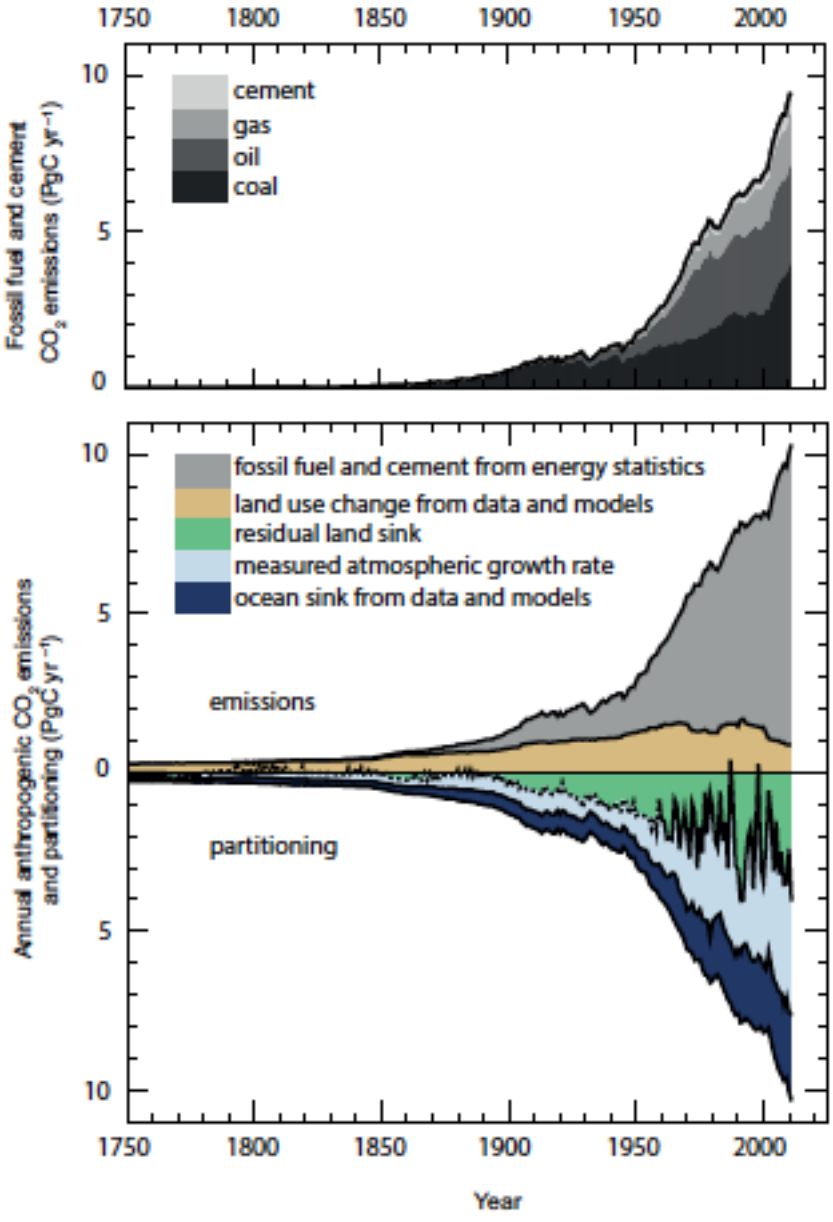

Figure 1.9: *Annual anthropogenic CO_2 emissions and their partitioning among the atmosphere, land and ocean ($Pgyr^{-1}$) from 1750 to 2011. (Top) Fossil fuel and cement CO_2 emissions by category. (Bottom) Fossil fuel and cement CO_2 emissions as above. CO_2 emissions from net land use change, mainly deforestation, are based on land cover change data and estimated for 1750-1850. Source: Working group I contribution to the fifth assessment report of IPCC 2013 (*[26]*).*

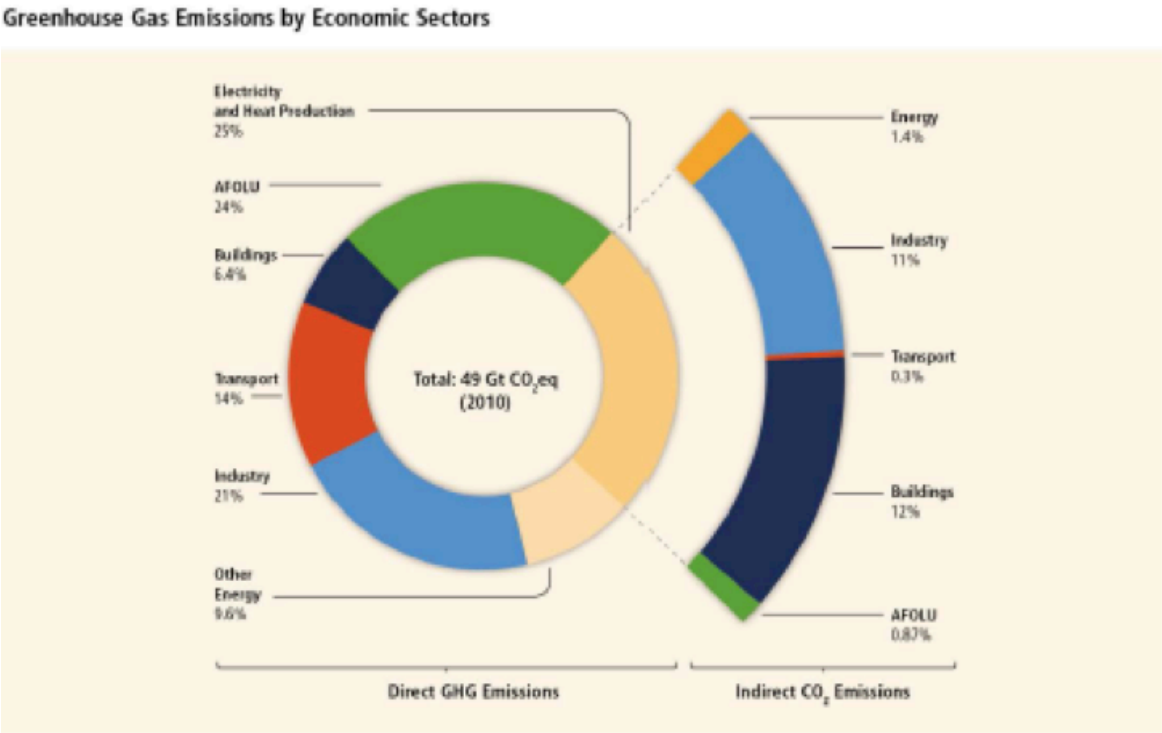

Figure 1.10: *Total anthropogenic GHG emissions ($GtCO_2$-eq/yr) from economic sectors in 2010. The circle shows the shares of direct GHG emissions (in % of total anthropogenic GHG emissions) from five economic sectors in 2010. The pull-out section shows how shares of indirect CO_2 emissions (in % of total anthropogenic GHG emissions) from electricity and heat production are attributed to sectors of final energy use. Source: IPCC synthesis report 2014* ([3]).

Carbon dioxide emissions in these sectors are generated by boilers and furnaces burning fossil fuels and are typically emitted from large exhaust stacks. These stacks can be described as large stationary sources, to distinguish them from mobile sources such as those in the transport sector and from smaller stationary sources including small heating boilers used in the residential sector. CO_2 emissions that account for the residential, commercial, transportation and agricultural sectors are typically not considered by the IPCC.

On the contrary, the emission sources considered as the main cause of anthropogenic CO_2 in the atmosphere include all large stationary sources (typically larger than 0.1 $MtCO_2$ per year) that involve fossil fuel and biomass utilization. These sources are present in three main areas, namely fuel combustion, industrial processes and natural gas processing. The

largest CO_2 emissions by far result from the oxidation of carbon when fossil fuels are burned. According to the IPCC report of 2005 ([1]), these emissions can be ascribed with high confidence to fossil fuel combustion in power plants, oil refineries and large industrial facilities, as summarized in Table 1.1.

Table 1.1: *Profile by process or industrial activity of worldwide large stationary CO_2 sources with emissions of more than 0.1 $MtCO_2$ per year. Source: IPCC 2005 (*[1]*).*

Process	Number of sources	Emissions [$MtCO_2$/yr]
Fossil fuels		
Power	4942	10539
Cement production	1175	932
Refineries	638	798
Iron and steel industry	269	646
Petrochemical industry	470	379
Oil and gas processing	n.a.	50
Other sources	90	33
Biomass		
Bioethanol and bioenergy	303	91
Total	7887	13466

In particular, still referring to data analyzed up to 2002 ([1]), the top 25% of all large stationary CO_2 emission sources accounted for over 85% of the cumulative emissions from these types of sources, as listed in Table 1.2. In 2002, there were 330 sources with individual emissions above 10 $MtCO_2$ per year. Of their cumulative emissions, 78% came from power plants, 20% from gas processing and the remainder from iron and steel plants. Carbon dioxide not related to combustion was emitted from a variety of industrial production processes that transform materials chemically, physically or biologically. Such processes include: the use of fuels as feedstock in petrochemical processes; the use of carbon as a reducing agent in the commercial production of metals from ores; the thermal decomposition (calcination) of limestone and dolomite in cement or lime production; the fermentation of biomass.

Table 1.2: *Profile of worldwide large CO_2 stationary sources emitting more than 0.1 $MtCO_2$ per year. Source: IPCC 2005 (*[1]*).*

Process	CO_2 concentration in gas stream [% by vol.]	Number of sources	Emissions [$MtCO_2$/yr]	% of total CO_2 emissions	Cumulative total CO_2 emissions [%]	Average emissions per source [$MtCO_2$/yr]
Power - CO_2 from fossil fuels						
Coal	12 to 15	2025	7984	59.69	59.69	3.94
Natural gas	3	8985	759	5.68	65.37	0.77
Natural gas	7 to 10	743	752	5.62	70.99	1.01
Fuel oil	8	515	654	4.89	75.88	1.27
Fuel oil	3	593	326	2.43	78.31	0.55
Other fuels	n.a.	79	61	0.45	78.77	0.77
Hydrogen	n.a.	2	3	0.02	78.79	1.27
Natural gas sweetening	n.a.	n.a.	50	0.37	79.16	
Cement production						
Combined	20	1175	932	6.97	86.13	0.79
Refineries	3 to 13	638	798	5.97	92.09	1.25
Iron and steel industry						
Integrated steel mills	15	180	630	4.71	96.81	3.50
Other processes	n.a.	89	16	0.12	96.92	0.17
Petrochemical industry						
Ethylene	12	240	258	1.93	98.85	1.08
Ammonia: process	100	194	113	0.84	99.70	0.58
Ammonia: fuel combustion	8	19	5	0.04	99.73	0.26
Ethylene oxide	100	17	3	0.02	99.75	0.15
Other sources						0.37
Not specified	n.a.	90	33	0.25	100	
Total		**7584**	**13375**	**100**		**1.76**
CO_2 from biomass						
Bioenergy	3 to 8	213	73			0.34
Fermentation	100	90	17.6			0.2

1.3 Mitigation actions

Because of the observed climate changes consistent with the expected responses to anthropogenic activities, there is a general agreement in the scientific community that mitigation policies and sustainable development practices have to be adopted. In order to attenuate the rate and magnitude of climate changes and the resulting global warming due to a constantly increase in GHG emissions, societies have to respond by adapting to impacts and adopting mitigation actions oriented to affordably and efficiently reduce these emissions, especially those of carbon dioxide. The capacity to adapt and mitigate is dependent on socio-economic and environmental circumstances, as well as the availability of information and technologies of each country. Since the energy generation industry produce nearly one-third of the global CO_2 emissions, besides the energy demand reduction/conservation, several possible options should be considered, such as energy efficiency improvements, switching to less carbon intensive fuels, use of low-cost renewable energy sources/supplies, widening of forests and the enhancement of other natural sinks for CO_2 accumulation. Additionally, life style changes could contribute to mitigation in several sectors, including changes in consumption patterns, in building occupant behavior, in education and trainings, in transport demand management. However, it is essential that policies provide incentives for low GHG products, technologies and processes ([2]). Unfortunately, there is not a single technology that is sufficient to mitigate all the global warming effects, and hence it is important to implement different mitigation actions in order to realize synergies and obtain results with positive long-term effects. Since international cooperation is essential to reduce the emissions, lowering costs and incrementing the action efficiency, United Nations Framework Convention on Climate Change (UNFCCC) instituted the Kyoto Protocol whose aim is to find a response to climate change problem stimulating an array of national policies, creating an international carbon market and establishing new institutional mechanisms that may provide new mitigation actions. To obtain the aims periodically fixed by the Protocol, different elements are considered, as emissions targets, sectorial, local, regional actions, research and development programs, common policies and financing instruments.

Currently, almost all atmospheric CO_2 stabilization scenarios discussed by the Kyoto Protocol require significant reductions in carbon dioxide arising from the existing

population of power plants based on fossil fuel combustion and gasification processes. Fossil fuels still account for about 80% of the global energy sources (Figure 1.11) ([27]) and the worldwide energy demand is still reliant on their utilization insomuch as it is unimaginable a complete retirements of all the current power generation systems/processes.

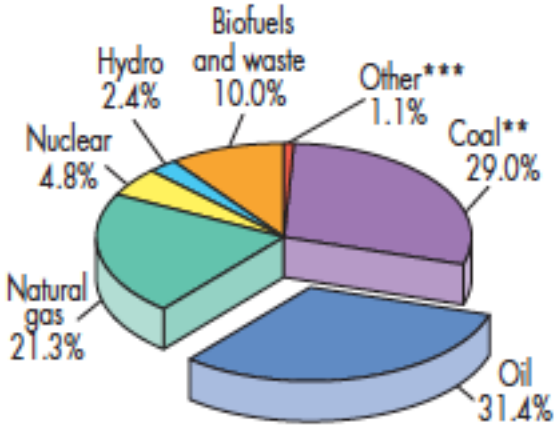

Figure 1.11: *World total primary energy supply by fuel in 2012. "Other" includes geothermal, solar, and wind. Source: IEA outlook report 2013 (*[27]*).*

Therefore, in order to stabilize atmospheric concentration of CO_2 and address concerns that anthropogenic GHG emissions are contributing to global climate change, as well as, at the same time, to retain fossil fuels as a still viable energy source, implementation of Carbon dioxide Capture and Storage (CCS) technologies play a central role.

1.4 Carbon dioxide capture and storage

Carbon dioxide Capture and Storage (CCS) comprises a range of technologies oriented to sequestrate CO_2 from industrial and energy-related sources and to transport it to storage locations providing long-term isolation from the atmosphere ([1]). It is considered one of the main options for reducing atmospheric emissions of CO_2 from human activities and, more specifically, a primary goal of CCS is the capture and concentration of carbon dioxide from gas streams of currently existing industrial power plants based on fossil fuel combustion and gasification processes. Involving the use of different technologies, carbon

dioxide capture can be applied to large point sources such as fossil fuel or biomass energy facilities, major CO_2 emitting industries, natural gas production, synthetic fuel plant and fossil fuel based hydrogen production plant, resulting in a net removal of CO_2 from the atmosphere, and ultimately allowing fossil fuels to be still used as energy sources, but ensuring lower emissions of GHGs ([1]).

The three main components of the CCS are: capture, transport and storage stages. The capture stage involves separating carbon dioxide from other gaseous products of industrial gas streams. For fuel-burning processes such as those in power plants, separation technologies can be used to capture CO_2 after combustion or to decarbonize the fuel before combustion. Once captured, CO_2 can be transported via pipeline or tanker to permanent storage sites located at a distance from the gas sources. To facilitate both transport and storage, the captured CO_2 gas is typically compressed to a high-density phase. Potential storage methods include: injection into underground geological formations, such as depleted oil and gas fields, saline formations and used up coal seams; injection into the deep ocean; industrial fixation in inorganic carbonates.

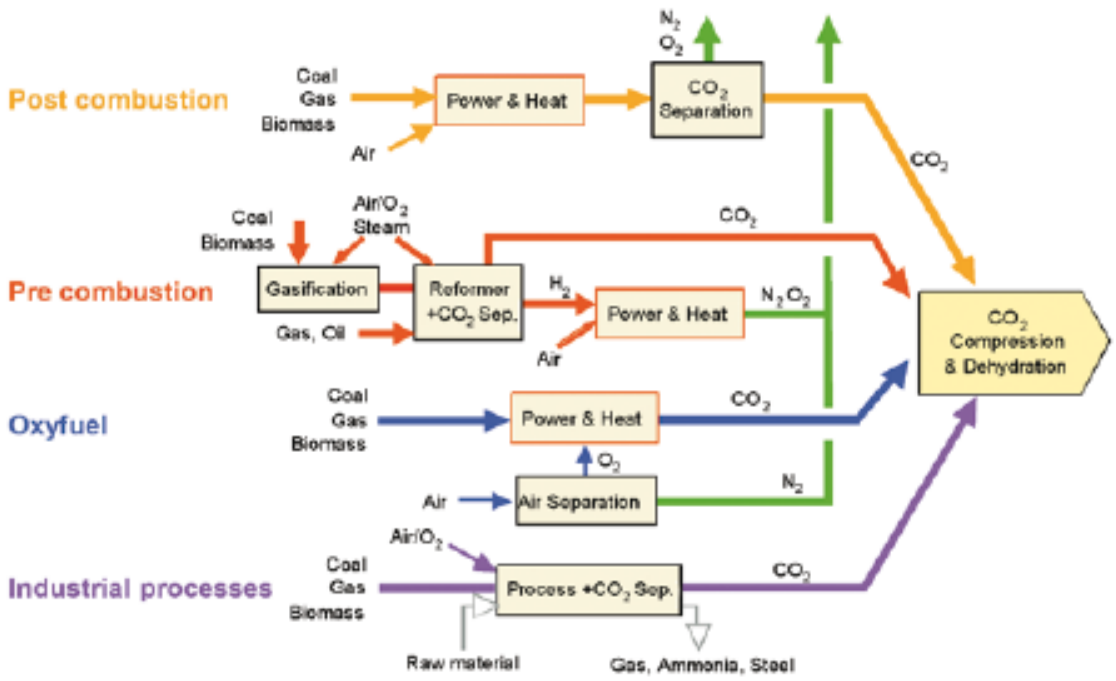

Figure 1.12: *Overview of CO_2 capture pathways. Source: IPCC 2005 (*[1]*).*

1.4.1 CO_2 sequestration

Depending on the process, there are three general categories of CO_2 capture approaches to sequestrate carbon dioxide from primary fossil fuel (coal, natural gas or oil), biomass, or mixtures of these fuels: post-combustion, pre-combustion and oxy-combustion systems (Figure 1.12) ([1], [4], [28]). Table 1.3 provides a summary of the characteristic advantages and disadvantages of each of these pathways.

Table 1.3: *Summary of advantages and disadvantages of different CO_2 capture approaches. Source: Figueroa et al., 2008 (*[29]*).*

System	Advantages	Barriers to implementation
Post-combustion	• Applicable to the majority of existing coal-fired based power plants • Retrofit technology option	Flue gas is … • Dilute in CO_2 • At ambient pressure … resulting in … • Low CO_2 partial pressure • Significantly higher performance or circulation volume required for high capture levels • CO_2 produced at low pressure compared to sequestration requirements
Pre-combustion	Synthesis gas is … • Concentrated in CO_2 • High pressure … resulting in … • High CO_2 partial pressure • Increased driving force for separation • More technology for separation • Potential for reduction in	• Applicable mainly to new plants, as few gasification plants currently in operation • Barriers to commercial application of gasification are common to pre-combustion capture • Availability • Cost of equipment • Extensive supporting system

	compression costs/loads	requirements
Oxy-combustion	• Very high CO_2 concentration in flue gas • Retrofit and repowering technology option	• Large cryogenic O_2 production requirement may be cost prohibitive • Cooled CO_2 recycled required to maintain temperatures within the limits of combustor materials • Decreased process efficiency • Added auxiliary load

Post-combustion systems separate CO_2 from the flue gases produced by the combustion of the primary fuel with air, as illustrated in Figure 1.13. It can be utilized in conventional coal-fired, oil-fired or gas-fired power plants where fuel is burned with air in a boiler in order to produce stream that, in turn, is used to drive a turbine/generator for producing electricity. Flue gases from the boiler consist mostly of nitrogen and CO_2. This configuration implies that the carbon dioxide capture is located downstream a further pollutant control unit used to limit emissions of nitrogen oxides (NO_x), particulate matter and sulfur dioxide (SO_2). The treated gas is characterized by high volumes in which CO_2 is dilute (molar % of CO_2 roughly of 12-14%) and where other pollutants present can negatively affect the carbon dioxide separation stage ([1], [4]).

Pre-combustion capture (Figure 1.14) is instead mainly applicable to gasification plants, where fuel is converted into gaseous components by means of the combined application of heat and pressure. Primary fuel is fed in a reactor with steam and air (or oxygen) in order to obtain synthesis gas ("syngas"), namely a mixture of H_2 and CO, which is in turn sent to a water-gas-shift reactor where CO is further converted to CO_2, increasing the H_2 production. The resulting mixture of H_2 and CO_2 then can be separated into a CO_2 gas stream, and a stream of hydrogen. If the CO_2 is captured, hydrogen is a carbon-free energy carrier that can be combusted to generate power and/or heat. Although the initial fuel conversion steps are more elaborate and costly than in post-combustion systems, the high concentrations of CO_2 produced by the shift reactor (molar % of CO_2 between 15 and

60%) and the high pressures often encountered in these applications are more favorable for CO_2 separation ([1], [4]).

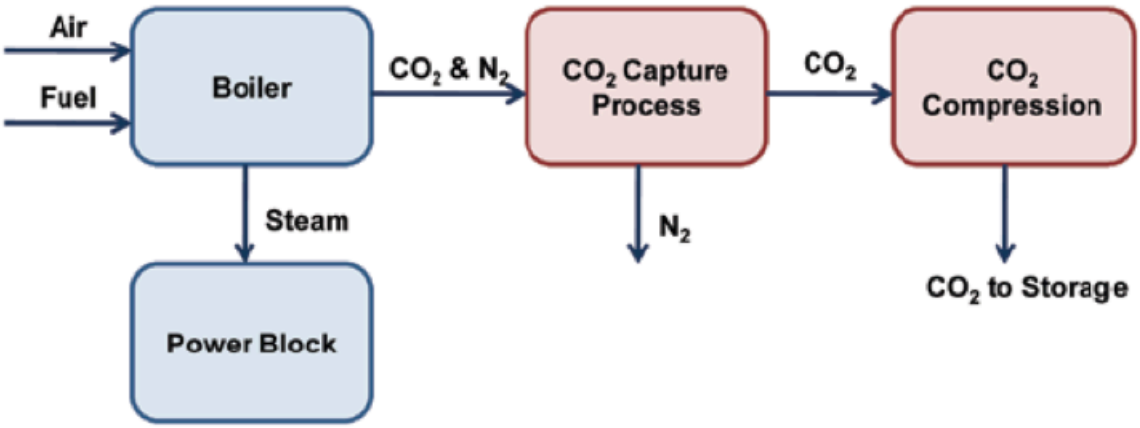

Figure 1.13: *Block diagram illustrating power plant with post-combustion CO_2 capture system. Source: U.S. DOE CCS Roadmap 2010 (*[4]*).*

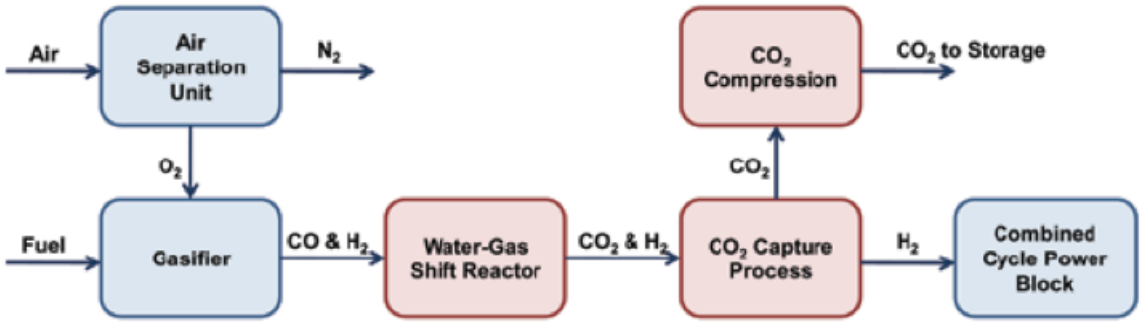

Figure 1.14: *Block diagram illustrating power plant with pre-combustion CO_2 capture system. Source: U.S. DOE CCS Roadmap 2010 (*[4]*).*

Finally there is oxy-combustion that can be applied to new and/or existing coal fired power plant. In this case (Figure 1.15), oxygen is used instead of air for the combustion of the primary fuel to produce a flue gas constituted by a large amount of CO_2 (80% by volume or more) and H_2O. The CO_2 separation is then obtained by water condensation through cooling and/or compression. This configuration allows to process small flue gas volumes and concentrated CO_2 streams are directly produced, even if further treatments of the flue

gas may be needed to remove air pollutants and non-condensed gases (such as nitrogen) before the CO_2 is sent to storage ([1], [4]).

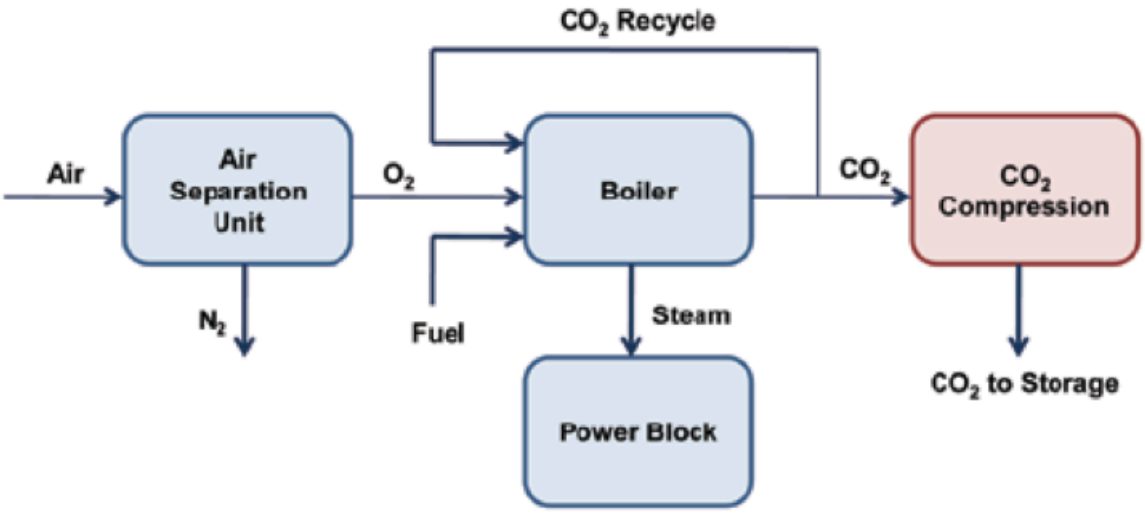

Figure 1.15: *Block diagram illustrating power plant with oxy-combustion CO_2 capture system. Source: U.S. DOE CCS Roadmap 2010 (*[4]*).*

1.4.2 Transport and storage

Except when plants are located directly above a geological storage site, once captured the CO_2 must be transported from the point of sequestration to a storage site. In order to make the transport of carbon dioxide easier and less costly, gaseous CO_2 is typically compressed to a pressure above 8 MPa, especially to avoid two-phase flow regimes and increase the density of the CO_2. Carbon dioxide can also be transported as a liquid, mainly using ship, road or rail tankers that carry CO_2 in insulated tanks at a temperature well below ambient, and at much lower pressures. Pipeline transport operates with carbon dioxide in the supercritical phase, at ambient temperature and high pressure, and CO_2 is driven by compressors. In other situations, transport of CO_2 by ship may be economically more attractive, particularly when the CO_2 has to be moved over large distances or overseas. In these cases, carbon dioxide is transported in the same way of liquefied petroleum gases,

roughly at a pressure of about 0.7 MPa. Road and rail tankers also are technically feasible options, transporting CO_2 at a temperature of −20°C and at 2 MPa pressure ([1], [25]).

In the matter of carbon dioxide storage, it is basically based on three main technologies namely, geological storage, ocean storage and mineral sequestration.

Geological storage refers to the underground accumulation of carbon dioxide by means of natural trapping of CO_2 in underground reservoirs. The injection of CO_2 into deep geological formations at carefully selected sites could store the gas underground for long periods of time. In fact, it has been estimated that 99 % or more of the injected CO_2 would be retained for roughly 1000 years. Depleted oil and gas reservoirs, possibly coal formations and particularly saline formations, can be used for this aim. To geologically store CO_2, it must be compressed, usually to the supercritical state of dense fluid. Depending on the rate that temperature increases with depth (the geothermal gradient), the density of CO_2 also increases with depth, until at about 800 m or higher, where the injected CO_2 would be again in a dense supercritical state. Carbon dioxide can remain trapped underground thanks to a number of mechanisms, such as trapping below an impermeable, confining layer; retention as an immobile phase trapped in the pore spaces of the storage formation; dissolution in-situ formation fluids; adsorption within organic matter in coal and shale. Additionally, carbon dioxide can be trapped through a reaction with the minerals in the storage formation, producing carbonate minerals.

Carbon dioxide could be also stored exploiting oceans as reservoir: captured CO_2 could be in fact injected into the oceans at great depth, in order to form CO_2 lakes on the sea floor where most of carbon dioxide would remain isolated from the atmosphere for centuries. CO_2 can be placed on a ship or injected directly into the ocean, and hence deposited on the sea floor. CO_2 loaded on ships could either be dispersed from a towed pipe or transported to fixed platforms feeding the CO_2 down to the sea floor. The formed CO_2 lakes should be deeper than 3 km where CO_2 would be denser than sea water. Numerical models of the ocean indicate that placing CO_2 in the deep ocean would isolate most of the CO_2 from the atmosphere for several centuries even if, over longer times, the ocean and atmosphere would equilibrate. However, putting CO_2 directly into the deep ocean means that the chemical environment of the deep ocean would be altered immediately and change in ocean chemistry would progressively increase, starting from a greater extent proximate to the release location. For ocean storage of CO_2, issues remain regarding environmental

consequences, public acceptance, implications of existing laws, safeguards and practices that would need to be developed, and gaps in current understanding of ocean CO_2 storage.
Finally, there is the mineral carbonation, which is based on the reaction between CO_2 and metal oxides that produces insoluble carbonates. Calcium and magnesium-based oxides are retained to be the most attractive materials because mineral carbonation refers to the fixation of CO_2 using alkaline and alkaline-earth oxides, such as magnesium oxide (MgO) and calcium oxide (CaO), which are present in naturally occurring silicate rocks. Chemical reactions between these materials and CO_2 produce compounds such as magnesium carbonate ($MgCO_3$) and calcium carbonate ($CaCO_3$, commonly known as limestone). This process produces silica and carbonates that are stable over long time scales and that can therefore be disposed of in areas such as silicate mines, or reused for construction purposes. Considering industrial applications, other uses of CO_2 include chemical and biological processes where CO_2 is a reactant, such as those used in urea and methanol production, as well as various technological applications that use CO_2 directly, for example in the horticulture industry, refrigeration, food packaging, welding, beverages and fire extinguishers ([1], [25]).

1.4.3 Costs

In general, currently available CCS technologies are expensive and very energy-intensive due to the large quantity of energy required to capture, transport and store carbon dioxide ([1], [4], [30]). Besides the necessity of retrofit the existing power plants with new technical equipment/facilities that leads to an evident increase of capital costs, the CCS systems require energy inputs that to date result in an overall net efficiency penalty of common power plants. This aspect, from a mere economic point of view, means that CCS systems are currently not cost-effective. Moreover, energy inputs requirements mean that the amount of fuel input (and therefore CO_2 emissions) increases per unit of net power output. As a result, the amount of CO_2 produced per unit of product (e.g., a MWh of electricity) is larger for the power plant with CCS than for the reference plant without CCS application, as shown in Figure 1.16.
However, to determine the effective CO_2 reductions attributable to CCS, it has to be compared CO_2 emissions of a plant with a carbon dioxide capture system to those of the

reference plant without CO_2 sequestration, thus obtaining the actual avoided emissions of CO_2. The main metrics used for comparing CCS projects and assessing their costs are the levelized costs of production and the cost per tonne of CO_2 avoided/not emitted relative to a normal process providing the same product or service without CCS.

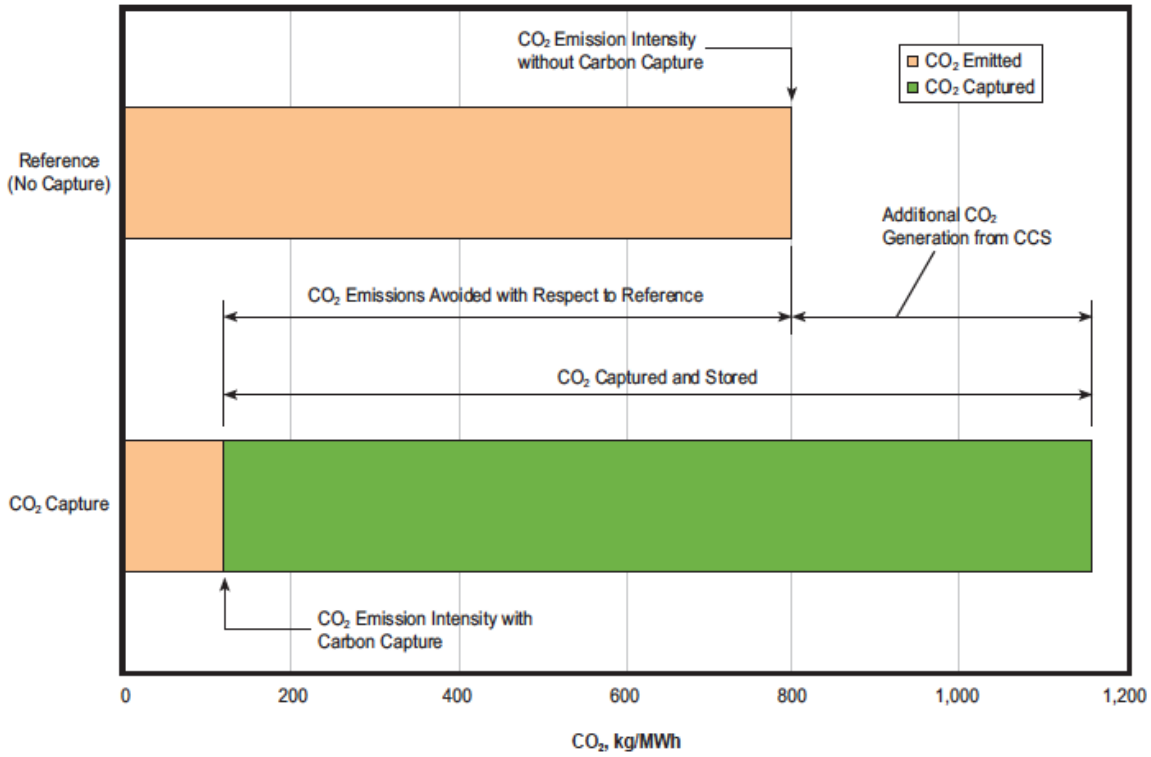

Figure 1.16: *CO_2 capture and storage from an hypothetical power generation plant: the increased CO_2production resulting from loss in overall efficiency of power plant due to the additional energy required for capture, transport and storage, and any leakage from transport result in a larger amount of CO_2 produced per unit of product (lower bar) relative to the reference plant (upper bar) without carbon dioxide capture. Source: Global CCS Institute - synthesis report 2009 (*[30]*).*

The levelized production costs represent the revenue per unit of product that must be met to break even over the lifetime of the plant, that is, a zero profit. For assessing CCS projects, the incremental increase is the cost resulting from the addition of CCS. All costs need to be considered, including capital and operating costs of each of the capture, transportation and storage elements of CCS. The difference between the cost of the plant with and without CCS is then the incremental change in the cost resulting from CCS. The advantage of the incremental levelized cost approach is that it provides an indication of the

cost increase incurred by a product from the implementation of CCS. This levelized production cost approach can be therefore used to directly estimate the impact of CCS on other industries and on the overall economy. In particular, the levelized cost of energy (LCOE) is used in the power industry as a measurement on the impact of all costs for electricity generation, including the impact of CCS. By comparing the LCOE for the CCS and non-CCS cases, the economic impact of CCS can clearly be determined ([30]).

The cost of CO_2 avoided is instead determined by combining the difference in the levelized costs with and without CCS, with the decrease in emissions respect to the reference case ([30]). Generally, the cost in US$/tonne avoided is therefore greater than the cost in US$/tonne captured. Additionally, the mitigation costs (US$/tonne of CO_2 not emitted) are context-specific and strongly depend on what is chosen as a reference plant. An example of the costs associated with CO_2 capture in terms of levelized cost of energy (LCOE) or cost per tonne of CO_2 avoided is shown in Figure 1.17. The LCOE can typically range from $116/MWh to $151/MWh, depending upon the type of facility and whether the application is for a new plant or a retrofit of an existing plant. In terms of costs per tonne of CO_2 avoided, values range from $60/tonne to $114/tonne ([4]).

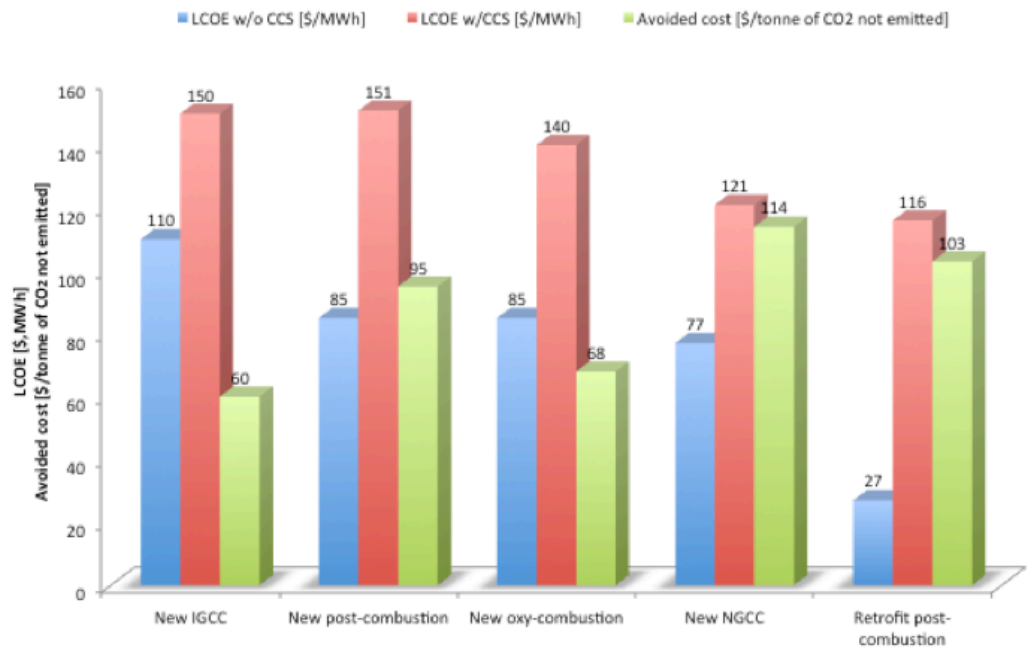

Figure 1.17: *Comparison of cost metrics for different types of configurations of power plants equipped with CCS. Source: DOE/NETL Roadmap 2010 (*[4]*).*

1.5 State-of-the-art in CO_2 capture systems

Even though a broad range of techniques are under investigation and some CO_2 capture technologies are already being used in various industrial applications, at their current state of development these technologies are not ready for a widespread employment on the industrial scale power plants. Almost all the technologies so far investigated have not been demonstrated at a large enough scale necessary for power plant application and, even if they would be successfully scaled-up, they would not be currently cost effective, mainly because of the "parasitic loads" of steam and power required to support CO_2 capture, that would significantly decrease the overall power generation capacity of the industrial power plants ([4]).

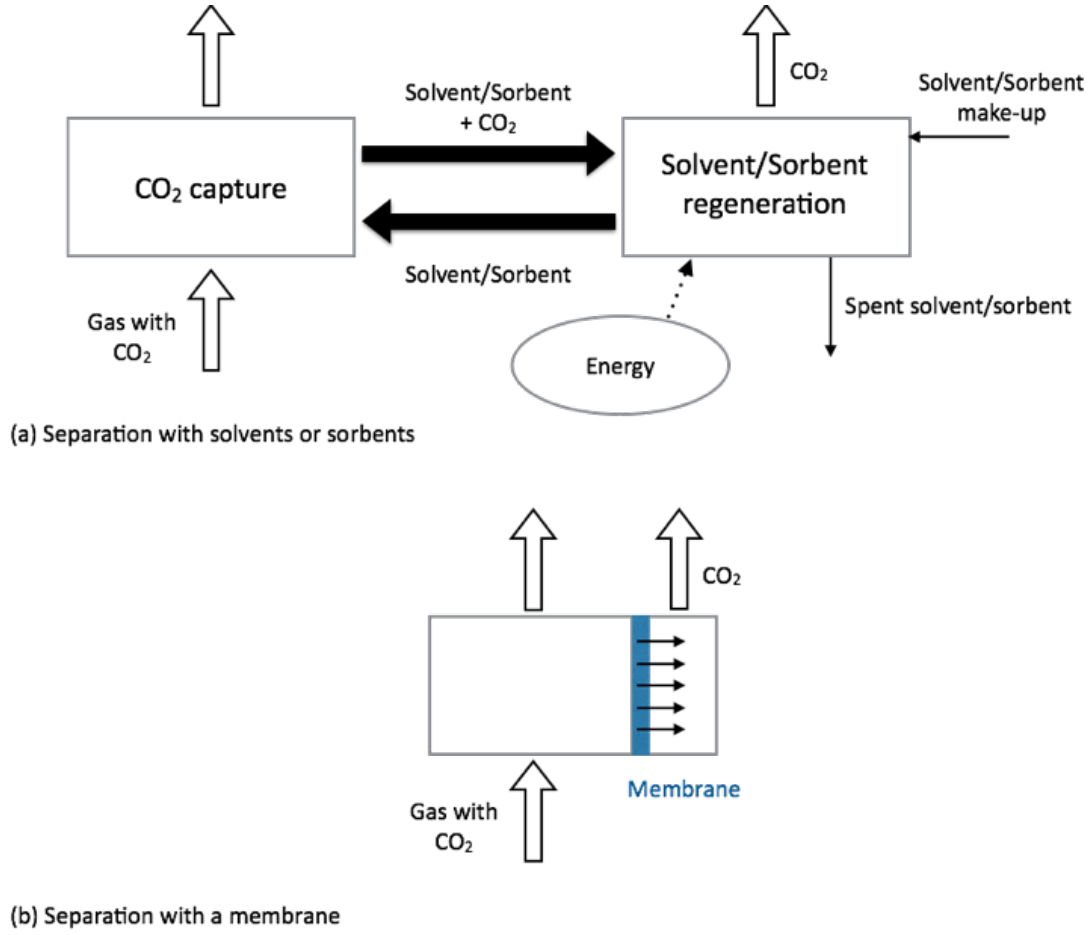

Figure 1.18: *General schemes of the main separation processes for CO_2 capture: (a) separation with solvents or sorbents, (b) separation with membranes.*

A continue research oriented to improve still existing technologies and to develop new cost effective CO_2 capture techniques that could be ready for fully scale demonstration and deployment has to be therefore carried out. The capturing technologies to perform CO_2 sequestration can be summarized in two main categories: solvent or sorbent-based systems and membrane-based processes (Figure 1.18) ([1]).

The separation with sorbents/solvents is achieved by passing the CO_2-rich gas in intimate contact with a liquid absorbent or a solid sorbent that is capable of capturing the CO_2. In the general case, once the solvent/sorbent has captured the CO_2, it is transported to a different vessel where CO_2 is released (solvent/sorbent regeneration) after being heated or after a pressure decrease. Regenerated solvent/sorbent is then sent back to the capture step establishing a cyclic process. A make-up flow of fresh solvent/sorbent is always required to compensate the natural decay of activity and sorbent losses. One common problem of these CO_2 capture systems is that the flow of solvent/sorbent between the vessels is large because it has to match the large flow of CO_2 being processed in the power plant. Therefore, equipment sizes and the energy required for solvent/sorbent regeneration are large, resulting in an important efficiency penalty and additional costs.

The current state-of-the-art of post-combustion CO_2 capture technologies employ chemical solvents that preferentially absorb carbon dioxide from flue gases and are capable of achieving up to 90% or more of CO_2 sequestration from gas streams with a low CO_2 partial pressure (i.e. CO_2 volume concentrations typically less than 15%). CO_2 removal using chemical solvents is based on cyclic stages of sorption and of stripping by means of the utilization of amine-based solvents, especially alkanolamines (commonly, monoethanolamin (MEA), diethanolamine (DEA) and methyldiethanolamine (MDEA)), under operating pressure of 1 bar and at temperatures in the range between 40 and 140°C ([29], [31]). It is considered the most mature technology for CO_2 capture because it has been utilized/studied for more than 60 years and it is suitable for an easy retrofit of the existing power plants. However, this process has not been demonstrated yet at a large-scale adequate for power plants (namely, amine-based solvents have not been applied yet to removing large volume of CO_2) and it suffers from a series of drawbacks such as the corrosive nature of the amines that leads to high equipment corrosion rates, the large equipment size due to the large volumes of the flue gases treated, and the high energy consumption due to the solvent regeneration step that leads to a high overall efficiency

penalty of the power generation processes. The high cost of solvent manufacturing and the degradation of alkanolamines are also important issues because they cause economic, operational and environmental problems. Amine degradation by SO_2, NO_2, and O_2 present in the flue gases basically causes the frequent replacement of exhaust solvents with expensive fresh alkanolamines and, on the other hand, leads to the handling and disposal of large quantities of degradation products and/or waste/spent solvents that, in turn, raises both environmental and health and safety concerns ([29], [4]).

Even though research pathways are being followed to improve amine-based system, mainly focusing on the increasing of heat integration (to reduce energy requirements) and the improvement both of solvent resistance to degradation and of regeneration procedures, at the same time other emerging technologies oriented to the carbon dioxide capture are under investigation and, recently, have been reviewed by several authors ([29], [31], [32], [28]). In order to avoid common problems encountered with amine-based solvents, intensive efforts have been made to study solid adsorbents characterized by the immobilization of organic amines on support materials by means of impregnation or grafting techniques. Investigation are being carried out to identify supports that could have a good affinity for amine molecules, high surface area and porosity, good mechanical strength and thermal stability. Alternative approaches are also being explored, such as ammonia-based wet scrubbing systems, which are similar in operation to amine-based processes and exploit the ability of ammonia and its derivatives to react with carbon dioxide via various mechanisms. One of these is the reaction of ammonium carbonate, CO_2 and water to form ammonium bicarbonates, with a significantly lower heat of reaction than amine-based systems that results in an energy saving. Ammonia-based absorption has a number of other advantages compared to amine-based systems, such as the potential for high CO_2 capacity, lack of degradation during absorption/desorption cycles, low cost and tolerance to oxygen impurities in the flue gases, but few concerns however exist, especially due to ammonia's high volatility and ammonia vapor losses from the systems during the operation ([29]). Similarly, carbonate systems are based on the reaction between a soluble alkali metal carbonate and the carbon dioxide to form again a bicarbonate that further can release CO_2 when heated to being reverted in the carbonate. Typically, carbon dioxide capture is effective within the temperature range of 50-100°C, while regeneration occurs in the range of 120-200°C. Na_2CO_3 and K_2CO_3-based adsorbents have been investigated and

analysis have indicated that the energy requirement due to the CO_2 sequestration process is 5% lower compared to MEA ([29], [32]). However, carbonate-based sorbents are more expensive than amines and some other issues, including sorbents durability, carbonation reaction rate and temperature control, energy management and sorbents deactivation due to SO_2 and HCl impurities in the flue gases must be solved.

Besides amine-enriched, ammonia-based sorbents and carbonate-based systems, other chemical/physical sorbents are being investigated, including zeolites and metal organic frameworks (MOFs). A temperature swing typically facilitates the regeneration of this kind of sorbents, whose application is mainly characterized by the absence of water that results in a sensible reduction of the heating and stripping energy requirements, typically affecting solvent-based systems. Zeolites are porous crystalline aluminosilicates containing cavities with molecular dimensions where CO_2 can be adsorbed by means of the interaction with cations. The adsorption and gas separation properties of zeolites are heavily dependent on the size, the charge density, and the distribution of these cations in the porous structure. Unfortunately, zeolite selectivity to CO_2 over other gases (N_2, CH_4, H_2O, etc.) is still low, and their adsorption capacity rapidly decline with increasing temperature above 30°C. Similarly, MOFs are a new class of hybrid materials built from metal ions with well-defined coordination geometry and organic bridging ligands. They have attracted significant interest due to their remarkable high surface areas and controllable pore structures, whit cavities that can be carefully sized in order to achieve an exceptional CO_2 adsorption capacity. However, additional work is needed to determine stability over thousand of adsorption/desorption cycles and to improve desirable characteristics such as low energy requirement for regeneration, good thermal stability, tolerance to contaminants, attrition resistance and low cost ([29], [31], [32]).

Ionic liquids (ILs) are a range of salts typically containing an organic cation and either an inorganic or organic anion that have attracted widespread attention thanks to their unique properties such as very low vapor pressure, good thermal stability, high-polarity and non-toxicity. They can be used to dissolve gaseous CO_2 under operating temperatures of several hundred centigrade degrees and hence, they offer the possibility of recovering carbon dioxide from flue gases without having to cool them first, as required with amine-based solvent processes. Also, since ionic liquids work as physical solvents, little heat is required for the regeneration stage. Unfortunately their high viscosity, in addition to their current

high cost, still call into question the large-scale applicability of this technology ([29], [31]). The current state-of-the-art of pre-combustion CO_2 capture technologies that could be applied to many industrial processes including nature gas, synthesis gas and hydrogen production with high carbon dioxide content, basically involve again physical solvents that preferentially absorb CO_2 from the gas mixtures. The selective absorption of CO_2 performed with physical solvents occurs without a chemical reaction and depends on the temperature and the CO_2 partial pressure, insomuch as high partial pressures and low temperatures would be typically preferred. Therefore, physical solvents, rather than chemical solvents, could be used in gasification processes because of the relatively high partial pressure of carbon dioxide in the syngas gas exiting from the water-gas-shift reactors. Commercial systems that use physical solvents include Selexol, Rectisol, Purisol and Fluor processes but, unfortunately, they are energy intensive due to their heat transfer requirement. In fact, physical solvent capacity is best at low temperatures, so that it is necessary to cool the gas mixtures before the carbon dioxide capture. Physical solvents with acceptable capacity at higher temperatures would improve the overall efficiency of gasification-based power plants ([29], [31]). An interesting less energy intensive alternative is represented by lithium silicate-based (Li_4SiO_4) sorbent materials, which are being developed in order to perform CO_2 removal in a broad range of high temperatures, roughly between 250 and 550°C. These sorbents seem to be highly effective also in a broad range of pressures (up to 20 atm), CO_2 concentrations (from 2 to 20% in volume), and in the presence of contaminants in the gas streams. In addition, they show excellent characteristic of regeneration along cycling applications as well as a good capability to promote the water-gas-shift reaction but, unfortunately, their manufacturing cost is still rather high ([29]).

The second approach for capturing carbon dioxide, namely the CO_2 separation with membranes, exploits the selective permeation of a gas through the membrane themselves ([4], [28], [29]). Membrane-based CO_2 capture systems use different permeable materials for the selective separation of carbon dioxide from flue gases and syngas. It is generally accomplished by some physical or chemical interactions between the membrane and the carbon dioxide that has to be separated, allowing CO_2 to pass through the membrane at faster rate than the other gas components. The selectivity of the membrane to different gases is intimately related to the nature of the material (e.g. polymers, metals and

ceramics), but the flow of gas through the membrane is usually driven by the pressure difference across the membrane ([4], [28], [29]). Therefore, high-pressure streams as those encountered in gasification-based power plants (i.e. in the pre-combustion approaches) are usually preferred for membrane separation. However, the selectivity of the membranes in one stage is insufficient to achieve the desired purity and degree of CO_2 recovery, so multiple stages and recycles may be required in actual operations, leading to increase complexity, energy consumption and capital costs. For these reasons, although membrane separation finds many current commercial applications in several industrial sectors, they have not yet been applied for the large scale and demanding conditions in terms of reliability and low-cost required for CO_2 capture systems.

Finally, an alternative method to capture the carbon dioxide from fuel gas or flue gas is to modify the combustion process in order to obtain a flue gas with a high concentration of CO_2. To accomplish this goal the oxy-combustion is a promising pathway because, as previously mentioned, it allows to produce a flue gas consisting predominantly of CO_2 and water that, in turn, can be easily removed by condensation. In the most frequently proposed version, this approach relies on the presence of a cryogenic air separation unit used to supply to the boiler high purity oxygen (approximately 95-99%), which is mixed with recycled flue gas to control the operating conditions. The cost of carbon capture in a oxy-combustion based power plant should be lower than those for a conventional combustion plant, as a result of the decreased flue gas volume (which allows to reduce the equipment size) and the increased concentration in CO_2, but the cost of air separation and flue gas recirculation significantly reduce the economic benefits. To drastically reduce the cost of oxy-combustion systems, improvement are required to reduce the cost of oxygen production ([29]). In these terms, chemical looping combustion technology ([4], [28], [29], [33], [34]) is under investigation/development because it enables the production of a concentrated CO_2 stream without the need of an expensive air separation unit. In fact, this technique involves the use of metal oxides or other compounds as O_2 carrier to transfer the combustive agent from the combustion air to the fuel, avoiding the direct contact between fuel and combustion air, and resulting in a flue gas without contaminants.

Chapter 2

CO_2 capture with CaO-based solid sorbents

One of the strategies for carbon dioxide capture and storage using solid sorbents is based on the carbonation reaction. Calcium oxide can be an effective sorbent for separating carbon dioxide at high temperatures and this reaction is the basis for the CO_2 capture systems when coupled with the calcination step to produce a pure stream of CO_2. Contrary to the calcination stage, the absorption process has not a trivial kinetics and several characteristic aspects have still to be clarified. After a fast chemical controlled stage, carbonation reaction shows a strong slowing down, leading to an incomplete CaO conversion. The transition between the fast and slow regimes occurs rather suddenly due to the trigger of the product layer diffusion control regime that determines the decrease of CO_2 absorption capacity of the sorbent particles, especially when sorbent particles undergo to an increase number of carbonation/calcination cycles. These features make the study of the carbonation reaction rate quite critical. In addition, during the reaction progress, the solid phase may undergo to structural changes that influence the reaction itself, and complicate the elaboration of mathematical models able to simulate both the carbonation process and the structural/morphological changes of the solid sorbent particles. Intrinsic kinetic parameters are also required but physical limitations typically affecting the thermo-gravimetric analysis still call into question the quality of the CaO conversion versus time profiles experimentally measured by means of this approach.

This chapter aims to present the main features of the carbonation reaction and the description of thermo-gravimetric analysis that was preliminary applied to investigate the carbonation reaction kinetics.

2.1 The calcium looping cycle

Problems associated with current CO_2 capture technologies constantly lead to research and investigate other methods of carbon dioxide capture. Among all the CCS approaches applicable to existing large point sources of CO_2, a promising cost-effective technology

under investigation involves the utilization of calcium based solid sorbents. This technique, known as "calcium looping cycle" or "Ca-looping" process, is widely discussed in the literature, and recently it has been reviewed by several authors ([5], [6], [7], [8]). It uses calcium oxide (CaO) as regenerable sorbent to capture carbon dioxide from combustion flue gases, basically exploiting the reversibility of the reaction between CaO with CO_2 that forms calcium carbonate ($CaCO_3$) under stringent operating conditions, especially at high temperatures, which are not reachable by the most part of the other CCS technologies currently developed/investigated and outlined in the previous § 1.5, such as amine-based and ionic liquid scrubbing systems, membranes or physical adsorbents like zeolites and metal organic frameworks (e.g. [29], [32], [31]).

The Ca-looping cycle can be applied both to post-combustion systems, where CO_2 is removed from the exhaust gas streams arising directly from the fuel burned, and to gasification/pre-combustion processes, where it can be used to increase hydrogen production by removing CO_2 from the products of the water-gas-shift reaction ([7], [4]). Both post-combustion and pre-combustion applications of the calcium looping cycle follow similar principles, such that calcium oxide sorbent particles are repeatedly cycled between stages of carbonation and of calcination, as schematically shown in Figure 2.1, which can be carried out by means of circulating fluidized bed reactors ([35], [10], [5]).

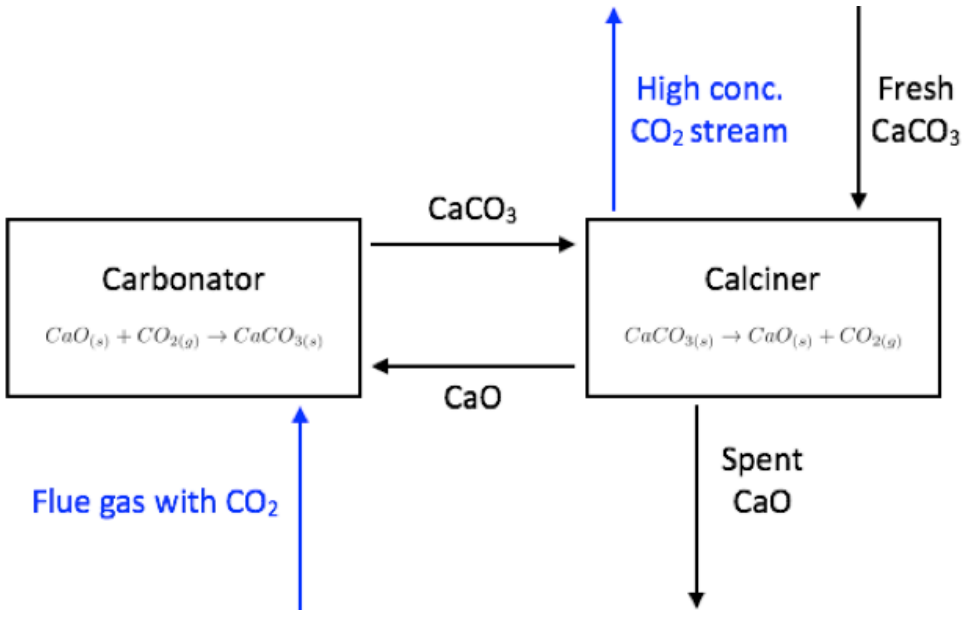

Figure 2.1: *Typical example flowchart for Ca-looping.*

Cycling of the sorbents between the carbonated and the calcined states can be performed by varying the temperature and/or CO_2 partial pressure, in accordance with the thermodynamic equilibrium of the reaction ([36]), as briefly discussed in the following § 2.2.1. The operating conditions during the calcination stage must be a compromise between the increase of the rate of decomposition obtained at higher temperatures and the reduced rate of degradation of the sorbents at lower temperatures. Similarly, the carbonation conditions should strike a balance between the increased equilibrium conversion obtained at lower temperatures and the theoretical increased of the reaction rate at higher temperatures. Therefore, in a typical post-combustion configuration, the CO_2 absorption is carried out at atmospheric pressure and temperature of around 600-650°C in a reactor (carbonator) where CaO sequestrates the carbon dioxide present in the combustion flue gas stream. The $CaCO_3$ formed is then thermally decomposed inside a separate decarbonation unit (calciner) by increasing the temperature to approximately 900-950°C, leaving a concentrated stream of CO_2 usable for further operations/applications, and resulting in the sorbent regeneration ([7], [35]). The CaO particles are in turn passed back to the carbonator so that the cycle is continued, and spent (unreactive) sorbent is continuously replaced by fresh (reactive) calcium oxide particles.

2.1.1 Advantages and issues

Compared with other CCS techniques, the carbon dioxide capture performed with calcium based solid sorbents offers a number of advantages ([7]), basically including a high sorption capacity for CO_2 at high temperatures, a low cost of sorbent manufacturing and regeneration, and the abundance of their natural precursors.

Whereas absorption and desorption can be performed at temperatures and pressures close to the power plant process conditions, lower efficiency penalties can be achieved, mainly by recovering some of the energy supplied by the fuel to regenerate the sorbents ([37]). In addition, heat from the exothermic carbonation of calcium oxide can be used to run a steam cycle, making up for some of the energy losses and contributing to a theoretical more cost-effective CO_2-capture system ([7]). Moreover, calcium based sorbents are cheaper than other chemical/physical solvents/sorbents, especially amine-based ones, because they can be obtained by abundant and naturally occurring precursors like calcium carbonate and/or

dolomite. They can be also used to simultaneously capture other pollutant gas species/impurities present in the fuel burned (e.g. sulfur oxides), and their final disposal does not raise environmental and safety concerns.

Unfortunately, the carbon dioxide capture performed through calcium based solid sorbents is affected by a few limitations, the most important of which is the rapid and gradual loss in CO_2 capture capacity that sorbents show with the increase of the number of carbonation and calcination cycles, as mentioned by several contributions including [38], [39], [37], [40], [41], [5], [7], [6], [8], [42] and [10]. Even though fresh calcined calcium oxide is a very reactive solid in the carbonation and ideally, as described by Eq. (2.1), CaO particles would be continually cycled between the carbonator and the calciner reacting with and evolving 1 mol of CO_2 per mol of calcium oxide each cycle, as a result of many carbonation-calcination cycles their effectiveness respect carbon dioxide absorption rapidly decreases (Figure 2.2).

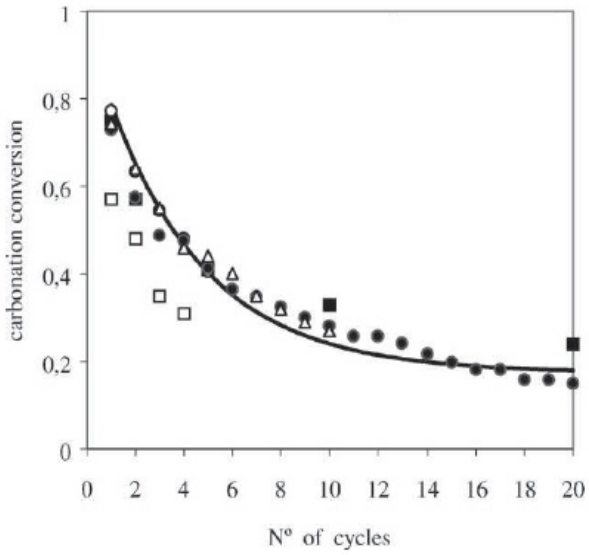

Figure 2.2: *Evolution of the maximum CO_2 absorption capacity of CaO (data from different authors) with the number of carbonation/calcination cycles. Source: Abanades (2002) (*[38]*).*

Loss in sorbent capacity can be due to several factors, including particle attrition within fluidized bed environments that cause both sorbent abrasion and loss of material due to elutriation, and/or competitive reactions (e.g. sulfation) that irreversibly deactivates CaO ([7], [43]). However, sintering is the most widely recognized cause of this sorbent shortcoming (e.g., [5], [7], [6], [44], [37], [39], [37], [45], [46], [47], [40]). The

phenomenon is favored by high temperature treatments and can take place at different extents depending on both temperature and CO_2 concentration/partial pressures ([41], [7]), in particular during the calcination phase, and on the characteristics of the parent carbonate, especially its particle/grain size and chemical purity ([43]). Typically, sintering induces alterations of the characteristic porous structure of the sorbent particles such as changes in pore shape, pore coarsening and pore shrinkage, causing an overall reduction in their reactive surface area over time and consequently a drop off in the CO_2 capture capacity during sorbent cycles. The CaO-CO_2 reaction is in fact closely related to the sorbent specific surface area because of the marked decrease in the molar volume that is achieved during the thermally induced transition from calcium carbonate (precursor) to calcium oxide (sorbent). Usually, larger surface areas and porosity of CaO particles enhance the CO_2 capture performance, and whether a sufficiently large pore volume is available for the carbonation reaction, it seems to occur more rapidly. Several strategies to improve the reactivity of CaO-based sorbents and to preserve their performance against sintering over time were investigated. So far, the methodologies analyzed include: thermal pre-treatments and optimization of calcination conditions; sorbent hydration techniques; doping of natural sorbents with trace amounts of organic salts; development/production of synthetic sorbents characterized by inert porous supports and/or foreign ions grafting ([48], [7], [8]). Nevertheless, the improvement of this technology and the development of new calcium-based solid sorbents are currently a matter of study and, despite the apparent simplicity of the chemistry involved, several aspects of the carbonation reaction are still not clearly understood.

2.2 Fundamental aspects of the carbonation reaction

The carbonation reaction is an heterogeneous reaction between a porous solid species (CaO) and a gas species (CO_2), that evolves producing a solid product phase ($CaCO_3$). It is an equilibrium reaction that can be represented by the chemical equation:

$$CaO_{(s)} + CO_{2(g)} \leftrightarrow CaCO_{3(s)} \qquad \Delta H_r^0 = -178\, kJ/mol \tag{2.1}$$

where the reaction enthalpy underlines how the forward step is exothermic, while the backward calcination step is endothermic. Thermal decomposition of initially non-porous $CaCO_3$ particles is known to lead to CaO with a high porosity (theoretical free volume of pores up to 54%) thanks to the molar volume reduction from 36.9 to 16.9 cm^3/mol caused by the thermally induced release of carbon dioxide. The resulting increase in specific surface area makes CaO porous particles particularly reactive towards the following CO_2 absorption stage, during whose progress the overall volume of the carbonate solid phase (i.e. product layer) increases, still due to the relative density difference between the calcium carbonate and the calcium oxide.

2.2.1 Thermodynamic equilibrium

The conditions at which the gas-solid reaction between CaO and CO_2 takes place can be predicted from the thermodynamics, insomuch as calcium oxide reacts with carbon dioxide when the CO_2 partial pressure in the reactant gas atmosphere is higher than its equilibrium partial pressure; conversely, $CaCO_3$ decomposes leading to CaO and CO_2 when carbon dioxide partial pressure is lower than the equilibrium partial pressure.

The determination of the equilibrium conditions, namely the equilibrium partial pressure of carbon dioxide ($pCO_{2,eq}$), was performed by several investigators ([36], [49], [50], [51], [52]). In these works, according to Eq. (2.1), the equilibrium vapor pressure of CO_2 over CaO was computed as a function of the system temperature. Specifically, a linear relationship can be emphasized in a plot of $log(pCO_{2,eq})$ versus $1/T$, as shown in Figure 2.3, where it can be observed as the various calculated values are in good agreement among the cited works, especially for high temperatures.

In order to predict the equilibrium conditions of the carbonation reaction, the most frequently quoted equation proposed by Baker (1962) ([36]) is used:

$$\log pCO_{2,eq} = 7.079 - \frac{38 \times 10^3}{4.574T} \tag{2.2}$$

where $pCO_{2,eq}$ is in atm and T in K. A plot of the Eq. (2.2) is reported in Figure 2.4, in which it can be observed that for partial pressure of CO_2 larger than the equilibrium, at a given temperature, the carbonation is favored while in conditions below the curve the

calcination occurs. From Figure 2.4, it is also clear that roughly above 900°C the carbonation cannot occur at atmospheric pressure because the chemical equilibrium is strongly shifted to the reactants of Eq. (2.1), thus identifying the thermodynamic conditions for the sorbent regeneration.

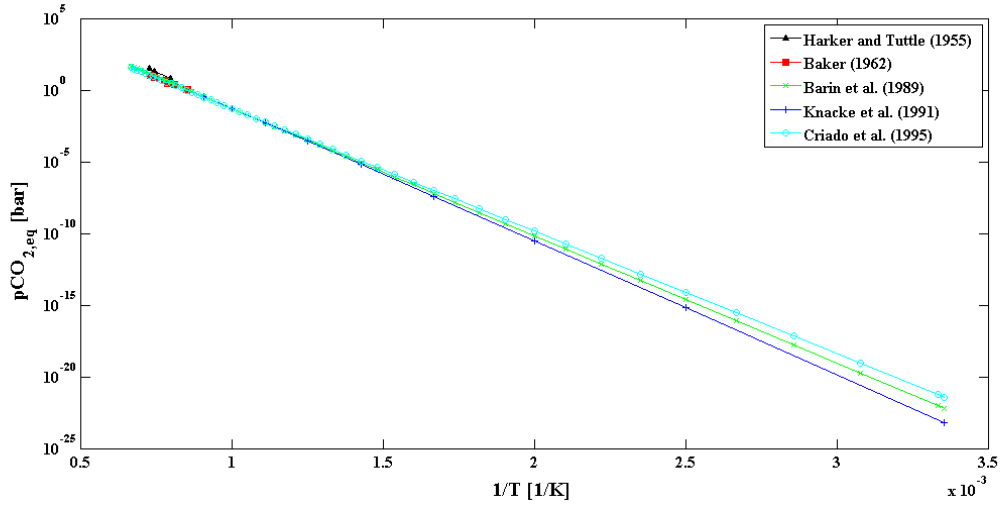

Figure 2.3: *The equilibrium partial pressure of CO_2 resulting form the thermal decomposition of $CaCO_3$. Data reproduced from literature evidences (*[36], [49], [50], [51], [52]*).*

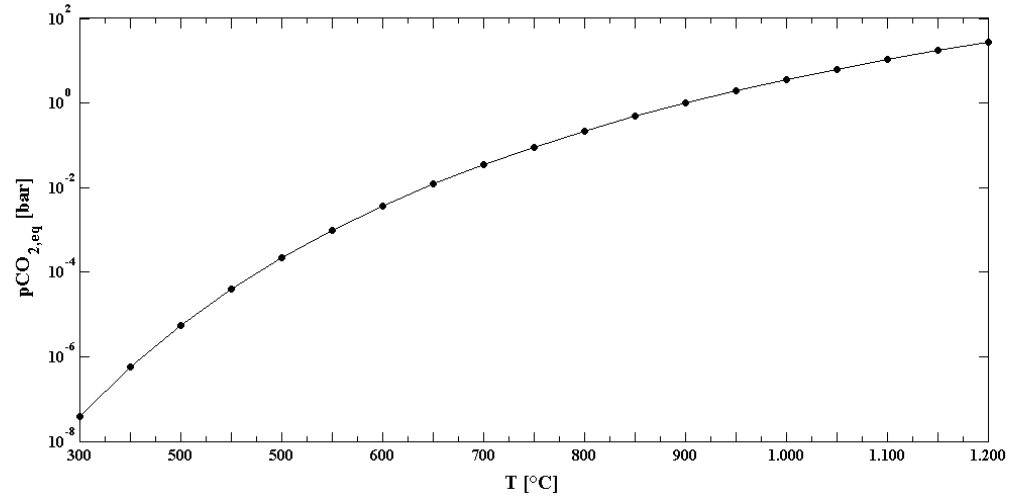

Figure 2.4: *The equilibrium partial pressure of CO_2 respect to CaO. Data reproduced using Eq. (2.2) from Baker (1962) (*[36]*).*

2.2.2 Stages of CaO-CO_2 reactions

Among the characteristics of the carbonation reaction, it is accepted that the chemisorption of carbon dioxide in CaO particles proceeds as a non-catalytic gas-solid reaction by means of a number of steps. These stages typically include external mass transfer, inter-particle diffusion (in case of particles form a particle bed), intra-particle diffusion (i.e. CO_2 diffusion inside the pores), diffusion through the carbonate product layer, and surface chemical reaction. When the gas phase mass transfer resistances (external, inter-particle, intra-particle diffusion) can be neglected, the carbonation reaction is controlled by the surface chemical reaction and by the product layer diffusion, as discussed in several contributions such as [53], [15], [11], [12], [9], [10], [13] or [21]. The diffusion through the solid product layer is a relevant aspect because at the interface between the solid and the gas reactant the formation and growth of a solid product layer of $CaCO_3$ takes place, making the contact between new molecules of carbon dioxide and a still existing portion of reactant CaO progressively more arduous. As a consequence, the carbonation is characterized by an initial very rapid reaction period, reasonably governed by the surface chemical reaction and the filling of small pores that characterize fresh calcined CaO particles, followed by a much slower stage limited by the diffusion of the reacting CO_2 through the product layer of $CaCO_3$. In Figure 2.5, typical CaO conversion versus time profiles that underline these features are shown.

The transition between these two stages is sharp and has been related to the formation of calcium carbonate that progressively dumps the CaO reactivity towards the carbon dioxide, until the thickness of $CaCO_3$ has reached a critical value beyond which the diffusion-controlled process becomes slower as the conversion increases. However, all the cited authors, which performed CO_2 absorption analysis in a wide range of operating conditions in terms of carbonation temperatures (typically ranging between 450°C and 750°C) and CO_2 partial pressures, report always CaO conversions below to 100%, that means calcium oxide never converts totally into carbonate.

Several models have also been proposed to describe the carbonation kinetics between CaO and CO_2 and they can be classified into different types including, apparent models ([14]), shrinking core models [61], random pore models ([54], [55], [15], [56], [10]) and grain models ([57], [18]). In particular, random pore and grain models are especially relevant for

the study of the carbonation reaction. The random pore model correlates the carbonation rate with the internal pore structure, while the grain model assumes that the sorbent is composed of small grains that are dispersed in gas, and each grain is converted according to the shrinking core model. A detailed description of these modeling approaches is outside the scope of this thesis. To a detailed discussion, the author cross-refers to other contributions, including [25].

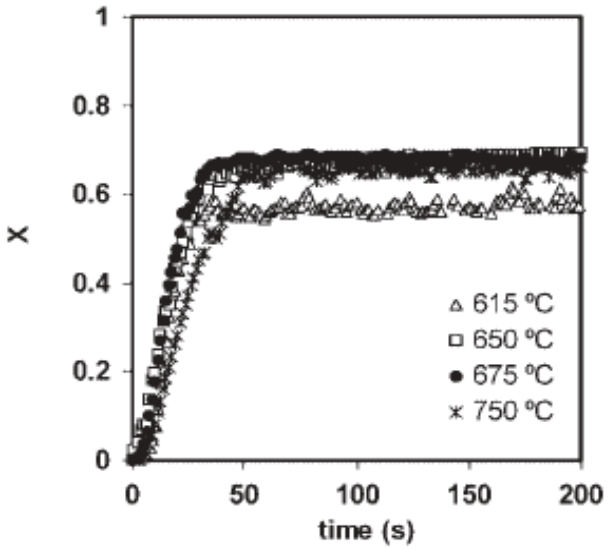

Figure 2.5: *Typical CaO conversion versus time profiles at different carbonation temperatures (pCO_2 during carbonation of about 0.01MPa). Source: Grasa et al. (2009) (*[10]*).*

2.2.3 The critical product layer

The concept of the critical carbonate product layer thickness at which the reaction becomes controlled by CO_2 diffusive limitations was initially introduced by Barker (1973) ([53]) who, assuming an homogeneous distribution of $CaCO_3$ over the entire internal surface area of calcium oxide sorbent particles, and taking into account the expansion of the solid associated with the variation in the molar volume between CaO and $CaCO_3$, estimated a critical carbonate thickness of 22 nm. He related the reactivity of fresh newly formed calcium oxide (mean particle size of about 10 μm) to the formation of small pores (in the range of about 40 and below 4 nm), which significantly increase the sorbent surface areas.

Excluding the effects arising from the complex morphology of porous CaO sorbent particles, Mess et al. (1999) ([58]) performed carbonation experiments utilizing nonporous crystals of calcium oxide (particle size of about 15-20 μm) and measured uniform product layer thicknesses up to 2 μm after long carbonations. Based on Mess et al. (1999) data ([58]), Abanades and Alvarez (2003, 2005) computed estimates between 130 nm and 220 nm for the carbonate thickness at the onset of the slow reaction period ([59], [60]). As suggested by Barker (1973), the CaO-CO_2 reaction is sensitive to the pore size distribution of the fresh sorbent particles and hence, the formation and growth of the calcium carbonate solid product reasonably causes the obstruction of the particle porous structure by filling the pores, making the diffusion of gaseous CO_2 through and inside the particle porosities more difficult ([53], [15]). Several other authors investigated this aspect combining pore models with experimentally determined pore size distributions (obtained by mercury porosimetry), CaO conversion profiles (typically measured by TGA experiments) and the qualitative analysis of the pore closure by means of optical and scanning electron microscopy. Bhatia and Perlmutter (1983) attributed the sharp transition from the first rapid regime to the product layer diffusion regime in the carbonation conversion profiles of fresh calcines to the filling of the small pores, with a size below 100-150 nm, at corresponding CaO conversions of about 0.6-0.65 ([15]). The threshold between small and large pores has to be set by the growth of the product layer, as asserted by Abanades and Alvarez (2003) ([59]), who early estimated a product layer with a critical thickness of 100-140 nm ([61]) from pore size distribution analysis and, in a further publication ([60]) computed an average critical product layer thickness of 49 nm acceptable for a wide range of sorbents and carbonation conditions, interpreting with a simple pore model the differences obtained from the comparison of mercury porosimetry curves of calcines and the carbonated counterparts. More recently, Grasa et al. (2009) reported critical product layer thicknesses between 30 and 40 nm (again in correspondence of CaO conversion of 0.55-0.6) ([10]), whereas Sun et al. (2008) applying a gas-solid reaction random pore model based on discrete pore size distribution measurements, proposed that the turning point from the fast stage of carbonation to the slow period should be ascribed to the consumption of all the pores smaller than 250-300 nm ([17]). In conclusion, several contributions related the transition from the fast regime to the slow product-layer diffusion controlled regime to the filling of small pores and/or to the development of a critical

carbonate layer, and focused the attention on the impact of the pore size distribution on the critical $CaCO_3$ product layer thickness. However, an unambiguous value of such critical thickness has not been identified yet and a direct measure of this parameter has never been provided as well.

2.2.4 Intrinsic kinetic parameters

Another crucial aspect concerning the carbonation reaction is represented by the surface reaction kinetic parameters and their determination. The design of the carbonator requires a fundamental understanding of the carbonation reaction rates of the CaO particles that are fed to the carbonator. High reaction rates during the carbon dioxide capture by CaO solid sorbents are required to design carbonator reactors of reasonable size, and hence the fast stage of carbonation is especially interesting because during this step CaO solid sorbents can achieve high degrees of conversion with short residence times. In the scientific literature there are only a few studies interested on the kinetics of the first stage of the carbonation reaction, including [15], [11], [12], [9], [10], [22] or [14], and among this limited number of works only a handful have focused on the intrinsic surface reaction kinetics ([15], [12], [9]). Nevertheless, information regarding the activation energy is often contradictory and uncertainty on the typical values of the reaction rate is documented.

Based on the argument that the activation energy of the calcination reaction is very close to the enthalpy of the reaction, Dennis and Hayhurst (1987) postulated a zero-activation energy for the CaO carbonation ([16]), confirming the result that Bhatia and Perlmutter (1983) obtained studying the kinetics of the early portion of their TGA experimental data by means of a random pore model ([15]). More recently, Sun et al. (2008) argued that a zero-activation energy is rather rare and performed a detailed study with regard to the (apparently) intrinsic kinetics of the carbonation reaction carrying out TGA experiments, even in a wide range of CO_2 partial pressures. Applying a grain model on the early instant of the CaO versus time profiles, Sun et al. (2008) observed that the activation energy for the fast stage of CaO-CO_2 reaction was small, but not zero, computing a value of about 29 kJ/mol ([9]). This value was somewhat lower than the activation energy of 78 kJ/mol determined by Kyaw et al. (1998) ([12]), but the discrepancy was attributed to structural differences in the sorbent particles that could potentially have affected the mechanism of

$CaCO_3$ formation ([9]). The knowledge of the sorbent particle structure (especially CaO pore size distribution and specific surface area at the beginning of carbonation) is essential for the application of random pore/grain models in the investigation of the carbonation reaction, but it represents also the main disadvantage of these approaches because of the complexity to collect information about the structural parameters characterizing sorbent samples, especially during the carbonation reaction progress.

The quality of the estimated surface reaction rate constants is also determined by the accuracy of the experimental data, specifically of the conversion versus time curves. To the best of the author's knowledge, in all the contributions available in literature investigating the intrinsic kinetics of the carbonation reaction the thermo-gravimetric approach was used to measure the conversion versus time curves ([15], [11], [12], [9], [10], [22]). A typical value of the initial and/or maximum reaction rate (expressed in terms of conversion rate at 615°C, with a CO_2 partial pressure equal to 10 kPa or higher) obtained through thermo-gravimetric measurements is 0.054 s^{-1} ([9]). Similar values were obtained by Bhatia and Perlmutter (1983) ([15]), and Kyaw et al. (1998) ([12]). However, as afterwards discussed, common thermo-gravimetric measurements can be affected by gas phase mass transfer limitations (external, inter-particle and intra-particle diffusion), especially for fast reactions such as the carbonation reaction ([62], [63], [64]). Usually, such resistances can be reduced by increasing the gas flow rate (external diffusion), decreasing the thickness of the particle bed (inter-particle diffusion), and decreasing the particle size (intra-particle diffusion). While reducing the particle bed down to a monolayer can theoretically minimize the inter-particle mass diffusion, it is questionable whether the external mass diffusion is negligible in the available carbonation reaction data obtained through thermo-gravimetric analysis. In fact, even though a few authors ([9], [10]) claimed that their TGA experimental results are independent of the gas flow rate (since they used high flow rates), the resulting conversion versus time curves and the reaction rates can still be dependent on the external diffusion. This could happen if, even at high gas flow rates, the local velocities around/inside the TGA crucible (close to the sorbent particles) are low and do not change significantly with the gas flow rate, and the high mole (CO_2) consumption rate due to the surface reaction is still limited by the external diffusion. Ultimately, improvements in the thermo-gravimetric approach should be taken, as well as measurement techniques alternative to the TGA should be also considered to provide CaO conversion versus time data (and reaction rates)

not limited by the external mass diffusion, and to check the validity of the available thermo-gravimetric data concerning the intrinsic CaO carbonation kinetics.

2.3 The thermo-gravimetric analysis of CaO carbonation reaction

Thermo-gravimetric analysis (TGA) is an analytical technique typically used to determine the thermal stability of a material and its fraction of volatile components by monitoring the weight change that occurs when a sample is heated. More specifically, this approach is widely used in the scientific literature in the investigation of the gas-solid reactions. Referring to the carbonation reaction, typical experiments are carried out feeding in a reaction chamber/furnace a reacting mixture of CO_2 in nitrogen or pure CO_2, and the CaO sorbent reactivity is measured by recording the change in a sample weight due to the carbon dioxide absorption, such that the monitored weight increase, as a function of the controlled gas atmosphere and of a temperature/time program, is related to the progress of the carbonation. In this work, a preliminary investigation of the CaO-CO_2 reaction was performed by means of the thermo-gravimetric technique with the initial goal of reproducing the carbonation reaction rates (and estimate the corresponding kinetic parameters) so far reported in the literature, as well as to familiarize with the effects of the physical limitations characterizing typical TGA experiments.

2.4 Experiments

A set of analysis of the carbonation reaction was performed using a SDT Q600 thermo-gravimetric apparatus, provided by TA Instruments®. The instrument is an horizontal-type thermo-balance that can work at temperatures up to roughly 1500°C, at atmospheric pressure. A typical experiment consisted on loading a known mass of sample within the TGA reaction crucible and then running a specified temperature program. An heating resistive system allows in fact to warm up the reaction chamber following a temperature profile set up by the user meanwhile, inside the tubular furnace, an arm linked to the thermo-balance measures both the temperature of the crucible and the change of the sample weight. The furnace atmosphere is typically fed with reactive/inert gases flowing through a tube connected to external gas lines. Specifically, they are axially injected into

the furnace by a sudden expansion (namely, from 0.79 mm of the reactive gas tube inner diameter to 22.86 mm of the furnace inner diameter) that allows the gases to reduce their mean velocity. The gases then flow around the crucibles (and hence above the sample powder), diffuse into the solid material, and unreacted and/or inert gases are then discharged outside the furnace In particular, downstream of the crucible the reaction chamber tapers until reaches the purge gas zone, where exhaust gases leave the reaction chamber, and whose design prevents back diffusion and removes efficiently decomposition products from the sample area ([25]).

The selected precursor material employed for studying the carbonation reaction was high purity commercial calcium carbonate provided by AppliChem®. The company declares that $CaCO_3$ purity is close to 99% without any trace of organic solvents and reports that the material is typically obtained from marble granular. The powder was sieved and classified on the basis of mean particle diameter and afterwards, only the 150 ÷ 160 μm class was considered for the thermo-gravimetric tests. This specific particle size was retained to be a good compromise between a low particle mobility and a negligible resistance particle diffusion during the reaction. In fact, during experiments too light/small particles could have been lifted by the gas flow, as well as smaller/lighter particles would have been cohesive and would have led to inter-particle sintering. A known amount of granular material (usually around 2.5 ÷ 10 mg) was thus poured into the crucible that was tapped in order to obtain (in as much as possible) a uniform particle layer. Afterwards the crucible was placed into the sample holder inside the furnace, thanks to an axially moving cover that allows the user to access the furnace by an opening and closing system. The furnace temperature was then increased with a heating rate of 50°C/min up to a desired calcination temperature, in order to produce CaO porous particles afterwards subjected to the carbon dioxide absorption process. Two different calcination temperatures were used, namely 650°C and 900°C, while several residence times at these maximum temperatures were selected, in the range between few seconds up to 120 min. At a defined calcination temperature, the time required to fully decompose a given amount of calcium carbonate decreases as the calcination temperature increases ([65], [66], [67], [68]) and hence the operational conditions were chosen in order to ensure the complete decomposition of $CaCO_3$ samples, as well as to verify how the calcination conditions can affect the following stage of CO_2 absorption. Additionally, since it has been generally observed that

the (local) CO_2 partial pressure markedly affects both the calcination rate ([69], [67], [49], [70], [71], [68]) and the sintering process ([72], [73], [74], [75], [76], [77], [78], [79], [80], [45]), the $CaCO_3$ thermal decomposition was performed in N_2 atmosphere (at a pressure of 1 bar), with a flow rate of approximately 250 NmL/min, to facilitate the removal of the CO_2 released at the reaction zone during the calcium carbonate decomposition away from the solid surface, aiming at reducing its contribution on the sintering that, as mentioned, can affect the sample during calcination stage at high temperature. After the complete thermal decomposition of $CaCO_3$, the new-formed CaO was cooled down (still keeping the sample under N_2) till the desired carbonation temperature, in the range between 450 ÷ 650 °C. These values were chosen on the basis of some typical values reported in the literature ([15], [12]), and depending on the equilibrium conditions expressed by Eq. (2.2), in order to establish a sufficient driving force in terms of CO_2 partial pressure to allow the occurring of carbonation reaction. When isothermal conditions were reached, a gas switch was performed by an automatic switching valve from the inert atmosphere to the reactive gas that consisted of pure CO_2 or a mixture of nitrogen and carbon dioxide, typically maintaining a constant gas flow rate of approximately 250 NmL/min by means of digital mass flow controllers. Again, concentration of carbon dioxide in the gas was selected on the basis of carbonation temperature applied, in order to guarantee an adequate driving force in terms of CO_2 partial pressure. Because the CaO-CO_2 reaction is typically characterized by a very rapid initial reaction period, followed by a much slower second stage, isothermal reaction conditions under reactant gas were arbitrarily maintained for about 20 ÷ 30 min, in order to focus the attention on the early instants of the carbonation.

The whole procedure is summarized in Figure 2.6, which represents the sample mass change (and its time derivative) and temperature profiles monitored during a typical experiment.

Finally, considering only the carbonation stage, since it is common to express the TGA results in the form of a fractional conversion, data collected were used to calculate the CaO conversions as:

$$X_{CaO}(t) = \frac{(m(t) - m_0)}{m_0\,\chi}\frac{MW_{CaO}}{MW_{CO_2}} \tag{2.3}$$

where m_0 is the initial mass of the fully calcined sample; $m(t)$ is the sample weight recorded during the experiment, at each time t; χ is the mass fraction of the active CaO in the sample, which takes the value of 1 in this work due to the high purity of $CaCO_3$ that decompose into CaO at the beginning of each test; MW_{CO_2} and MW_{CaO} are the molecular weights of the two phases involved in the carbonation, respectively carbon dioxide (44 g/mol) and calcium oxide (56.08 g/mol). Moreover, it has be noted that the full decomposition of $CaCO_3$ (MW_{CaCO_3} = 100.08 g/mol) led to a sample weight change of 44%, in agreement with the mass loss due to the CO_2 release from the initial solid particles.

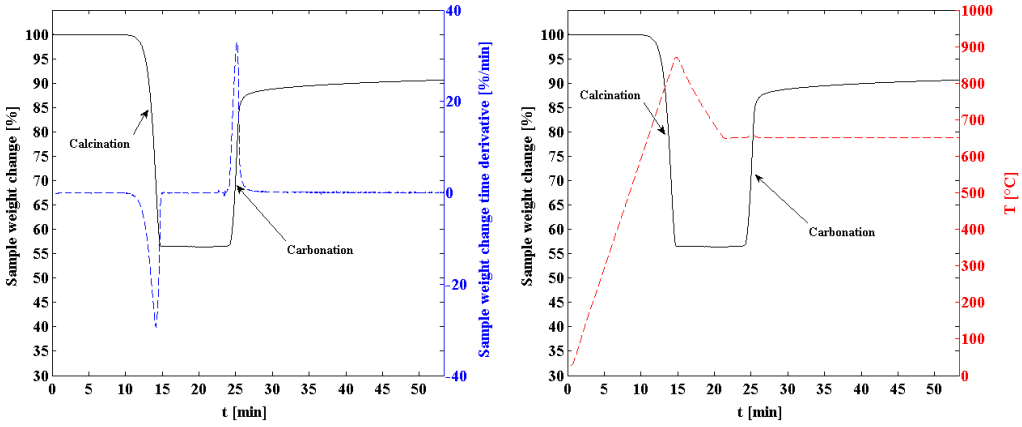

Figure 2.6: *Typical TGA experiment result obtained by TA SDT Q600. Sample weight change as a function of the time, during both the initial calcium carbonate thermal decomposition stage and the consecutive carbonation process (left) and corresponding temperature evolution (right).*

2.4.1 Results

As widely described by several authors, such as [81], [63], [62], or [64], it is known that TGA results may be affected by physical limitations due to the specific features of the instrument used, the experimental procedure employed and/or the sample properties. The main factors that lead to such issues typically include: temperature and gas flow rate (operating conditions); geometries of the furnace and of the crucible, and sensitivity of the recording system (instrumental factors); sample weight and particle size (sample properties) ([25]). In this work, some of these aspects have been investigated and afterwards, an estimate of the activation energy of the CaO carbonation reaction has been

computed, exploiting the conversion versus time profiles obtained by the TGA experimentations.

2.4.1.1 Influence of the temperature on the carbonation reaction

A typical plot showing the observed effects of the carbonation temperature maintained during TGA experiments on the reaction kinetics is shown in Figure 2.7, where the complete conversion profiles (up to 30 min of carbonation) are shown on the left side while a view of the reaction rates (expressed in terms of conversion time derivatives *dX/dt*) is plotted on the right side.

In this case, the behavior of three samples of calcium carbonate (initial amount of about 10 mg) calcined at 900°C for few seconds under a gas flow rate of N_2 of 250 NmL/min is reported. The following CO_2 absorption stages carried out at 450°C (blue curve), 550°C (red curve) and 650°C (green curve), underline that the higher the carbonation temperature, the higher the final conversion achieved at the end of each test. The influence is rather strong, mainly for temperatures over 450°C, whereas a relative increase of about 10% in the CaO conversion after 30 min was observed comparing the conversion versus time profiles at 550°C (with final X of about 0.7) and 650°C (final X equal to approximately 0.78). Differently, this increase moves to 35% if the carbonation curve at 450°C (final X of roughly 0.5) is considered.

In Figure 2.7 the typical features of the carbonation reaction are also clearly observable, with a fast initial reaction stage proceeding up to a point where an abrupt change in the carbonation rate leads to the second stage that, in turn, is characterized by a slower reaction rate typically associated with the occurring of the product layer diffusion controlled regime ([15], [12], [11], [9] or [10]). The first stage of the carbonation, taking place in the early instants of the reaction, was complete roughly within 2 min and is affected by the carbonation temperature insomuch as the higher the temperature, the higher the CaO conversion reached at the end of this stage, as well as the higher the reaction rate. In particular, increases of the maximum reaction rates of about 40% and 60% were observed moving from 450°C (~ 0.30 min^{-1}) to 550°C (~ 0.54 min^{-1}) and 650°C (~ 0.75 min^{-1}), respectively. Reasonably this phenomenon could be explained considering the kinetic constant (*k*) that usually increases in an exponential way following the well-known Arrhenius equation:

$$k = k_0 \exp\left(-\frac{E_a}{RT}\right) \tag{2.4}$$

where k_0 is the pre-exponential factor, E_a is the activation energy of the carbonation reaction (J/mol) , R is the universal constant of gases equal to 8.314 J/mol K , and T is the temperature of the system expressed in K.

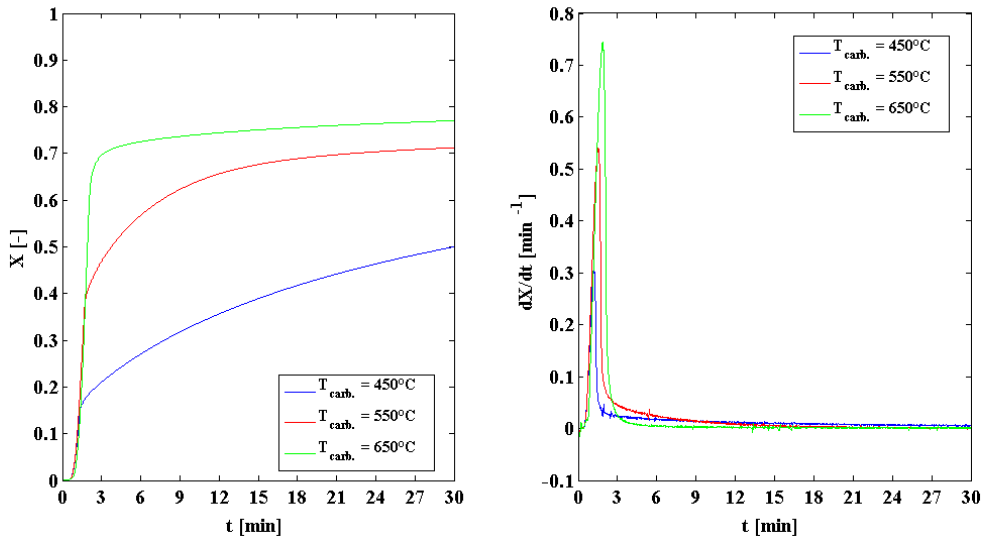

Figure 2.7: *Typical CaO conversion versus time profiles at different carbonation temperatures (left), and corresponding time derivative curves (right), obtained by TA SDT Q600. Sample weight of 10 mg, particle size 150 ÷ 160 μm, P = 1 bar, 100% of CO_2, gas flow rate of 250 NmL/min. Calcination conditions: HR of about 50°C/min up to 900°C and residence time at high temperature for few seconds (N_2 gas flow rate of 250 NmL/min).*

However, the transition between the two regimes did not occur at a specific (and constant) CaO conversion value that, on the contrary, increases following the temperature variations. Thus, this aspect has to be explained differently, for example assuming that even during the initial part of the carbonation progress the product layer diffusion could be involved. According to Bhatia and Perlmutter (1983) ([15]), the product layer diffusion is also retained a temperature activated mechanism that follows an Arrhenius-like equation, so that the product layer diffusion coefficient (D_p) can be expressed as:

$$D_p = k_d \exp\left(-\frac{E_{a,D}}{RT}\right) \tag{2.5}$$

where k_d is the pre-exponential factor and $E_{a,D}$ is the activation energy of the product layer diffusion (J/mol). Therefore, the higher the carbonation temperature, the higher should be the carbon dioxide diffusivity through the $CaCO_3$ layer and towards the unreacted portions of CaO sorbent particles. Consequently, a better gas (CO_2) diffusivity (due to an higher temperature) reasonably contributes to achieve higher conversion values during the first stage of the carbonation, suggesting how it is likely that product layer diffusion effects could be present even in the early instant of the reaction (Figure 2.7).

2.4.1.2 Influence of the gas flow rate on the carbonation reaction

The investigation of the reactant gas flow rate effects on the carbonation kinetics can be summarized by the results reported in Figure 2.8. A comparison of the carbonation behavior at 650°C of two samples of CaO obtained by calcination at 900°C, with a residence time of few seconds, is shown. Again, the complete conversion profile (up to 20 min of carbonation) is shown on the left side while a view of the reaction rate (in terms of conversion time derivative) is plotted on the right side.

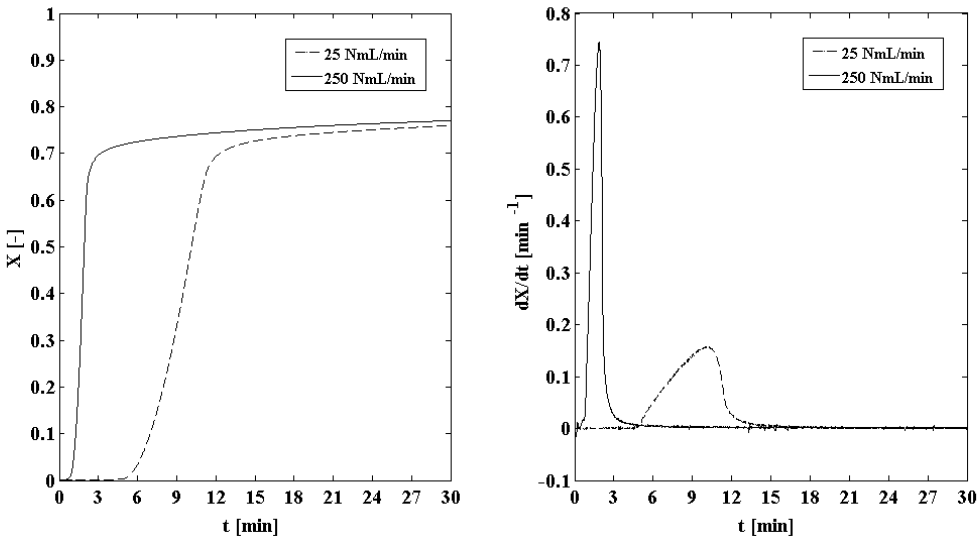

Figure 2.8: *Effect of the gas flow rate on both the CaO conversion versus time profiles (left) and the corresponding time derivative curves (right), obtained by TA SDT Q600 during carbonation experiments at 650°C. Sample weight of 10 mg, particle size 150 ÷ 160 μm, P = 1 bar, 100% of CO_2, gas flow rate of 250 NmL/min. Calcination conditions: HR of about 50°C/min up to 900°C and residence time at high temperature for few seconds (N_2 gas flow rate of 250 NmL/min).*

Typically, the higher the gas flow rate, the faster the reactant gas front reaches the sample surface, consequently reducing the time required to record with a TGA the first change in the sample weight caused by the reaction. In the case highlighted in Figure 2.8, a gas flow rate increase of one order of magnitude (specifically, from 25 to 250 NmL/min) moves the trigger of the carbonation reaction from approximately 5 min down to around 1 min.

Furthermore, the increase of the gas flow rate inside a given geometry usually results in an increase in the average gas velocity within the system. Therefore, when the reactant gas flows with an higher spatial velocity, the gas mass transport from the bulk to the particle layer is increased and goes to support the gas mole consumption due to the reaction. Similarly, in the case here described, the mass transport realized increasing the gas flow rate from 25 NmL/min up to 250 NmL/min went to support the CO_2 mole consumption due to the surface chemical reaction that occurred at the gas-solid reaction interface, resulting in a higher reaction rate, as shown in the plot. Specifically, with an increase of one order of magnitude in the gas flow rate, an increase of roughly 5 times of the maximum reaction rate (again expressed in terms of conversion time derivative) was measured, namely from approximately 0.16 min^{-1} to 0.74 min^{-1}.

2.4.1.3 Influence of the gas composition on the carbonation kinetics measured by TGA

The reaction kinetics of a generic gas-solid reaction typically depends on the gas reactant composition. In particular, considering the carbonation reaction and its thermodynamic equilibrium curve shown in Figure 2.4, a higher partial pressure of CO_2, at a given temperature, should mean a higher driving force for the reaction.

Specifically, in this work it has been observed that an increase of the carbon dioxide concentration in the reacting gas mixture fed in the TGA furnace causes the increase both of the final CaO conversion (measured at the end of the experiments) and of the reaction rate. According to the carbonation experiments carried out at 450°C with CaO sorbent samples obtained by isothermal calcination at 900°C for 120 min, and reported in Figure 2.9, varying the pCO_2 from 0.05 bar to 0.25 bar resulted in a variation of about 30% of the final CaO conversion and of the maximum reaction rate from roughly 0.067 min^{-1} to 0.137 min^{-1} (approximately 50% more).

While an increase of the reaction rate is somehow expected because, as mentioned, the higher the CO_2 partial pressure, the higher the driving force for the carbonation reaction,

the increase in the CaO conversion value can be explained assuming the establish of a better mass transport of the gaseous CO_2 from the bulk to the reaction interface, which was obtained increasing the molar concentration of CO_2 in the reactant gas fed to the TGA furnace working at isobaric conditions of 1 bar (total pressure).

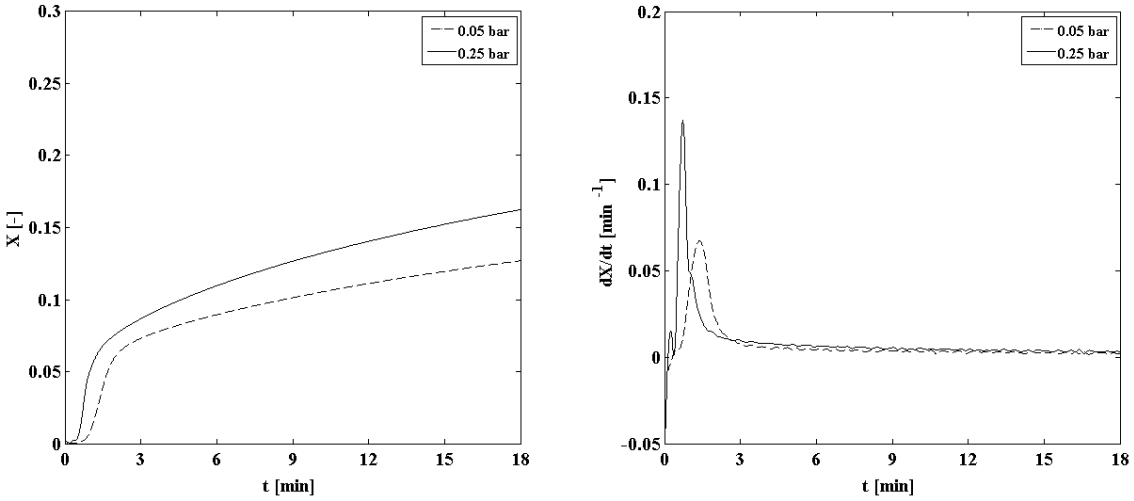

Figure 2.9: *Effect of CO_2 partial pressure on both the CaO conversion versus time profiles (left) and the corresponding time derivative curves (right), obtained by TA SDT Q600 during carbonation experiments at 450°C. Initial sample weight of 2.5 mg, particle size 150÷160 μm, P = 1 bar, gas flow rate of 250 NmL/min. Calcinations at 900°C for 120 min, in a N_2 atmosphere (gas flow rate of 250 NmL/min).*

A similar trend of the reaction rate respect to the CO_2 partial pressure used during the carbonation process can be found in the literature, as reported for example by Grasa et al. (2009) ([10]) and shown in Figure 2.10.

Nevertheless, Sun et al. (2008) recently performed CO_2 absorption experiments in a wide range of CO_2 partial pressure (pCO_2) and verified that when ($pCO_2 - pCO_{2,eq}$) ≤ 10 kPa the reaction follows a first-order kinetics while, beyond 10 kPa in CO_2 driving force, the carbonation becomes a zero-order reaction respect to the carbon dioxide partial pressure ([9]). The transition from a 0^{th} order to 1^{st} order reaction is very sharp, as shown in Figure 2.11, but it is in agreement with the observation reported in other previous works where only a narrow range of CO_2 partial pressure were typically used. For example, Bhatia and Perlmutter (1983) applying pCO_2 ≤ 10 kPa (at 615°C) reported 1^{st} order carbonation

kinetics ([15]), whereas Kyaw et al. (1996) using pCO_2 > 20 kPa observed a 0th reaction order ([11]).

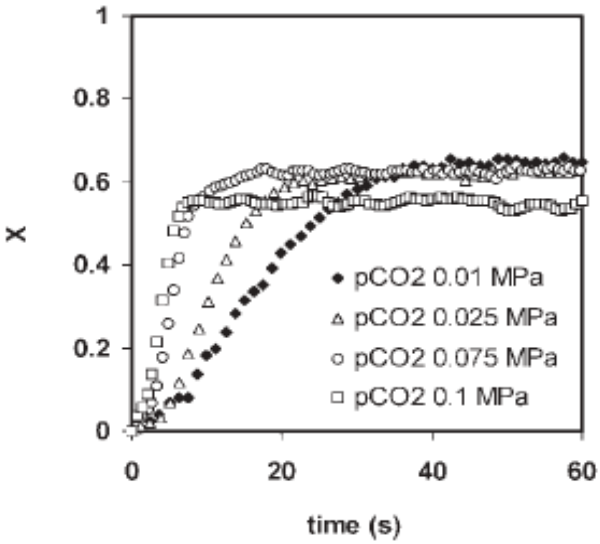

Figure 2.10: *CaO conversion versus time curves for different CO_2 partial pressures. Carbonation experiment carried out at 650°C. Source: Grasa et al. (2009) (*[10]*).*

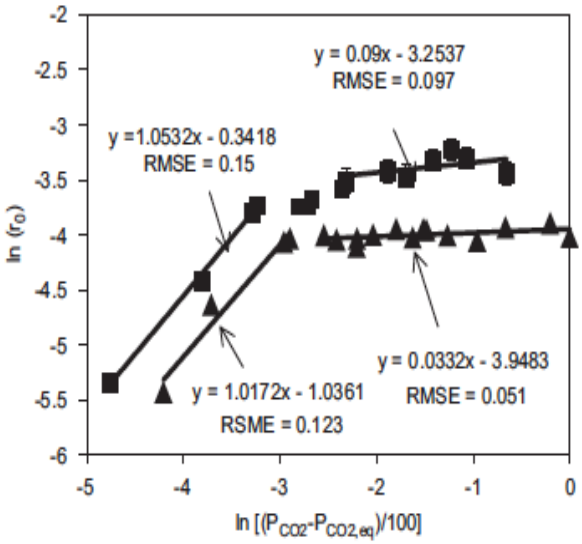

Figure 2.11: *Reaction order plot for fully calcined $CaCO_3$. Carbonation at 800°C (squares) and 650°C (triangles), under different CO_2 partial pressures, with r_0 equal to the specific reaction rate at time t = 0. RMSE, root mean square error. Source: Sun et al. (2008) (*[9]*).*

2.4.1.4 Influence of the calcination operating conditions on the carbonation kinetics

Gas-solid reactions typically depend on the morphological properties of solid phase, mainly in terms of interphase specific surface area so that the solid phase is usually employed in the form of particles in order to increase this parameter. However, the gain in surface area due to a large number of particles is low compared to the same number of porous particles that are characterized by pore networks. These networks generate an internal surface (i.e. within each particle) significantly larger than the external particle surface and, for this reason, one of the main goals of the preliminary calcination stage carried out with calcium carbonate precursor is indeed the thermal activation of the solid material in terms of pore opening and specific surface increase. Unfortunately, high temperature treatments typically promote sintering processes that in turn determine a progressive reduction of the specific surface of CaO porous particles, especially as the residence time at these temperature increases (e.g. [74], [76]). Therefore, the calcination conditions reasonably affect the CO_2 absorption performances of CaO sorbent samples, as furthermore observed in the literature.

This feature has been studied also in this work, performing carbonation experiments with CaO samples previously obtained through different calcination stages, namely at 900°C for 5 min, 900°C for 90 min, and at 650°C for 120 min, under a N_2 flow rate of 250 NmL/min. In Figure 2.12 the conversion versus time curves measured at 650°C (up to 30 min of carbonation) are shown on the left side while the conversion time derivatives are plotted on the right side.

From the plots it can be observed that increasing the calcination temperature and/or the residence time under the calcination conditions, both the final CaO conversion values and the maximum conversion rates decrease. At 900°C, prolonging the residence time in calcination from 5 (blue curve) up to 90 min (red curve) results in a reduction of the calcium oxide conversion after 30 min of about 15%, which is also proportional to the relative decrease in the maximum conversion rate values. However, the effect of the calcination temperature is even more important than that one of the calcination time: comparing the carbonation behavior of CaO particles produced at 650°C for 120 min (green curve) with that one of a sample obtained after 5 min at 900°C (blue curve), it has been observed how, even if the residence time during calcination is significantly higher, a

lower calcination temperature allows to reach both higher final CaO conversion (approximately 0.85) and higher conversion rate (of about 0.82 min^{-1}).

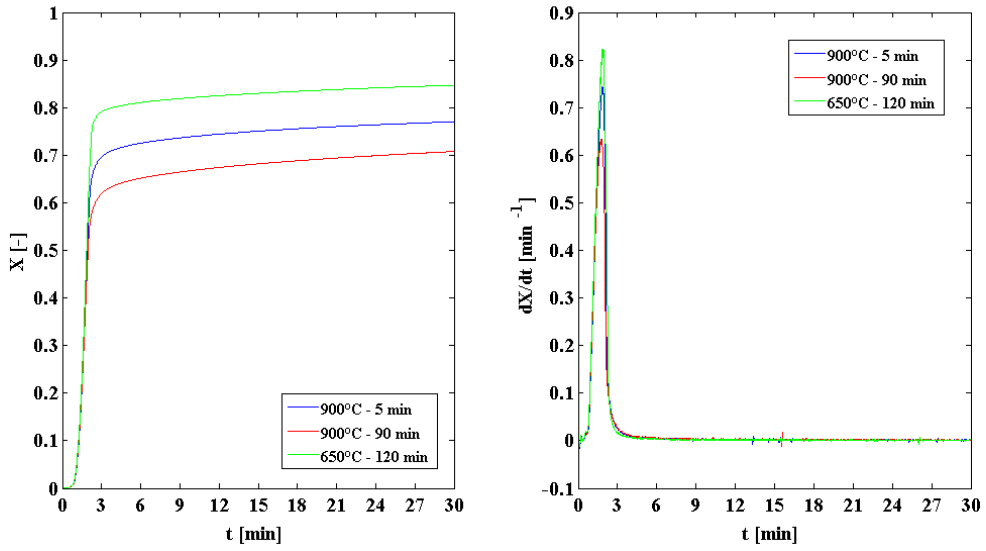

Figure 2.12: *Effect of the calcination conditions on the following carbonation kinetics at 650°C (CO_2 partial pressure of 1 bar, gas flow rate of 250 NmL/min). Initial sample weight of 10 mg, particle size 150÷160 μm, P = 1 bar, gas flow rate of 250 NmL/min.*

As mentioned, these results reasonably reflect the specific surface of calcium oxide particles since it is known to influence the kinetics of carbonation: high specific surface area means both a high reactivity due to the high gas-solid interface that is established; instead a sample with a low specific surface presents a poor reactivity and it may undergo to incomplete conversion.

The range of specific surface values reported in the literature for CaO particles obtained from the calcium carbonate thermal decomposition is rather large, as observed by several contributions such as [82], [73], [83], [74], [76], [84], [85], [48], [79] or [86]. Borgwardt (1989) asserted that nascent CaO particles should be typically characterized by specific surfaces very high, on average of 104 m^2/g ([76]). However, the author also specified that in the initial stage of sintering, the specific surfaces significantly declined (from 104 to 80 m^2/g) suggesting that prolonged residence times at high temperatures can penalize the specific surface area of CaO sorbent particles. The author also observed that calcination of $CaCO_3$ sample powders in a temperature range between 600 and 950°C, under a N_2

atmosphere, led to CaO particles with initial surface area on average of 79 $m^2/g \pm 6$ m^2/g. However, increasing the calcination temperature/time and/or changing the gas atmosphere of calcination, the specific surface area can be reduced to lower values, down to about 15 ÷ 30 m^2/g in the first moments of the decomposition and then decreased to an asymptotic value at infinite time ([74], [49]). Specific surfaces of about 5 m^2/g obtained maintaining the sample at 950°C for 30 min (possibly in a stagnant atmosphere) are also reported. In addition, Beruto et al. (1980) ([82]) asserted that CaO obtained from the thermal decomposition of limestone particles in air/CO_2 environments is characterized by small values of specific surface, approximately of 10 m^2/g. In particular, the authors performed calcination stages in a TGA apparatus, in a static air atmosphere at temperatures up to 1200°C with an heating rate of 10°C/min and measured specific surfaces ranging between 11 and 12.5 m^2/g. Similarly, calcination performed in a special designed TGA instrument, at temperature > 850°C, allowed Grasa et al. (2009) to measure specific surfaces of CaO sorbent particles of 12.6 m^2/g and 10.5 m^2/g ([10]), while Sun et al. (2008) reported specific surfaces of fresh calcines equals to 29 m^2/g ([9]). More recently, Zhou et al. (2011) showed that calcination experiments performed in a chamber calciner (N_2 atmosphere) with nano $CaCO_3$ particles (particle size of 70 nm) in a temperature range between 750 and 900°C and residence times of 10, 60, 120, 240 and 480 min resulted in sorbent samples with specific surfaces between 15 and 4 m^2/g, depending on calcination temperature and residence time ([86]).

In conclusion, the TGA results previously described should be also discussed in terms of changes in the specific surface that CaO particles show because of the calcination treatments. For this reason BET analysis, which is typically employed to estimate the total specific surface of a sample powder, was applied also in this study. Unfortunately, sample amounts used in the TGA experiments (at maximum ~ 10 mg) prevented the possibility to directly apply BET analysis to characterize the sorbent sample used in the thermo-gravimetric tests because of their low values. In fact, assuming to characterize a sample powder with a presumed specific surface of about 10 m^2/g, the sample amount required by the N_2 adsorption analysis to obtain reasonable results has to be usually one order of magnitude higher than those one used in the TGA tests ([87]).

Therefore, in order to collect larger sample masses of fresh calcined CaO, afterwards subjected both to the specific surface characterization by means of the BET analysis and to

a CO_2 absorption process carried out in TGA, calcium oxide particles were produced through calcination stages performed in a muffle. Specifically, several calcination experiments were conducted in a muffle furnace (Nabertherm® LE/6/11 P300) under an atmosphere of stagnant air, at the standard pressure of 1 bar. Calcium carbonate samples were settled on a ceramic plate and heated from room temperature up to 900°C, imposing an heating rate of about 10°C/min. Residence times at this maximum temperature varying between 5 min up to 120 min were maintained. It has to be noted that in bulky samples the thermal decomposition could be inhibited because of possible occurring local high CO_2 concentrations. Indeed, carbon dioxide can be held in the pores of the particles, or in the interstices of the particle bed. Therefore, in order to reduce this inconvenient, a quantity of calcium carbonate powder of approximately 2 g was loaded and arranged to obtain (in as much as possible) a thin layer. After that, calcined samples were degassed using a vacuum system, and then stored under nitrogen in a dry-box to prevent the hydration of CaO particles. BET analysis was then applied on the collected samples, using N_2 as gaseous adsorbent in a Quantachrome Autosorb iQ-MP instrument.

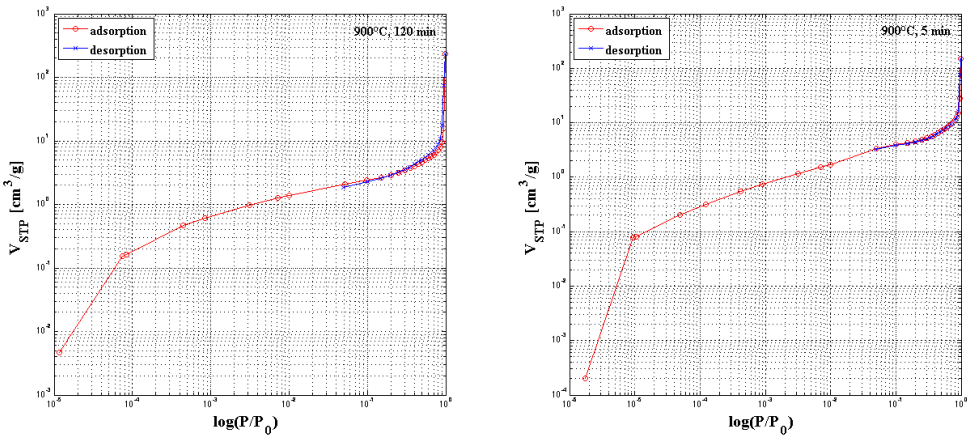

Figure 2.13: *BET analysis results of CaO sorbent particles obtained from $CaCO_3$ decomposition performed in a muffle furnace. Log-log scale isotherms for CaO particles produced at 900°C for 120 min (left) and at 900°C for 5 min (right). V_{STP}, volume of the gas adsorbed at the relative pressure P/P_0. P, pressure imposed; P_0, saturation pressure of the bulk fluid.*

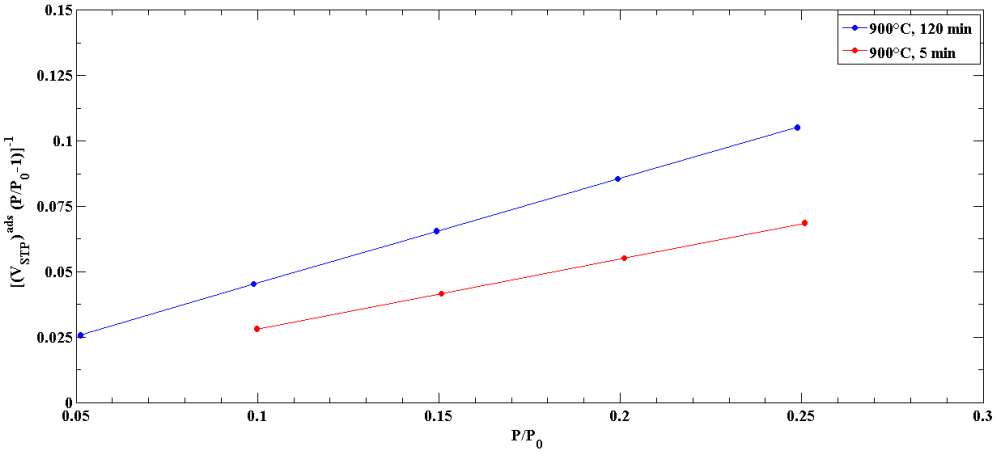

Figure 2.14: *Multipoint BET method diagrams for the comparison of BET analysis results between the two samples of calcium oxide, obtained with calcination temperature of 900°C at 120 min and 5 min.*

Figure 2.13 and Figure 2.14 show the comparison between two of the calcium oxide powder samples produced. As expected, the low residence time calcined sample presents higher adsorption (and also desorption) profile in the log-log scale isotherm (Figure 2.13) than the other sample obtained with a prolonged calcination. This aspect results in an higher specific surface, namely 16.1 m^2/g against 10.7 m^2/g, as determined by the multipoint BET method ([87]) which data are summarized in Figure 2.14.

2.4.1.5 Carbonation reaction rates from TGA experiments

Sorbent samples obtained through the thermal decomposition stage performed with the procedure above described were in turn tested in carbonation experiments carried out in the TGA, in order to verify sorbent performances in the CO_2 absorption process and compare the various results collected from the thermo-gravimetric analysis, especially in terms of reaction rates.

Carbonation tests were thus carried out in a temperature range of 450°C ÷ 650°C, with a carbon dioxide partial pressure of 1 bar. To reduce in as much as possible the external diffusion resistance, the gas flow rate was set at 250 NmL/min, which was the maximum value permitted in the TGA utilized. Instead, in order to avoid inter-particle diffusion, sample amounts of about 2.5 mg were chosen.

In Figure 2.15 the CaO versus time profiles (and the corresponding conversion time derivatives) of the two samples previously taken as reference are shown.

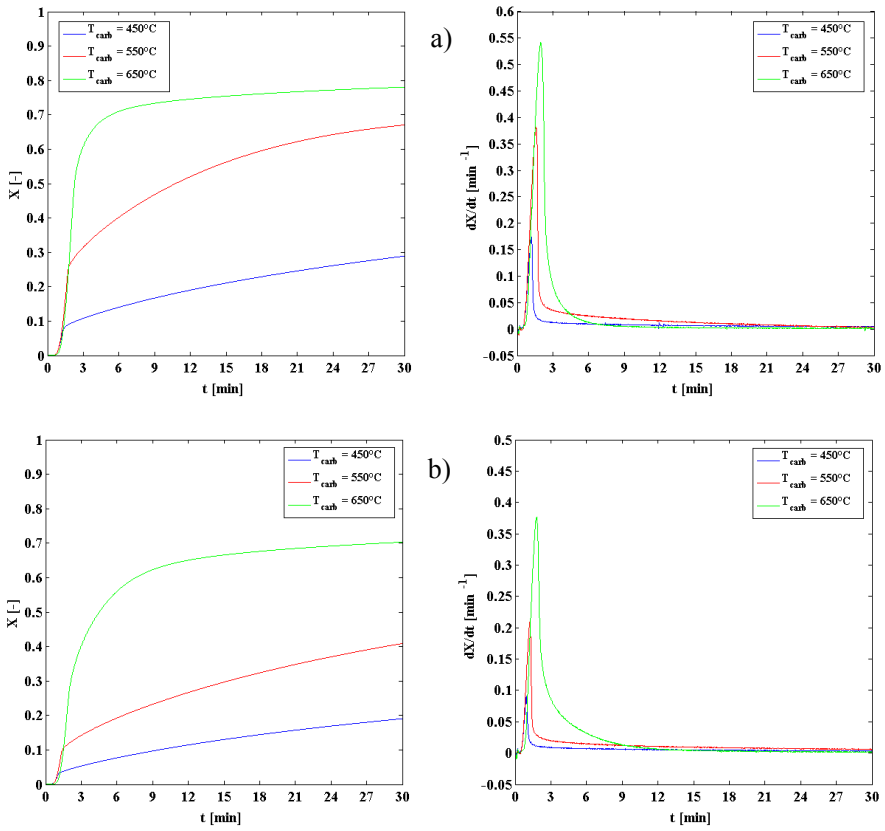

Figure 2.15: *CaO conversion versus time profiles (left), and corresponding time derivative curves (right), as a function of the carbonation temperature. Samples (2.5 mg) obtained by thermal decomposition of calcium carbonate carried out in a muffle furnace at 900°C for 5 min (a) and 120 (b), in stagnant air. Carbonation with pCO_2 of 1 bar and gas flow rates of 250 NmL/min.*

As expected from the evidences of Figure 2.12 and the related considerations, from the plots it can be clearly observed the contribution of the specific surface area on the conversion achieved by the CaO sorbent samples tested: at a given temperature, the higher the specific surface area of fresh calcined calcium oxide particles, the higher the final conversion achieved at the end of each carbonation experiment. This effect is evidently reflected by the conversion time derivatives used to express the reaction rates, whose maximum values are summarized in Table 2.1.

A more accurate comparison between reaction rates measured from different experiments should be performed considering the specific rate defined as *dX/dt* divided by *1-X*. However, even considering the specific rates, the tendency of the maximum conversion time derivatives observed thus far does not change, as shown in Table 2.1.

Table 2.1: *Summary of the maximum reaction rates as a function of the carbonation temperature measured from the conversion profiles of two CaO samples, previously obtained from different calcination condition.*

Samples	Calcination		Carbonation	Maximum dX/dt		Maximum dX/dt/(1-X)	Specific surface area [m^2/g]
	T [°C]	t [min]	T [°C]	[min^{-1}]	[s^{-1}]	[s^{-1}]	
a	900°C	5	450°C	0.175	0.003	0.003	16.1
			550°C	0.381	0.006	0.008	
			650°C	0.542	0.009	0.016	
b	900°C	120	450°C	0.09	0.002	0.002	10.7
			550°C	0.21	0.004	0.004	
			650°C	0.38	0.006	0.008	

In these terms, the most noteworthy aspect is the general observation according to which the maximum time derivatives (i.e. reaction rates) measured in these experiments (on average in the order of 0.006 s^{-1}) were lower than the typical values mentioned so far in the literature.

It could be argued that a such difference can be ascribed to the operating conditions used during the carbonation stages, but a maximum reaction rate equal to 0.054 s^{-1} reported by Sun et al. (2008) ([9]), which was obtained from carbonation experiments carried out at 615°C, with a CO_2 partial pressure of 10 kPa, is anyway higher (up to about 3 times) than that one measured in the thermo-gravimetric tests performed in this work with a similar carbonation temperature (650°C).

In addition, it has to be noted that the maximum time derivative typically refers to the conversion time derivative at time zero, when a grain model is applied to describe the intrinsic reaction rate due to the surface chemical reaction. However, looking at the CaO conversion time derivatives measured in this work, it can be observed that the maximum time derivatives were recorded after approximately 1.5 min, which is a rather high value compared to the early few second of reaction analyzed by Sun et al. (2008) ([9]). Therefore, it can be reasonably asserted that some resistances damped the CO_2 absorption processes monitored in this work. For example, external mass transfer limitations may have occurred, penalizing CO_2 diffusion towards the solid sorbent surface and, in turn, limiting the carbon dioxide mole consumption due to the chemical reaction.

Consequently, this aspect reflects on the estimate of the kinetic parameters. In a first approximation, if the gas-solid model proposed by Sun et al. (2008) is assumed to compute an estimate of the (intrinsic) kinetic parameters for the surface chemical reaction stage of the carbonation (a more detailed discussion about this calculation is reported in the Chapter 4) using the data shown in Table 2.1, an activation energy of about 45 kJ/mol is obtained. However, it has to be noted that even though the maximum time derivatives were identified in the fast reaction stage of the CaO conversion versus time profiles (Figure 2.15), the carbonation reaction rate measured cannot be interpreted as the specific rate controlled by the (intrinsic) surface chemical reaction. Indeed, since only at time close to zero (at low CaO conversions) it is correct to assume that the diffusional effects through the product layer of $CaCO_3$ are negligible, the computed maximum conversion time derivatives reasonably underestimate the true intrinsic reaction rates, especially because they may be affected by some product layer diffusion effects.

In conclusion, the activation energy computed at this stage of the research (which is between the values of about 20 kJ/mol ([9], [10]) and 78 kJ/mol ([12]) mentioned in § 2.2.4) contributes to the uncertainty about the reliability of the kinetics data discussed thus far in the literature, but reasonably confirms that the quality of the estimate kinetic parameters depends on the accuracy of the experimental data.

2.4.2 Physical limitations in TGA tests: the intrinsic kinetic problem

From the discussion at previous sections, it should be clear that many phenomena occur during carbonation tests performed by means of a TGA apparatus, and each one of them has its own contribution and rate. These phenomena may verify simultaneously or one after the other depending of the operative conditions. With the aim to determinate kinetic parameters of the carbonation reaction, physical limitations should be reduced. This can be achieved when all other processes are faster than the surface chemical reaction, so that they can be neglected and the carbonation reaction can be considered simply under the kinetic controlled regime.

Considering the results so far discussed, it is reasonable to assume that TGA tests carried out in this work measured an apparent kinetic rate, which is the combination of the rates of

several phenomena. This has led to measure an activation energy that is reasonably affected by mass transfer resistances.

As previously anticipated, when the TGA furnace has reached isothermal conditions, the gas flow rate is switched from an inert gas to carbon dioxide. In this precisely instant several physical limitations begin. Specifically, such resistances are due to:

i. external diffusion: the reactant gas employs a certain time to reach the crucible positions from the outlet of the reactive gas tube and this can be regarded as a delay related to the gas flow rate. When the front arrives to the crucible, mass transport of carbon dioxide occurs from the bulk flow to the sample surface, adding another time delay to the carbonation process;
ii. inter-particle diffusion: the reactant gas must diffuse within the sample through molecular diffusion from the particle layer surface down to the bottom of the crucibles. A concentration profile is established inside the sample powder;
iii. intra-particle diffusion: the carbon dioxide diffuses inside the pore network of each particle, realizing a concentration profile inside the solid particles;
iv. product layer diffusion: during the early stages the reaction takes place inside the pore surface and this fast kinetic regime occurs until a thick product layer is generated. Afterwards, the reactant gas must be adsorbed on the product layer surface and diffuse inside the solid matrix reaching the unreacted calcium oxide where reaction occurs. This last stage becomes the slower one when a critical product layer is reached and changes the process regime in the product diffusion controlled one.

The problem to estimate the intrinsic kinetic rate of CaO carbonation has been already discussed in the scientific literature in several contributions such as [9] or [10]. Several strategies have been developed in order to eliminate the mass transfer resistances that affect the intrinsic kinetic measurements performed by the thermo-gravimetric approach. Typically, the trick of increasing the gas flow rate up to reduce the external diffusion is preferred, but it cannot be completely eliminated because the TGA only works in laminar conditions. Moreover, high flow rates influence balance measurements giving noisy responses. Crucibles with short height or a porous structure could be therefore selected in order to find an acceptable compromise between an increase in the gas flow rate and a rather stable signal of the sample weight change recorded by the thermo-balance. However,

crucible height cannot be too low because the gas flow rate may drift the sample particle causing instrument degradation, while the crucible porosity would add another physical resistance in the mass transfer of the reacting gas towards the sample powder.
Particle layer resistance instead increases with the sample thickness and the particle packing. Low sample mass means low particle layer thickness and hence it would be preferred because when the sample mass is small enough, a monolayer can be generated. Finally, the intra-particle limitation, which is a rather difficult aspect to control, is due to the molecular diffusion of the reactant gas inside the particle pores, and hence larger particle diameters typically produce concentration profiles that may become the controlling step with low particle porosity or high particle tortuosity ([25]).

In front of the complexity to control all these variables, measurement techniques alternative to the TGA were considered to provide CaO conversion versus time data reasonably not limited by the physical limitations mentioned. Specifically, in the next chapters the application of the X-ray powder diffraction technique on the investigation of the CaO carbonation reaction will be presented.

Chapter 3

Application of the X-ray powder diffraction technique to the $CaO\text{-}CO_2$ reaction

X-ray powder diffraction (XRPD) is a useful instrument to determine characteristic properties of crystalline materials. Following the Bragg's law of diffraction, a polycrystalline material reflects an incident X-ray beam leading to obtain diffraction patterns that are characterized by diffraction peaks with a specific position and a specific intensity. These pieces of information can be used to identify both qualitatively and quantitatively one or more crystalline phases present in a sample. The application of these concepts, combined to the Rietveld whole profile refinement method and the Scherrer equation, has been used to investigate the $CaO\text{-}CO_2$ reaction, collecting information about the structural changes of the solid sorbent particles, specifically in terms of $CaO/CaCO_3$ crystal phase evolution and of their crystallite size variations occurring during the carbonation process.

This chapter aims to briefly discuss the X-ray diffraction theory and how it has been used to investigate the carbonation reaction.

3.1 Principles of powder diffraction

The X-ray diffraction phenomenon involving crystals is due to an interaction process between the electromagnetic radiation (i.e. X-ray beam) and the matter. X-rays are electromagnetic waves with a much shorter wavelength (λ) than visible light, typically in the order of 1 Å ($= 1\times10^{-10}$ m). A crystalline material is an arrangement of atoms that can be described as an infinitely repeating motif, known as *unit cell*, in a three-dimensional lattice. The arrangement of atoms within the unit cell typically exhibit characteristic repetition properties (e.g. long-range order) as a collection or group of symmetries that, in turn, determine in the crystal structure the presence of specific crystallographic or lattice planes with characteristic spatial orientations ([88], [89], [90]). When an X-ray beam hits a

sample containing many small crystallites (such as a typical powder of polycrystalline particles), the electromagnetic radiation interacts with the atoms that make up the substance and a scattering process takes place between the photons and the electrons surrounding the atomic nuclei present in these crystallites. Therefore, the X-ray diffraction technique involves the measurements of the intensity of X-rays scattered from the electrons bound to the atoms arranged in the crystalline structures, with the aim to collect significant information about the structural properties of a sample such as, the spatial distribution and periodicity of the unit cells within the crystallographic lattices, atom arrangement in the unit cells, and morphological details (size, shape and defects) of the crystallites.

A detailed description of the diffraction theory is beyond the scope of this work of thesis, and hence the author cross-refers to the large number of scientific contributions existing in the literature for further in-depth studies, such as for example [88], [89] or [91]. However, in the following sections a few concepts will be briefly discussed to help the reader's understanding both of the explanation of the experiments and of the main results reported hereafter in this work.

3.1.1 Bragg's law

The easiest way to describe X-ray diffraction theory and to access to the structural information obtainable from the powder diffraction is via the well-known Bragg's law. It describes the principle of the X-ray diffraction in terms of a reflection of X-rays by a set of lattice planes. Lattice planes are crystallographic planes characterized by the so-called Miller indices, namely the index triplet *hkl* that defines the spatial orientation of each specific crystalline plan present in the crystalline structures of a sample. Parallel planes have the same indices and are equally spaced, separated by the distance d_{hkl} ([90]).

Considering the schematic representation in Figure 3.1, where s_0 and s are the direction of the incident X-ray beam and of the diffracted one, respectively, it is possible to assume the *hkl* crystalline planes as reflecting surfaces for the X-rays.

Even though X-rays are not actually reflected by planes but are scattered by electrons bound to the atoms, in a first approximation Bragg analysis treats X-rays like visible light that is reflected by the surface of a mirror insomuch as X-rays are specularly reflected by the lattice planes. However, in contrast to the lower energy visible light, the X-rays

penetrate deep inside the material where additional reflections occur at consecutive parallel planes. Since all X-rays are reflected in the same direction, superposition of the scattered X-rays occurs.

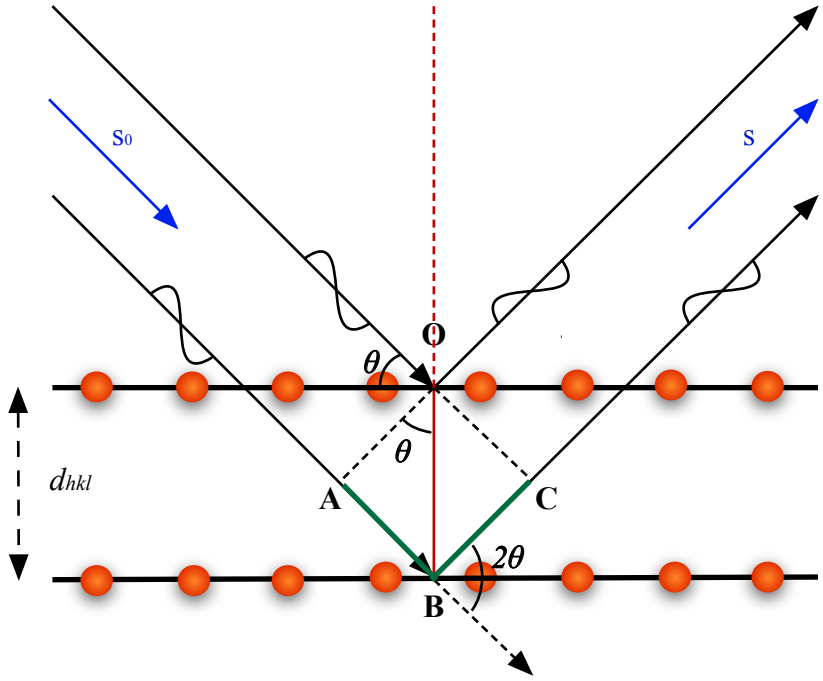

Figure 3.1: *Schematic illustration of the geometry used for a simplified derivation of Bragg's law.*

From Figure 3.1, it follows that the second wave travels a longer distance before (AB) and after (BC) a reflection takes place (i.e. optical path difference marked by green segments in Figure 3.1). Specifically, constructive interferences between waves occurs only if the optical path difference Δ = AB + BC is an integer number multiple (n) of the X-ray beam wavelength (λ) ([89]):

$$\Delta = n\lambda \tag{3.1}$$

When Eq. (3.1) is satisfied, a diffracted intensity emerges from the sample and can be detected. In particular, this happens only at specific angles of diffraction, where Eq. (3.1) holds. On the contrary, in all other cases, destructive interferences result and no diffracted X-rays can be observed. As it can be easily seen from Figure 3.1, geometric considerations lead to obtain a similar expression for the optical path difference ([89]):

$$\Delta = 2d_{hkl} \sin\theta \tag{3.2}$$

where d_{hkl} is the interplanar spacing of parallel lattice planes and 2θ is the diffraction angle, namely the angle between the incoming and outgoing X-ray beam, that leads to a constructive interference of the X-ray reflections.
Combining Eq. (3.1) and (3.2), we finally get the famous Bragg equation ([89]):

$$n\lambda = 2d_{hkl} \sin\theta \tag{3.3}$$

Bragg equation shows that for a given radiation of wavelength λ and a diffraction angle 2θ, a constructive interference exists only for those crystallographic planes characterized by the same *hkl* indices, which provide a unique definition for a set of parallel planes with a specific spatial orientation. Therefore, for a crystalline material, both mono- or poly-crystalline, X-ray diffraction can occur at different scattering angle 2θ only for different crystallographic planes. In particular, a polycrystalline material is defined as a group of microcrystals or crystalline domains which are distributed along several spatial orientations, each one characterized by its crystallographic planes, whereas a powder of polycrystalline particles is an ideally random distribution of these crystals ([89]).
Therefore, the result of a powder diffraction experiment consists of a diffraction pattern, namely a sequence of peaks (i.e. Bragg reflections) in the d-spacing dimension (or similarly in the 2θ-scale), resting on a slowly varying background (one-dimensional case), or a pattern of rings arranged around a common center in order to form the so called Debye-Scherrer rings (two-dimensional case), as shown in Figure 3.2, which represent the sum of the diffracted intensities arising from all the crystallographic planes contained in a powder sample that exactly satisfy Eq (3.3) ([89]).
Since crystallographic planes and their interplanar distances (d_{hkl}) are a specific feature of each crystalline phase present in a sample, the combination of positions and intensities of the Bragg peaks is a feature of each crystalline phase as well, and it can be exploited both to identify one or more phases within a sample, and to define their own structural properties.

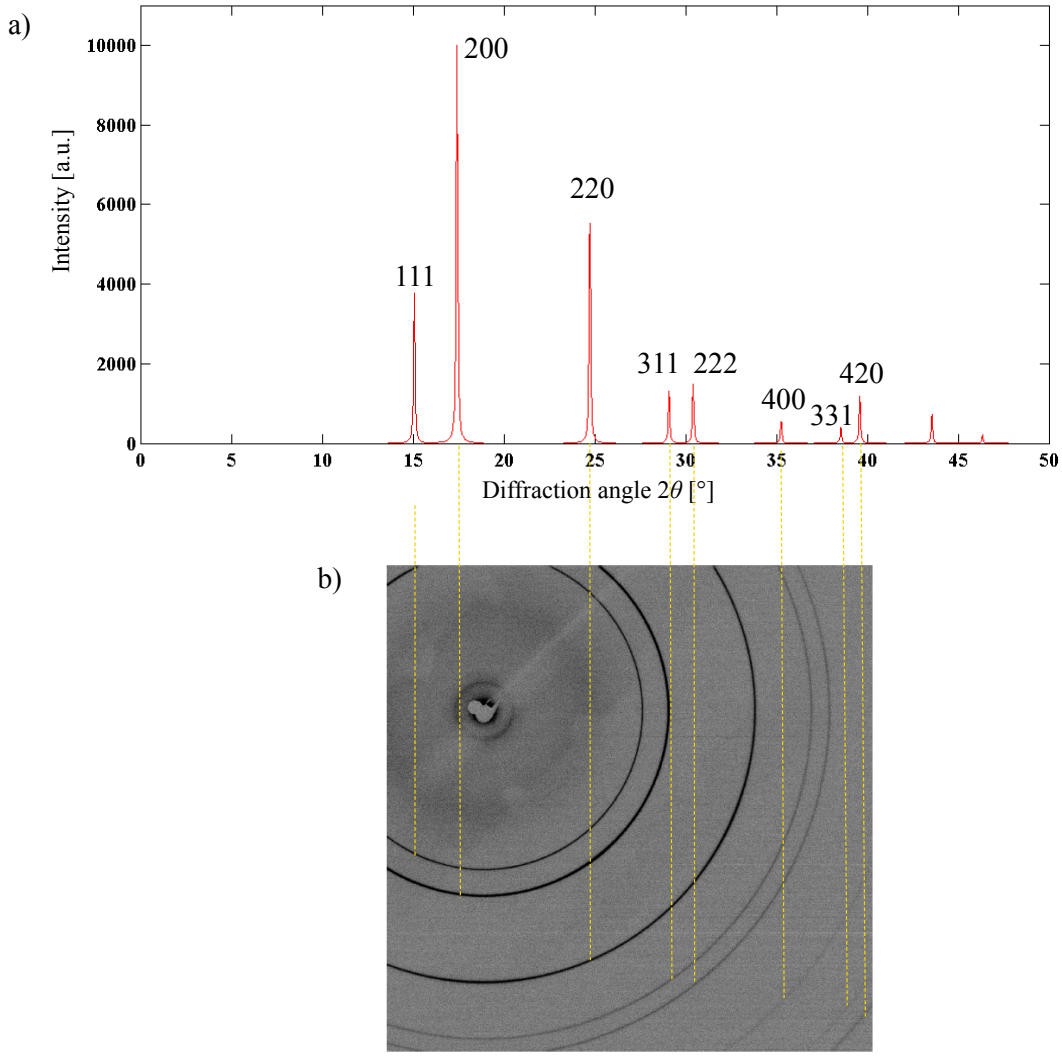

Figure 3.2: *Example of diffraction patterns: typical sequence of Bragg peaks (a) and the corresponding pattern of the Debye-Scherrer rings (b) for the characteristic crystallographic planes (hkl) of CaO (λ = 0.7296 Å).*

3.1.2 Scherrer equation

Assuming an infinite stack of parallel lattice planes, in the reciprocal space of the interplanar distances d_{hkl} or, similarly, in the space of the diffraction angle 2θ, the Bragg equation gives the position of Bragg peaks that theoretically should have a delta-function shape ([89]). However, because of several factors, including both instrumental set-up (i.e.

related to X-ray source, optics, detectors etc.) and features of the sample microstructure, finite size crystallites give rise to Bragg peaks of finite width, as shown in Figure 3.2a.
This peak broadening is typically used to obtain information about the shape and size of the crystallite forming each phase within a sample. In particular, it is commonly described by the Scherrer equation ([89]) that is especially exploited to estimate the average size of the coherently scattering crystalline domains present in a crystalline material.
Considering the thickness (i.e. the characteristic size) of a crystallite in the direction of *p* crystallographic planes of the generic *hkl* family, with separation d_{hkl}, as:

$$L_{hkl} = p\, d_{hkl} \tag{3.4}$$

a full treatment of the intensity distribution for the diffracted X-rays from these lattice planes leads to the well-known Scherrer equation ([89]):

$$\beta_{hkl}(2\theta) = \frac{K\lambda}{L_{hkl}\cos\theta} \tag{3.5}$$

where K is a scale factor (i.e. Scherrer constant) typically close to unity that depends on the crystallites shape (e.g. K is equal to 0.9 for cubic shape crystals), and β_{hkl} is the line broadening at half of the maximum intensity (FWHM) of the characteristic *hkl* reflection (in radians). Sometimes β_{hkl} is also defined as the integral breadth, which is the ratio between the integral intensity of a diffraction peak and its maximum intensity ([91]).
From the Eq (3.5), the characteristic size (L_{hkl}, in nm) of a set of crystallographic planes is determined, and applying the same equation to all the Bragg reflections in a diffraction pattern, an average value of the size of all the characteristic lattice planes forming the crystallites of a sample can be computed, resulting in a mean value of the crystal size.
Similarly, the Scherrer equation is also valid in the general case of a polycrystalline material, in which the crystalline domains are characterized by a size distribution, leading to the expression ([91]):

$$\beta_{hkl}(2\theta) = \frac{K\lambda}{< D >_V \cos\theta} \tag{3.6}$$

where $< D >_V$ indicates a volumetric average of the characteristic size of the crystallites contained within a sample.

3.1.3 Rietveld refinement method

As discussed so far, X-ray diffraction basically consists on the measurement of the reflections intensities scattered from a sample hit by an electromagnetic radiation. Whether the sample is crystalline, a constructive interference between the radiation and the crystal lattice takes place, and the diffracted intensities are modulated to form the Bragg peaks of diffraction, which are recorded by a detector. Several pieces of information can be extracted from a diffraction profile including: i) the peak position in the reciprocal space of the interplanar distances d_{hkl} (then scaled in the space of the diffraction angle 2θ), ii) the peak intensity and iii) the intensity distribution around the theoretical position of each Bragg reflection (i.e. peak shape). The collected set of data is then typically used i) to identify both qualitatively and quantitatively the crystalline species contained in the sample, ii) to refine their crystallographic structures, and iii) to characterize the microstructural and textural properties of the crystallites. In general, these analysis are performed separately, using specific software and approaches, but it is also possible to carry out a single analysis of the whole diffraction profile, especially trying to model and optimize all the physical aspects referred to both the sample (e.g. nature and crystallographic structure of the phases, microstructural and textural properties, etc.) and the experimental set-up used (e.g. radiation wavelength and source, optic devices, detector etc.), which affect the features of a diffraction pattern. This type of analysis is defined as *whole pattern profile analysis* (WPPA) ([91]) and it was initially introduced by H.M. Rietveld ([92], [93]). Commonly known as *Rietveld method*, this approach is based on the idea to simulate an experimental diffraction profile by means of a mathematical model which consists of a set of analytical functions (e.g. Gaussian, Lorentzian, polynomial, exponential and pulse functions) containing several parameters. These parameters are in turn optimized through a non-linear least mean square approach, minimizing the differences between the experimental profile and that one computed with the model, so that specific details about the sample can be deduced.

Considering an X-ray beam of constant wavelength λ and a generic polycrystalline sample formed by *j* crystalline phases, the general expression used to compute/simulate the diffraction pattern from a diffraction experiment is ([91]):

$$Y_c(i) = \sum_j S_j T_j(i) \left[\sum_{\mathbf{h}} I_{\mathbf{h}} L_{p_{\mathbf{h}}} P(i,\mathbf{h}) A(i,\mathbf{h}) O(\mathbf{h}) \right]_j + Y_b(i) \tag{3.7}$$

where $Y_c(i)$ is the approximate diffraction profile portion calculated at the *i*-th step of the whole diffraction pattern experimentally recorded (namely, at a specific value of the diffraction angle considering a 2θ-scale diffraction pattern profile). A summation of the contributions due to the **h** reflections of each single phase appears in Eq. (3.7), as well as a second summation that takes into account the contribution to the **h** reflections of all the *j*-th phases within the system ([91]). Moreover, as underlined by Eq. (3.7), this correlation represents a combination of analytical expressions, including: S_j, the scale factor, relative to each crystalline phase contained in the sample (i.e. phase factor); I_h, the integrated intensity of the Bragg reflection, which is computed for each feasible reflection due to crystallographic planes identified by **h** (= *hkl*), and that is proportional to the square of the *structure factors* (namely, it depends on characteristic unit cell structure of each species) ([88], [91], [94]) ; $P(i,\mathbf{h})$, the analytical function used to describe shape and size of the Bragg peak; L_{p_h}, the Lorentz-polarization factor; $A(i,\mathbf{h})$ and $O(\mathbf{h})$, characteristic functions used to describe possible peak asymmetry and preferred orientation effects, respectively; T_j(i), the transmission factor, which takes into account the attenuation of the diffraction intensities caused by the sample X-ray absorption phenomenon; $Y_b(i)$, a polynomial function applied to approximate the diffraction profile background ([91]).

In this work, a detailed analysis of these terms is avoided and, as previously stated, for additional information the author cross-refers to other contribution elsewhere (e.g. [88], [89], [91]). Nevertheless, among all the factors that appear in Eq. (3.7), a particular interest has to be addressed to the functions focused on the description/estimate of the shape and size broadening of the Bragg peaks. For this purpose, normalized functions (i.e. with unitary integral area), centered to the theoretically position of the Bragg reflections ($2\theta_h$) are typically used. In particular, a Pseudo-Voigt function $PV(i,\mathbf{h})$ is usually preferred, being a linear combination of a Gaussian function and a Lorentzian one, as reported in Eq. (3.8), whit η a mixing parameter.

$$PV(i,\mathbf{h}) = \eta L(i,\mathbf{h}) + (1-\eta)G(i,\mathbf{h}) \tag{3.8}$$

The Gaussian $G(i,\mathbf{h})$ and Lorentzian $L(i,\mathbf{h})$ functions, expressed by Eq. (3.9) and (3.10), basically weigh the contribution in determining the shape and size of the Bragg peak due to instrumental factors and microstructure properties of the sample, respectively.

$$G(i,\mathbf{h}) = \left(\frac{C_0}{\pi}\right)^2 \frac{1}{H_\mathbf{h}} \exp\left[-C_0(2\theta_i - 2\theta_\mathbf{h})^2/H_\mathbf{h}^2\right] \tag{3.9}$$

$$L(i,\mathbf{h}) = \frac{2}{\pi H_\mathbf{h}}\left[1 + 4(2\theta_i - 2\theta_\mathbf{h})^2/H_\mathbf{h}^2\right]^{-1} \tag{3.10}$$

In Eq. (3.9) and (3.10), C_0 is a dimensionless constant equal to $4ln2$, $2\theta_i$ represents the actual measured angle at the i-th step of the whole diffraction pattern, and H_h is the full width at half of the maximum intensity (FWHM) of the Bragg peak ([91]).
Specifically, H_h and η factors can be expressed as a function both of a Gaussian FHWM (H_G) term and a Lorentzian FWHM (H_L) one, so that $H_h = f(H_G,H_L)$ and $\eta = f(H_h,H_L)$. H_G and H_L changes as a function of the diffraction angle 2θ and can be computed through the following relationships:

$$H_G^2 = U\tan^2\theta_\mathbf{h} + V\tan\theta_\mathbf{h} + W + P/\cos\theta_\mathbf{h} \tag{3.11}$$

$$H_L = LX/\cos\theta_\mathbf{h} + LY/\tan\theta_\mathbf{h} \tag{3.12}$$

where U, V, W, P, *LX* and *LY* are the parameters that must be ultimately modeled and optimized to describe the shape and size of the diffraction peaks ([91]). In particular, since U, V and W, participate in the expression of the Gaussian term, they are related to instrumental effects, while *LX* and *LY* represent the Lorentzian parameters that can be used to estimate the specific contribution of the sample properties (i.e. crystallite size and micro-strain effect) in determining the peak broadening.

Referring instead to the quantitatively analysis of the crystalline species within the sample, it can be performed computing the weight fraction of each phase contained in the material. Specifically, the weight fraction of each phase w_j can be deduced from the corresponding scale/phase factor (S_j) through the following expression ([91]):

$$w_j = \frac{S_j m_{(u.c.)j}}{\sum_j S_j m_{(u.c.)j}} \tag{3.13}$$

where $m_{(u.c.)j}$ is the mass of the characteristic unit cell for the *j*-th crystalline species.
Finally, the set of parameters that appears in the mathematical model used to calculate the diffraction pattern is optimized with the method of the least squares. The minimization function is ([91]):

$$\chi^2 = \sum_i \omega_i \left[Y_0(i) - Y_c(i) \right]^2 \tag{3.14}$$

where $Y_0(i)$ is the experimental diffraction pattern portion compared with the diffraction profile calculated at the *i*-th step of the whole diffraction pattern. Each *i*-th count (at which corresponds an experimental point in the powder diffraction profile) is a statistically independent observation of weight ω_i equal to the observation variance ([91]). The correlation between the most of the parameters is nonlinear so that the minimization process requires an iterative procedure. The quality of the minimization process can be observed through a visual comparison of the experimental pattern and the calculated one, but it is also typically evaluated through statistical indicators, known as residuals.

$$R_{wp} = \left\{ \sum_i \omega_i \left[Y_0(i) - Y_c(i) \right]^2 \Big/ \sum_i \omega_i \left[Y_0(i) \right]^2 \right\}^{\frac{1}{2}} \tag{3.15}$$

The R_{wp} term reported by Eq. (3.15) is the *weight residual*, and a low value (e.g. roughly close to zero) generally indicates a good quality of the minimization or refinement process.

3.2 X-ray powder diffraction analysis of the carbonation reaction

As already mentioned, the carbonation is a gas-solid reaction that involves the presence of a solid phase of calcium oxide that reacts with gaseous carbon dioxide to form an

additional solid product phase of calcium carbonate. Specifically, CaO and $CaCO_3$ are both crystalline phases: usually, CaO porous particles consist of a number of crystalline domains, each one characterized by a different spatial orientation, as schematically represented in Figure 3.3.

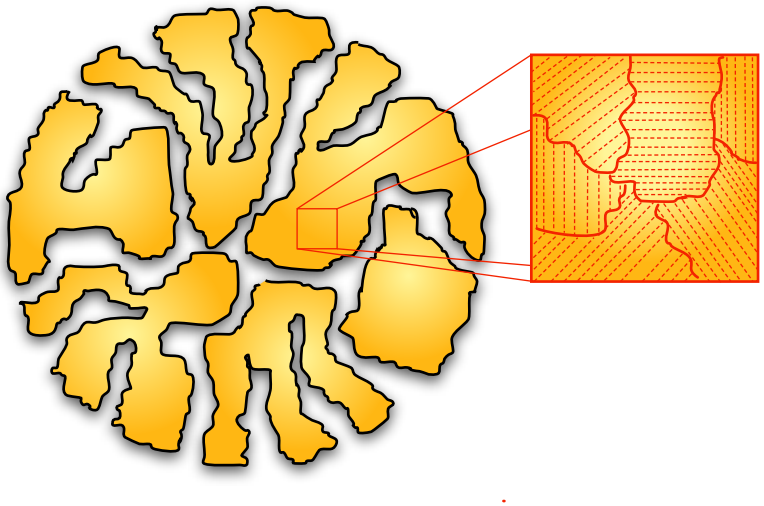

Figure 3.3: *Schematic representation of crystalline domains in a CaO porous particle, assumed spherical.*

Similarly, calcium carbonate produced by the reaction of CaO crystallites with CO_2 is a product layer made up of a number of crystallites that distribute over the specific surface of calcium oxide particles which is available for a gradual CaCO3 crystal growth. Therefore, the theory of X-ray diffraction can be reasonably applied to characterize solid sorbent particles used in the calcium looping cycle process, especially in terms of their crystalline domains and crystalline phase. Additionally, thanks to the possibility of carrying out in-situ X-ray diffraction experiments, crystalline structure evolution of CaO/$CaCO_3$ species (and of their related properties such as the average size of the crystalline domains) can be measured during the carbonation reaction progress. In situ X-ray diffraction technique provides in fact a method by which structural and/or chemical changes occurring in a sample can be monitored in real time while it is subjected to external variables, mainly temperature and/or atmosphere, simply following the variations in the characteristic Bragg reflections of the species present in the system (§ 3.1.1), as shown in Figure 3.4.

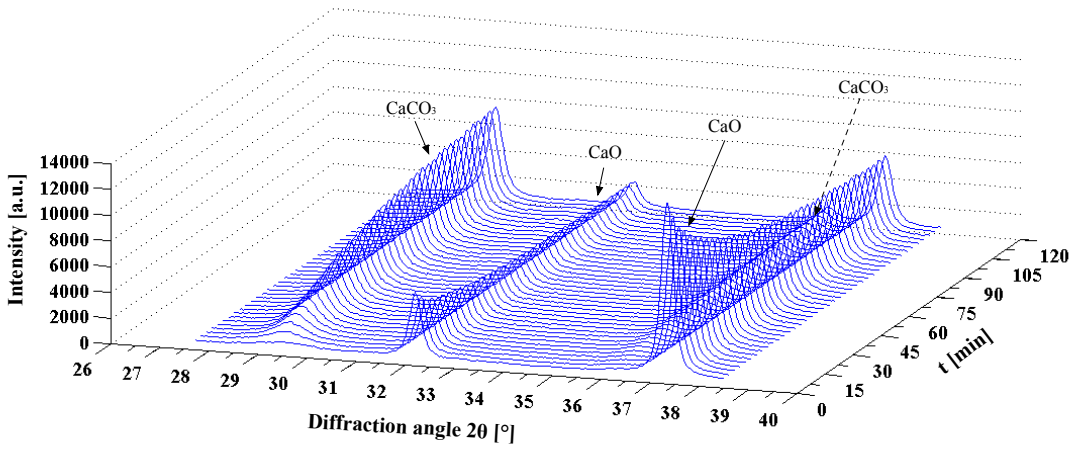

Figure 3.4: *Example of the evolution of the Bragg reflections (in the range 27.5-38.5 of the diffraction angle 2θ) for the system CaO/CaCO₃ during calcium oxide carbonation at 400°C.*

A number of works in the scientific literature discuss the influence of crystalline structures of a material both on its macroscopic properties and, in case of a reactive system involving solid structure changes, on the reaction kinetics (e.g. [95], [96] or [97]). Referring to CaO-based sorbents, the dependence of the carbonation reaction on the sorbent structural properties is a crucial aspect. Thus far, many contributions have focused attention on the impact of porosity and specific surface area, or on the impact of the pore size distribution, on the carbonation reaction and its kinetics, by using different versions both of random pore and grain models ([15], [17], [10], [13], [18], [19]). Instead, the impact of the calcium oxide/carbonate crystallite size on the sorbent performances is a piece of information not available in the literature when referring to the carbonation reaction with CaO-based solid sorbents. Several contributions report the characterization and phase identification of CaO and $CaCO_3$ species, performed by means of X-ray diffraction analysis carried out even with the ex-situ approach, especially referring to the calcination stage of the reversible chemical reaction shown in Eq. (2.1) ([98], [99], [100] or [71]). Very few contributions instead focused on the carbonation reaction. Molinder et al. (2012) ([101]) recently used X-ray diffraction to measure the crystallite size of partially hydrated CaO sorbents in a study on simultaneous hydration and carbonation of CaO, partially hydrated CaO and of $Ca(OH)_2$. However, to the best of author's knowledge, the dependence of the carbonation

kinetics on the calcium oxide and calcium carbonate crystallite size has never been investigated even if, reasonably, these properties could affect the CO_2 absorption capacity of CaO sorbent particles and the carbonation kinetics.

Therefore, in this work time-resolved X-ray powder diffraction was applied to investigate the kinetics of the chemical transformations and the microstructural evolution of the CaO-based sorbent samples during the CO_2 absorption process, in order to identify relationships between the calcium oxide conversion and the average crystallite size both of calcium carbonate and calcium oxide.

3.2.1 In-situ X-ray diffraction experiments – part I

A preliminary investigation of the carbonation reaction through the X-ray powder diffraction technique was carried out with a standard laboratory-scale θ-θ diffractometer purchased by Panalytical® (model X'Pert Powder). The instrument was equipped with a high-temperature resistance heating chamber especially provided by Anton Paar® (model HTK 16N) that allows the control of the main environmental parameters including temperature and gas atmosphere (Figure 3.5). Several experiments were performed, basically monitoring the diffracted intensities from a powder sample in which both calcium oxide and calcium carbonate species coexisted. Specifically, cycles of calcination and of carbonation stages were carried out such that initial $CaCO_3$ sample were first thermally decomposed to obtain porous CaO particles, afterwards subjected to the carbon dioxide absorption process.

A small amount of calcium carbonate (about 10 mg) was placed directly above a thin plate of platinum and gently pressed to obtain a regular surface. Below the strip, a resistive element provided the sample heating (Figure 3.6) while a K-type thermocouple, placed under the platinum support, quite in proximity to the powder, was used both for sample temperature monitoring and control. An external cover completed the powder isolation from the ambient atmosphere. The cover was characterized by two windows realized in Kapton®, a special material that thanks to its high transmittance to X-rays and a low outgassing rate reduces interferences in the diffraction measurements (especially, along the X-rays optical path) and guarantees the control of the gas atmosphere within the reaction chamber (usually down to a total pressure inside the cell of about 10^{-3} bar and up to 2 bar).

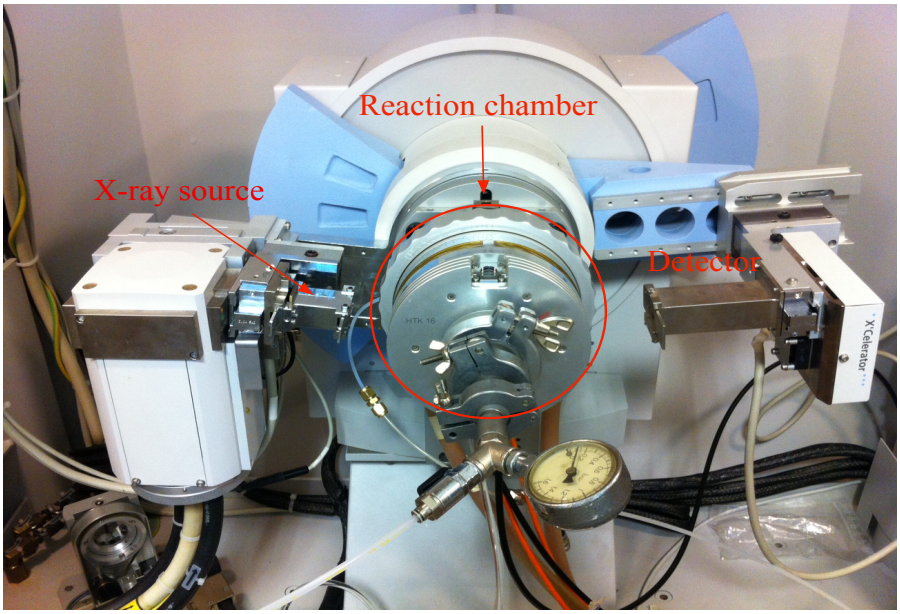

Figure 3.5: *X'Pert Powder diffractometer equipped with the reaction chamber furnace.*

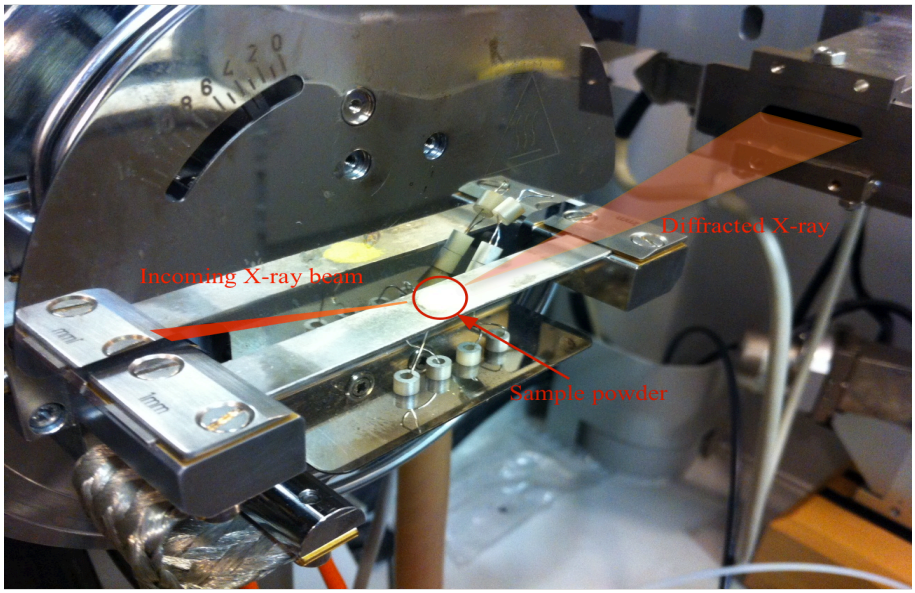

Figure 3.6: *Detailed view of the sample powder loaded inside the reaction chamber; sorbent particles (dp 10 μm) adequately distributed above a platinum strip, in order to form a thin layer.*

Through a set of tubes and fittings, the gas was forced to flow into the furnace, filling the whole cell volume and, in turn, surrounding the sample powder. It has to be noted that the

starting material, previously sieved to collect a fraction of powder with a controlled average particle diameter in the range of 150-160 μm (§ 2.4) (whose declared chemical purity higher than 99% was in this case verified through the X-ray diffraction analysis), was further grinded in an agate mortar in order to reduce its particle size to a more suitable value (roughly 10 μm) for conducting X-ray diffraction experiments, as typically suggested to avoid/reduce both preferential orientations and sample displacement effects ([88], [89]). The cover was finally arranged upon the support of the platinum strip, in turn mounted on the goniometer head of the diffractometer, resulting in the Bragg-Brentano configuration observable in Figure 3.5.

The diffraction intensities were thus recorded using an X'Celerator 1D silicon strip detector, which is able to collect data with a quality good enough for the subsequent satisfying phase quantification and diffractogram refinement down to a few minutes. Because carbonation is a very fast reaction, the collection of the diffraction data was performed limiting the diffraction angle range to the interval 27.6-38.4° of 2θ, which was scanned with an integrated step size of 0.033° of 2θ using a total time for data acquisition of about 3 min (angular speed equal to 0.071°/s). This corresponds to a scan procedure with a virtual counting statistic of 60 s/step (for a conventional detector). The detector active length (aperture) is 2.122º, and this enables signal collection over a large angular range at the same time, reducing the total time of the scan. In the mentioned range, the main Bragg reflections for both CaO and $CaCO_3$ could be detected with the shortest possible time needed for collecting a single pattern. An X-ray radiation with the Cu Kα wavelength (λ = 1.5405(6)) was used, and the instrumental parameters were calibrated using LaB_6 as reference material. Finally, the data were analyzed by the Rietveld profile refinement method using the X'Pert High Score Plus software, especially provided by Panalytical. In particular, the sequential profile refinement approach was used to process consecutive analysis (time-resolved measurements) and hence to obtain results as a function both of calcination and carbonation time.

A schematic representation of the diffraction experiments performed is shown in Figure 3.7. Calcination stages were performed mostly in N_2 atmosphere (at a pressure of 1 bar), with a flow rate of approximately 250 NmL/min and a heating rate of 50°C/min. The calcination temperature was set at 900°C, as reported by Dean et al. (2011) for a typical

application of the calcium looping cycle ([7]), and with the aim to reproduce operating conditions similar to those ones applied during the TGA experiments.

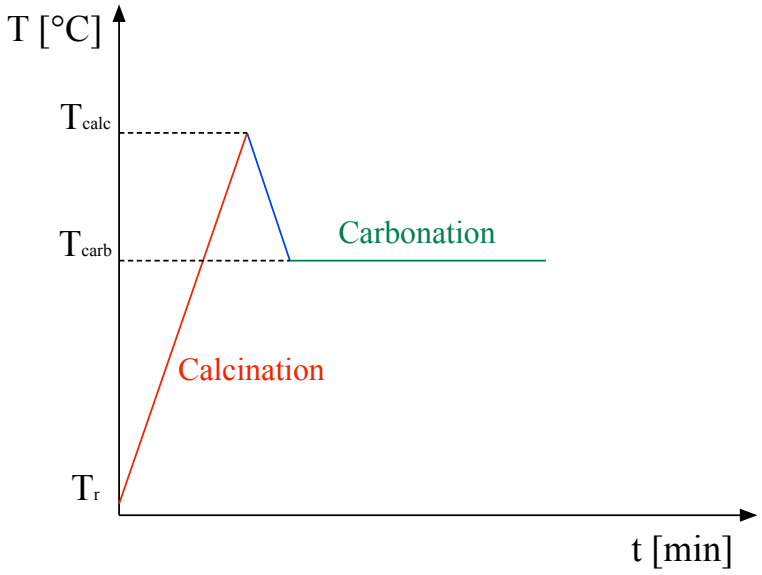

Figure 3.7: *Schematic representation of a cycle of calcination and of carbonation performed during a typical XRD experiment performed at this stage of the research.*

As already mentioned, the time required to fully decompose a given amount of calcium carbonate (at a defined temperature) decreases as the calcination temperature increases ([65], [66], [67], [68]) and hence the operational conditions were chosen in order to primarily ensure the complete decomposition of $CaCO_3$ samples in a short time. Specifically, it was observed that as soon as 900°C were reached, calcium carbonate was completely calcined. Otherwise, in a few experiments carried out at calcination temperature of 650°C, calcium carbonate usually showed to be fully calcined roughly above 60 min. Moreover, as discussed in a further section, different operating conditions in terms of calcination temperatures and residence times during the thermal decomposition of calcium carbonate were selected to obtain fresh calcines with different average sizes of the initial (at the beginning of carbonation) CaO crystalline domains. Furthermore, N_2 flow was used also in these experiments to facilitate the removal of the CO_2 released by the calcium carbonate decomposition away from the reaction interface, aiming at reducing its contribution on the sintering that typically affect the sample during calcination stage at high temperature, as reported in several contributions including [72], [73], [74], [76], [75],

[77], [78], [79], [80], or [45]). However, other gas atmospheres during the calcination stage (especially air and CO_2) were partially studied in order to verify their effect both on the CaO average crystallite size evolution as a function of the calcination time and on the CO_2 capture performances of sorbent particles in the following carbonation stage.

After the complete thermal decomposition of $CaCO_3$, the new-formed CaO was thus cooled down (at 50°C/min, still keeping the sample under N_2) to the desired carbonation temperature. The carbonation stage was thus carried out isothermally at several temperatures between 400°C and 650°C. At this stage of the research activity, the overall carbonation time was set arbitrarily for each of the tests, usually around 120 minutes. An atmosphere of pure CO_2 was used maintaining a constant flow rate of approximately 250 NmL/min at a pressure of 1 bar. The gas flow was provided by external variable area flow meters and the transition between N_2 and CO_2 atmosphere was realized by means of manual switching valves.

Once the data were recorded, information about the structural changes of the sorbent samples, mainly $CaCO_3$/CaO phase and crystallite size evolution over time, as a function of both calcination conditions and carbonation temperature, were obtained by means of the Rietveld profile refinement method, as previously discussed (§ 3.1.3). In particular, calcium oxide mass fractions were estimated from the quantitative phase analysis (QPA) of the diffraction data refining phase scale factors and then applying Eq. (3.13). Therefore, they were used to calculate the CaO conversion *X(t)* during the CO_2 absorption stages as:

$$X(t) = \frac{1 - w_{CaO}(t)}{1 - w_{CaO}(t) + w_{CaO}(t)\frac{MW_{CaCO_3}}{MW_{CaO}}} \tag{3.16}$$

where $w_{CaO}(t)$ is the calcium oxide mass fraction evaluated at consecutive diffraction analysis/scans (namely at a different time *t*) recorded during the experiments, while *MW* is the molecular weight of the species involved in the carbonation.

Considering the estimate of the average crystallite size, at this stage of the research the attention was limited to the characterization of calcium oxide crystalline domains while, in the Chapter 4, the dependence of the carbonation kinetics on the calcium carbonate average crystallite size profiles over time will be analyzed. Additionally, it has to be specified that, even though the Rietveld refinement method typically provides high quality and complete structural information of the crystalline species within a sample, when it is applied in a

short range of the diffraction angle of 2θ, with a low concentration of Bragg reflections as in the case under investigation, its accuracy is reduced, especially in the description of the peak size broadening (namely, of the crystallite size). In fact, a limited angular range makes profile parameters instable and the crystallite size estimates not so reliable. When data of high quality are unavailable (e.g. in the case of lab-scale in-situ analysis or non-ambient measurements) a simple analysis of integral breadths or of FWHM may be appropriate for obtaining semi-quantitative estimates of crystallite size ([102]). These methods are used best when trying to identify trends in the change of the microstructure by comparing samples belonging to a series of experiments ([103]), like in this study. For these reasons, the estimate of the crystallite size of CaO was performed focusing directly on the FWHM of the main Bragg peak of calcium oxide (i.e. single peak), thus resulting in a better quality of the computed average crystallite sizes. Specifically, the average crystallite size of CaO (*CS*, in nm) was calculated applying the Scherrer equation (Eq. 3.6), arranged in the following expression:

$$CS = \frac{\lambda K}{(\beta_{obs} - \beta_{std}) \cos\theta} \tag{3.17}$$

where λ is the x-ray wavelength used (0.15405 nm); K is a dimensionless constant related to the crystallite shape taken as 0.9; β_{obs} and β_{std} are the line broadening at half of the maximum intensity (FWHM) of the characteristic *200* reflection for the CaO at the 2θ angle of ~ 37°, and the FWHM of the characteristic reflection for the standard reference LaB_6 at the most close diffraction angle (in radians), respectively.

3.2.2 Results

During this stage of the research, the data collected from the time-resolved measurements were used to calculate the profiles of the CaO conversion utilized for the reaction kinetics investigation, and of the calcium oxide average crystallite size trends during the CO_2 absorption process, in order to identify relationships between the carbonation rate/conversion and the structural properties of the crystalline species (CaO) involved in the reaction. A summary of the first set of experiments performed is reported in Table 3.1, especially underlining the corresponding operating conditions. The average size of the

initial CaO crystalline domains was calculated once each sample had reached the desired carbonation temperature (after the cooling down of the sorbent from the calcination conditions), and before switching the gas atmosphere from N_2 to CO_2 inside the reaction chamber. The errors in the average crystallite size estimates were computed from the standard deviation of FWHM values of the main calcium oxide Bragg reflection, which were used in the crystallite size calculation, made applying the Eq. 3.17.

Table 3.1*: Summary of the experimental operating conditions and estimate of the corresponding CaO average crystallite size at the beginning of carbonation.*

Run	Calcination			Carbonation	Initial CaO average crystallite size [nm]
	T [°C]	Gas	t [min]	T [°C]	
A	900	N_2	< 1	400	44 (± 1)
A cycle II	900	N_2		400	74 (± 3)
B	900	N_2		500	47 (± 2)
C	900	N_2		500	42 (± 2)
C cycle II	650	N_2	120	500	57 (± 3)
D	900	N_2	< 1	550	40 (± 2)
D cycle II	900	N_2		550	91 (± 3)
E	900	N_2		550	45 (± 1)
E cycle II	950	CO_2		550	254 (± 5)
F	900	N_2	40	550	62 (± 2)
G	900	N_2	120	550	75 (± 2)
H	900	N_2	< 1	550	45 (± 1)
I	900	N_2		600	47 (± 1)
I cycle II	900	N_2		600	84 (± 3)
J	900	N_2		600	45 (± 2)
K	900	N_2		650	43 (± 1)
K cycle II	900	N_2		650	54 (± 2)

3.2.2.1 Profiles of calcium oxide conversion and carbonation temperature effect

Several curves of calcium oxide conversion versus time were obtained from experiments performed at different carbonation temperatures, initially using CaO sorbents prepared through calcination stages carried out in ramp of temperature up to 900°C, at which the

sample powders were maintained just for a few seconds (< 1 min) and then cooled down to the desired carbonation temperature. Only in a few cases the residence time was prolonged in order to substantially modify the average size of the CaO crystalline domains, as demonstrated in the following section § 3.2.2.3.

In Figure 3.8, an example of the conversion profiles as a function of the carbonation temperature is reported. From the plot it can be observed as the carbonation kinetics is apparently affected by the temperature maintained during each isothermal CO_2 absorption stage, and reflects the dependence from the carbonation temperature observed in the TGA experiments (§ 2.4): a higher temperature seems to speed up the reaction and, at a given time, higher CaO conversion extents are achieved.

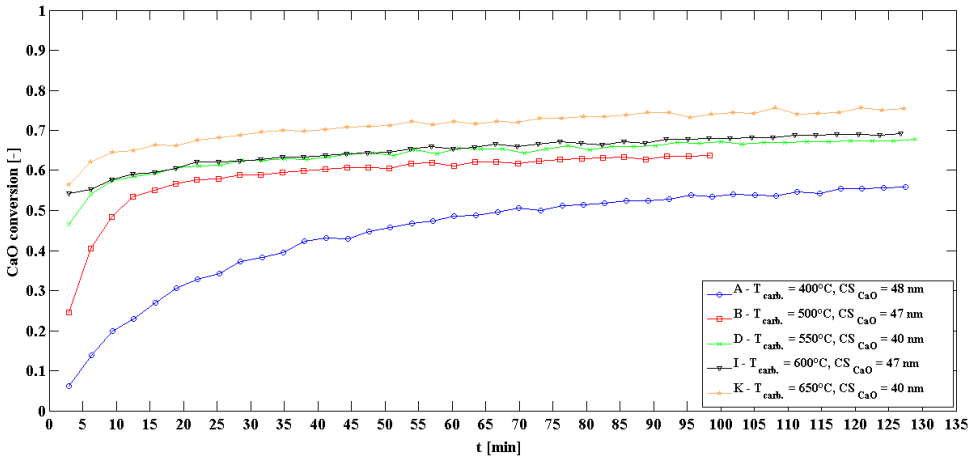

Figure 3.8: *CaO conversion versus time profiles, as a function of the carbonation temperature.*

Nevertheless, at 400°C (curve A) the first rapid stage typically characterizing the carbonation reaction cannot be distinguished, as well as a sharp transition to the product layer diffusion controlled regime is not observable. Increasing the carbonation temperature up to 500°C (curve B), a faster conversion rate is instead visible, and higher CaO conversion values (with a relative increase of about 15% after 90 min) were measured. For a further increase of the temperature up to 550°C (curve D), 600°C (curve I) and 650°C (curve K) respectively, CaO conversion at a given time significantly increases till typical values of about 0.6 ÷ 0.7, as observed in the thermo-gravimetric experiments carried out with similar operating conditions during the calcination stage (§ 2.4.1). Furthermore, the conversion curves continue to show a slight increase as long as the carbonation proceeds,

indicating that the maximum conversion potentially achievable from the sorbent particles was not reached in any experiment. For temperature over 500°C, the fast stage of the carbonation reaction accomplishes in a few minutes and, as observable, were not recorded below 3 min (i.e. the time required to complete a single scan/analysis), mainly because of the low time resolution of the instrumentation used to perform this kind of X-ray diffraction experiments. However, this aspect confirms both the observations collected through the TGA tests concerning the 'characteristic time' for the occurring of the first rapid stage, and that the carbonation is a very fast reaction.

Additionally, as discussed in § 2.4.1.1, it has to be reminded that the temperature contributes to improve the product layer diffusivity so that, at high temperature (approximately ≥ 500°C), its effect on the reaction kinetics reasonably becomes negligible during the first rapid stage of the carbonation; the reaction is accelerated in the early minutes of reaction (thus becoming not countable from the detector), while a rather high conversion (quite close to the value measured at the end of each experiment) is reached.

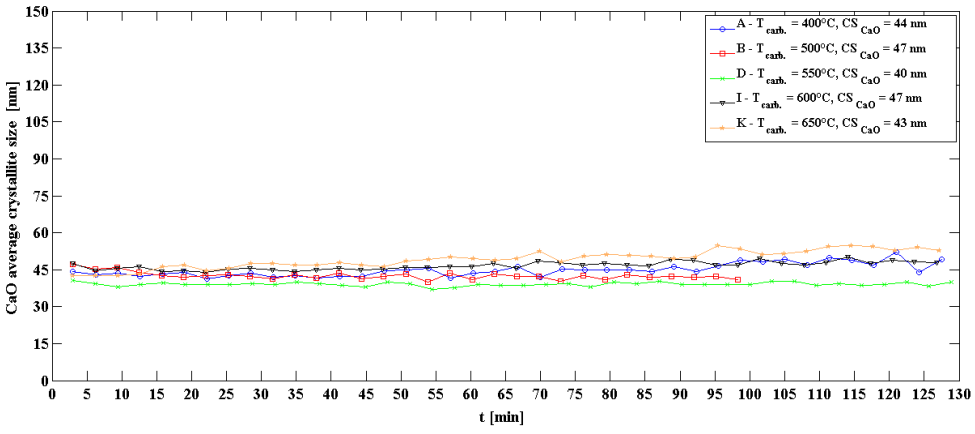

Figure 3.9: *Evolution of the CaO average crystallite size as a function of the carbonation temperature.*

Another aspect that has to be noted refers to the crystallite size of the calcium oxide particles: in the set of experiments whose conversion profiles are shown in Figure 3.8, the average sizes of the CaO crystallite domains evaluated at the beginning of each CO_2 absorption stage, were very similar, ranging from 47 nm and 40 nm, which was the lowest value measured during this stage of the research. Since the structural properties of the sorbent particles (among which, the crystallite size) are affected by the calcination conditions ([66], [74], [104], [80], [79]), this aspect suggested that the reproducibility of

the $CaCO_3$ thermal decomposition stages was rather good, since for equal operating conditions during the calcination equal values for the crystallite size of fresh calcined CaO were reasonably computed. Moreover, it was observed that as long as the carbonation proceeds, the average size of CaO crystallites does not change significantly (Figure 3.9).

3.2.2.2 Profiles of calcium oxide conversion and CaO average crystallite size effect

In order to perform a straightforward comparison among different conversion profiles as a function of only the average size of the calcium oxide crystalline domains, sorbent particles obtained through calcination stages carried out with different operating conditions were required. In particular, for this scope the residence time at the maximum temperature of 900°C was increased both to 40 min (run F) and to 120 min (run G), and then the carbonation behavior of these samples were tested at the same carbonation temperature of 550°C. In Figure 3.10, the comparison of several conversion versus time profiles is reported.

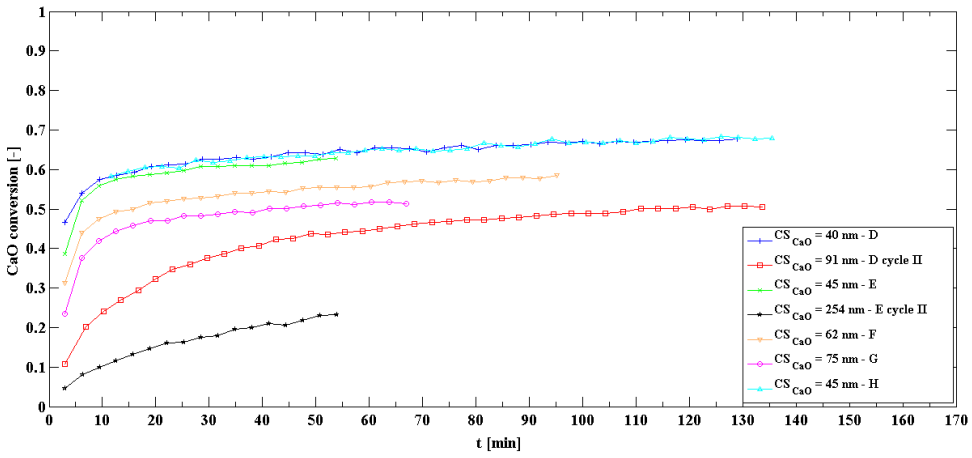

Figure 3.10: *CaO conversion versus time curves, as a function of the initial CaO average crystallite size. Carbonation tests carried at 550°C, pCO_2 = 1 bar. Different calcination stages.*

The plot points out a remarkable result, namely that a certain proportionality exists between the average crystallite size of calcium oxide and the corresponding conversion achieved after a given carbonation time, insomuch as the lower the crystallite size, the higher the CaO conversion extent.

More specifically, Figure 3.10 underlines that:

i. Powder samples characterized by similar values of the CaO crystallite sizes (in the order of 40 nm) show a similar carbonation kinetics, achiving the same conversion values all along the entire profile (curves D, E and H).

ii. At the given carbonation time of 60 min, moving from a crystallite size of about 40 nm to roughly 60 nm (curve F), a relative reduction in the conversion extent of about 10% is measured; this reduction increases till 15% when the crystallite size changes up to 75 nm (curve G).

iii. If a further cycle of calcination (at the same operating conditions) is added (curve D cycle II), a significant reduction of the average size of CaO crystalline domains is observed (from 40 nm to 91 nm), and a worse CO_2 absorption perfomance of the sorbent particles is measured. This result confirms the observations reported in the literature about the negative effects of the increase in the number of calcination/carbonation cycles on the CO_2 capture sorbent performances ([38], [41], [7], [39]). Additionally, if the second cycle of calcination is carried out under an atmosphere of pure CO_2 (curve E cycle II), the average size of CaO crystallites at the beginning of the second carbonation stage significantly increases (up to roughly 250 nm), resulting in a drastic decrease of the sorbent absorption reactivity/capacity, and confirming the negative effects on the sorbent particle structural properties that a gas atmosphere containing carbon dioxide determines during the calcination stage ([75], [72], [69], [105], [49], [16]).

iv. Insufficient information is still available concerning the rate of the reaction during the first stage of the carbonation, even if the penalization due to a significant increase of the CaO crystallite size is rather clear (curves D cycle II and E cycle II).

The effect on the sorbent performances during the carbonation due to the increase of the initial (at the beginning of the carbonation) crystallite size of CaO, caused by a further cycle of calcination, was also verified in relationship with the effect of the carbonation temperature on the reaction kinetics. In Figure 3.11, the conversion versus time curves of CaO particles produced with one stage of calcination are shown (solid curves), compared to the carbonation behavior of the same sorbent samples obtained through a second stage of calcination (dashed curves).

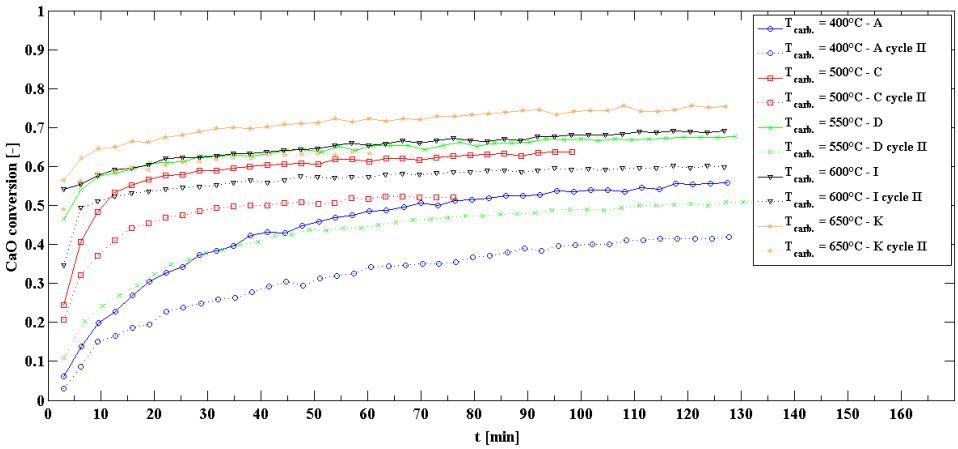

Figure 3.11: *CaO conversion versus time profiles: comparison between first and second cycle of carbonation*

As previously observed, the additional calcination stage leads to fresh calcined CaO particles characterized by crystalline domains with a higher average size. Even though the apparent dependence of the conversion from the carbonation temperature is conserved, for a given time *t* of carbonation, lower values of the CaO conversion are achieved by sorbent particles obtained from a second stage of calcination, especially for higher carbonation times. Once more, this result, which is in agreement with the observations already reported in the literature concerning the loss in sorbent capacity as the number of absorption/desorption cycle increases, apparently confirms that the sorbent performances could be affected by the average crystallite size that CaO particles have at the beginning of the CO_2 absorption stage.

However, because of thermal treatments at high temperature used to produce the CaO particles typically promote sintering process, with a resulting modification/reduction both of the specific surface and of the pore volume of sorbent particles, it could be argued that the behavior of calcium oxide powders thus far observed could be more affected by these properties of the sorbent samples rather than from the initial average size of the CaO crystalline domains. Nevertheless, it is reasonable to assume that the average value of the initial CaO crystallite size could reflect the morphological properties (specifically, the porosity) characterizing the sorbents at the beginning of the carbonation. In fact, this aspect will lead to an interesting consideration presented in the following Chapter 4.

Instead, at this stage of the research, in order to neglect effects on the CO_2 capture performances of CaO sorbent particles mainly due to possible variations in their specific surface and/or porosity taking place during the calcination at high temperatures, sorbent samples were obtained from calcination stages carried out at low temperature, whereas sintering effects can be reasonably neglected. In particular, calcium carbonate powders were calcined at 650°C, just prolonging the residence time at this temperature up to 120 min, in order to ensure a full decomposition of $CaCO_3$ particles and then, still maintaining a temperature of 650°C, the carbonation processes were carried out switching the gas atmosphere within the reaction chamber from N_2 to pure CO_2. The corresponding CaO conversion versus time profile obtained is shown in Figure 3.12, in which the effect of some consecutive cycles of calcination (at the same operating conditions) on the following carbonation kinetics is also observable.

Table 3.2: *Summary of the experimental operating conditions and estimate of the corresponding CaO average crystallite size at the beginning of carbonation. Sorbent samples obtained with calcination stages at carried out at 650°C under a gas flow of N_2.*

Run	Calcination			Carbonation	Initial CaO average crystallite size [nm]
	T [°C]	Gas	t [min]	T [°C]	
L	650	N_2	120	650	40
L cycle II	650	N_2	120	650	54
L cycle III	650	N_2	120	650	69
L cycle IV	650	N_2	120	650	80
L cycle V	650	N_2	120	650	84

Even though a characterization of sorbent particles used in these experiments in terms of specific surface area and porosity was not performed, thanks to the low temperature of calcination it can be reasonably assumed that these morphological properties should be quite constant (as observed for the crystallite size in § 3.2.2.3) between CaO particles subjected to each carbonation stage. On the contrary, it is pointed out once more as the increase of the number of absorption/desorption cycles progressively increase the CaO average crystallite size, as also summarized in Table 3.2. In particular, it is noticeable as for the lowest value of CaO crystallite size (of about 40 nm), the conversion achieved after

30 min of carbonation (roughly 0.84) is in agreement with the value measured in a similar carbonation test performed at the TGA with a sample obtained through a calcination stage carried out using analogous operating conditions (Figure 2.12).

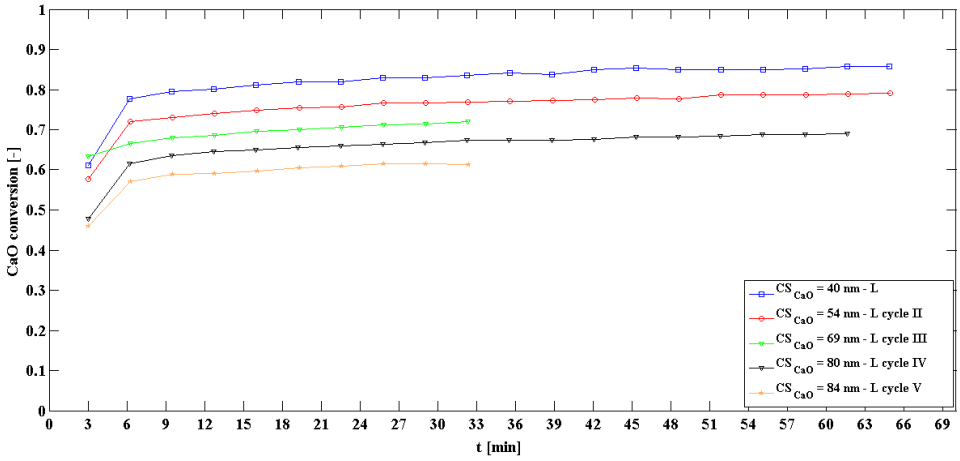

Figure 3.12: *CaO conversion versus time profiles as a function of the number of calcination/carbonation cycles. Carbonation tests at 650°C, pCO_2 = 1 bar. Calcination at 650°C for 120 min in N_2 atmosphere (gas flow rate of about 250 NmL/min).*

3.2.2.3 CaO crystallite size evolution during the calcination stage

Since it was clearly observed that the average size of CaO crystalline domains at the beginning of the carbonation reaction seems to affect the reaction kinetics, especially in terms of the carbon dioxide capture capacity of CaO sorbent particles, the effect of the calcination conditions in determining the size of CaO crystallites was analyzed. Therefore, some calcination experiments were carried out monitoring the evolution of the CaO crystallites as a function both of the calcination temperature and of the gas atmosphere maintained during the thermal decomposition of $CaCO_3$ particles. Specifically, temperatures in the range between 650°C and 950°C were used, while the gaseous species utilized to control the atmosphere were pure N_2 (gas flow rate of about 250 NmL/min) and stagnant air. In Figure 3.13, the time resolved measurements of the CaO crystallite size are reported for each of the different calcination conditions used.

From the plot, it is clearly visible that the increase both of the calcination temperature and of the residence time at that temperature causes a progressively increase of CaO crystallite size. In a N_2 atmosphere, for temperature $\leq$ 700°C the crystallite size of CaO is rather

constant as long as the calcination proceeds. Differently, calcination temperatures ≥ 800°C slightly and progressively accelerate the crystallite growth rate, insomuch as the average size of CaO crystalline domains changes from roughly 40 nm (at 700°C) to around 73 nm (at 950°C) after 120 min of calcination.

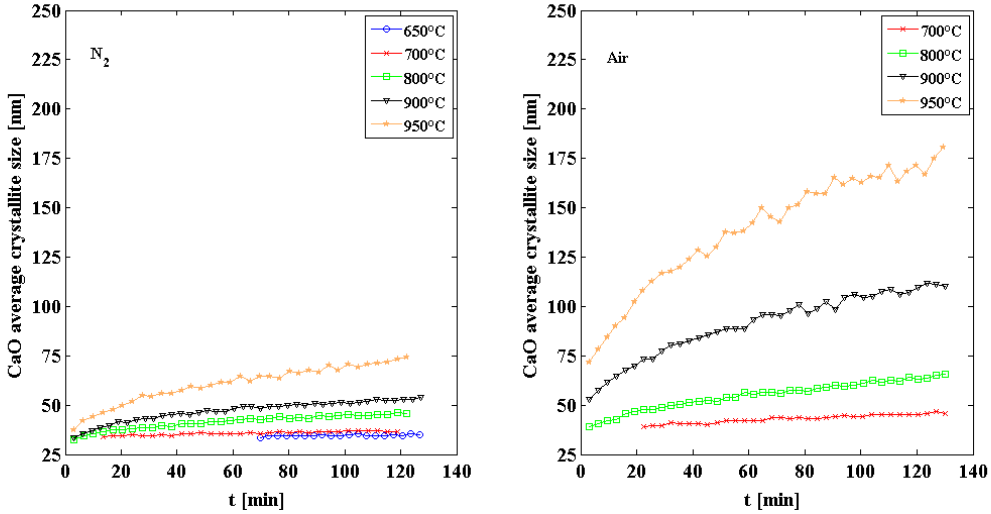

Figure 3.13: *Evolution of the CaO average crystallite size, as a function of the calcination temperature, in a gas atmosphere both of N_2 (gas flow rate of about 250 NmL/min) (left) and of stagnant air (right).*

In an atmosphere of stagnant air, the effect so far described is also more evident: a little increase in the crystallite size is noticeable already at 700°C and above 800°C the crystal growth becomes really significant. Moreover, at 650°C the thermal decomposition of calcium carbonate does not occur anymore within 120 min. These results can be reasonably explained considering two aspects:

i. In absence of a flow of purge gas, CO_2 (whose negative effect in determining the sorbent particle (morphological) properties has been already documented) released during the thermal decomposition of $CaCO_3$ is not removed from the solid interface, thus increasing its local concentration inside/around the sample powder, and promoting annealing effects on CaO crystallites.

ii. Carbon dioxide concentration in the air surrounding the sample powder increases the equilibrium partial pressure of CO_2 at a given temperature so that, considering a calcination temperature of 650°C, the equilibrium partial pressure of CO_2 (0.012 bar) is very close to the pCO_2 in the air in which the experiments were carried out,

thus preventing the occurring of the thermal decomposition of $CaCO_3$ at this temperature during the monitored calcination time.

Even though similar studies have been documented in order to investigated how the calcination conditions (include the CO_2 effect) may affect the morphological properties of CaO sorbent particles (e.g. [79], [49], [75], [45]), to the best of author's knowledge the entire crystal size evolution during calcination is not widely discussed when referring to the CaO, and only an handful of studies can be found, including [86] or [74]. For this reason, work is in progress in order to both investigate/elaborate a mathematical model able to describe the observed crystal growth process, and verify an hypothetical correspondence between CaO crystallite size and morphological properties (i.e. specific surface and porosity) of sorbent particles, as it will be discussed in the next chapter.

3.2.3 Issues with 'lab-scale' experiments

Although interesting results have been presented in the previous sections, a few issues arising from the utilization of a laboratory-scale instrument limited the investigation of the CaO-CO_2 reaction by means of the X-ray diffraction technique described so far.

The first critical aspect concerns the comparison between the time required to collect a single diffraction pattern and the 'characteristic' reaction kinetics: the carbonation reaction is rather fast, especially considering its first stage that, as measured, accelerates as the carbonation temperature increases, and lasts few minutes (< 3 min). On the contrary, the time needed to perform a single X-ray diffraction analysis was roughly 3 min. Therefore, it should be clear that:

i. All the transformations taking place in the sample powders, from the instant at which the transition between N_2 and CO_2 was realized to the end of the first diffraction measurement, were lost. For this reason, the first stage of the carbonation reaction was not (completely) monitored, especially in those experiments carried out at high temperatures of carbonation;
ii. Each single diffraction pattern provides a set of information regarding a time interval of approximately 3 min; all the changes occurring during this period of time are recorded in a single diffractogram which gives only an

average/qualitatively image about the microstructure evolution of the sample occurred in that same time range.

The second crucial aspect involves instead the range of the diffraction angle 2θ considered. Typically, the broader the range of the diffraction angle considered during an X-ray diffraction analysis, the more accurate the profile fit refinement performed through the Rietveld method, because of a good counting statistic of the diffracted intensities and a consequently stability of the profile fit parameters. Despite that, in the case of the CaO carbonation, the investigation carried out during this stage of the research focused on a narrow range of the diffraction angle, where only few Bragg reflections could be detected. Even though the evaluation of calcium oxide and calcium carbonate contents were feasible applying the Rietveld refinement, the limited angular range made profile parameters instable and CS estimates not reliable, so that it was necessary to estimate the CaO crystallite size simply with the Scherrer formula applied to a single peak, with a consequently increase in the time needed to post-process the diffraction data collected.

For these reasons, since the technique was reasonably considered as a promising method to investigate the evolution of a material (characterized by the presence of crystalline species), even in the occurring of a chemical reaction, several improvements were adopted. Specifically, the utilization of the synchrotron radiation was considered in order to perform high time resolution experiments, which have been essential to investigate rapid transformations such as those occurring during the first stage of the calcium oxide carbonation.

Chapter 4

Investigation of the carbonation reaction using synchrotron radiation

The in-situ X-ray diffraction technique provides an alternative method to the thermo-gravimetric analysis by which chemical changes affecting a sample can be monitored in real time following the crystalline structural evolution of the species within the material. Time-resolved X-ray powder diffraction using synchrotron radiation (SR-XRPD) has been applied to investigate the kinetics of the chemical transformations and the microstructural evolution of the samples during the CO_2 absorption process, in order to identify relationships between the calcium oxide conversion and the calcium oxide/calcium carbonate average crystallite sizes. Synchrotron radiation, which is characterized by a high brilliance, has been chosen because it produces X-ray data with excellent accuracy and a high time resolution that are essential to investigate a rapid reaction such as the first stage of calcium oxide carbonation.

This chapter aims to describe the experiments performed at the Advanced Photon Source (APS) facilities at the Argonne National Laboratory (IL, USA) and the novel results introduced in the scientific literature of the CaO carbonation reaction.

4.1 The synchrotron radiation

Commonly, synchrotron radiation is a generic term used to describe radiation from charged particles (mainly electrons) travelling at relativistic speeds in applied magnetic fields that force them to travel along curved paths. As schematically shown in Figure 4.1, synchrotron radiation is produced in storage rings where electrons are kept circulating at constant energy. In a storage ring the synchrotron radiation is produced either in the bending magnets, needed to keep the electrons in a closed orbit, or in insertion devices such as wigglers or undulators situated in the straight sections of the storage ring, where an alternating magnetic field forces the electrons to follow oscillating paths rather than

moving in a straight line ([94]). All these features determine the properties and quality of the X-ray beam produced, which is typically characterized by high energy. In particular, these features can be combined into a single quantity, called the *brilliance*, which allows to compare the quality of X-ray beams from different sources ([91], [94]).

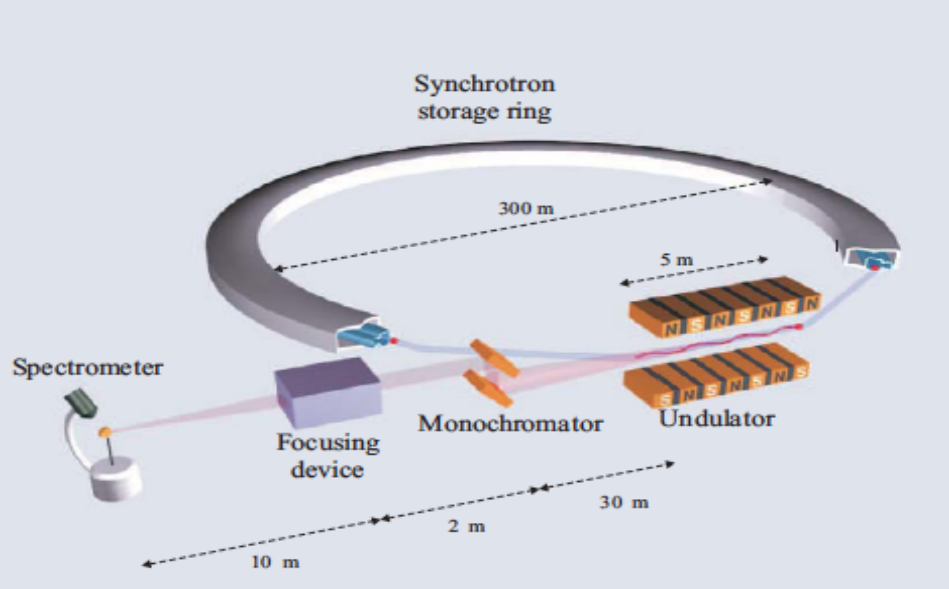

Figure 4.1: *A schematic of a typical X-ray beamline at a third generation X-ray source. Bunches of charged particles (electrons) circulate in a storage ring (typical diameter around 300 m). The ring is designed with straight sections, where an insertion device, such as an undulator, is placed. The lattice of magnets in an insertion device forces the particles to execute small oscillations, which produce intense beams of radiation. This radiation then passes through a number of optical elements, such as a monochromator, focusing device, etc., so that a beam of radiation with the desired properties is delivered to the sample. Typical distances are indicated. Source: "Elements of modern X-ray physics"* [94].

Even though a detailed discussion about the synchrotron radiation is outside the scope of this work of thesis, it has to be reminded that the brilliance is a function of the photon energy and for the 3rd generation synchrotrons is approximately 10 orders of magnitude higher than the typical laboratory-scale X-ray sources. This high brilliance provides a considerable experimental versatility, including the possibility to insert several optic devices (e.g. monochromators), which are useful to define the quality of the diffraction patterns, without compromising the counting statistics of the diffracted intensity performed by the detector, as well as, in addition to an high beam collimation, it reduces the aberrations related to the experimental set-up typically encountered with laboratory

equipment, then resulting in great benefit for the shape and symmetry of the detected peaks. Moreover, if combined with 2D detectors, which are characterized by both an high detective quantum efficiency and an high sensitivity, the high brilliance of the X-ray synchrotron radiation allows to perform high quality measurements characterized by high peak/background ratios with a very short acquisition time. Furthermore, the high energy of the synchrotron radiation allows to reduce several sources of error in the Rietveld profile fit refinement, making the refined parameters (and the structural information derived form them) more reliable ([91]).

In the light of these features/benefits, synchrotron radiation was chosen in order to improve the investigation of calcium oxide carbonation by means of the X-ray diffraction technique.

4.2 Experimental procedure

The in-situ SR-XRPD investigation of the CaO-CO_2 reaction was performed at the beamline 17-BM-B of the Advanced Photon Source (APS), at Argonne National Laboratory. Similarly to what described in § 3.2.1, the experiments consisted of monitoring X-ray powder diffraction data during a single cycle of calcination and carbonation stages such that initial $CaCO_3$ samples were first thermally decomposed to obtain porous CaO, afterwards subjected to the carbon dioxide absorption process. The measurements were carried out applying a Debye-Scherrer experimental configuration based on a transmission geometry with the sample loaded within a capillary, and using a versatile set-up especially designed for conducting in-situ X-ray diffraction studies in non-ambient environments. The system, well described by Chupas et al. (2008) ([20]) and schematically shown in Figure 4.2, is based on a flow cell/furnace that allows the control of several environmental parameters including temperature (up to 900°C) and atmosphere/gas flow conditions.

A small amount of sample (about 5 mg) was loaded into a 1 mm quartz glass capillary (0.1 mm wall thickness, 75 mm long), filling approximately 3-5 mm of the capillary. The capillary was arranged upon the flow cell system, in turn mounted on the instrument using a standard goniometer head (Figure 4.3). Through a set of tubes and fittings, the gas was forced to flow into the capillary, through the sample particles. In order to prevent any change in the position of the powder during the experiments, mainly due to the gas flow,

the sample inside the capillary was stabilized by means of quartz wool positioned nearby the powder, at both capillary extremities. Heating was provided by two resistive elements placed immediately above and below the sample capillary. A K-type thermocouple, placed within the capillary in close proximity to the powder, was used both for sample temperature monitoring and control.

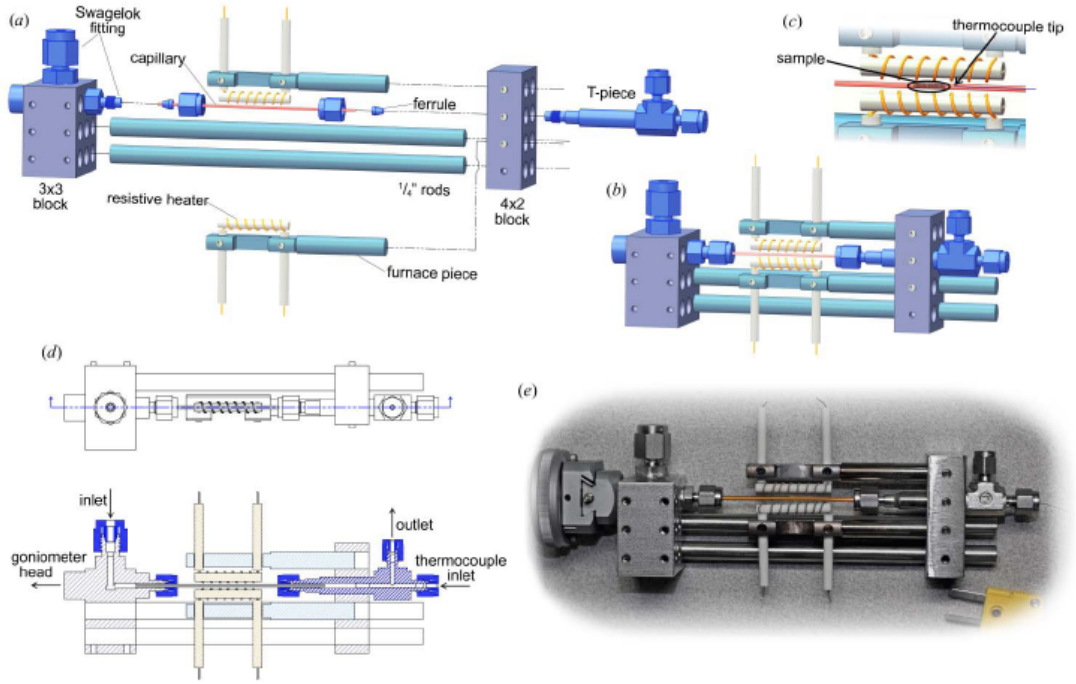

Figure 4.2: *An 'exploded' representation of the flow-cell/furnace components, indicating how they fit together (a); the fully assembled flow-cell/furnace (b); an expanded view of the sample region, indicating the relative position of the sample and thermocouple tip within the furnace hot zone (c); a top view of the flow-cell/furnace, with a corresponding cross-section through the sample plane showing the gas/fluid path (d); a photograph of the flow-cell/furnace, in turn mounted in a goniometer head (e). Source: Chupas et al. (2008)* ([20]).

Experimental data were collected using an amorphous silicon-based flat plate detector from Perkin-Elmer (model XRD 1621 CN3-EHS, detector size of 2048x2048 pixels, pixel size of 200x200 μm). The wavelength (λ = 0.72959(3) Å with a focused beam of 300 μm) and the sample-to-detector distance (d = 450 mm, giving a usable range of 2θ of 1-43°) were calibrated using LaB_6 as a reference material. Because the CaO-CO_2 reaction is characterized by a very rapid initial reaction period, followed by a much slower second stage, the collection of the diffraction data during the carbonation stage was performed for

a total time of only 20 min and, in order to obtain results with a time scale suitable for kinetics studies, data were recorded continuously using a frame rate of 0.25 s per frame for the first 5 min of the reaction (i.e. 1200 patterns), followed by a frame rate of 1 s per frame for the next 15 min (i.e. 900 patterns).

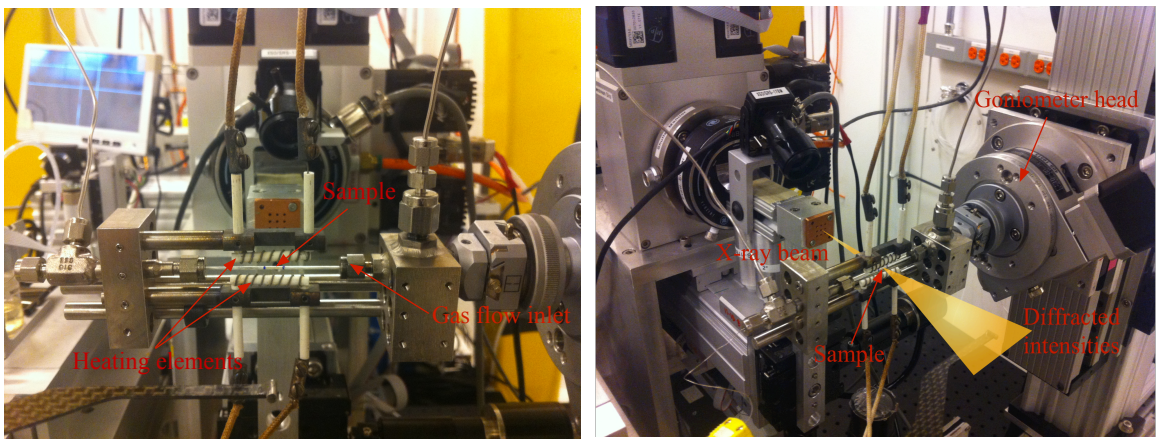

Figure 4.3: *Overview of the experimental set-up at the 17-BM-B beamline: Glass capillary and resistive heating elements mounted on the flow cell device (left), in turn positioned on a standard goniometer head (right).*

The raw images were reduced to one-dimensional diffraction patterns by means of FIT-2D software ([106], [107]). Finally, the data were analyzed by the Rietveld profile refinement method discussed in § 3.1.3, using the General Structure Analysis System (GSAS) software ([108]). In particular, the sequential profile refinement approach was used to process consecutive analysis (time-resolved measurements) and hence to collect results as a function of the carbonation time.

The starting material used for all the experiments was the same commercial calcium carbonate purchased by AppliChem® introduced in the Chapter 2. Since particles were polycrystalline and their size would not have affected the diffraction significantly, the fraction of powder with the controlled average particle diameter in the range of 150-160 μm was maintained as reference. Additionally, this selected size ensured both a low compaction of the material within the capillary used for conducting in-situ X-ray powder diffraction experiments, and a minimal graininess in the 2-D diffraction raw images recorded. It has to be noted that the minimal graininess of the 2-D diffraction images is an indication that the samples initially loaded in the capillary are characterized by a nearly ideal random distribution of the coherently scattering $CaCO_3$ crystalline domains (namely,

by the absence of initial preferred orientations) and confirms the quality of the diffraction data. Calcium carbonate samples were therefore decomposed to investigate the CaO reactivity during the carbonation stage. In fact, as previously mentioned, calcination of initially non-porous $CaCO_3$ particles leads to an increase in the specific surface of CaO that makes sorbent samples more reactive towards the following CO_2 absorption stage. Calcination stages were therefore performed in N_2 atmosphere (at a pressure of 1 bar), with a flow rate of approximately 10 NmL/min and a heating rate of 10°C/min. The calcination temperature was varied in the range between 700°C and 900°C, while two different residence times at these maximum temperatures were selected, namely 5 min and 60 min. As usual, the operational conditions were chosen in order to ensure the complete decomposition of $CaCO_3$ samples, as well as (following the experimental evidences reported in § 3.2.2.3) to obtain fresh calcines with different average size of nascent CaO crystalline domains. The strategy to carry out the calcination experiments under N_2, feeding the inert gas within the capillary, was maintained to facilitate the removal of the CO_2 released at the reaction zone during the calcium carbonate decomposition away from the solid surface, thus reducing its contribution on the sintering phenomenon that can affect the sample during calcination stage at high temperature.

After the complete thermal decomposition of $CaCO_3$, the new-formed CaO was cooled down (at 10°C/min, still keeping the sample under N_2) to the desired carbonation temperature. Afterwards, the carbonation stage was carried out isothermally at several temperatures between 450°C and 750°C. As mentioned, the overall carbonation time was set at 20 min for each of the tests. An atmosphere of pure CO_2 was used maintaining a constant flow rate of approximately 10 NmL/min at a pressure of 1 bar. The transition between N_2 and CO_2 atmosphere was realized by means of an automatic switching valve.

The Rietveld profile refinement method was finally applied to extract information about the structural changes of the sorbent samples in terms of $CaCO_3$/CaO phase and crystallite size evolution over time, as a function of both calcination conditions and carbonation temperature. As reported in §3.2.1, calcium oxide mass fractions were estimated from the quantitative phase analysis (QPA) of the diffraction data refining phase scale factors ([108]), and were used to calculate the CaO conversion during the carbonation stages through the Eq. 3.16.

Contrarily to the preliminary estimates discussed in § 3.2.1, in this case the average size of the $CaCO_3$/CaO crystallites making up the material was instead evaluated directly from the Rietveld refinements of the profile parameters. In particular, GSAS fits crystallite size broadening with the Lorentzian isotropic crystallite size-broadening factor *LX* (§ 3.1.3), The relationship between this (dimensionless) parameter and the average crystallite size (*CS*, in nm), for each crystalline phase within the material, was obtained by the following equation ([108]):

$$CS = \frac{18 \times 10^3 K\lambda}{\pi LX} \tag{4.1}$$

where λ is the x-ray wavelength (0.07296 nm) and *K* is a dimensionless constant related to the crystallite shape taken as 0.9. During the refinements, only the Lorentzian size-broadening profile parameter was refined while the strain-broadening factor (*LY*, § 3.1.3) did not show a significant contribution. The Thompson-Cox-Hastings pseudo-Voigt-type function was used to fit the Lorentzian term and describe the peak shapes ([108]). The temperature factors ([108]) were adjusted to take into account the effect of the different carbonation temperatures on the crystalline structure evolution, namely the attenuation of the X-ray scattering caused by the thermal motion of the atoms within the crystal lattice ([89], [94], [88]). A cosine Chebyshev function of 12 polynomial terms was applied to fit the profile background. The structure models for the starting material (CaO) and the crystalline reaction product ($CaCO_3$) were taken from the literature; 261847-ICSD and 20179-ICSD were selected for lime and calcite respectively. The instrumental contribution to the line broadening was evaluated by refining the profile parameters for LaB_6. Finally, to achieve a careful control of the sequential refinement, in the analysis of the time-resolved patterns only the angular range of 10.5-31.5° of 2θ was used for the refinement of the global and the peak shape broadening parameters, as well as for the phase specific scale factors.

The quality of the fitting was then evaluated using the weighted residual factor (*wRp*) of the refined analysis of each diffraction pattern, in agreement with the method of the least squares used by GSAS as main refinement technique ([108]). Good fittings for all the cases were obtained, with an average value of *wRp* of about 0.08 (± 1% of standard deviation) for the different time-resolved experiments performed. No preferred orientation corrections

were required to obtain satisfactory fits of both $CaCO_3$ and CaO. A typical 1D-diffraction pattern and the related fit are shown in Figure 4.4, to highlight the quality of the fitting obtained in this work.

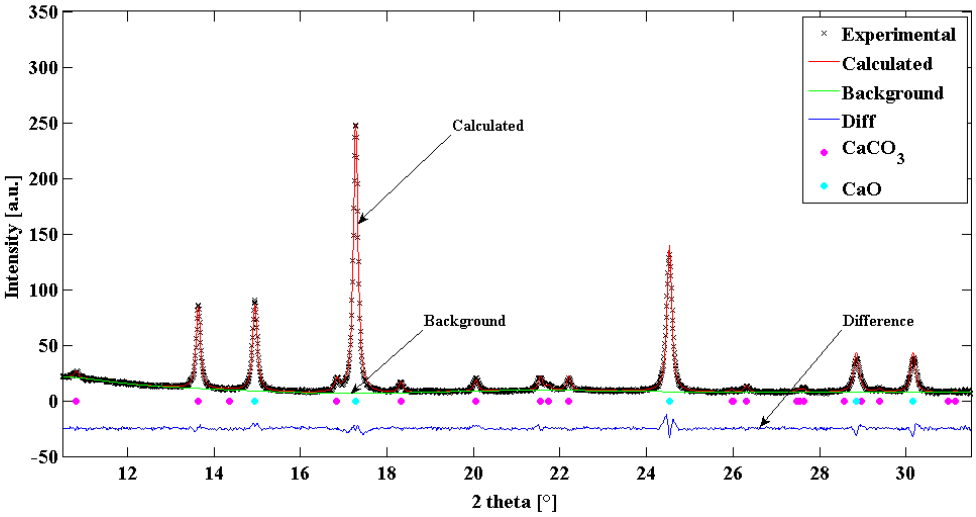

Figure 4.4: *Typical profile refinement for a diffraction pattern obtained at a CaO conversion of 20% and at a carbonation temperature of 450°C. Measured (black crosses) and calculated (red solid line) values are compared (their difference is plotted by the blue solid line). The position of the Bragg peaks for $CaCO_3$ and CaO are shown by pink and cyan blue dots respectively.*

4.3 In-situ X-ray diffraction experiments – part II

Similarly to the X-ray diffraction experiments discussed in the Chapter 3, the data collected from the time-resolved measurements carried out at the synchrotron beamline 17-BM-B were used to calculate the profiles of the CaO conversion utilized for the reaction kinetics investigation, and of the calcium oxide/calcium carbonate average crystallite size trends during the CO_2 absorption process, in order to identify relationships between the carbonation rate/conversion and the structural properties of the crystalline species involved in the reaction. A summary of all the experiments performed is reported in Table 4.1, underlining both the corresponding operating conditions and the main results obtained by Rietveld refinements for each test. As mentioned, in this work 20 min of carbonation was arbitrarily taken as reference time to estimate the final conversion for each experiment, as well as the final $CaCO_3$ average crystallite size. The average size of the initial CaO

crystalline domains was calculated once each sample had reached the desired carbonation temperature (after the cooling down of the sorbent from the calcination conditions), and before switching the gas atmosphere from N_2 to CO_2 inside the capillary. The errors in the average crystallite size calculation were estimated from the standard deviation values provided by GSAS for the *LX* parameters, afterwards used in the crystallite size calculation.

Table 4.1: *Summary of experimental operating conditions and corresponding results (final conversion, CaO average crystallite size at the beginning of carbonation, final average size of $CaCO_3$ crystalline domains) obtained by Rietveld refinement.*

Run	Calcination		Carbonation	Final CaO conversion X [-]	Initial CaO Average Crystallite Size [nm]	Final $CaCO_3$ Average Crystallite Size [nm]
	T [°C]	t [min]	T [°C]			
A	900	5	450	0.63	39 (± 2)	59 (± 3)
B	900	5	550	(0.26)	100 (± 3)	42 (± 6)
C	700	60	650	0.72	29 (± 2)	175 (± 5)
D	700	60	450	0.63	38 (± 2)	65 (± 3)
E	700	60	550	(0.58)	61 (± 3)	99 (± 4)
F	900	5	500	(0.21)	109 (± 2)	27 (± 5)
G	900	5	750	0.57	156 (± 3)	375 (± 7)
H	900	60	650	0.42	255 (± 5)	327 (± 7)
I	900	60	450	(0.07)	124 (± 2)	15 (± 10)
J	900	5	650	0.64	52 (± 2)	134 (± 5)
K	750	5	650	0.75	31 (± 2)	186 (± 6)
L	800	5	650	0.71	35 (± 2)	181 (± 5)
M	900	60	550	0.53	44 (± 1)	86 (± 3)
N	900	5	600	0.66	50 (± 2)	118 (± 3)
O	700	60	500	(0.19)	63 (± 3)	29 (± 6)

4.3.1.1 Profiles of calcium oxide conversion

Curves of calcium oxide conversion (*X*) versus time (*t*) were obtained from the experiments performed at different carbonation temperatures, using CaO sorbents

previously prepared through calcination stages carried out at several operating conditions. Two types of comparison were performed between the conversion profiles, namely i) as a function of the carbonation temperature, with CaO sorbent samples produced with the same calcination conditions (Figures 4.5 - 4.7) and, ii) at the same carbonation temperature, comparing the behavior of sorbent particles obtained from different calcination stages (Figures 4.8 - 4.10). In particular, different operating conditions during the thermal decomposition of calcium carbonate were selected to obtain fresh calcines with different average sizes of the CaO crystalline domains (§ 3.2.2.3). In each of the Figures from Figure 4.5 to 4.10 the complete conversion profile (up to 20 min of carbonation) is shown on the left side while a detailed view of the first instants of the reaction is plotted on the right side.

Conversion profiles as a function of the carbonation temperature were collected performing carbonation experiments with calcium oxide particles produced through three different calcination stages, namely at 900°C for 5 min (Figure 4.5), 900°C for 60 min (Figure 4.6) and at 700°C for 60 min (Figure 4.7). All the curves exhibit the characteristic shape of the carbonation reaction, including the fast initial reaction stage, up to a point/knee where there is an abrupt change in the carbonation rate that leads to the second slower stage. The first stage of the carbonation, occurring in the early instants of the reaction, is now clearly visible even if it was complete roughly after 5 s (compared to the previous XRD observations), showing reaction rates significantly higher than those both measured in the experiments discussed in the previous chapters, and typically reported in several contributions in the literature including [15], [11], [12], [14], [9], [10], [13], [21], [18], [22], [23], or [19]. The second phase of carbonation is characterized by a plateau that was associated with the occurring of the product layer diffusion controlled regime. In most of the runs, it seems that a maximum extent of conversion was achieved after 20 min of reaction. However, in a few experiments (curves B and F in Figure 4.5, curves E and O in Figure 4.7) the conversion profiles still exhibit a slow increase in the CaO conversion trend after 20 min of carbonation. The majority of the profiles show final conversions above 50%, with the highest values around 70%, while only few experiments resulted in final conversions around 20% or below.

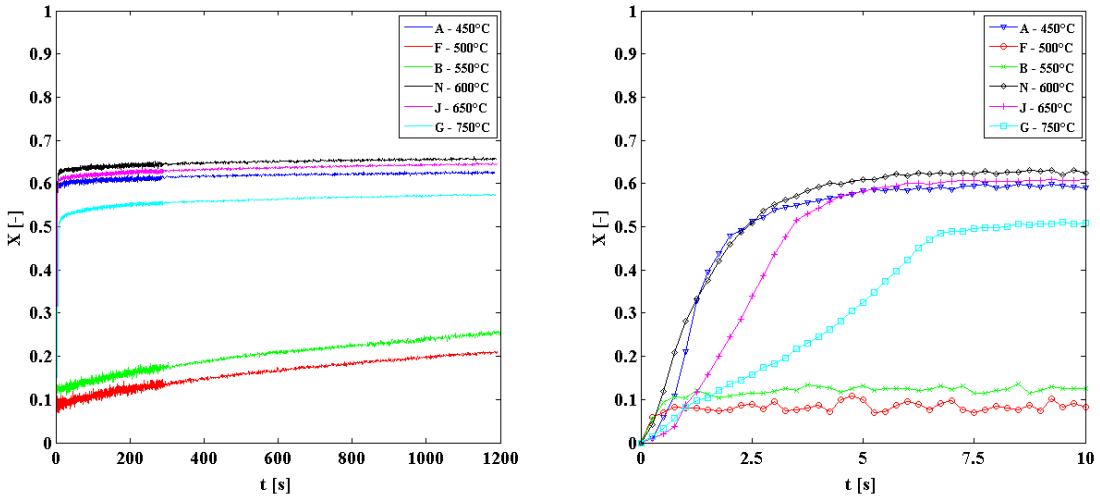

Figure 4.5: *Calcium oxide conversion for isothermal carbonation at different temperatures (calcination at 900°C for 5 min). Profiles corresponding to 20 min (left) and 10 s (right) of carbonation.*

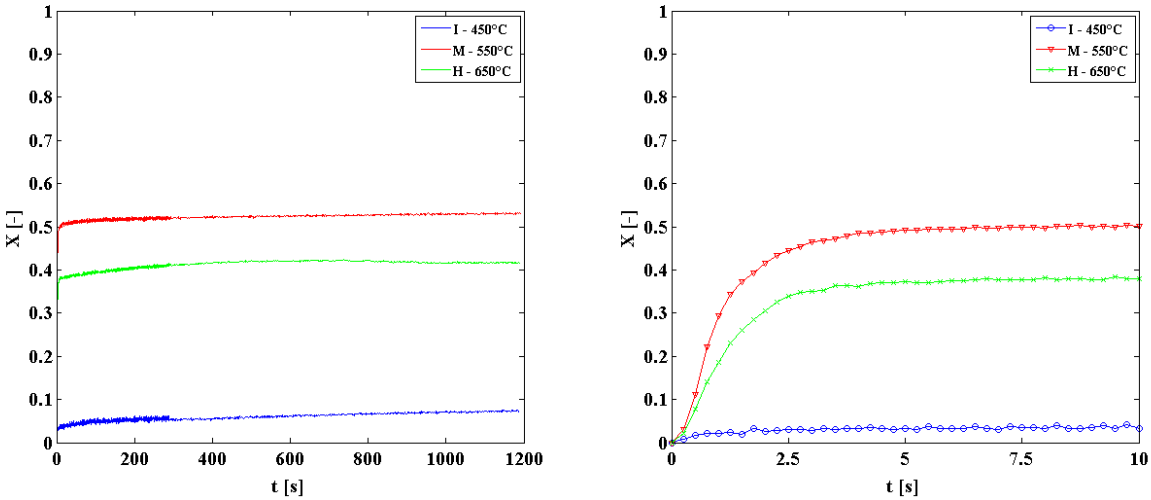

Figure 4.6: *Calcium oxide conversion for isothermal carbonation at different temperatures (calcination at 900°C for 60 min). Profiles corresponding to 20 min (left) and 10 s (right) of carbonation.*

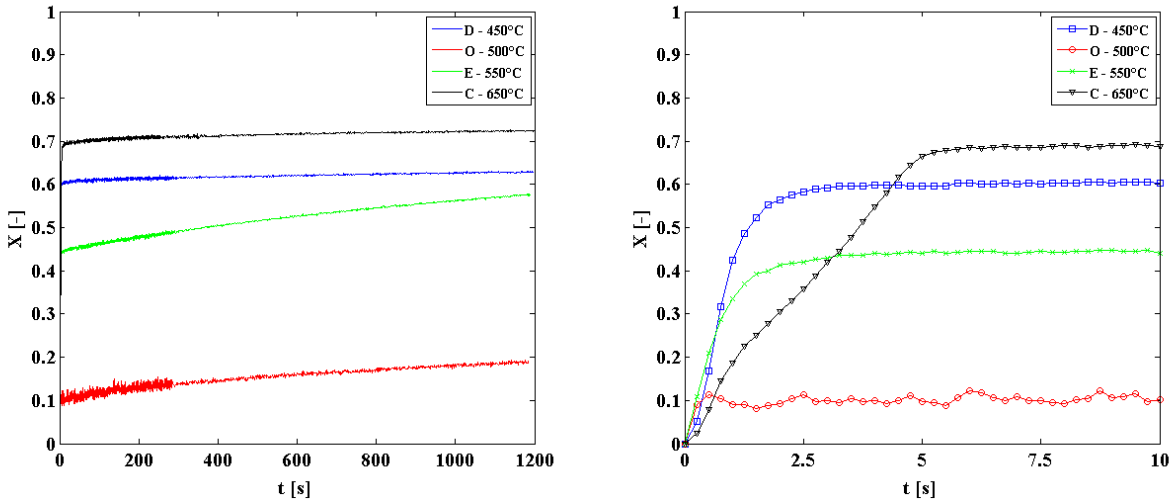

Figure 4.7: *Calcium oxide conversion for isothermal carbonation at different temperatures (calcination at 700°C for 60 min). Profiles corresponding to 20 min (left) and 10 s (right) of carbonation.*

Even though at a CO_2 partial pressure of 1 bar, in the range between 450°C and 750°C, higher carbonation temperatures generally lead to higher calcium oxide conversions at a given carbonation time, as observed from both TGA and X-ray diffraction experiments previously discussed, according to these profiles the carbonation temperature apparently does not affect the value of the final conversions in the expected way. Experiments carried out at 450°C showed final conversions of approximately 60% (curves A and D in Figure 4.5 and Figure 4.7 respectively), which were higher than those observed at a carbonation temperature of 500°C (curves F and O in Figure 4.5 and Figure 4.7 respectively), 550°C (curves B and E in Figure 4.5 and Figure 4.7 respectively) and 750°C (curve G in Figure 4.5), as well as in the carbonation test performed at 550°C (curve M in Figure 4.6) a final conversion higher than that one measured for the corresponding experiment at 650°C (curve H) was observed. These unexpected trends of the final conversion as a function of the carbonation temperature indicate that other aspects may affect the CaO-CO_2 reaction. In particular, it can be noted that the majority of the sorbent samples produced with the same calcination conditions show large differences in the values of the initial CaO average crystallite size (see Table 4.1). To emphasize the effect of the calcium oxide initial (measured at the beginning of the CO_2 absorption process) average crystallite size on the reaction kinetics, conversion profiles for isothermal carbonations performed at

temperatures of 650, 550 and 450°C were compared, as shown in Figures 4.8, 4.9 and 4.10 respectively. At a carbonation temperature of 650°C (Figure 4.8), CaO sorbents with an initial average crystallite size of about 30 nm (curves C, K and L) achieved conversions of approximately 70% after 20 min of reaction, clearly higher than that ones obtained with sorbent samples characterized by an initial average size of their crystalline domains of about 50 nm (about 60%, curve J) and 250 nm (about 40%, curve H). A similar trend was observed for carbonation temperatures of 550°C (Figure 4.9) and 450°C (Figure 4.10) where particles with crystalline domains of about 40 nm (curves M, D and A) were converted to values higher than those achieved by sorbent samples with average crystallite sizes of 100 (curve B) and 124 nm (curve I) respectively.

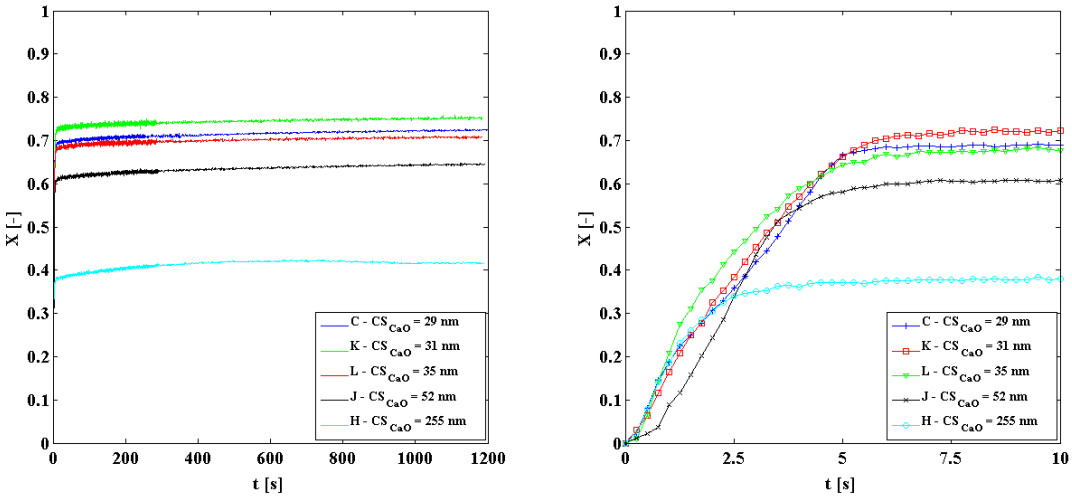

Figure 4.8: *Calcium oxide conversion for carbonation at 650°C using sorbents with different initial CaO crystallite size. Profiles corresponding to 20 min (left) and 10 s (right) of carbonation.*

Therefore, the conversion profiles point out (and confirm previous observations) that generally calcium oxide sorbents with a lower average crystallite size at the beginning of the carbonation reaction show a higher CO_2 capture capacity. In this way, the apparently unexpected dependence of the conversion profiles on the carbonation temperature (Figures 4.5, 4.6 and 4.7) can be explained: even though the sample are produced with the same (macroscopically) operating conditions during calcination, the particle properties (particularly the CaO crystallite size) are different and, therefore, in each of the Figures

from 4.5 to 4.7 both the carbonation temperatures and the particle properties are different among different runs. In conclusion, for each of the Figures from 4.5 to 4.7, a straightforward comparison among different profiles as a function of only the carbonation temperature cannot be performed.

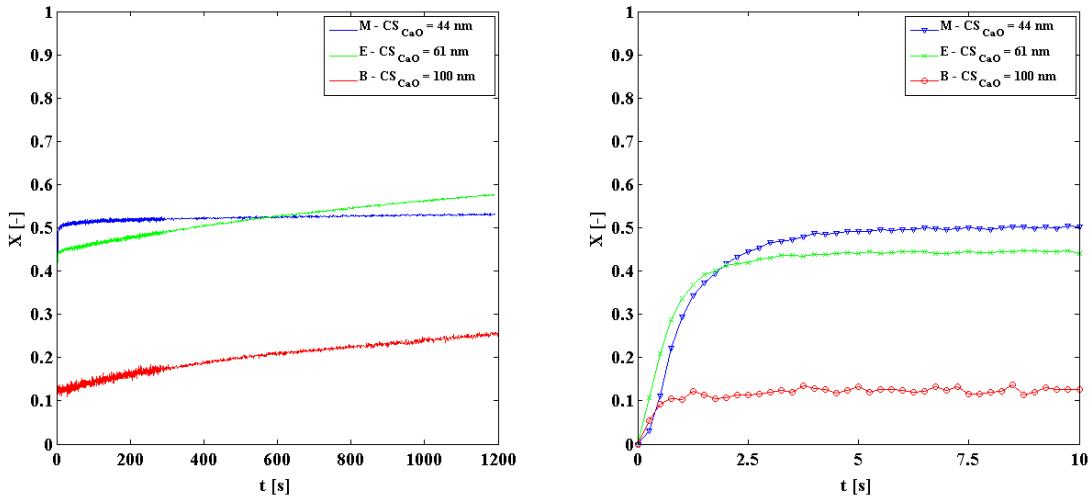

Figure 4.9: *Calcium oxide conversion for carbonation at 550°C using sorbents with different initial CaO crystallite size. Profiles corresponding to 20 min (left) and 10 s (right) of carbonation.*

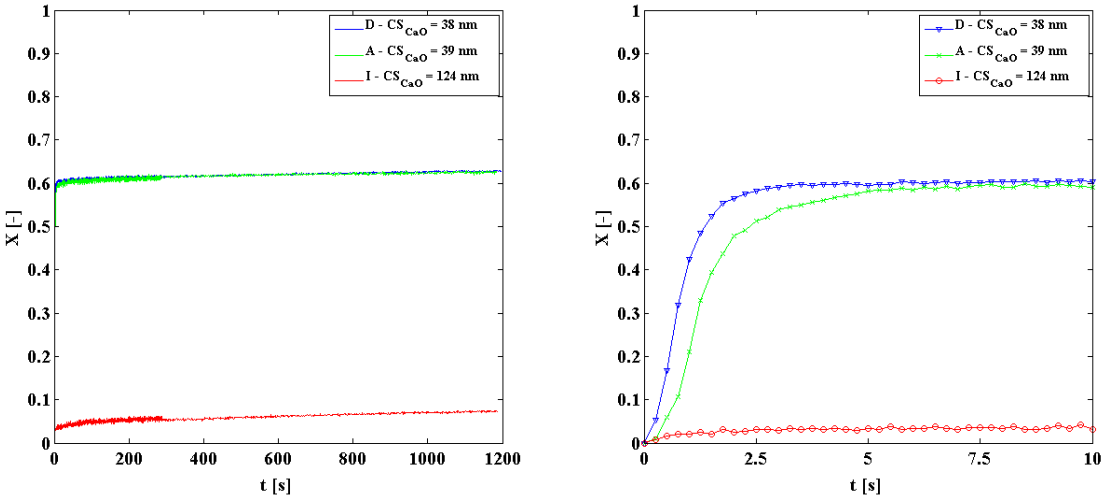

Figure 4.10: *Calcium oxide conversion for carbonation at 450°C using sorbents with different initial CaO crystallite size. Profiles corresponding to 20 min (left) and 10 s (right) of carbonation.*

The reason why at the same (macroscopically) calcination conditions sorbent particles with different calcium oxide crystallite size were produced still needs to be explained. Even though it was observed that keeping the same operating conditions during the calcination stages resulted in CaO sorbent particles characterized by similar crystallite sizes (§ 3.2.2.1) and, afterwards, by rather equal conversion versus time curves, something different it could be occurred during the experiments carried out at this stage of the research. In particular, it should be reminded that the diffraction data used to build these last conversion profiles of the CaO based sorbent samples reflect the behavior of only a small volume of the powder loaded inside the capillary. Because the size of the X-ray beam was about 300 μm and the internal diameter of the capillary was 1 mm, each conversion profile represents the CO_2 capture performance of a volume of less than 0.07 mm^3. Assuming that the 150 μm calcium carbonate particles are spherical, the number of particles inside the volume spanned by the X-ray beam was small, namely of the order of 10-30 particles. Additionally, even though each sample was loaded inside the capillary with the same procedure, it is notable that the compaction of the particles was not verifiable and it is likely that it was different among all the experiments performed. Therefore, it can be hypothesized that even with the same (macroscopically) calcination conditions and the same compaction procedure, the local (specifically, in the volume spanned by the X-ray beam) compaction extent could be different, thus determining different local fluid dynamic conditions, carbon dioxide concentrations and ultimately different local calcination conditions. Moreover, it can be reasonably assumed that sintering processes, favored at high temperature, occurred during the thermal decomposition of the calcium carbonate samples inducing alterations of the characteristic porous structure and of the crystallite size of the fresh CaO particles afterwards used for the carbonation experiments ([74], [76], [75], [77], [42], [86]). Specifically, it can be hypothesized that sintering phenomena took place at different extents among the different runs (even in those carried out with identical macroscopically operating conditions during the calcination) because of the in-homogenous local calcination conditions, determining morphological differences in the produced CaO calcines, especially in terms of crystallite size, as well as in terms of specific surface area and porosity.

Finally, it has to be specified that the change in the conversion accuracy, which can be observed in each profile in the Figures from 4.5 to 4.10 after the first 5 minutes of

carbonation, reflects the change of exposure time applied during the collection of the X-ray data. As mentioned in § 4.2, data were recorded continuously with a frame rate of 0.25 s per frame during the first 5 min of the reaction such that the first 1200 diffraction patterns arise from the data measured with an exposure time of the same duration of the frame rate, namely 0.25 s. After that, during the remaining 15 min of carbonation, the frame rate was increased to 1 s resulting in a longer exposure time (namely, 1 s) for each frame that determines the higher accuracy of the last 900 scans.

4.3.1.2 Effect of the initial CaO average crystallite size on the carbonation reaction

The comparison of the different values measured for the initial average crystallite size of the CaO based sorbents and the corresponding final conversions obtained for each experiment (summarized in Table 4.1) points out an interesting result. The values of the final conversion are plotted in Figure 4.11 as a function of the initial CaO average crystallite size. Focusing on the runs in which the conversion was not significantly increasing after 20 min of carbonation (black circles in Figure 4.11), it can be observed that the lower is the initial average crystallite size of the new-formed calcium oxide, the higher the conversion of the sorbent particles evaluated at the end of the absorption experiments. A linear fitting of such experimental data provides the following relationship (solid line in Figure 4.11):

$$X_{\max} = -11 \times 10^{-4} CS_{CaO} + 0.705 \tag{4.2}$$

where $X_{\max}$ is the final (maximum) CaO conversion (obtained after 20 min of carbonation) and CS_{CaO} is the average size (in nm) of the CaO crystalline domains measured at the beginning of the carbonation reaction. This correlation is independent from the carbonation temperature maintained during each run, as well as from the operating conditions used to produce the initial CaO sorbent particles. It should be noted that the red crosses in Figure 4.11 represent the conversions measured after 20 min of carbonation in those experiments in which the conversion profiles were still increasing at the end of the carbonation. Since the reactions were evidently incomplete, the final conversions evaluated in these runs were not considered as accurate values for the maximum conversion potentially achievable from the sorbent particles.

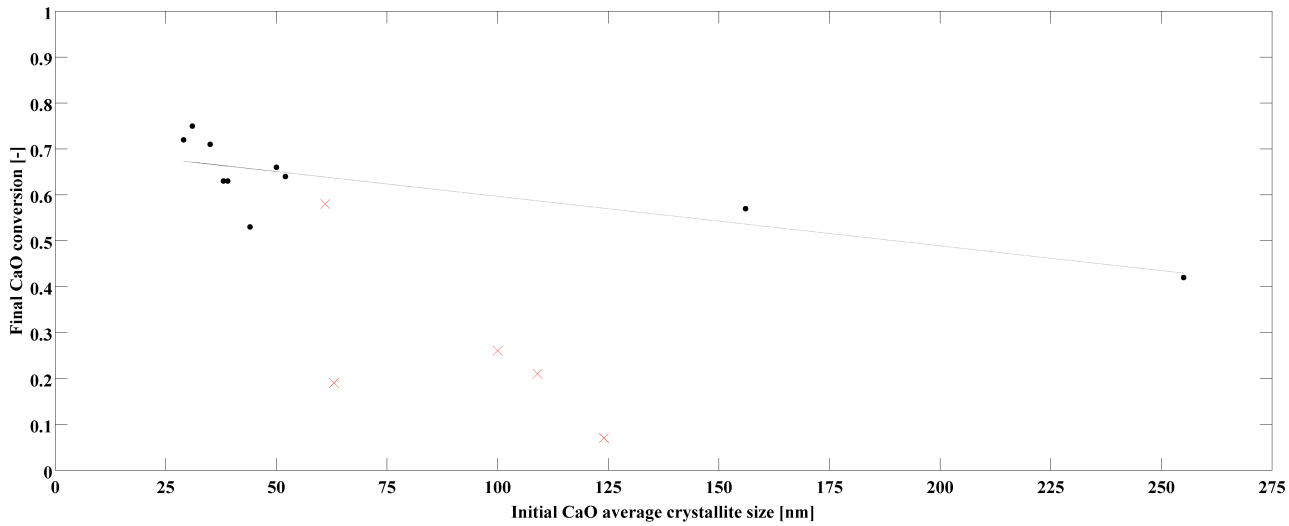

Figure 4.11: *Relationship between the final CaO conversion and the initial CaO average crystallite size. The solid line represents a linear fitting of the results for runs in which conversion was not significantly increasing at the end of carbonation (black circles). Red crosses represent runs in which conversion was still increasing at the end of carbonation.*

The maximum CaO conversion (X_{max}) can be estimated from the initial sorbent porosity through the following relationship ([42]):

$$X_{\max} = \frac{\varepsilon_0}{\left(\frac{1}{Z} - 1\right)\left(1 - \varepsilon_0\right)} \tag{4.3}$$

where ε_0 is the initial sample porosity available for the carbonation and Z is the molar volume ratio of calcium oxide to calcium carbonate that is equal to 0.46. Eq. (4.3) is obtained assuming that the porosity is zero when the maximum conversion is reached. According to Eq. (4.3) different maximum conversions at the end of carbonation can be obtained as a function of the initial sorbent porosity, which depends on the high temperature thermal treatment carried out during the preliminary calcination stage. However, it is reasonable to assume that the average value of the CaO initial crystallite size could reflect the morphological properties (specifically, the porosity) characterizing the sorbents at the beginning of the carbonation.

Rearranging Eq. (4.3), the initial porosity of the solid sorbents can be directly related to the maximum conversion reachable:

$$\varepsilon_0 = \frac{X_{\max}\left(\frac{1}{Z}-1\right)}{\left[1+X_{\max}\left(\frac{1}{Z}-1\right)\right]} \tag{4.4}$$

Using Eq. (4.4), an estimate of the initial porosity of the CaO sorbent samples in each carbonation experiment was performed (see Table 4.2), and then correlated with the corresponding values of the average crystallite size of calcium oxide at the beginning of the CO_2 absorption processes, as shown in Figure 4.12.

Table 4.2: *Summary of initial CaO particle porosity estimates computed by Eq. (4.4).*

Run	Calcination		Carbonation	Initial CaO Porosity [-]
	T [°C]	t [min]	T [°C]	
A	900	5	450	0.43
B	900	5	550	-
C	700	60	650	0.46
D	700	60	450	0.43
E	700	60	550	-
F	900	5	500	-
G	900	5	750	0.40
H	900	60	650	0.33
I	900	60	450	-
J	900	5	650	0.43
K	750	5	650	0.47
L	800	5	650	0.45
M	900	60	550	0.38
N	900	5	600	0.44
O	700	60	500	-

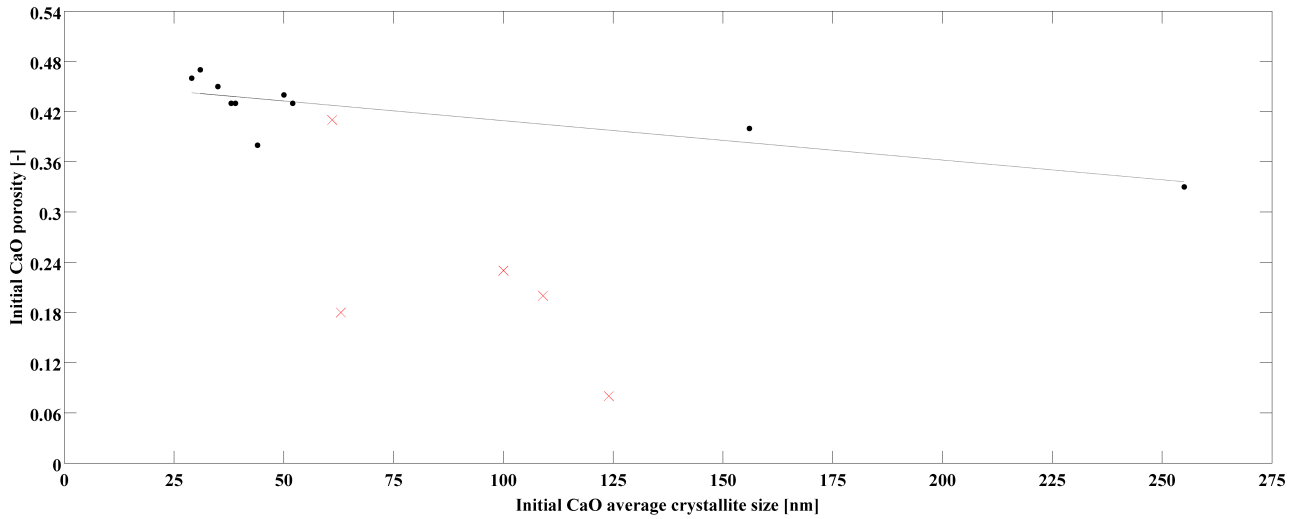

Figure 4.12: *Theoretical estimation of the initial CaO porosity from the initial CaO average crystallite size. The solid line represents a linear fitting of the results for runs in which conversion was not significantly increasing at the end of carbonation (black circles). Red crosses represent runs in which conversion was still increasing at the end of carbonation.*

The relationship, highlighted by the solid line in Figure 4.12, has been formalized through a linear fitting of the data calculated, leading to the following expression:

$$\varepsilon_0 = -4.707 \times 10^{-4} CS_{CaO} + 0.456 \tag{4.5}$$

As previously mentioned, because the evaluation of the initial porosity requires to consider only the maximum conversion physically attainable, those experiments that had not reached clearly a reasonable value of the maximum conversion at the end of the carbonation experiments (red crosses in Figures 4.11 and 4.12) were omitted from the calculation of the correlation reported. The trends emerging from Figures 4.11 and 4.12 suggest that sorbent samples with a smaller size of CaO crystalline domains at the beginning of the carbonation should have a higher initial porosity and hence more pore volume available for the calcium carbonate growth that consequently leads to a higher final carbonation conversion.

4.3.1.3 Intrinsic reaction rate in the first stage of the carbonation reaction

In addition to the determination of the average sizes of the CaO crystalline domains that characterize the solid sorbents at the beginning of the carbonation reaction, the in-situ X-ray powder diffraction analysis permitted a detailed analysis of the rapid first stage of the $CaO\text{-}CO_2$ reaction providing remarkable results about the carbonation rates. The reaction rate of the calcium oxide carbonation is usually defined as a specific rate, namely as the CaO conversion time derivative dX/dt divided by $1\text{-}X$. Typically, the conversion time derivative at time zero (beginning of carbonation) is used in order to compare rates from different experiments. In particular, in the initial part of the first rapid stage of the carbonation reaction (at low conversions), the measured conversion rates are representative of the intrinsic reaction rate due to the surface chemical reaction because the product layer diffusion can be reasonably neglected. The conversion time derivative at time zero is equal to the maximum time derivative in grain models ([9]) and in random pore models ([15]) in the regime controlled by the chemical kinetics when the structural parameter is smaller than 2 (such value is within the typical range for CaO based sorbents). Therefore, the estimate of the initial conversion time derivative characterizing the first stage of the carbonation reaction was performed in two ways, namely i) considering the maximum values of dX/dt for each CaO conversion profile, and ii) selecting a portion of the initial fast stage where the experimental curves of conversion versus time could be fitted through a linear relationship. In the former case, the values of CaO conversion at which the maximum conversion rates were computed were always lower than 0.2 (and always within the first second of reaction). In the latter case, for each run the experimental points used in the linear fitting were selected considering the data below both 25% and 50% of the corresponding final conversions, as shown for example in Figure 4.13, starting from the first non-zero value of the conversion.

The carbonation reaction during the fast reaction stage is frequently interpreted as controlled by the (intrinsic) surface chemical reaction ([15]). Accordingly, the effects of the product layer diffusion are neglected. However, other authors claimed that it is more reasonable to assume a regime of simultaneous chemical kinetics and product layer diffusion even during the first stage of carbonation, then followed by a pure diffusion controlled regime after that the product layer of $CaCO_3$ has reached a critical value ([9], [17], [13]). Therefore, only at low values of CaO conversion it is correct to assume that the

diffusional effects through the product layer of $CaCO_3$ are negligible. Therefore, the computed initial conversion time derivatives could underestimate the true values, because they could be partially affected by some product layer diffusion effects.

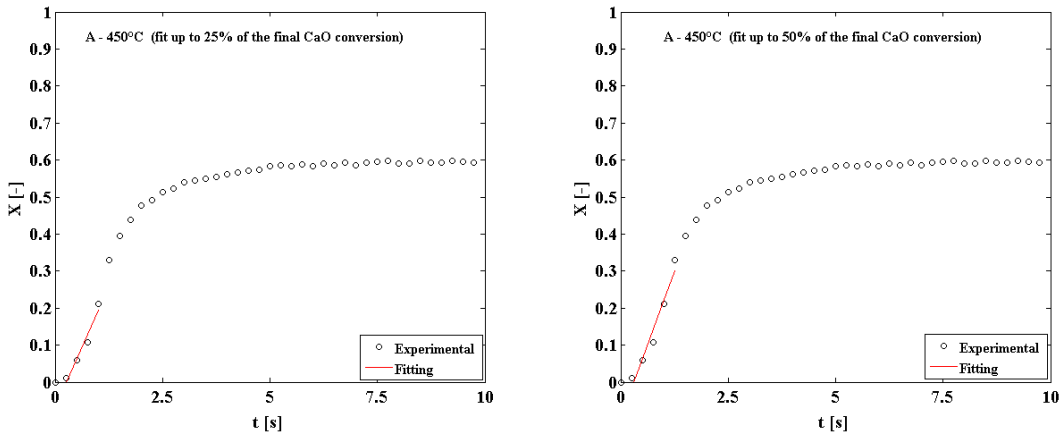

Figure 4.13: *Linear fitting of the first part of the CaO conversion profiles, used to estimate the initial conversion rates in the first stage of carbonation. Example on the conversion curve at a carbonation temperature of 450°C.*

Despite that, both the approaches applied here to estimate the initial conversion rates underline a significant difference with the data reported in the literature. A summary of the calculated conversion time derivatives is reported in Table 4.3 (the estimate of the conversion rate using the linear fitting up to 50% of the final CaO conversion was not possible for carbonation profiles with final conversion lower than approximately 20%, namely for runs B, F, I and O).

Even though the results in Table 4.3 show values of standard deviations between 9.6% and 13.2%, the carbonation rates observed during the first stage of each carbonation experiment are unequivocally a noteworthy result. In fact, such high conversion rates, with average values of the conversion time derivative between 0.280 s^{-1} and 0.239 s^{-1}, have never been previously measured for the CO_2 carbonation using CaO based solid sorbents. Typical values of about 0.05 s^{-1} reported so far in the literature by several authors are far from the values measured through these kind of experiments: as mentioned, Sun et al. (2008) estimated an initial maximum reaction rate of 0.054 s^{-1} at 615°C with CO_2 partial pressure equal or higher to 10 kPa ([9]). A corresponding similar value was obtained from

the data of Bathia and Perlmutter (1983), namely 0.041 s^{-1} ([9]). Kyaw et al. (1998) calculated comparable reaction rates as well, with maximum conversion time derivatives below approximately 0.06 s^{-1} in a range of carbonation temperatures between 600°C and 800°C and in a range of CO_2 partial pressures between 60 kPa and at 101 kPa ([12]).

Table 4.3: *Initial conversion time derivatives estimated from experimental profiles of CaO conversion (X) as a function of the reaction time (t) during the first rapid carbonation stage.*

Run	dX/dt [s^{-1}]		
	Maximum	**Linear fitting up to 25% of the final CaO conversion**	**Linear fitting up to 50% of the final CaO conversion**
A	0.391	0.261	0.317
B	0.242	0.185	-
C	0.221	0.198	0.150
D	0.541	0.336	0.427
E	0.468	0.420	0.387
F	0.239	0.239	-
G	0.106	0.067	0.060
H	0.216	0.192	0.196
I	0.040	0.028	-
J	0.180	0.118	0.140
K	0.207	0.170	0.160
L	0.320	0.221	0.223
M	0.377	0.298	0.311
N	0.333	0.282	0.283
O	0.314	0.362	-
Average	**0.280** (± 13.2% stand. dev.)	**0.239** (± 9.6% stand. dev.)	**0.240** (± 11.4% stand. dev.)

Additionally, these literature data suggest that the significant differences respect to the reaction rates presented in this work cannot be due to the different operating conditions used during the absorption process, mainly the partial pressure of CO_2 and the carbonation temperature. In fact, Kyaw et al. (1998) ([12]) explored operational conditions similar to the values used in this study (partial pressure of CO_2 equal to 101 kPa). Further, as mentioned in § 2.4.1.3, Sun et al. (2008) ([9]) analyzing their experimental data noted that the CaO carbonation intrinsic kinetics can be described as a zero-order reaction respect to

the CO_2 partial pressure (relative to the equilibrium partial pressure), when such quantity is equal or higher than 10 kPa, confirming that the high reaction rates (conversion time derivatives between 0.280 s^{-1} and 0.239 s^{-1}) measured during this stage of the research cannot be ascribed to the pure CO_2 atmosphere used to carry out the carbonation experiments.

The explanation of such high carbonation rates is more reasonably found considering the characteristic geometry of the flow cell/furnace used to perform the carbonation experiments at the 17-BM-B beamline. As reported in the Chapter 2, thus far the most popular and widely used approach to investigate the CaO-CO_2 reaction has been the thermo-gravimetric analysis (TGA). To the best of the author's knowledge, all the kinetic studies on the carbonation reaction available in literature are based on thermo-gravimetric experiments ([15], [11], [12], [9], [17], [10], [22]). With this technique, carbonation experiments are typically carried out feeding in a reaction chamber/furnace a reacting mixture of CO_2 in nitrogen or pure CO_2, and the CaO sorbent reactivity is measured by recording the change in sample weight due to the carbon dioxide absorption such that the monitored weight increase, as a function of a controlled gas atmosphere and of a temperature/time program, is related to the progress of the carbonation. Preliminary tests are usually performed to identify the operating conditions required to reduce/eliminate the physical limitations (external, inter-particle, intra-particle mass diffusion) that can affect TGA measurements. In particular, the external mass transfer, which limits the gas (CO_2) diffusion towards the solid sorbent (CaO) surface, cannot easily experimentally eliminated and still calls into question the quality of the CaO conversion versus time profiles thus far obtained with this technique. The external mass transfer is related to the total gas flow rate and it is typically reduced applying high gas flow rates. However, even when working at high gas flow rates, thus far it has not been demonstrated that the local velocities inside the TGA sample holder (i.e. above the sorbent particles) are high enough to support a high CO_2 consumption rate due to the rapid surface chemical reaction (namely, CaO carbonation). Even though a few authors ([9], [10]) claim that their TGA experimental data (conversion versus time curves) are independent of the gas flow rate (using high flow rates) because they did not observe a significant change in their CaO conversion versus time profiles when increasing the gas flow rate, author's opinion is that such results could be still dependent on the external mass diffusion. Indeed, even though the cited authors

were capable to reduce the resistance due to the external mass diffusion during the CaO carbonation using high gas flow rates (as well as observed in the TGA experiments discussed in § 2.4.1.2), this does not mean that such resistance was completely eliminated. The local velocities reached around/inside a TGA crucible (especially above the sorbent particles contained in the sample holder) can be low even if the average velocity in the furnace is increased by increasing the gas flow rate and hence, the local velocities around/inside a TGA crucible cannot be increased enough to compensate the very high mole (CO_2) consumption rate due to the fast carbonation surface reaction. Therefore, the fact that at high gas flow rates the conversion versus time curves don't change when increasing the gas flow rate does not mean that the external mass diffusion resistance is eliminated, but only that such resistance cannot be further reduced in the TGA geometry and operating conditions used.

On the contrary, during the experiments carried out at the 17-BM-M beamline, the carbon dioxide was forced to flow inside a capillary, directly through the sample particles with high gas velocities around the sample particles, so that it can be reasonably assumed that the external CO_2 mass transfer limitation was minimized (likely it was completely eliminated). Specifically, the gas flow rates used in these X-ray diffraction experiments (approximately 10 NmL/min) allowed to obtain gas velocities insides the capillary used as sample holder higher than 20 cm/s. This reference value was calculated at room temperature, at the inlet of the flow cell utilized. Differently, considering the thermo-gravimetric experiments discussed in this work of thesis, the TGA geometry used, even applying high gas flow rates (maximum value available of about 250 NmL/min), allowed to reach average gas velocities almost fifteen times lower (namely, of about 1.3 cm/s at room temperature) than those realized in the synchrotron experiments at the flow cell inlet. Such difference is even larger considering that in these last experiments the velocity through the particle bed porosities in the capillary is even higher than at the flow cell inlet. More importantly, the gas velocity value computed for a typical TGA experiment (1.3 cm/s at room temperature) refers to the average velocity in the furnace cross section, not to the local gas velocity close to the particles; this local velocity, which determines the external mass diffusion resistance, is actually lower than the average velocity gas velocity.

In conclusion, because of the high velocities achieved and of the results obtained in terms of reaction rates (higher than those ones commonly reported in the literature), it can be

reasonably assumed that the described carbonation experiments were not affected by external mass transfer limitations, as well as the experimental data reported represent the surface chemical reaction step, namely the intrinsic carbonation reaction rate.

4.3.1.4 Apparent effect of the initial CaO average crystallite size on the reaction rate

The maximum conversion rates presented in the previous section are plotted in Figure 4.14 as a function of the average crystallite size of the corresponding CaO samples at the beginning of each carbonation run.

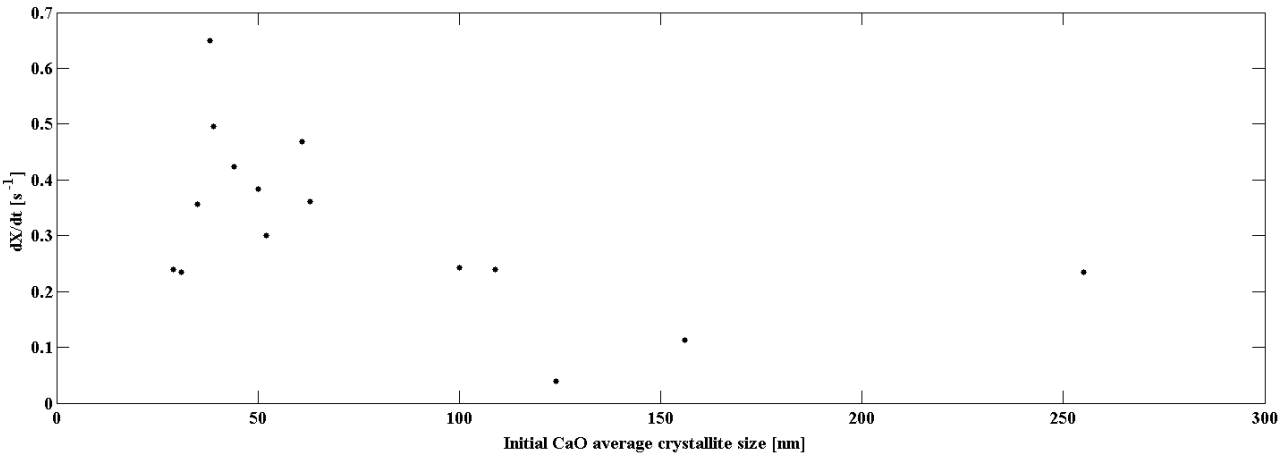

Figure 4.14: *Maximum conversion time derivatives as a function of the CaO average crystallite size at the beginning of carbonation.*

As shown in Figure 4.14, even though the data look somehow scattered, it seems reasonable to identify a relationship of inverse proportionality between the maximum conversion rates and the average size of the CaO crystalline domains.

An hypothesis to explain such relationship is that the initial carbonation conversion rate (which can be estimated by the maximum conversion rate) is related to the active (not the total) specific surface area that characterizes the sorbent particle internal surface and that the active surface area depends on the initial CaO crystallite size. Specifically, according to such hypothesis, smaller CaO crystallite sizes indicate a larger length of crystallite boundaries per unit of surface area and consequently a larger active specific surface area for the occurring CaO-CO_2 reaction, the number of reactive sites being proportional to the length of crystallite boundaries. This would result in an increase of the reaction rate per

unit of surface area. In support of such hypothesis, Mess et al. (1999) ([58]), in an investigation on the product layer diffusion during the carbonation reaction of non-porous calcium oxide, modeled the reaction between CO_2 and CaO assuming that a contribution to the conversion rate is proportional to the access of the carbon dioxide to the calcium oxide surface by grain boundary diffusion, which was in turn proportional to the grain boundary length per unit of surface area. Also in their work the grain boundary length per unit of surface area was assumed to be inversely proportional to the grain size.

4.3.1.5 $CaCO_3$ average crystallite size profiles over time

Similarly to the profiles of the CaO conversion, the data collected from the time-resolved measurements were also used to calculate the calcium carbonate average crystallite size trends during the CO_2 absorption process, in order to identify relationships between the carbonation rate/conversion and the structural properties of the crystalline species ($CaCO_3$) produced by the reaction. According to the curves of calcium oxide conversion versus time previously described, the corresponding evolution of the average $CaCO_3$ crystallite size as a function of the carbonation time were similarly obtained from the experiments performed at different carbonation temperatures, using the CaO sorbents previously prepared through calcination stages carried out at several operating conditions. Specifically, the two types of comparison performed with the conversion profiles reflected those previously described, namely i) as a function of the carbonation temperature, with CaO sorbent samples produced through the same calcination conditions (Figures 4.15 - 4.17) and, ii) at the same carbonation temperature, comparing the size changes of the calcium carbonate crystallites in sorbent particles obtained from different calcination stages (Figures 4.19 - 4.21). Again, in each of the Figures from 4.15 to 4.17, and from 4.19 to 4.21, the complete profiles (up to 20 min of carbonation) are shown on the left side while a detailed view of the calcium carbonate crystallite size trend during the first instants of the reaction is plotted on the right side. Additionally, as previously underlined, it has to be specified that the change in the accuracy observable in each profile after the first 5 minutes of carbonation reflects the change of the exposure time applied during the collection of the X-ray data (§ 4.2).

Figures 4.15, 4.16 and 4.17 show the $CaCO_3$ average crystallite size profiles, as a function of the carbonation temperature, obtained from CO_2 absorption experiments performed with calcium oxide particles produced respectively at 900°C for 5 min (Figure 4.15), 900°C for

60 min (Figure 4.16) and at 700°C for 60 min (Figure 4.17). All the curves exhibit a shape denoting the characteristic tendency of the carbonation reaction, with a fast initial $CaCO_3$ crystal growth stage that proceeds up to a turning point where there is an abrupt change in the carbonate crystal growth rate, that in turn leads to a second slower period alike to that one typically observed in the CaO conversion versus time profiles. The second phase of carbonation is typically associated with the occurring of the product layer diffusion-controlled regime that, in the calcium oxide conversion curves, is generally characterized by a plateau (§ 4.3.1.1). Referring instead to the $CaCO_3$ crystal growth curves, after the sharp transition the majority of the profiles still exhibit an increase in the average size of the carbonate crystalline domains as the carbonation time increases, with the exception of few experiments (curve A in Figure 4.15, curves I and M in Figure 4.16 and curve D in Figure 4.17), mainly characterized by a carbonation temperature of 450°C.

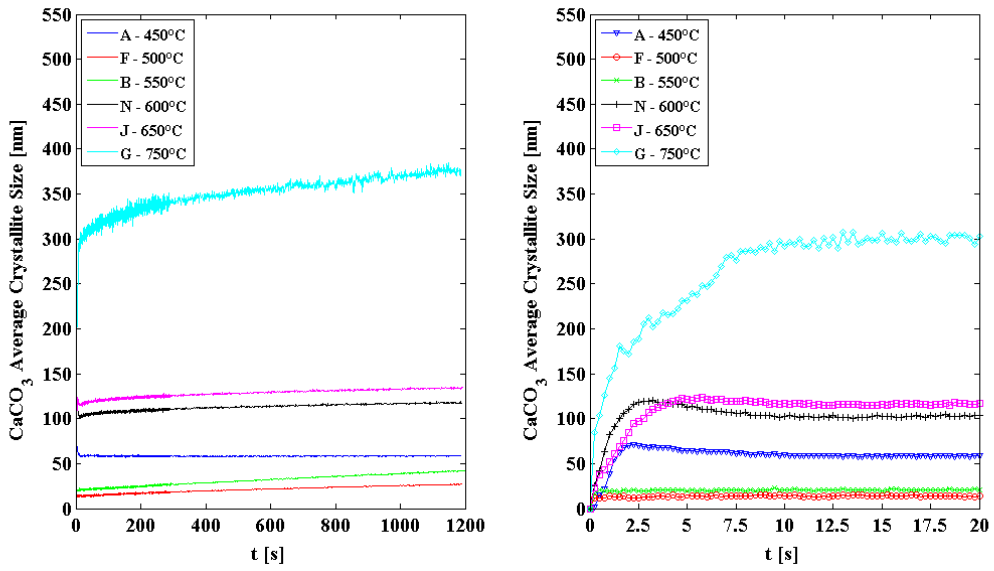

Figure 4.15: *$CaCO_3$ average crystallite size evolution for isothermal carbonation at different temperatures (calcination at 900°C for 5 min). Profiles corresponding to 20 min (left) and 20 s (right) of carbonation.*

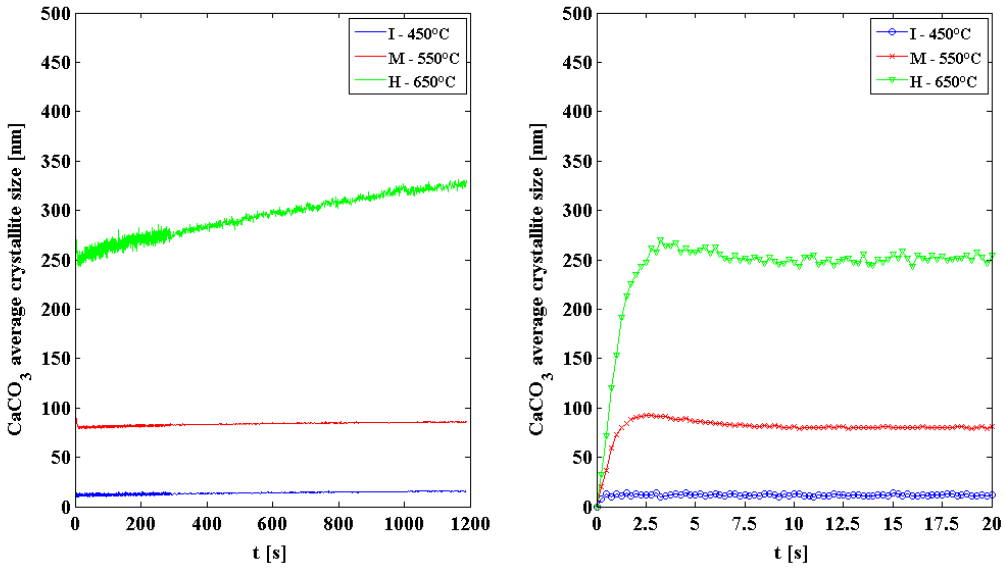

Figure 4.16: *$CaCO_3$ average crystallite size evolution for isothermal carbonation at different temperatures (calcination at 900°C for 60 min). Profiles corresponding to 20 min (left) and 20 s (right) of carbonation.*

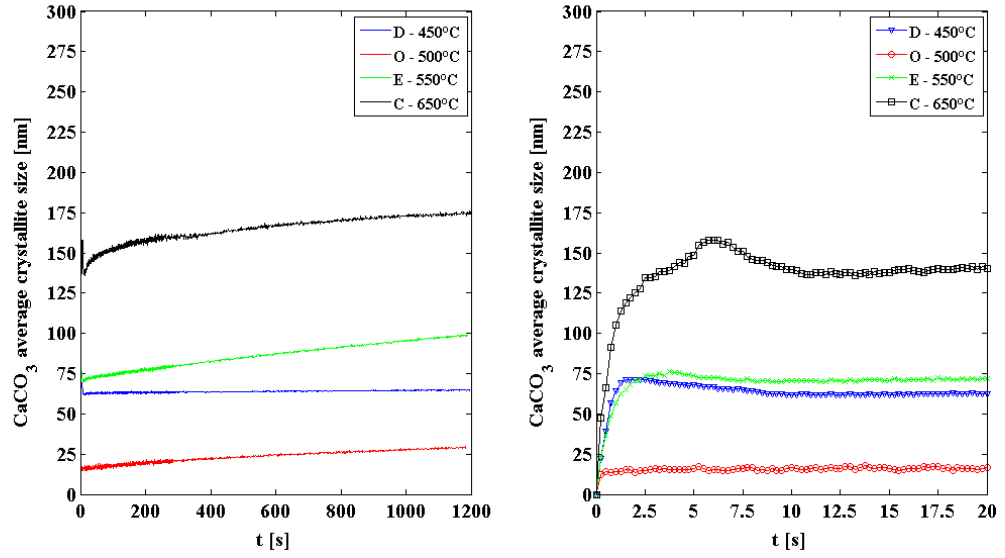

Figure 4.17: *$CaCO_3$ average crystallite size evolution for isothermal carbonation at different temperatures (calcination at 700°C for 60 min). Profiles corresponding to 20 min (left) and 20 s (right) of carbonation.*

According to these profiles, the carbonation temperature apparently contributes to the carbonate crystal growth insomuch as higher is the temperature maintained during the isothermal carbonation, higher is the final $CaCO_3$ average crystallite size measured after 20

min of reaction. Calcium carbonate crystalline domains with average size in the range between 120 and 180 nm were measured at the end of carbonations performed at 600 and 650°C (curves N and J in Figure 4.15 and curve C in Figure 4.17), while final sizes smaller than 100 nm are always observed for lower carbonation temperatures, namely at 450°C (curves A, I and D in Figure 4.15, 4.16, and 4.17 respectively), 500°C (curve F in Figure 4.15 and curve O in Figure 4.17) and 550°C (curves B, M and E in Figures 4.15, 4.16, and 4.17, respectively). Average crystallite size higher than 300 nm were also identified in $CaCO_3$ crystals produced after CO_2 absorption processes carried out at 650°C (curve H in Figure 4.16) and especially at 750°C (curve G in Figure 4.15). In Figure 4.18, the plot of the carbonate average size measured at the end of each experiment as a function of the carbonation temperature clearly underlines the effect of the temperature on the calcium carbonate crystallite size evolution.

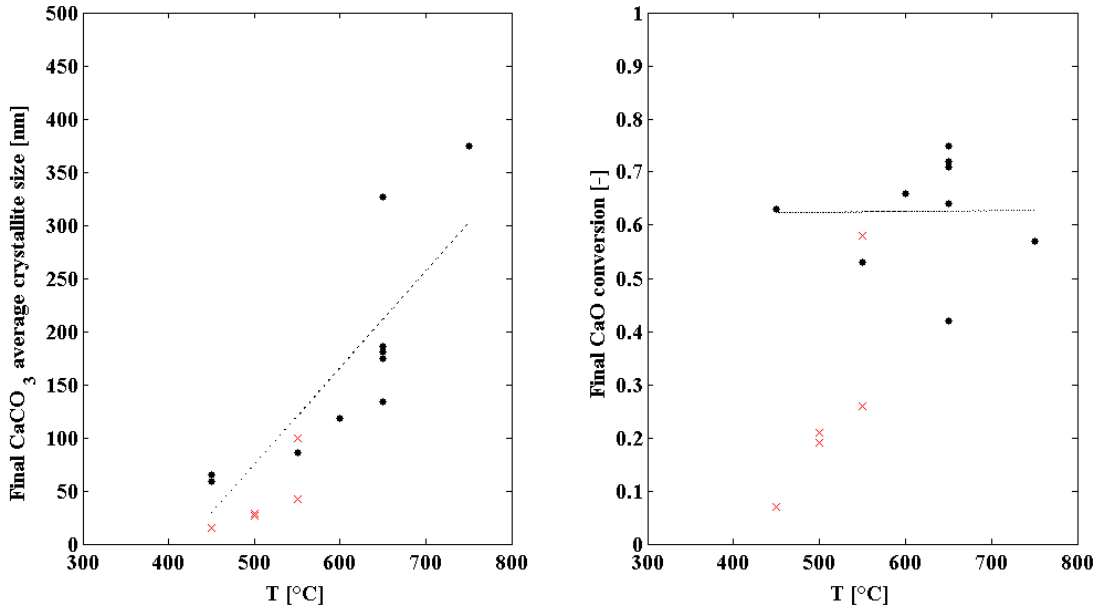

Figure 4.18: *Final $CaCO_3$ average crystallite size (left) and final CaO conversion (right) as a function of the carbonation temperature. Hypothetical linear correlations (dashed lines) assumed excluding experimental points that did not achieve reasonable values of the final conversion (red crosses).*

However, as emphasized assuming linear correlations (dashed lines in Figure 4.18), the dependence is not reproduced by the corresponding trend of the final CaO conversion (see Table 1) as a function of the carbonation temperature (evaluated excluding those

experiments that did not reach clearly a reasonable value of the maximum conversion at the end of the carbonation tests (red crosses in Figure 4.18)).

Therefore, the progressively increase of the carbonate crystallite size observable in almost all the profiles (Figures 4.15 - 4.17) cannot be ascribed to a simultaneous increase in the calcium oxide conversion that, after the transition to the slower carbonation period, is damped by the CO_2 diffusion through the carbonate product layer, as shown in Figures 4.5 - 4.7. More reasonably, a $CaCO_3$ crystal growth process occurs, mainly due to sintering phenomena that in turn are typically promoted by high temperature treatment. In particular, it is known that driving forces of sintering (e.g. solid state diffusion mechanisms) become relevant when the operating temperature exceeds the Tammann temperature of the material considered. In the case of $CaCO_3$, the Tammann temperature is around 500°C ([15]), and might explain the reason why, for carbonation temperature beyond this value, the increase of the crystallite size is still observable after the end of the CO_2 absorption experiments. However, as observed for the corresponding CaO conversion profiles, a straightforward comparison among different profiles as a function of only the carbonation temperature cannot be performed because, even though the samples were produced with the same (macroscopically) operating conditions during calcination, particle properties including initial CaO average crystallite size and porosity resulted different (see Tables 4.1 and 4.2), insomuch as in each of the Figures from 4.15 to 4.17 both the carbonation temperatures and the particle properties are different among different runs.

An additional comparison (originally focused to emphasize the effect of the initial calcium oxide average crystallite size on the evolution of the average size of $CaCO_3$ crystalline domains), was performed using the carbonate crystallite size versus time curves obtained from the isothermal carbonations carried out at temperatures of 650, 550 and 450°C, in which CaO sorbent samples with different values of the initial crystallite size were produced through different calcination conditions. The comparison is shown in Figures 4.19, 4.20 and 4.21 respectively. At a carbonation temperature of 650°C (Figure 4.19), CaO sorbents with an initial average crystallite size of about 30 nm (curves C, K and L) show a very similar trend, leading to $CaCO_3$ crystals with sizes of about 180 nm after 20 min of reaction, higher than the ones obtained with sorbent sample characterized by an initial average size of its crystalline domains of about 50 nm (about 130 nm, curve J), but clearly smaller respect the value measured using CaO sorbent particles with initial average

crystallite size of 250 nm (over 300 nm, curve H). A similar trend was observed for carbonation temperatures of 550°C (Figure 4.19) and 450°C (Figure 4.20) where particles with crystalline domains of about 40 nm (curves M, D and A) lead to carbonate products with final values of their crystallite size higher than those achieved by sorbent samples with initial CaO average crystallite sizes of 100 (curve B) and 124 nm (curve I) respectively.

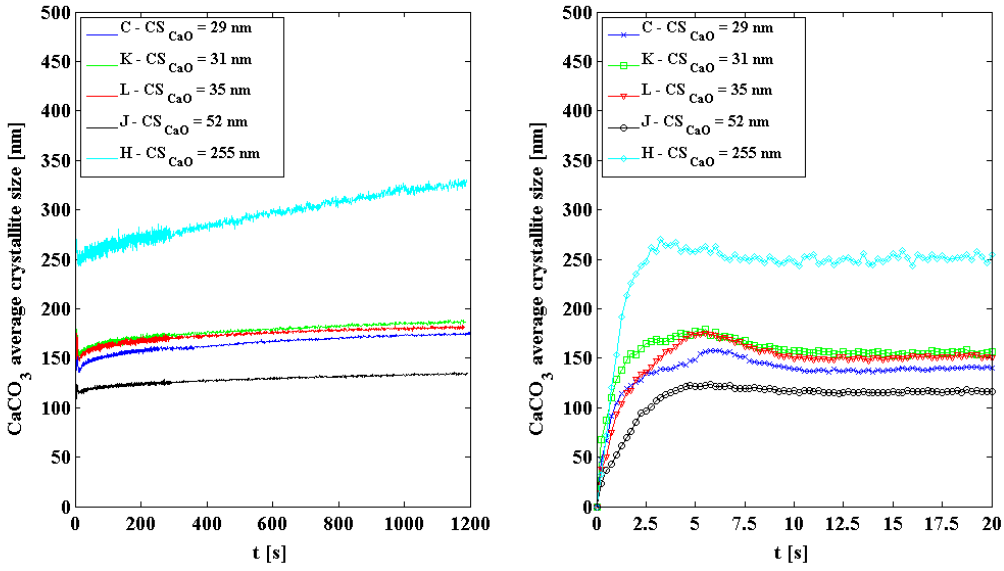

Figure 4.19: *$CaCO_3$ average crystallite size evolution for carbonation at 650°C using sorbents with different initial CaO crystallite size. Profiles corresponding to 20 min (left) and 20 s (right) of carbonation.*

Even though calcium oxide sorbents with a lower average crystallite size at the beginning of the carbonation reaction apparently determine higher final carbonate crystal sizes, the influence of the initial CaO crystallite size on the average size of the carbonate crystalline domains versus time curves is not so clear. Moreover, it has to be noted that an unambiguous comparison among all the profiles as a function of only the initial average crystallite of the calcium oxide particles cannot be performed neither in this case because, excluding the effects of the carbonation temperature, differences in the sorbent initial porosities are still present.

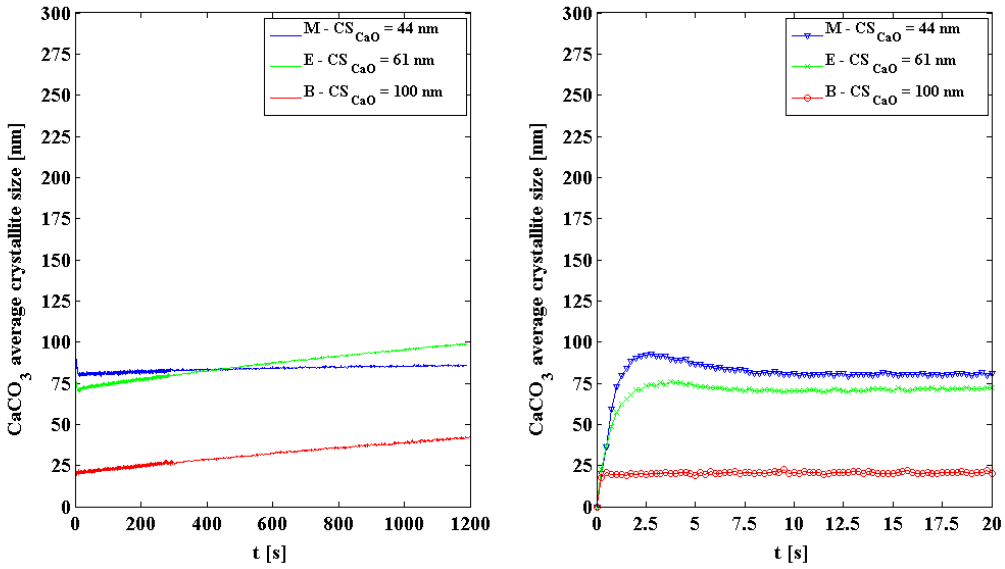

Figure 4.20: *$CaCO_3$ average crystallite size evolution for carbonation at 550°C using sorbents with different initial CaO crystallite size. Profiles corresponding to 20 min (left) and 20 s (right) of carbonation.*

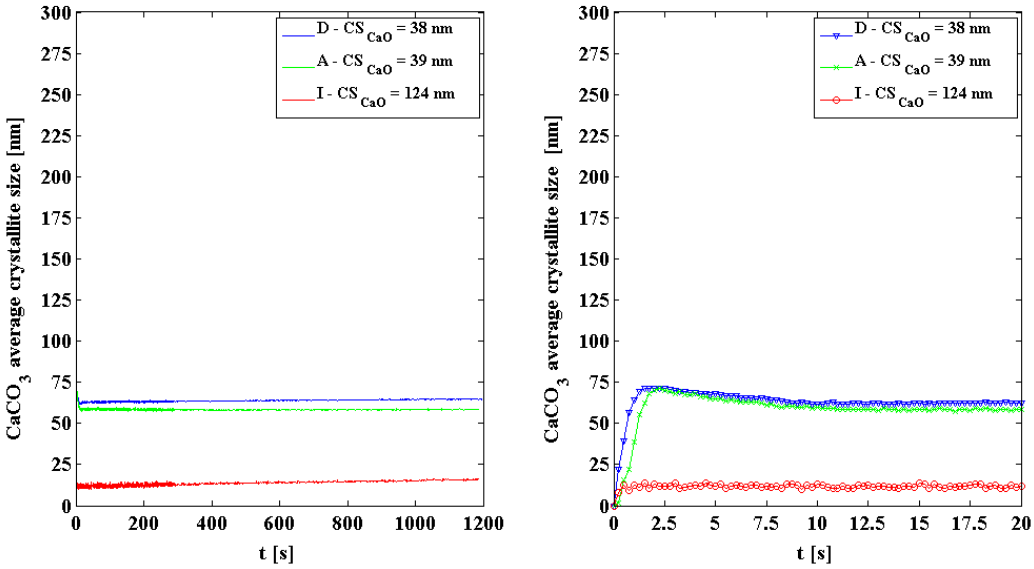

Figure 4.21: *$CaCO_3$ average crystallite size evolution for carbonation at 450°C using sorbents with different initial CaO crystallite size. Profiles corresponding to 20 min (left) and 20 s (right) of carbonation.*

4.3.1.6 Determination of $CaCO_3$ critical product layer thickness

The most evident feature revealed by the calcium carbonate crystallite size versus time curves is the marked change in the crystallite size growth rate. As observed, all the curves in Figures 4.15 - 4.17 and 4.19 - 4.21 show a characteristic trend that reflects the typical evolution of the carbonation reaction, with a fast initial $CaCO_3$ crystalline growth stage that proceeds up to a point where a sharp change in the carbonate crystal growth rate determines the transition to a second slower reaction period. This aspect, very similar to that one typically observed in the carbonation conversion versus time profiles, suggested therefore to compare the different $CaCO_3$ average crystallite size curves with the counterpart CaO conversion trends, leading to obtain an interesting result. Specifically, as shown for example in Figure 4.22 considering a carbonation experiment performed at 450°C (run A), it was observed that where the average $CaCO_3$ crystallite size reaches a (local) maximum value in its profile, it is possible to identify a corresponding value in the CaO conversion versus time curve (red dot in Figure 4.22) that reasonably represents the point marking the actual inception of the product layer diffusion controlled reaction regime, as well as, in some cases, the end of the fast carbonation period.

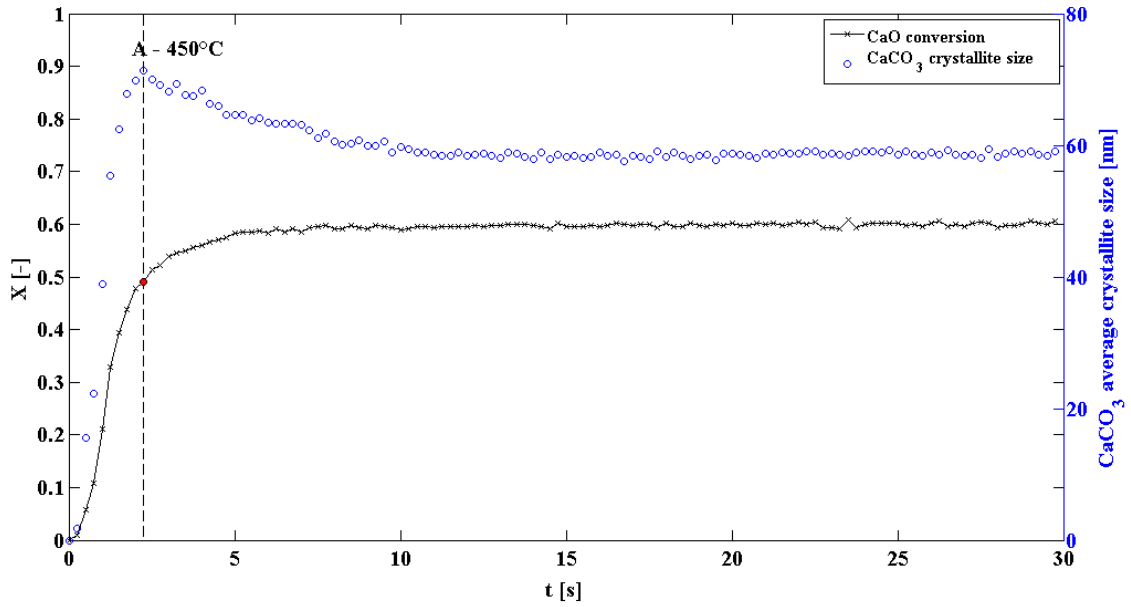

Figure 4.22: *Comparison between $CaCO_3$ average crystallite size and CaO conversion versus time curves (carbonation at 450°C). Example of evaluation for the critical carbonate product layer thickness.*

This feature is observable in almost all the experiments (see Appendix for additional plots) during the early instants of carbonation (approximately within the first 5 s), in the form of a peak in the $CaCO_3$ crystallite size versus time profile, with the exception of the tests in which the lowest values of the CaO conversion after 20 min of carbonation were measured (runs B, F, I and O), and in the data recorded for the CO_2 absorption process carried out at 750°C (run G). Nevertheless, also in these few cases an abrupt change in the crystal growth rate was observed and reasonably associated with the transition from the simultaneous chemical and diffusion controlled regime to the pure/product layer diffusion controlled stage.

The $CaCO_3$ crystallite size versus time curves show the mean size evolution of calcium carbonate crystallites that, as long as the CaO-CO_2 reaction proceeds, contribute to form the overall carbonate product layer. Therefore, the characteristic shape of the profiles can be explained supposing that, on average, $CaCO_3$ crystalline domains can grow during the first part of the carbonation until a maximum/critical size is achieved, and beyond which the growth of the newly formed carbonate crystals is damped because of the consumption of the free specific surface area initially available in the sorbent particles and the increase of the product layer diffusion resistance.

Even though it should be noted that the crystallite size measured by means of the X-ray data corresponds with the average diameter of coherently scattering domains present in a sample, and not with the size of the grains forming the sample itself, the values identified in this way looking at the features of the $CaCO_3$ crystallite size evolution during the first instants of reaction, can be assumed in any case as (average) values of calcium carbonate crystalline domains at which the CO_2 diffusion through the carbonate product layer becomes relevant in each of the carbonation experiment carried out. Consequently, they have also been assumed, in a first approximation, as the average values of the critical product layer thickness because, at least, $CaCO_3$ grains that actually form the product layer cannot be smaller than their constituent crystallites. The list of all the critical thicknesses (h) determined in this way is reported in Table 4.4 with the corresponding CaO conversion (X_h) at which each parameter was observed.

Similarly to what can be observed in the literature on the uncertainty concerning the existence of a single value for the critical product layer thickness, several different values of the product layer thickness were measured in this work.

Table 4.4: *Summary of the experimental results about $CaCO_3$ average crystallite sizes used as estimates of the critical carbonate product layer thickness (h) and the corresponding CaO conversion (X_h).*

Run	Critical $CaCO_3$ product layer thickness (h) [nm]	Corresponding CaO conversion (X_h) [-]
A	71 (± 3)	0.49
B	21 (± 3)	0.09
C	158 (± 5)	0.68
D	71 (± 3)	0.56
E	75 (± 3)	0.43
F	12 (± 2)	0.06
G	282 (± 8)	0.49
H	270 (± 8)	0.35
I	12 (± 8)	0.02
J	122 (± 7)	0.58
K	179 (± 5)	0.69
L	174 (± 5)	0.63
M	92 (± 3)	0.45
N	120 (± 3)	0.56
O	14 (± 3)	0.11

Even though a direct measurement of the pore size distribution for the sorbent samples used in each experiment was not available and the critical product layer thickness is typically related to the pore size distribution of the sorbent particles, mainly to the filling of the small pores ([15], [17]), in this work a comparison between the critical product layer thicknesses experimentally collected and the estimate of initial porosity of each calcium oxide sample was performed, as shown in Figure 4.23. However, from the plot it can be observed as the data look somehow scattered, insomuch as an evident correlation between the initial porosity available for the CaO samples and the average size of the $CaCO_3$ crystalline domains assumed as the critical carbonate product layer thickness (h) cannot be identified.

Therefore, it is not clear whether low values of the initial CaO sorbent porosity could be ascribed to fractions of large pores that could provide a larger space available for the

development of the product layer on the calcium oxide sorbent surface and for the consequent $CaCO_3$ crystal growth, especially till a point at which the product layer diffusion becomes the most relevant rate-controlling step for the CaO-CO_2 reaction.

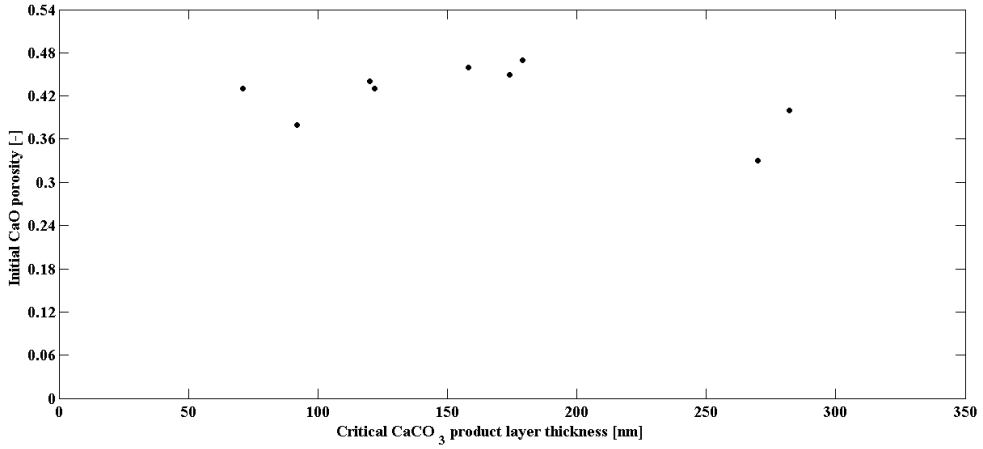

Figure 4.23: *Relationship between the critical average $CaCO_3$ product layer thickness and the initial porosity of CaO sorbent particles.*

4.3.1.7 Estimate of the specific surface area for the CaO sorbent particles

Appling a simple model that assumes a carbonate product layer of uniform thickness distributed over the entire surface area in the CaO sorbent particles, the experimental evidences discussed so far about the critical product layer thickness were used to estimate the specific surface area available for the carbonation during the initial (surface chemical) reaction stage.

As reported by some authors such as [53] and [60], taking into account the expansion of the solid sorbent particles associated with the molar volume increase from CaO to $CaCO_3$, the carbonate critical thickness (h, in nm) can be estimated, in a first approximation, from the conversion reasonably achieved by the sorbent sample at the end of the first stage of reaction (X_h) and the initial (at the beginning of the carbonation) specific surface area per unit of mass of CaO (S_0, in m^2/g) through the following relationship ([60]):

$$h = \frac{V_{CaCO_3}^m}{MW_{CaO}} \frac{X_h}{S_0} \times 10^3 \tag{4.6}$$

where $V_{CaCO_3}^m$ is the calcium carbonate molar volume (cm^3/mol) and MW_{CaO} is the molecular weight of calcium oxide. Therefore, rearranging Eq. (4.6), the specific surface area of solid sorbent at time zero (S_0) can be directly related to the critical product layer thickness (h) and the corresponding CaO conversion achieved:

$$S_0 = \frac{V_{CaCO_3}^m}{MW_{CaO}} \frac{X_h}{h} \times 10^3 \tag{4.7}$$

so that, using Eq. (4.7) and applying the experimental data previously discussed and reported in Table 4.4, an estimate of the specific surface area of calcium oxide sorbent particles at the beginning of the carbonation was performed. A summary of such calculated values is reported in Table 4.5, indicating moreover the maximum specific reaction rates experimentally measured from the CaO conversion profiles shown in § 4.3.1.1, and afterwards utilized to determine the intrinsic kinetics parameters of the carbonation reaction.

Table 4.5: *List of the estimated initial (at the beginning of carbonation) surface of calcium oxide sorbent particles and the maximum specific reaction rates calculated from the CaO conversion versus time profiles.*

Run	Specific reaction rate dX/dt/(1-X) [s^{-1}]	Initial CaO specific surface area [m^2/g]
A	0.496	4.52
B	0.242	(2.85)
C	0.240	2.84
D	0.650	5.17
E	0.468	3.77
F	0.239	(3.36)
G	0.113	1.14

H	0.235	0.85
I	0.040	(1.06)
J	0.203	3.12
K	0.234	2.54
L	0.342	2.39
M	0.424	3.21
N	0.383	3.07
O	0.314	(5.06)

In Figure 4.24, a plot of S_0 values calculated by means of the Eq. (4.7) as a function of the critical $CaCO_3$ average product layer measured is also shown.

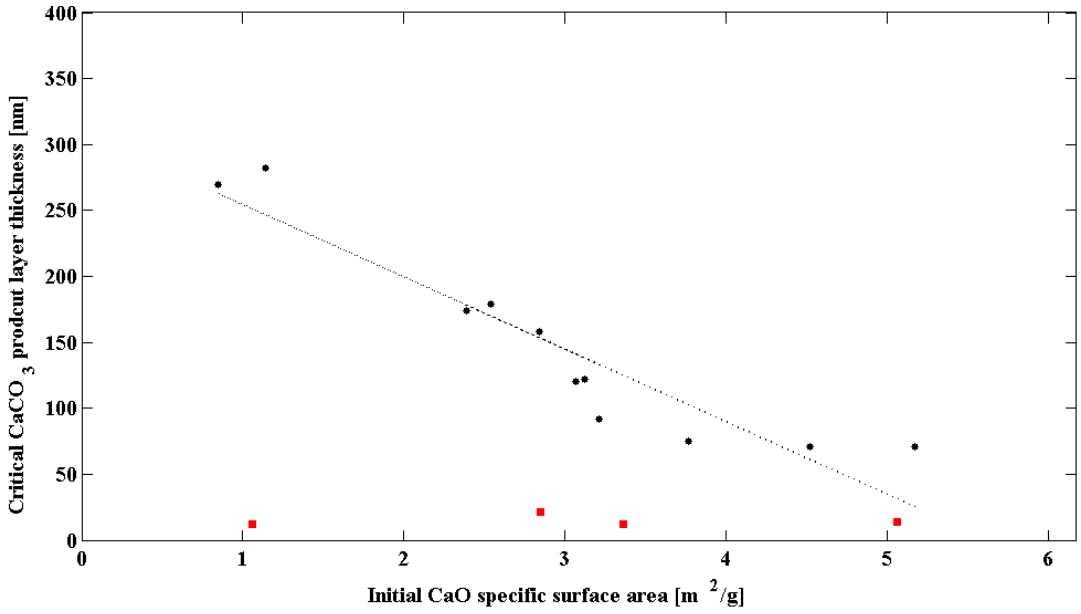

Figure 4.24: *Relationship between the critical $CaCO_3$ product layer thickness and the initial (at the beginning of carbonation) specific surface area characterizing CaO sorbent particles. Linear correlation (solid line) computed excluding runs that achieved low values of the final conversion (red squares, see Table 1).*

Even though Eq. (4.7) conveys an inverse proportionality between S_0 and h (not considering the effect of the conversion X_h), a few results, namely those obtained from experiments that achieved low values of the final CaO conversion (red squares in Figure 4.24; runs B, F, I and O in Tables 4.1 and 4.5 (values in brackets)), do not respect this

trend. Therefore, for this set of experiments it was supposed that X_h and/or h probably were not evaluated in the right way or, alternatively, that the carbonation reactions occurred in these specific runs did not involve the whole effective surface area available in the sorbent particles.

Excluding such data, a further relationship has been instead identified (as highlighted by the dashed line in Figure 4.24) and formalized through a linear fitting of the remaining calculated data. The correlation has led to the following expression:

$$h = -5.51 \times 10^{1} S_0 + 3.10 \times 10^{2} \tag{4.8}$$

by means of which, the relationship between the initial specific surface area of calcium oxide sorbent particles (S_0) and the critical carbonate product layer (h) becomes independent from the CaO conversion at which there is the transition between the two stages of carbonation, from the carbonation temperature maintained during each run and from the operating conditions used to produce the initial calcium oxide sorbent particles.

Additionally, the calculated values of S_0 have been compared with the values of the initial porosity of CaO sorbent particles (ε_0) already discussed (§ 4.3.1.2).

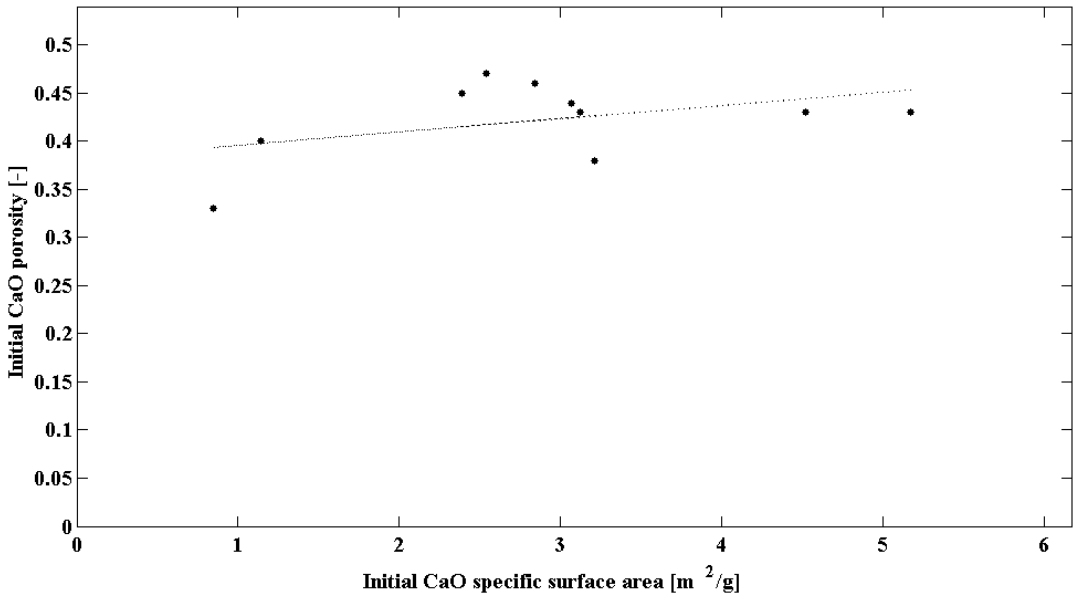

Figure 4.25: *Correlation between the initial (at the beginning of carbonation) specific surface area characterizing CaO sorbent particles and their counterpart porosity.*

Even though the data appear somehow scattered, a linear correlation between these two sets of data was imposed (dashed line in Figure 4.25), and formalized by the following expression:

$$\varepsilon_0 = 1.38 \times 10^{-2} S_0 + 3.82 \times 10^{-1} \quad (4.9)$$

Also in this case, the correlation is independent from both the temperature used during the isothermal carbonation experiments, and the operating conditions utilized for the calcination of the starting $CaCO_3$ samples. Moreover, since it is known that small pores determine higher specific surface areas, this result reasonably confirms that CaO sorbent particles with higher initial porosity values should be characterized by a larger fraction of small pores that, in turn, provide a smaller space available for the carbonate product layer growth.

4.3.1.8 Determination of (intrinsic) surface chemical reaction kinetics parameters

The estimate of the initial specific surface area of CaO sorbent particles obtained from the experimental data highlighted by the $CaCO_3$ average crystallite versus time profiles represents an important element that was utilized in order to complete the investigation of CaO conversion rates, especially in the determination of the kinetics parameters for the intrinsic surface chemical stage of the carbonation reaction. As shown, in addition to the monitoring of the average size evolution of the $CaCO_3$ crystalline domains during the carbonation reaction, the in-situ X-ray powder diffraction experiments has permitted a detailed analysis of the rapid first stage of the CaO-CO_2 reaction, that in turn has allowed to identify high conversion rates never measured before for the carbonation reaction using CaO based solid sorbents.

As previously mentioned, in the initial part of the first rapid stage of the carbonation (at low conversions), the measured reaction rate of the calcium oxide carbonation, usually defined as a specific rate (namely as the CaO conversion time derivative *dX/dt* divided by 1-*X*), is representative of the intrinsic reaction rate due to the surface chemical reaction, since the product layer diffusion can be neglected. When the reaction is under this kinetic-controlled regime, the specific rate (in s^{-1}) can be expressed in a power law form respect to

the CO_2 partial pressure, as a function of the specific surface area S of CaO sorbent particles, such as:

$$\frac{dX}{dt}\frac{1}{(1-X)} = k(P_{CO_2} - P_{CO_2}^{eq})^n SMW_{CaO} \tag{4.10}$$

with $k = k_0 \exp(-E_a / RT)$ being the Arrhenius rate constant (in mol/m^2 s), and $(P_{CO_2} - P_{CO_2}^{eq})$ being the reaction driving force (n is the reaction order), namely the difference between the operating CO_2 partial pressure and its equilibrium value at the carbonation temperature maintained during the CO_2 absorption experiment. Since the conversion time derivative at time zero (at the beginning of carbonation), which is equal to the maximum time derivative in grain models ([9]), is typically used in order to compare rates from different experiments, the values of the specific reaction rate at time zero were measured from the CaO conversion versus time profiles (§ 4.3.1.1). All these experimental data have been reported in Table 4.5.

At the beginning of the reaction (t = 0), the surface area S is then equal to the initial specific surface area S_0 of CaO sorbent particles so that, sustituting the molecular weight of calcium oxide (MW_{CaO} = 56 g/mol), Eq. (4.10) becomes:

$$\left.\frac{dX}{dt}\frac{1}{(1-X)}\right|_{t\to 0} = k(P_{CO_2} - P_{CO_2}^{eq})^n S_0 56 \tag{4.11}$$

or, in logarithmic form:

$$\ln K = \ln k + n\ln(P_{CO_2} - P_{CO_2}^{eq}) \tag{4.12}$$

where K is equal to $\frac{dX}{dt}\frac{1}{(1-X)}\frac{1}{S_0 56}$.

At this point, it can be noted that in order to calculate the specific reaction rate of CaO-CO_2 reaction by means of the application of Eq. (4.11) or, alternatively, to determine the reaction rate constant k (and afterwards the kinetics parameters) from Eq (4.12) using experimental data about the specific reaction rates of the first stage of carbonation,

information about S_0 is required. Since a direct measure of S_0 for the sorbent samples utilized in our carbonation experiments was not feasible, the estimate values provided by Eq. (4.7) as a function of the critical carbonate product layers were therefore considered and, combining the experimental data reported in Table 4.5, used in this work to calculate the kinetics parameters for the intrinsic carbonation reaction.

Specifically, applying the Arrhenius form and assuming $n = 0$ according to the already mentioned observation of Sun et al. (2008) ([9]) that noted how the CaO carbonation intrinsic kinetics can be described as a zero-order reaction respect to the CO_2 partial pressure (relative to the equilibrium partial pressure) when such quantity is equal or higher than 10 kPa, Eq. (4.12) is rewritten as:

$$\ln K = \ln k_0 - \frac{E_a}{RT} \tag{4.13}$$

Therefore, the two kinetics parameters, activation energy (E_a) and pre-exponential factor (k_0), were obtained by a linear fitting of the experimental data of K reported as a function of the carbonation temperature in a plot of ln$K$ versus 1/T, as shown in Figure 4.26.

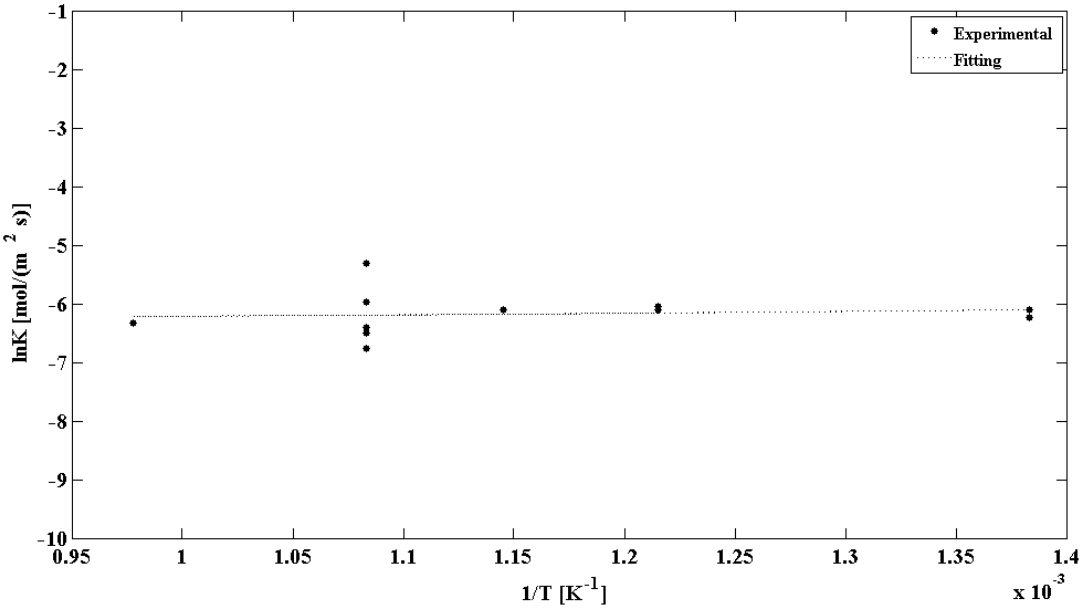

Figure 4.26: *Arrhenius plot for carbonation experiments performed in the temperature range between 450°C and 750°C with CO_2 partial pressure of 1 bar. CaO sorbent particles obtained through calcination of commercial calcium carbonate powder (particle size of 150 ÷ 160 μm).*

The linear fitting of the Arrhenius equation (4.12) led to obatain the parameters $k_0 = 1.50 \times 10^{-3}$ mol/m^2 s and $E_a = -2.36$ kJ/mol. Even though some authors assert that a zero-activation energy is rare and that, more likely, the activation energy for the carbonation is very small, close to zero but not actually zero, the value calculated in this work can be reasonably assumed, on the contrary, as a zero-activation energy estimate. Despite values of 78 kJ/mol ([12]), 29 kJ/mol ([9]), 21.3 kJ/mol and 19.2 kJ/mol ([10]) and, more recently, 30.2 kJ/mol ([22]) have been reported, our result is supported by Dennis and Hayhurst (1987) based on equilibrium analysis and calcination data ([16]), as well as by Bathia and Perlmutter (1983) who, in a kinetics study based on a random pore model of the initial stage of their carbonation data, determined a zero-activation energy for the CaO-CO_2 reaction in the kinetic-controlled regime ([15]).

In addittion, under the hypothesis of zero-order reaction (n = 0) respect to the reaction driving force $(P_{CO_2} - P_{CO_2}^{eq})$, it can be osserved that Eq. (4.10) should represent a linear expression of the specific reaction rate at time zero as a function of the specifi surface area of CaO sorbent particles at the beginning of the carbonation, with intercept equal to zero and slope equal to 56k, if only the Arrhenius reaction rate constant k is indipendent form the carbonation temperature (i.e. E_a = 0).

In Figure 4.27, a plot of the experimental specific reaction rate at time zero as a function of the calculated initial specific surface area characterizing CaO sorbent particles is shown. It points out that, in general, higher specific reaction rates can be achieved when higher is the initial specifc surface area of the CaO sorbent particles (S_0), and that a rather clear linear dependence exists and can be formalized by the following expression:

$$\frac{dX}{dt}\frac{1}{(1-X)} = 1.06 \times 10^{-1} S_0 + 3.14 \times 10^{-2} \tag{4.14}$$

If the intercept is approximated to zero, the slope, scaled by the molecular weight of calcium oxide, defines a new reaction rate constant namely $k = 1.89 \times 10^{-3}$ (mol/ m^2 s), which is essentially indipendent from the carbonation temperature.

Still assuming a zero-order reaction for CO_2 partial pressure and applying the estimated reaction rate constant in the Eq. (4.11), a comparison between the experimental data and those ones calculated was also performed. The result, shown in Figure 4.28, confirms a

good correspondence between experimental and calculated values of $\frac{dX}{dt}\frac{1}{(1-X)}$, and helps to explain the trend of the specific reaction rate respect to the temperature used during the isothermal carbonation experiments, as can be observed in Figure 4.28.

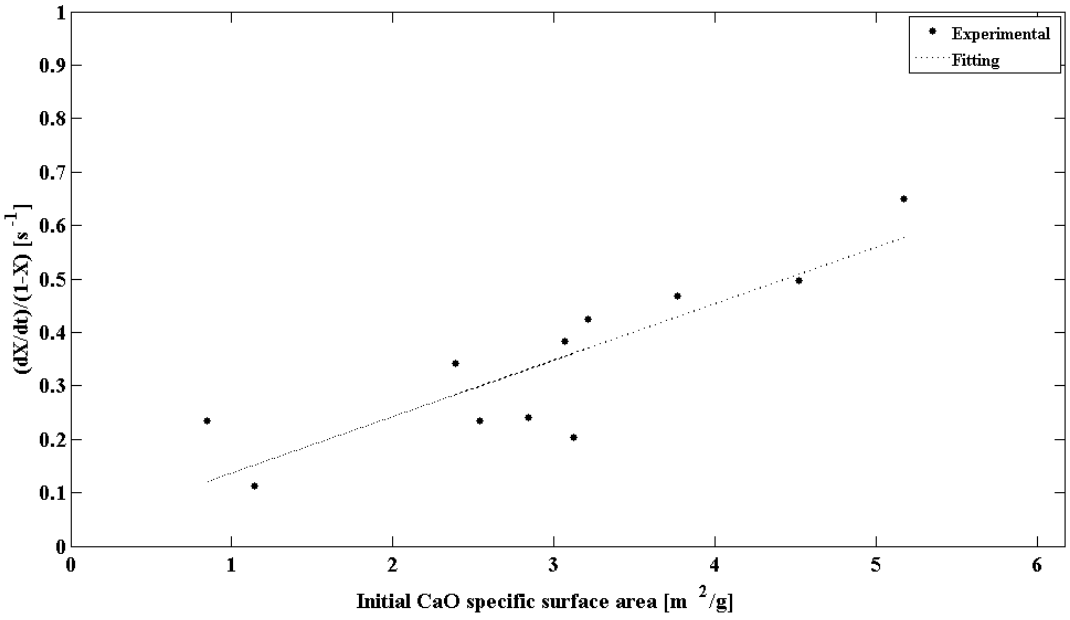

Figure 4.27: *Relationship between the initial (at the beginning of carbonation) specific surface area characterizing CaO sorbent particles and the experimental specific reaction rate at time zero. Linear correlation (solid line) obtained excluding runs that achieved low values of the final conversion (see values in brackets in Table 4.1 and Table 4.5).*

It can be concluded that the specific reaction rate at time zero is affected by the specific surface area of CaO sorbent particles available for CO_2 absortion at the beginning of the reaction. Considering the broad range of values for the specific surface area observable in the literature and discussed in § 2.4.1.4, the values of S_0 computed in this work are in agreement with those ones resulting from the thermal decomposition of calcium carbonate carried out under very stringent operating conditions (i.e. high temperatures, high residence time and stagnat/no-inert atmosphere) that promote sintering phenomena, as mentioned in some contributions such as [84], [85] or [82].

However, it has to be noted that some of the S_0 identified are low, and looking at both the calcination condition used in the experiments described and CaO conversion versus time

profiles, sintering effects reasonably occurred during the calcination stages could not explain by themselves such small specific surfaces.

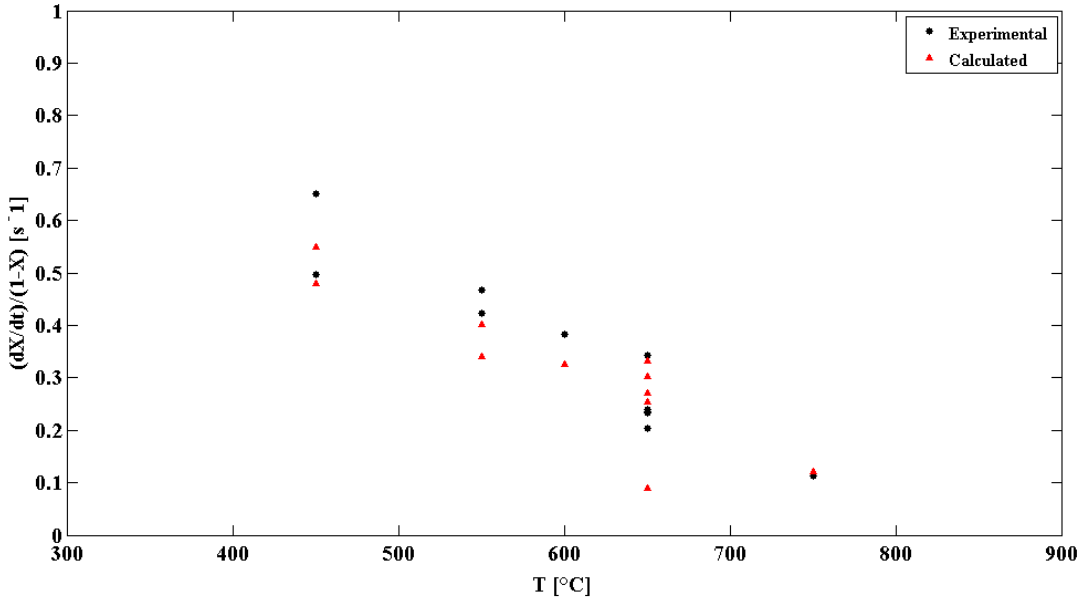

Figure 4.28: *Specific reaction rate as a function of the carbonation temperature. Comparison between the experimental data and values calculated applying Eq. (4.11) with zero-order respect the CO_2 partial pressure and the estimated temperature-independent reaction rate constant.*

An additional explanation of such low specific surfaces could be found assuming that the specific surface area calculated applying Eq. (4.7) and using the experimental data about the critical $CaCO_3$ product layer thickness, probably provides an estiamte of only the active (not the total) specific surface area of sorbent particles. In particular, the concept of active surface area can reasonably find a support in the rate equation theory proposed by Li et al. (2012), by means of which the authors investigated the nucleation and growth of $CaCO_3$ product during the carbonation reaction of CaO with CO_2 ([21]). For calcium oxide carbonation the first stage of reaction is characterized by critical steps including, in addition to the surface reaction, the nucleation and growth of $CaCO_3$ product on CaO surface. Specifically, they described the formation of $CaCO_3$ crystals through a mechanism based on the evolution of carbonate product islands, consisting in clusters of $CaCO_3$ molecules/crystallites distributed over the surface of CaO particles , whose size is typically controlled by surface, grain boundary and lattice diffusion processes ([21]). Since the nucleation of solid product is a key step for a gas-solid reaction, it can be hypothesized that

the active surface area identified in thi work could corresponde to the nucleation points where calcium carbonate crystallites/product islands initially form and afterwards grow. In support to this theory, it should be noted that, among their results, Li et al. (2012) observed that with the increasing of carbonation temperature, the product island density (approximately the number of carbonate molecule clusters per unit of specific surface of CaO) decrease while the $CaCO_3$ island size increase ([21]).

As shown in Figure 4.29, a comparable trend can be observed assuming, for similarity, the initial active surface area as the nucleation points in the CaO sorbent particles where the product islands start to form, and the critical crystallite size of $CaCO_3$ as the average size of these islands.

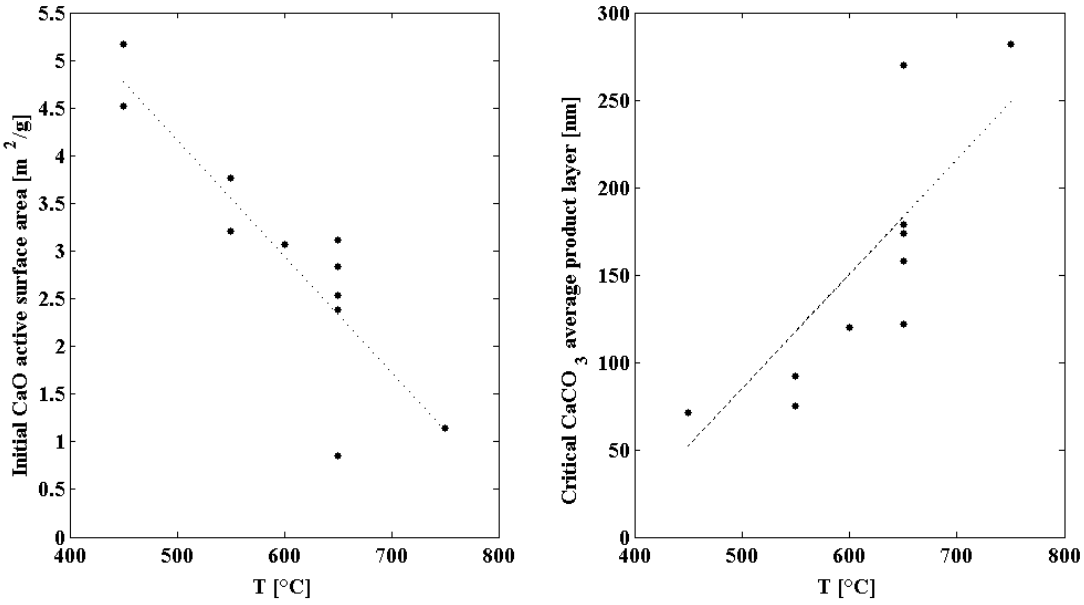

Figure 4.29: *Effect of the carbonation temperature on the estimate of both (initial) active specific surface area (right) and critical $CaCO_3$ product layer thickness (left).*

According to these trends (dashed lines in Figure 4.29), higher is the carbonation temperature, lower is the (initial) active surface area estimated from each experiment, while higher is the average size of the $CaCO_3$ crystallite domains that constitute the product layer. Therefore, it could be assumed that the initial active surface areas estimated in this work is reasonably related to the available surface of solid reactant where the direct formation/nucleation of carbonate product islands actually occurs. In these terms, such

result could support the rate equation theory as a physical explanation of the mechanism involved during the $CaO\text{-}CO_2$ reaction.

Conclusions and future perspectives

The research project summarized in this work of thesis consists of an experimental study focused on the investigation/characterization of calcium based solid sorbents that can be used in a promising carbon dioxide capture technology in the Carbon Capture and Storage (CCS) context. Even though the technique, which is based on the reversible reaction $CaO_{(s)} + CO_{2(g)} \leftrightarrow CaCO_{3(s)}$, is widely discussed in the literature (e.g. [7], [8]), the improvement of this technology and the development of new calcium-based solid sorbents are currently a matter of study.

In particular, this research project started from the consideration that several aspects of the carbonation reaction and its kinetics were still not clearly understood and needed to be clarified, including:

i. The determination of the surface reaction kinetic parameters from experimental data (i.e. CaO conversion versus time curves) whose quality is not affected by mass transfer limitations (mainly external gas diffusion), which still affect the most of TGA instruments typically used to perform kinetic investigation of the CO_2 absorption process.
ii. The characterization of the dependence of carbonation kinetics on the calcium oxide and calcium carbonate average crystallite size, and the estimated of the impact that these features of crystalline species have on the sorbent performances.

Although the thermo-gravimetric approach is actually widely used and discussed in the literature when referring to the investigation of the carbonation reaction (e.g. [11], [12], [9], [10]) and was initially applied in this study as well, the X-ray powder diffraction technique has been preferred, alternatively to the TGA analysis, to characterize CaO-based sorbent and their carbonation kinetics.

In particular, noteworthy results have been obtained through the time-resolved synchrotron radiation X-ray powder diffraction (SR XRPD) technique, which was applied for the first time to the CO_2 carbonation reaction to investigate the kinetics of the chemical transformations during the CO_2 absorption process and to simultaneously measure the calcium oxide and calcium carbonate crystallite sizes. Specifically, CaO conversion profiles were estimated applying the Rietveld refinement method on the synchrotron X-ray

diffraction data collected at the beamline 17-BM-B of the Advanced Photon Source (APS) at the Argonne National Laboratory.

The study of the carbonation curves (obtained in the temperature range between 450°C and 750°C, at a CO_2 partial pressure of 1 bar) has pointed out that the reaction rates of the characteristic rapid first stage of the carbonation are surprisingly higher than the typical values reported in the literature, obtained by TGA. An average maximum conversion time derivative of about 0.280 s^{-1} (± 13.2% of standard deviation) was observed, which is about five times higher than the values thus far reported in literature (e.g. [15], [11], [12], or [9]). This result highlights that the capillary system/flow cell furnace used to carry out the CO_2 absorption experiments allowed to minimize (up to probably eliminate) the external mass transfer limitations that instead likely affected the CaO carbonation results obtained by TGA. The external mass transfer limitations were minimized thanks to the high gas velocity around the CaO sorbent particles that reasonably supported the high CO_2 consumption rate due to the surface chemical reaction. Therefore, it can be stated that the experimental data (conversion-time curves) presented in this work represent the intrinsic chemical kinetics of the carbonation reaction (due to surface chemical reaction).

Additionally, the dependence of the conversion-time curves on the initial (at the beginning of carbonation) crystallite size was investigated. Specifically, the final conversion of the calcium oxide particles was compared with the average size of the CaO crystalline domains measured at the beginning of the carbonation reaction. The comparison has shown that the lower is the initial average crystallite size of the fresh calcium oxide, the higher is the conversion of the sorbent particles evaluated at the end of the absorption experiments. The obtained linear relationship between the final conversion and the initial CaO crystallite size was found to be independent from both the carbonation temperature maintained during the experiments and from the operating conditions used to produce the initial CaO sorbent particles from commercial calcium carbonate. Consequently, the initial CaO crystallite size is likely a good indicator of the initial particle porosity, which determines the final maximum conversion reachable. An hypothesis was also formulated to explain the dependence of inverse proportionality between the initial/maximum conversion rates and the initial CaO crystallite size. According to such hypothesis, small CaO crystallites imply a high crystallite boundary length per unit of (internal) surface area, which would determine a high number of active sites for the carbonation, namely a high active specific

surface area, and consequently a high conversion rate. The time-resolved X-ray powder diffraction was also applied to investigate the chemical transformations occurring during the CO_2 absorption process and their effects on the carbonation kinetics. Specifically, the evolution of the average size of $CaCO_3$ crystalline domains was analyzed. The most evident feature revealed by the calcium carbonate crystallite size versus time curves has been the marked change in the crystallite size growth rate that reflects the typical evolution of carbonation reaction, with a fast initial $CaCO_3$ crystalline growth stage that proceeds up to a turning point where a sharp change in the carbonate crystal growth rate determines the transition to the reaction stage controlled by the product layer diffusion regime. It has been observed that where there is an abrupt change in the $CaCO_3$ crystallite profile, it is possible to identify a corresponding value in the CaO conversion versus time curve that can be reasonably assumed as the end of the first stage of carbonation. This feature has been used to estimate average values of the critical product layer thickness, assuming that this thickness cannot be larger than the average size of the calcium carbonate crystalline domains forming the product layer itself.

The simultaneous study of the carbonation curves and the corresponding $CaCO_3$ crystallite size versus time profiles has additionally pointed out that $CaCO_3$ crystal growth processes occur during the carbonation reaction, probably due to sintering phenomena, so that the progressive increase of the carbonate crystallite size typically observed as long as the carbonation proceeds cannot be ascribed to a simultaneous increase in the calcium oxide conversion that, after the transition to the slower carbonation period, is damped by the CO_2 diffusion through the carbonate product layer.

Afterwards, the carbonate product layer thickness estimates have been used to determine the specific surface area available for the carbonation reaction during the early instants of the fast (surface chemical) reaction stage. Linear correlations between the specific surface area of CaO sorbent particles (at the beginning of carbonation) and both the initial CaO porosity and the critical product layer thickness have been calculated, highlighting to be independent from the CaO conversion at which there is the transition between the two reaction stages, as well as from the temperature applied during the isothermal CO_2 absorption tests and the operating conditions used to produce the starting calcium oxide sorbent particles. Moreover, the indirect estimate of such specific surface areas allowed to determine the kinetic parameters for the intrinsic surface chemical stage of the carbonation

reaction. Specifically, combining the specific reaction rates (at time zero) with the specific surface areas resulted from the critical product layer values measured, allowed to calculated a new reaction rate constant of about 1.89×10^{-3} (mol/ m^2 s), which is essentially independent from the carbonation temperature and a zero-activation energy was found.

Finally, an hypothesis was formulated to explain the low values estimated for the initial specific surface area of our CaO sorbent particles (excluding effects due to sintering). According to such hypothesis, the CaO-CO_2 reaction could be likely described by the rate equation theory proposed by Li et al. (2012) ([21]), so that the specific surface areas calculated from the X-ray diffraction experiments could correspond to the active sites for the carbonation, namely the nucleation points where calcium carbonate crystallites initially forms as product islands and afterwards grow. In these terms, an estimate of only the active specific surface area has been provided. However, this hypothesis need to be further elucidated and validated in order to clarify the mechanisms involved in the CaO-CO_2 reaction.

The study summarized in this work of thesis have opened new perspectives in the investigation of a gas-solid reaction such as the CaO carbonation, especially considering the utilization of X-ray powder diffraction technique in the reaction kinetics characterization. Even though novel results have been presented concerning the relationship between the reaction kinetics and the evolution of CaO/$CaCO_3$ average crystallite sizes, additional aspects referred to the CaO-CO_2 reaction could be considered in a future research.

Since it has been demonstrated that the flow cell/capillary system applied during the SR-XRPD experiments allows to reduce external mass transfer resistances, a similar investigation of the calcium oxide carbonation reaction performed with the described technique in a wider range of CO_2 partial pressures could be useful to validate the information thus far reported about the reaction order respect to the CO_2 partial pressure maintained during the carbonation process.

Moreover, a more general correlation between morphological properties (i.e. specific surface area and/or porosity) and structural features (i.e. crystallize size) of fresh calcined CaO sorbent particles should be studied in-depth, especially combining ex-situ X-ray

diffraction analysis and N_2 adsorption measurements (i.e. BET method) on sorbent samples produced from calcination stages carried out in a wide range of operating conditions.

Finally, another interesting area of investigation could be the monitoring of the carbonate product layer formation during the absorption stage through the Hard X-ray nanotomography technique. Nanotomography is a rather novel approach ([109], [110]), which have never been utilized before for the CaO-based sorbents investigation, and it can be reasonably considered particularly useful for studying changes of the porous morphology of CaO sorbent particles both due to the marked decrease in the molar volume achieved during the thermally induced transition from the carbonate to the oxide, and to the carbonate product layer formation that occurs during the carbonation process. Specifically, analyzing CaO sorbent samples with specific extents of conversion previously obtained by CO_2 absorption experiments, it would be possible to understand the spatial distribution of the solid phases (namely CaO and $CaCO_3$) inside the sorbent particles, clarifying the structural/morphological changes at which sorbent particles have been subjected because of the carbonation reaction.

References

[1] B. Metz, “IPCC special report on carbon dioxide capture and storage”. C*ambridge University Press for the Intergovernmental Panel on Climate Change*, 2005.

[2] L. Bernstein, R. K. Pachauri, A. Reisinger, “Climate Change 2007: Synthesis Report”. IPCC, *Cambridge University Pres for the Intergovernmental Panel on Climate Change s*, 2008.

[3] R. K. Pachauri, “Climate Change 2014: Synthesis Report”. IPCC, *Cambridge University Press for the Intergovernmental Panel on Climate Change*, 2014.

[4] J. Ciferno, J. Litynski, S. Plasynski, and J. Murphy, “DOE/NETL carbon dioxide capture and storage RD&D roadmap,” 2010.

[5] B. Stanmore and P. Gilot, “Review - calcination and carbonation of limestone during thermal cycling for CO_2 sequestration,” *Fuel Process. Technol.*, vol. 86, pp. 1707–1743, 2005.

[6] J. Blamey, E. J. Anthony, J. Wang, and P. S. Fennell, “The calcium looping cycle for large-scale CO_2 capture,” *Prog. Energy Combust. Sci.*, vol. 36, no. 2, pp. 260 - 279, Apr. 2010.

[7] C. C. Dean, J. Blamey, N. H. Florin, M. J. Al-Jeboori, and P. S. Fennell, “The calcium looping cycle for CO_2 capture from power generation, cement manufacture and hydrogen production,” *Chem. Eng. Res. Des.*, vol. 89, no. 6, pp. 836 - 855, Jun. 2011.

[8] A. Kierzkowska, R. Pacciani, and C. Müller, “CaO-based CO_2 Sorbents - from fundamentals to the development of new, highly effective materials,” *ChemSusChem*, vol.6, pp. 1130 -1148, 2013.

[9] P. Sun, J. Grace, C. Lim, and E. Anthony, “Determination of intrinsic rate constants of the CaO-CO_2 reaction,” *Chem. Eng. Sci.*, vol. 63, pp. 47 - 56, 2008.

[10] G. Grasa, R. Murillo, M. Alonso, and J. C. Abanades, “Application of the random pore model to the carbonation cyclic reaction,” *AIChE J.*, vol. 55, no. 5, pp. 1246 - 1255, May 2009.

[11] K. Kyaw and M. Kanamori, “Study of Carbonation Reactions of Ca-Mg Oxides for High Temperature Energy Storage and Heat Transformation.,” *J. Chem. Eng. of Japan,* vol.29, no. 1, pp. 112 -118, 1996.

[12] K. Kyaw, M. Kubota, and F. Watanabe, “Study of Carbonation of CaO for high temperature thermal energy storage,” *J. Chem. Eng. of Japan*, vol. 31, no. 2, pp. 281 - 284, 1998.

[13] B. Khoshandam, R. V. Kumar, and L. Allahgholi, "Mathematical modeling of CO_2 removal using carbonation with CaO: The grain model," *Korean J. Chem. Eng.*, vol. 27, no. 3, pp. 766–776, Mar. 2010.

[14] D. Lee, "An apparent kinetic model for the carbonation of calcium oxide by carbon dioxide," *Chem. Eng. J.*, vol. 100, no. 1–3, pp. 71–77, Jul. 2004.

[15] S. K. Bhatia and D. D. Perlmutter, "Effect of the product layer on the kinetics of the CO_2-lime reaction," *AIChE J.*, vol. 29, no. 1, pp. 79–86, 1983.

[16] J. S. Dennis and A. N. Hayhurst, "the effect of CO_2 on the kinetics and extent of calcination of limestone and dolomite particles in fluidised beds," *Chem. Eng. Sci.*, vol. 42, no. 10, pp. 2361–2372, 1987.

[17] P. Sun, J. Grace, C. Lim, and E. Anthony, "A discrete-pore-size-distribution-based gas–solid model and its application to the CaO+CO_2 reaction," *Chem. Eng. Sci.*, vol. 63, pp. 57–70, 2008.

[18] Y. S. Yu, W. Q. Liu, H. An, F. S. Yang, G. X. Wang, B. Feng, Z. X. Zhang, and V. Rudolph, "Modeling of the carbonation behavior of a calcium based sorbent for CO_2 capture," *Int. J. Greenh. Gas Control*, vol. 10, pp. 510–519, Sep. 2012.

[19] Z. Zhou, P. Xu, M. Xie, Z. Cheng, and W. Yuan, "Modeling of the carbonation kinetics of a synthetic CaO-based sorbent," *Chem. Eng. Sci.*, vol. 95, pp. 283–290, May 2013.

[20] P. J. Chupas, K. W. Chapman, C. Kurtz, J. C. Hanson, P. L. Lee, and C. P. Grey, "A versatile sample-environment cell for non-ambient X-ray scattering experiments," *J. Appl. Crystallogr.*, vol. 41, no. 4, pp. 822–824, Jul. 2008.

[21] Z. Li, H. Sun, and N. Cai, "Rate Equation Theory for the Carbonation Reaction of CaO with CO_2," *Energy & Fuels*, vol. 26, no. 7, pp. 4607–4616, Jul. 2012.

[22] S. F. Wu and P. Q. Lan, "A kinetic model of nano-CaO reactions with CO_2 in a sorption complex catalyst," *AIChE J.*, vol. 58, no. 5, pp. 1570–1577, May 2012.

[23] L. Rouchon, L. Favergeon, and M. Pijolat, "Analysis of the kinetic slowing down during carbonation of CaO by CO_2," in *Journal of Thermal Analysis and Calorimetry*, 2013, vol. 113, no. 3, pp. 1145–1155.

[24] S. Dottor, "Utilization of calcium-magnesium based solid sorbents for high temperature CO_2 capture," University of Padova, 2012.

[25] A. Benedetti, "Investigation of the CO_2 carbonation reaction: kinetic models, CFD simulations and thermogravimetric data analysis," (*Confidential Information*) University of Padova, 2014.

[26] T. Stocker and D. Qin, “Climate change 2013: The physical science basis,” *Cambridge University Press,* 2013.

[27] U.S. Energy Information Amministration, “EIA Outlook 2013.” .

[28] H. Yang, Z. Xu, M. Fan, and R. Gupta, “Progress in carbon dioxide separation and capture: A review,” *J. Environ. Sci.*, vol. 20, pp. 14–27, 2008.

[29] J. D. Figueroa, T. Fout, S. Plasynski, H. McIlvried, and R. D. Srivastava, “Advances in CO_2 capture technology - The U.S. Department of Energy’s Carbon Sequestration Program,” *Int. J. Greenh. Gas Control*, vol. 2, no. 1, pp. 9–20, Jan. 2008.

[30] W. Parsons, “Strategic Analysis of the Global Status of Carbon Capture and Storage,” *Global CCS Institute*, 2009.

[31] C. H. Yu, “A Review of CO_2 Capture by Absorption and Adsorption,” *Aerosol Air Qual. Res.*, pp. 745–769, 2012.

[32] Q. Wang, J. Luo, Z. Zhong, and A. Borgna, “CO_2 capture by solid adsorbents and their applications: current status and new trends,” *Energy Environ. Sci.*, vol. 4, no. 1, p. 42, 2011.

[33] L. S. Fan and F. Li, “Chemical Looping Technology and Its Fossil Energy Conversion Applications,” *Ind. Eng. Chem. Res.*, vol. 49, no. 21, pp. 10200–10211, Nov. 2010.

[34] P. C. Chiu, “Chemical Looping Process - A Novel Technology for Inherent CO_2 Capture,” *Aerosol Air Qual. Res.*, pp. 1421–1432, 2012.

[35] T. Shimizu, T. Hirama, and H. Hosoda, “A twin fluid-bed reactor for removal of CO_2 from combustion processes,” *Trans IChemE*, vol. 77, January, 1999.

[36] E. H. Baker, “The calcium oxide-carbon dioxide system in the pressure range 1-300 atmospheres,” *J. Chem. Soc.*, pp. 464–470, 1962.

[37] G. Grasa, J. Abanades, M. Alonso, and B. Gonzalez, “Reactivity of highly cycled particles of CaO in a carbonation/calcination loop,” *Chem. Eng. J.*, vol. 137, no. 3, pp. 561–567, Apr. 2008.

[38] J. Abanades, “The maximum capture efficiency of CO_2 using a carbonation/calcination cycle of $CaO/CaCO_3$,” *Chem. Eng. J.*, vol. 90, pp. 303–306, 2002.

[39] G. S. Grasa and J. C. Abanades, “CO_2 Capture Capacity of CaO in Long Series of Carbonation/Calcination Cycles,” *Ind. Eng. Chem. Res.*, vol. 45, no. 26, pp. 8846–8851, 2006.

[40] J. Wang, V. Manovic, Y. Wu, and E. J. Anthony, "A study on the activity of CaO-based sorbents for capturing CO_2 in clean energy processes," *Appl. Energy*, vol. 87, no. 4, pp. 1453–1458, Apr. 2010.

[41] J. W. Butler, C. J. Lim, and J. R. Grace, "CO_2 capture capacity of CaO in long series of pressure swing sorption cycles," *Chem. Eng. Res. Des.*, vol. 89, no. 9, pp. 1794–1804, Sep. 2011.

[42] P. Sun, J. Grace, C. Lim, and E. Anthony, "The effect of CaO sintering on cyclic CO_2 capture in energy systems," *AIChE J.*, vol. 53, no. 9, 2007.

[43] D. Alvarez, M. Pena, and A. Borrego, "Behavior of different calcium-based sorbents in a calcination/carbonation cycle for CO_2 capture," *Energy & fuels*, vol. 21, no. 3, pp. 1534–1542, 2007.

[44] B. Feng, W. Liu, X. Li, and H. An, "Overcoming the problem of loss-in-capacity of calcium oxide in CO_2 capture," *Energy & Fuels*, no. 12, pp. 2417–2420, 2006.

[45] V. Manovic, J.-P. Charland, J. Blamey, P. S. Fennell, D. Y. Lu, and E. J. Anthony, "Influence of calcination conditions on carrying capacity of CaO-based sorbent in CO_2 looping cycles," *Fuel*, vol. 88, no. 10, pp. 1893–1900, Oct. 2009.

[46] V. Manovic, E. J. Anthony, and D. Loncarevic, "looping cycles with CaO-based sorbent pretreated in at high temperature," *Chem. Eng. Sci.*, vol. 64, no. 14, pp. 3236–3245, Jul. 2009.

[47] V. Manovic and E. J. Anthony, "Sintering and Formation of a Nonporous Carbonate Shell at the Surface of CaO-Based Sorbent Particles during CO_2 -Capture Cycles," *Energy & Fuels*, vol. 24, no. 10, pp. 5790–5796, Oct. 2010.

[48] N. Florin and A. Harris, "Screening CaO-based sorbents for CO_2 capture in biomass gasifiers," *Energy & fuels*, no. 3, pp. 2734–2742, 2008.

[49] J. Criado, M. González, J. Málek, and A. Ortega, "The effect of the CO_2 pressure on the thermal decomposition kinetics of calcium carbonate," *Thermochim. Acta*, 1995.

[50] I. Barin, O. Knacke, and O. Kubaschewski, "Thermochemical properties of inorganic substances: supplement", *Springer-Verlag*, 1977.

[51] R. Harker and O. Tuttle, "Studies in the system CaO-MgO-CO_2; Part 1, Thermal dissociation of calcite, dolomite and magnesite," *Am. J. Sci.*, vol. 235, pp. 209-244, 1955.

[52] O. Knacke, O. Kubaschewski, and K. Hesselmann, "Thermochemical properties of inorganic substances ", *Springer-Verlag*, 1991.

[53] R. Barker, "The reversibility of the reaction $CaCO_3 \rightleftarrows CaO+CO_2$," *J. Appl. Chem. Biotechnol.*, vol. 23, no. 10, pp. 733–742, Apr. 1973.

[54] S. K. Bhatia and D. D. Perlmutter, "A random pore model for fluid-solid reactions: I. Isothermal, kinetic control," *AIChE J.*, vol. 26, no. 3, pp. 379–386, 1980.

[55] S. K. Bhatia and D. D. Perlmutter, "A random pore model for fluid-solid reactions: II. Diffusion and transport effects," *AIChE J.*, vol. 27, no. 2, pp. 247–254, 1981.

[56] S. K. Bhatia, "Analysis of distributed pore closure in gas-solid reactions," *AIChE J.*, vol. 31, no. 4, pp. 642–648, 1985.

[57] W. Liu, J. S. Dennis, D. S. Sultan, S. a. T. Redfern, and S. a. Scott, "An investigation of the kinetics of CO2 uptake by a synthetic calcium based sorbent," *Chem. Eng. Sci.*, vol. 69, no. 1, pp. 644–658, Feb. 2012.

[58] D. Mess, A. Sarofim, and J. Longwell, "Product layer diffusion during the reaction of calcium oxide with carbon dioxide," *Energy & Fuels*, vol. 69, no. 3, pp. 999–1005, 1999.

[59] J. Abanades and D. Alvarez, "Conversion limits in the reaction of CO_2 with lime," *Energy & Fuels*, vol. 17, no. 10, pp. 308–315, 2003.

[60] D. Alvarez and J. Abanades, "Determination of the critical product layer thickness in the reaction of CaO with CO_2," *Ind. Eng. Chem. ...*, vol. 44, no. 15, pp. 5608–5615, 2005.

[61] D. Alvarez and J. Abanades, "Pore-size and shape effects on the recarbonation performance of calcium oxide submitted to repeated calcination/recarbonation cycles," *Energy & Fuels*, vol. 90, no. 9, pp. 270–278, 2005.

[62] P. Ollero, A. Serrera, R. Arjona, and S. Alcantarilla, "Diffusional effects in TGA gasification experiments for kinetic determination," *Fuel*, vol. 81, pp. 1989–2000, 2002.

[63] A. Gomez-barea, P. Ollero, and R. Arjona, "Reaction-diffusion model of TGA gasification experiments for estimating diffusional effects," *Fuel*, vol. 84, pp. 1695–1704, Apr. 2005.

[64] Q. Song, B. He, Q. Yao, Z. Meng, and C. Chen, "Influence of diffusion on thermogravimetric analysis of carbon black oxidation," *Energy & fuels*, no. 12, pp. 1895–1900, 2006.

[65] P. K. Gallagher and D. W. Johnson Jr, "The effects of sample size and heating rate on the kinetics of the thermal decomposition of $CaCO_3$," *Thermochim. Acta*, vol. 6, no. 1, pp. 67–83, 1973.

[66] R. H. Borgwardt, "Calcination kinetics and surface area of dispersed limestone particles," *AIChE J.*, vol. 31, no. 1, pp. 103–111, 1985.

[67] J. H. Sharp, F. W. Wilburn, and R. M. McIntosh, "The effect of procedural variables on TG, DTG and DTA curves of magnesite and dolomite," *J. Therm. Anal.*, vol. 37, no. 9, pp. 2021–2029, 1991.

[68] I. Galan, F. P. Glasser, and C. Andrade, "Calcium carbonate decomposition," *J. Therm. Anal. Calorim.*, vol. 111, no. 2, pp. 1197–1202, 2013.

[69] P. K. Gallagher and D. W. Johnson, "Kinetics of the thermal decomposition of $CaCO_3$ in CO_2 and some observations on the kinetic compensation effect," *Thermochimica Acta*, vol. 14, no. 3. pp. 255–261, 1976.

[70] Y. Wang and W. Thomson, "The effect of sample preparation on the thermal decomposition of $CaCO_3$," *Thermochim. Acta*, vol. 255, pp. 383–390, 1995.

[71] Y. Wang and W. J. Thomson, "The effects of steam and carbon dioxide on calcite decomposition using dynamic X-ray diffraction," *Chemical Engineering Science*, vol. 50, no. 9. pp. 1373–1382, 1995.

[72] J. Ewing, D. Beruto, and A. W. Searcy, "The nature of CaO produced by calcite powder decomposition in vacuum and in CO_2," *J. Am. Ceram. Soc.*, vol. 62, no. 11–12, pp. 580–584, 1979.

[73] D. Beruto, L. Barco, and A. W. Searcy, "CO_2-Catalyzed Surface Area and Porosity Changes in High-Surface-Area CaO Aggregates," *J. Am. Ceram. Soc.*, vol. 67, no. 7, pp. 512–516, 1984.

[74] R. H. Borgwardt, N. F. Roache, and K. R. Bruce, "Method for variation of grain size in studies of gas-solid reactions involving calcium oxide," *Ind. Eng. Chem. Fundam.*, vol. 25, no. 1, pp. 165–169, Feb. 1986.

[75] R. H. Borgwardt, "Calcium oxide sintering in atmospheres containing water and carbon dioxide," *Ind. Eng. Chem. Res.*, vol. 28, no. 4, pp. 493–500, Apr. 1989.

[76] R. H. Borgwardt, "Sintering of nascent calcium oxide," *Chem. Eng. Sci.*, vol. 44, no. 1, pp. 53–60, 1989.

[77] M. C. Mai and T. F. Edgar, "Surface area evolution of calcium hydroxide during calcination and sintering," *AIChE J.*, vol. 35, no. 1, pp. 30–36, 1989.

[78] C. R. Milne, G. D. Silcox, and D. W. Pershing, "Calcination and sintering models for alppication to high temperature, short time sulfation of calcium based sorbents," *Ind. Eng. Chem. Res.*, vol. 29, pp. 139–149, 1990.

[79] A. B. Fuertes, D. Alvarez, F. Rubiera, J. J. Pis, G. Marbán, and J. M. Palacos, "Surface area and pore size changes during sintering of calcium oxide particles," *Chem. Eng. Commun.*, vol. 109, no. 1, pp. 73–88, 1991.

[80] V. Fierro, J. Adánez, and F. García-Labiano, "Effect of pore geometry on the sintering of Ca-based sorbents during calcination at high temperatures," *Fuel*, vol. 83, no. 13, pp. 1733–1742, Sep. 2004.

[81] M. Alonso, Y. A. Criado, J. C. Abanades, and G. Grasa, "Undesired effects in the determination of CO_2 carrying capacities of CaO during TG testing," *Fuel*, vol. 127, pp. 52–61, Jul. 2014.

[82] D. Beruto, L. Barco, A. W. Searcy, and G. Spinolo, "Characterization of the Porous CaO Particles Formed by Decomposition of $CaCO_3$ and $Ca(OH)_2$ in Vacuum," *J. Am. Ceram. Soc.*, vol. 63, no. 7–8, pp. 439–443, 1980.

[83] D. T. Beruto, R. Botter, a. Lagazzo, and E. Finocchio, "Calcium oxides for CO_2 capture obtained from the thermal decomposition of $CaCO_3$ particles coprecipitated with Al^{3+} ions," *J. Eur. Ceram. Soc.*, vol. 32, no. 2, pp. 307–315, Feb. 2012.

[84] R. H. Borgwardt, K. R. Bruce, and J. Blake, "An investigation of product-layer diffusivity for calcium oxide sulfation," *Ind. Eng. Chem. Res.*, vol. 26, no. 10, pp. 1993–1998, Oct. 1987.

[85] R. H. Borgwardt, N. F. Roache, and K. R. Bruce, "Surface area of calcium oxide and kinetics of calcium sulfide formation," *Environ. Prog.*, vol. 3, no. 2, pp. 129–135, May 1984.

[86] Y. Zhu, S. Wu, and X. Wang, "Nano CaO grain characteristics and growth model under calcination," *Chem. Eng. J.*, vol. 175, pp. 512–518, Nov. 2011.

[87] M. . Lowell, S., Shields, J.E., Thomas, M.A., Thommes, "Characterization of porous solids and powders: surface area, pore size and density." *Springer US*, 2004.

[88] V. K. . Pecharsky and P. Y. Zavalij, "Fundamentals of powder diffraction and structural characterization of materials." *Springer US*, 2003.

[89] R. E. Dinnebier and S. J. L. Billinge, "Powder Diffraction - Theory and Practice " *The Royal Society of Chemistry*, 2008.

[90] C. Hammond, "Introduction to crystallography." *Zanichelli*, 1994.

[91] A. Guagliardi, N. Masciocchi, "Analisi di materiali policristallini mediante tecniche di diffrazione." *Insubria University Press*, 2007.

[92] H. Rietveld, "Line profiles of neutron powder-diffraction peaks for structure refinement," *Acta Crystallogr.*, vol. 22, no. 1, pp. 151–152, Jan. 1967.

[93] H. Rietveld, "A profile refinement method for nuclear and magnetic structures," *J. Appl. Crystallogr.*, vol. 2, no. 2, pp. 65–71, Jun. 1969.

[94] J. Als-Nielsen and D. McMorrow, *Elements of modern X-ray physics*. 2011.

[95] C. Babé, M. Tayakout-Fayolle, C. Geantet, M. Vrinat, G. Bergeret, T. Huard, and D. Bazer-Bachi, "Crystallite size effect in the sulfidation of ZnO by H_2S: Geometric and kinetic modelling of the transformation," *Chem. Eng. Sci.*, vol. 82, pp. 73–83, Sep. 2012.

[96] S. Syed-Hassan and C. Li, "Effects of crystallite size on the kinetics and mechanism of NiO reduction with H2," *Int. J. Chem. Kin.*, 2011.

[97] R. V. Denys, A. B. Riabov, J. P. Maehlen, M. V. Lototsky, J. K. Solberg, and V. A. Yartys, "In situ synchrotron X-ray diffraction studies of hydrogen desorption and absorption properties of Mg and Mg–Mm–Ni after reactive ball milling in hydrogen," *Acta Materialia*, vol. 57, no. 13. pp. 3989–4000, 2009.

[98] C. Rodriguez-Navarro, E. Ruiz-Agudo, A. Luque, A. B. Rodriguez-Navarro, and M. Ortega-Huertas, "Thermal decomposition of calcite: Mechanisms of formation and textural evolution of CaO nanocrystals," *Am. Mineral.*, vol. 94, no. 4, pp. 578–593, 2009.

[99] C. Rodriguez-Navarro, K. Kudlacz, and E. Ruiz-Agudo, "The mechanism of thermal decomposition of dolomite, New insights from 2D XRD and TEM analyses," *Am. Mineral.*, vol. 97, pp. 38–51, 2012.

[100] P. Engler, M. W. Santana, M. L. Mittleman, and D. Balazs, "Non-isothermal, in situ XRD analysis of dolomite decomposition," *Thermochimica Acta*, vol. 140. pp. 67–76, 1989.

[101] R. Molinder, T. P. Comyn, N. Hondow, J. E. Parker, and V. Dupont, "In situ X-ray diffraction of CaO based CO_2 sorbents," *Energy Environ. Sci.*, vol. 5, no. 10, pp. 8958–8969, 2012.

[102] E. J. Mittemeijer and U. Welzel, "The 'state of the art' of the diffraction analysis of crystallite size and lattice strain," *Zeitschrift für Kristallographie Supplements*, vol. 2008, no. 27. pp. 99–99, 2008.

[103] P. Scardi, M. Leoni, and R. Delhez, "Line broadening analysis using integral breadth methods: A critical review," *Journal of Applied Crystallography*, vol. 37, no. 3. pp. 381–390, 2004.

[104] M. Broda, A. M. Kierzkowska, and C. R. Müller, "Influence of the Calcination and Carbonation Conditions on the CO_2 Uptake of Synthetic Ca-Based CO_2 Sorbents," *Environ. Sci. Technol.*, vol. 46, no. 19, pp. 10849–10856, Sep. 2012.

[105] F. García-Labiano, A. Abad, L. de Diego, P. Gayán, and J. Adánez, "Calcination of calcium based sorbents at pressure in a broad range of CO_2 concentrations.," *Chem. Eng. Sci.*, vol. 57, pp. 2381–2393, 2002.

[106] A. P. Hammersley, "FIT2D: An introduction and Overview," ESRF Internal Report, ESRF97HA02T, 1997

[107] A. P. Hammersley, S. O. Svensson, M. Hanfland, A. N. Fitch, and D. Hausermann, "Two-dimensional detector software: From real detector to idealised image or two-theta scan," *High Press. Res.*, vol. 14, no. 4–6, pp. 235–248, 1996.

[108] A. Larson and R. Von Dreele, "General Structure Analysis System (GSAS) ", *Los Alamos National Laboratory Report, LAUR*, 1994.

[109] M. Holt, R. Harder, R. Winarski, and V. Rose, "Nanoscale Hard X-Ray Microscopy Methods for Materials Studies," *Annu. Rev. Mater. Res.*, vol. 43, no. 1, pp. 183–211, 2013.

[110] J. L. Provis, V. Rose, R. P. Winarski, and J. S. J. Van Deventer, "Hard X-ray nanotomography of amorphous aluminosilicate cements," *Scr. Mater.*, vol. 65, no. 4, pp. 316–319, 2011.

Appendix

This appendix reports the comparison between $CaCO_3$ average crystallite size and CaO conversion versus time curves obtained from the carbonation experiments performed at the beamline 17-BM-B, using the synchrotron radiation X-ray powder diffraction technique. The operating conditions of each experiment are indicated in Table 4.1. As discussed in § 4.3.1.6, these data were used to evaluate the critical carbonate product layer thicknesses.

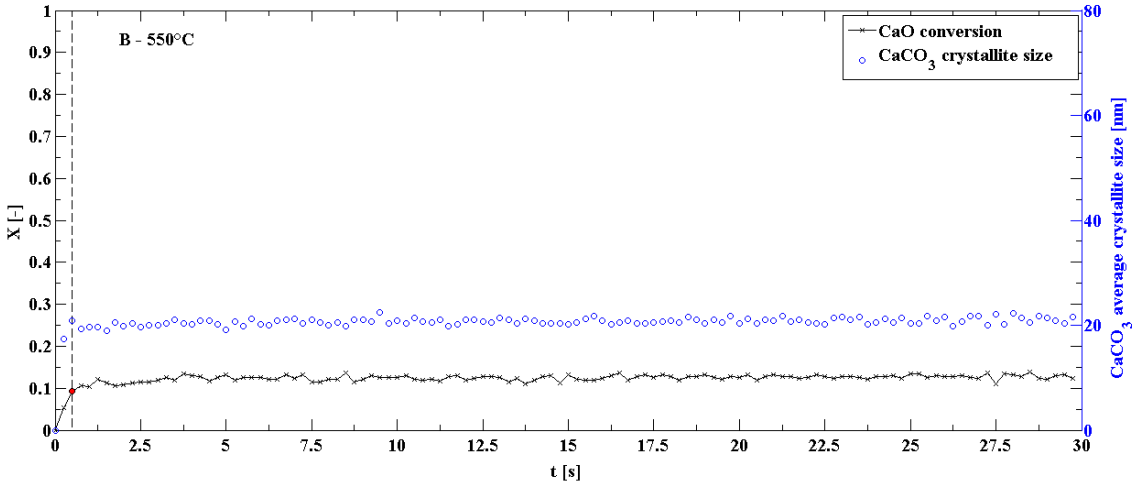

Figure A.1: *Comparison between $CaCO_3$ average crystallite size and CaO conversion versus time curves used to evaluate the critical carbonate product layer thickness. Run B (Table 4.1).*

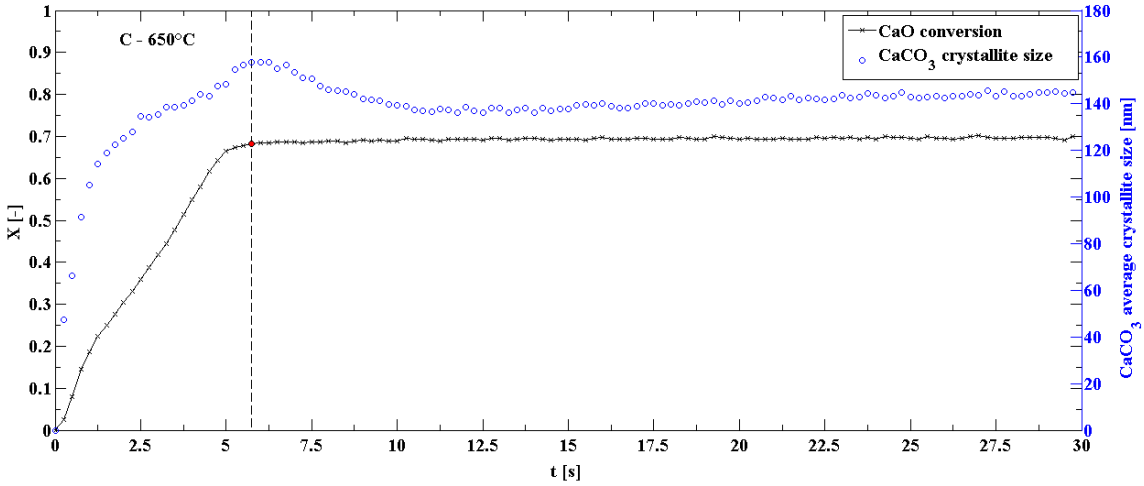

Figure A.2: *Comparison between $CaCO_3$ average crystallite size and CaO conversion versus time curves used to evaluate the critical carbonate product layer thickness. Run C (Table 4.1).*

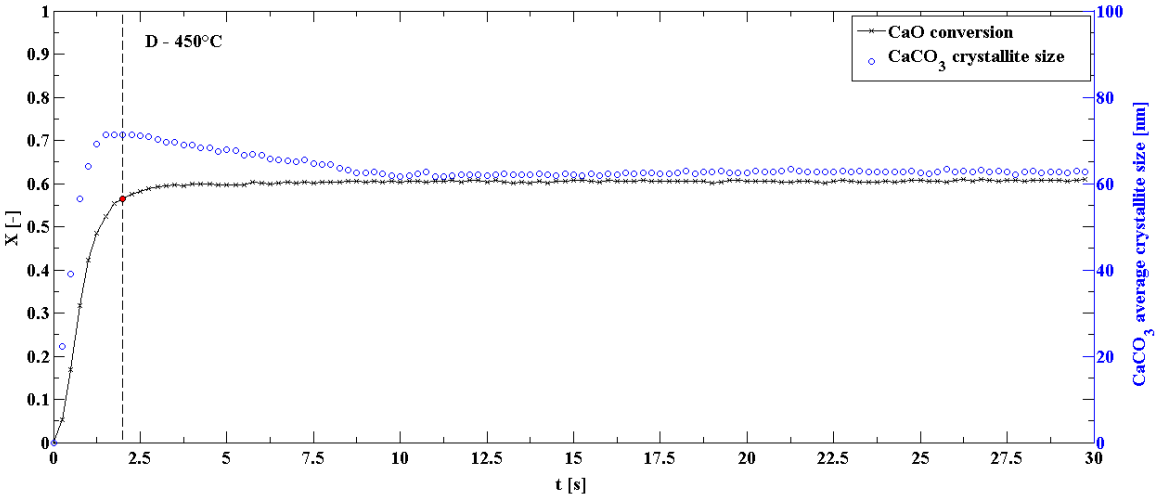

Figure A.3: *Comparison between $CaCO_3$ average crystallite size and CaO conversion versus time curves used to evaluate the critical carbonate product layer thickness. Run D (Table 4.1).*

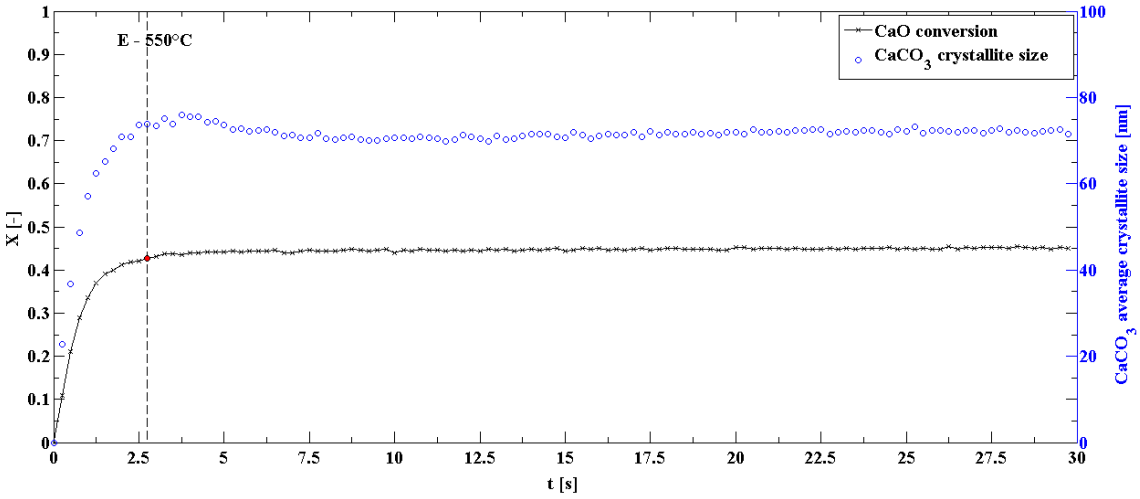

Figure A.4: *Comparison between $CaCO_3$ average crystallite size and CaO conversion versus time curves used to evaluate the critical carbonate product layer thickness. Run E (Table 4.1).*

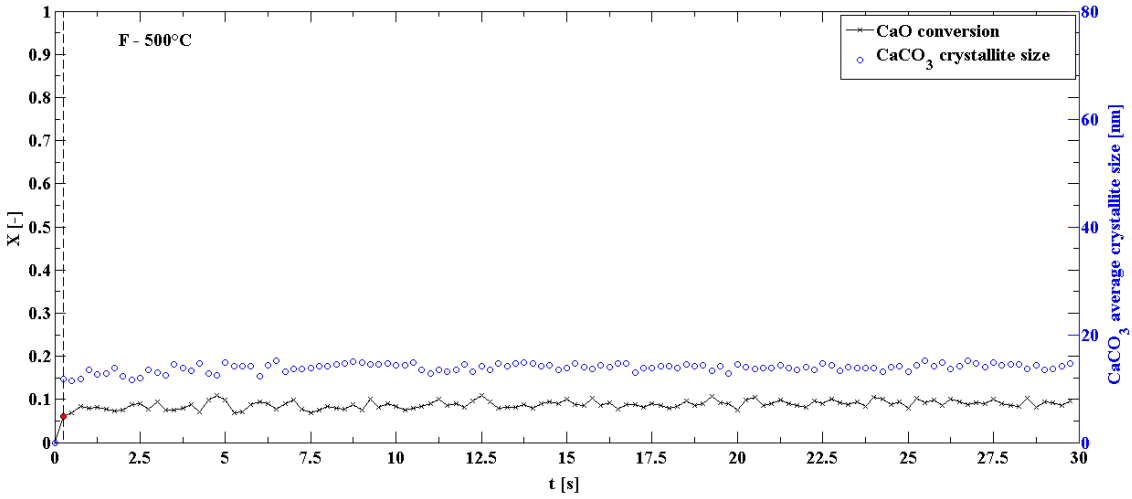

Figure A.5: *Comparison between $CaCO_3$ average crystallite size and CaO conversion versus time curves used to evaluate the critical carbonate product layer thickness. Run F (Table 4.1).*

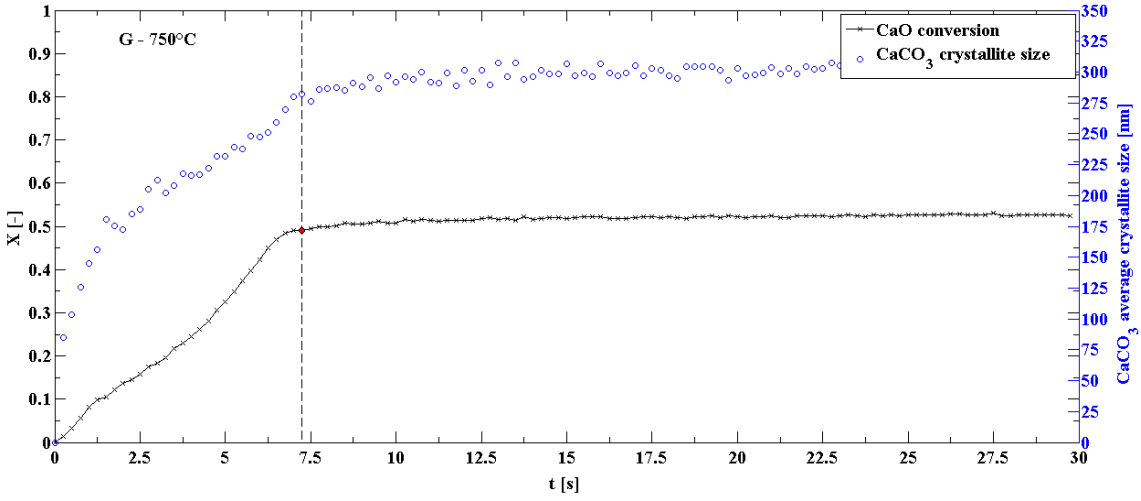

Figure A.6: *Comparison between $CaCO_3$ average crystallite size and CaO conversion versus time curves used to evaluate the critical carbonate product layer thickness. Run G (Table 4.1).*

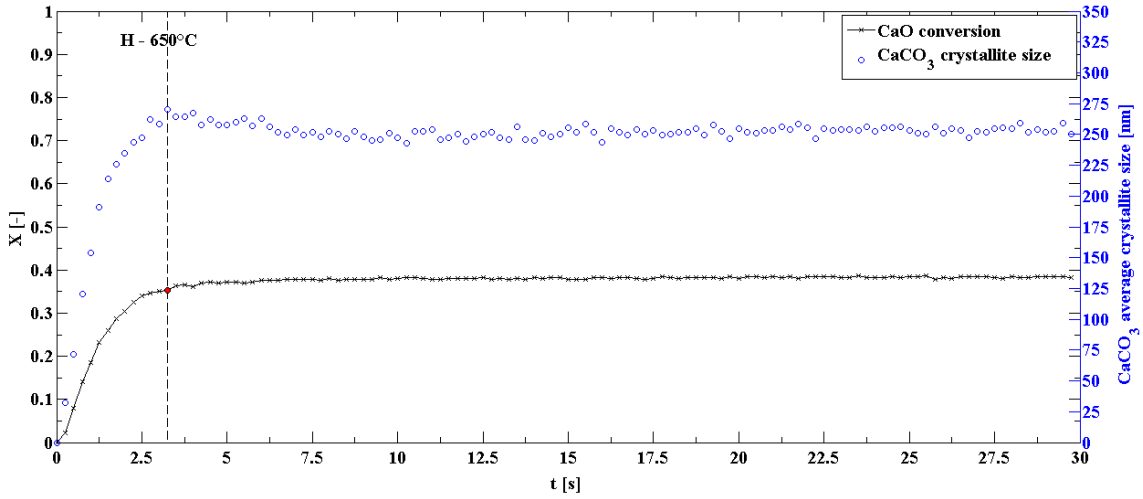

Figure A.7: *Comparison between $CaCO_3$ average crystallite size and CaO conversion versus time curves used to evaluate the critical carbonate product layer thickness. Run H (Table 4.1).*

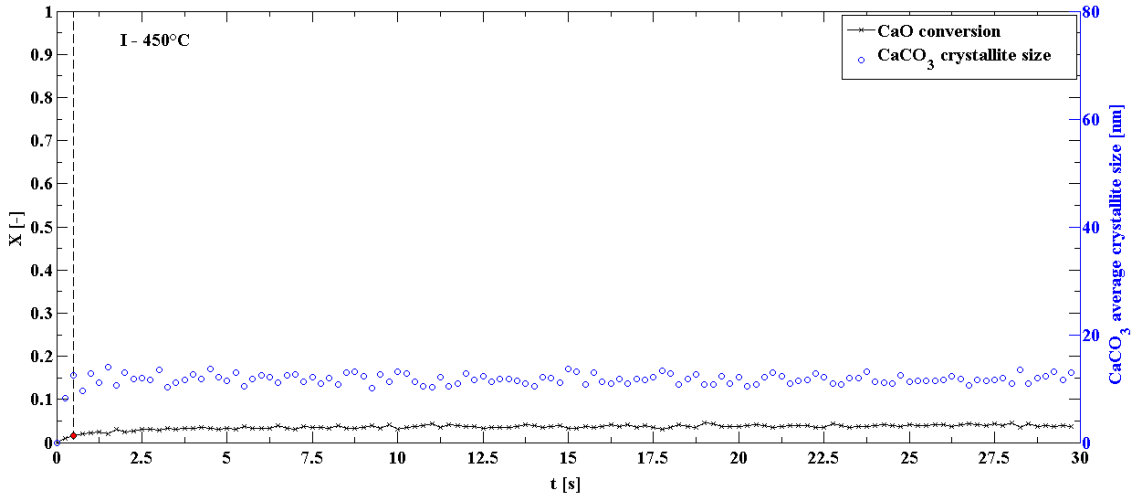

Figure A.8: *Comparison between $CaCO_3$ average crystallite size and CaO conversion versus time curves used to evaluate the critical carbonate product layer thickness. Run I (Table 4.1).*

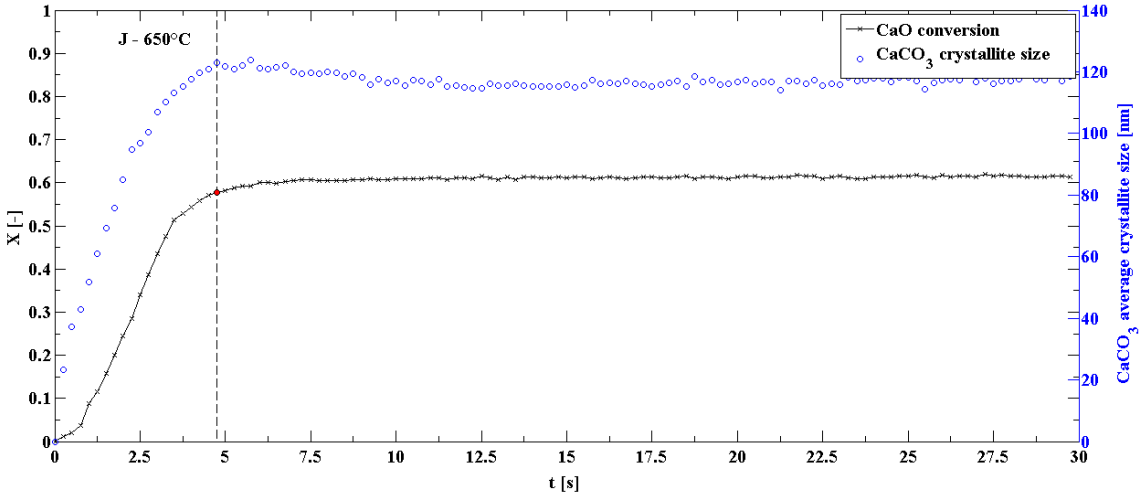

Figure A.9: *Comparison between $CaCO_3$ average crystallite size and CaO conversion versus time curves used to evaluate the critical carbonate product layer thickness. Run J (Table 4.1).*

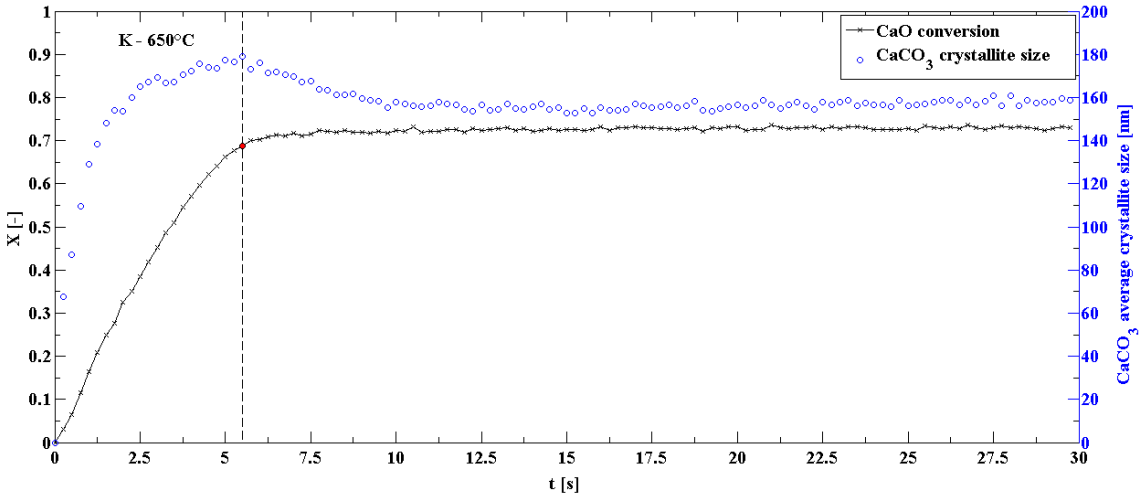

Figure A.10: *Comparison between $CaCO_3$ average crystallite size and CaO conversion versus time curves used to evaluate the critical carbonate product layer thickness. Run K (Table 4.1).*

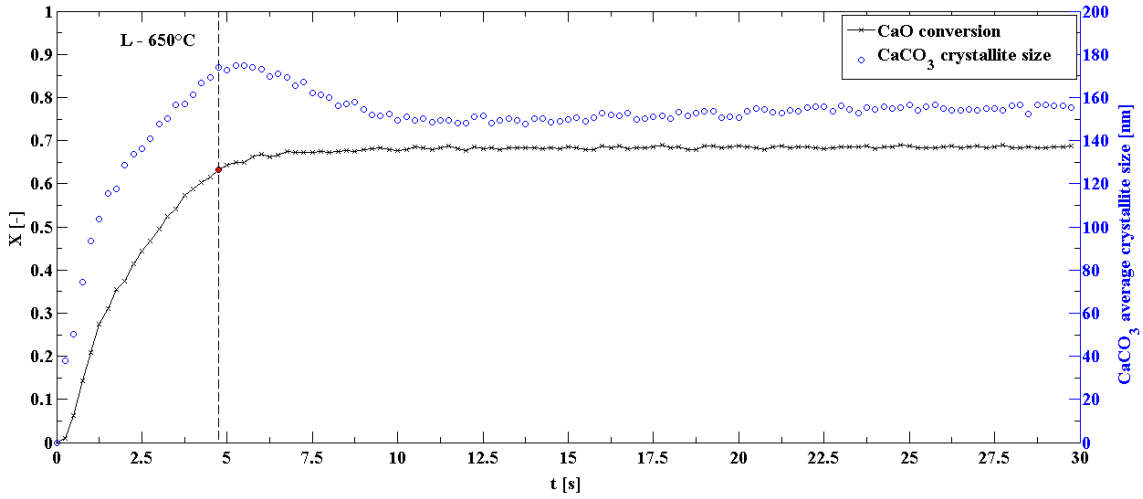

Figure A.11: *Comparison between $CaCO_3$ average crystallite size and CaO conversion versus time curves used to evaluate the critical carbonate product layer thickness. Run L (Table 4.1).*

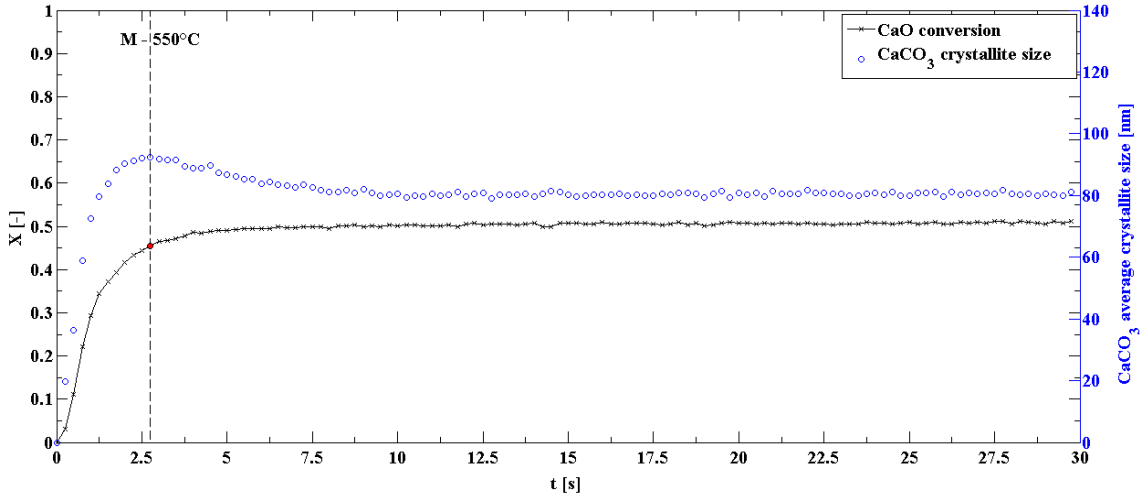

Figure A.12: *Comparison between $CaCO_3$ average crystallite size and CaO conversion versus time curves used to evaluate the critical carbonate product layer thickness. Run M (Table 4.1).*

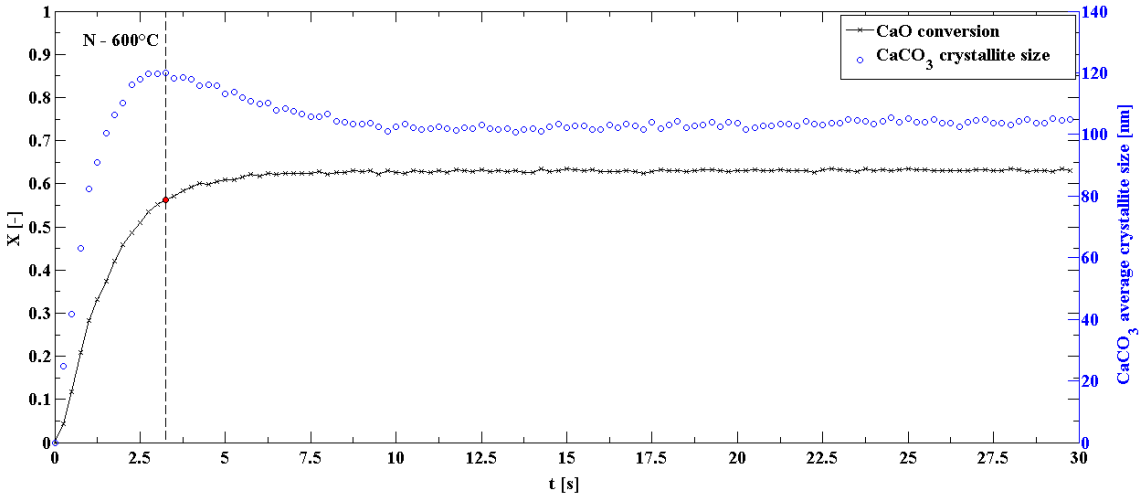

Figure A.13: *Comparison between $CaCO_3$ average crystallite size and CaO conversion versus time curves used to evaluate the critical carbonate product layer thickness. Run N (Table 4.1).*

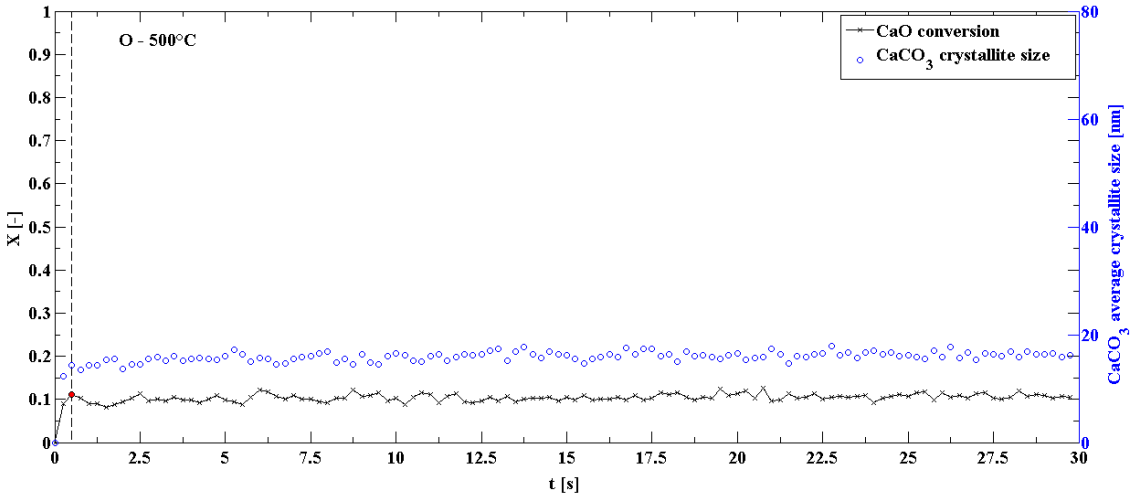

Figure A.14: *Comparison between $CaCO_3$ average crystallite size and CaO conversion versus time curves used to evaluate the critical carbonate product layer thickness. Run O (Table 4.1).*

Acknowledgements

I think that the great things everyone can reach in his own life cannot be achieved by himself. For this reason, at the end of this journey there are many people I have to thank for their intellectual, emotional and technical contribution to this work and for their support throughout this “challenging adventure”.

I would like to express my gratitude to my supervisor, Prof. Matteo Strumendo, for giving me the opportunity to work on this exciting research topic. Thank you for the support, encouragement, patience and help along these three years of collaboration.

A special mention goes to Prof. Gabriella Salviulo and Dr. Federico Zorzi, for their observations and criticisms that helped during this scientific work. In particular, I would like to express my immense and warm appreciation to Federico because this thesis would have not been the same without all his teachings and suggestions. Thank you for your essential contribution to my professional growth and for your kind help.

Valuable help and advices were received by many people during the development of this project, especially Eng. Silvia Dottor and Eng. Alberto Benedetti together with I shared part of my research activity. Thank you guys for ideas and great discussions, not only related to work. A special encouragement/wish goes to Alberto for his new experience as a PhD student. My acknowledgements go also to Prof. Roberta Bertani for her availability and teachings; to Dr. Stefano Besco and Prof. Alessandra Lorenzetti for our discussions about TGA; to Dr. Giovanni Capurso for his helpfulness and friendship.

This research project allowed me to live a wonderful (even if too short!) experience as a “brain drain” in the United States. Remembering this amazing period, I will always be grateful to Prof. Carlo U. Segre for his incomparable help and guidance in the work carried out at the APS, and for his kindness and support during my visit in Chicago and at the Illinois Institute of Technology. My sincere acknowledgement for giving me the possibility to work at IIT, for the “introduction to synchrotron radiation”, for being brilliant in science and so human in life.

My acknowledge goes also to APS for providing us the beamtime and to all the people I met there. In particular, my special thanks are directed to Dr. G. J. Halder and Dr. A. Yakovenko for their help during the work at the 17-BM-B beamline: your skilful assistance during the synchrotron radiation experiments has been greatly appreciated. Additionally, special gratitude is also directed to Dr. James A. Kaduk for his valuable advices and suggestions regarding the Rietveld refinement method.

In addition, I have to thank all the kind guys I had the chance to meet in my "American experience" and which have become my "brothers". Razib, Shankar, Nathaniel and all the guys of the Department of Physics: thank you for your friendship and for helping me to improve my English.
I would like also to express my immense gratitude to Tracy and Angela, my favorite "American women"! Thank you very much for all that you made for me, for your kindness and for sharing precious moment of life with me. Listening to jazz music it's not the same thing without you! I really miss you and Chicago.
Warm thanks to Stefano, Solidea and all the other friends I met during my permanence in the "Windy City": I will never forget you and the happy moments we had together.

Certainly, I cannot forget to thank my nice office mates in Padova, Micol and Nicola, without whom this period of my life would have been more wearing. Thank you for your positive attitude in front of the difficulties and your respect.

I have to be grateful to all my friends and my family for their unconditional care and support throughout the years. My family members have always encouraged me and this work could not have been completed without the enormous backing and love from them.
A special thought goes to the person that makes me great in all positive ways: Francesca thank you for infinite patience, love and to have a special place in your heart.

Finally, a special thought and thank to God for watching over me always, for giving me the serenity to accept things I cannot change, the courage to change things I can change and, especially, the smile to light up the world!